

Magnetic Interface Structures in Exchange Bias Systems

Joseph Gompertz

Doctor of Philosophy

University of York
Physics

September 2019

Abstract

Systematic measurements were performed on sputtered polycrystalline multilayer thin films containing CoFe (5 nm)/IrMn (10 nm). A number of phenomena were described and explained for the first time. The York Model of Exchange Bias was used to interpret the effect of the interface between the ferromagnetic (F)/antiferromagnetic (AF) layers.

An ultra-thin interfacial layer of Mn with a thickness between 0 and 0.6 nm was added between the F and AF layers to alter the interfacial composition. The films were analysed by X-ray diffraction (XRD) and transmission electron microscope (TEM) imaging. Their magnetic behaviour was measured using temperature-controlled vibrating sample magnetometry (VSM).

A marked irreversibility in the loop shift H_{ex} after setting was observed together with large increases in the coercivity H_c ($\times 4$) and athermal training ΔH_{c1} . These latter effects are attributed to spin cluster freezing which also increased H_{ex} by up to 50 %. The cluster freezing was observed to occur over a wide range of temperatures (> 200 K) and to below 5 K. This is consistent with diffusion of Mn at the F/AF interface which varied with the thickness of the Mn interfacial layer.

An asymmetry of the saturation magnetisation Δm_s between the set and reversed directions was measured in detail. This was found to be consistent with the F alignment of a single Mn atomic layer at the surface of the IrMn. Δm_s was observed to exhibit a peak at < 10 K. At present this observation is unexplained.

Contents

Abstract	ii
Contents	iii
List of Tables	vii
List of Figures	viii
Acknowledgements	xiii
Author Declaration	xiv
1 Introduction	1
1.1 Note on Units and Errors	5
2 Magnetism in Thin Films	6
2.1 Exchange Interactions	6
2.1.1 Direct Exchange	6
2.1.2 Indirect Exchange	8
2.1.3 Superexchange	9
2.1.4 Dzyaloshinskii-Moriya Interaction	9
2.1.5 Ferrimagnetism	10
2.2 Anisotropy	10
2.2.1 Magnetocrystalline Anisotropy	10
2.2.2 Anisotropy and Domains	13
2.2.3 The Stoner-Wohlfarth Model	15
2.2.4 AF Anisotropy	19
2.2.5 Other Anisotropies	20
2.2.6 Exchange Anisotropy	22
2.2.7 Temperature Dependence of Anisotropy	24
2.3 Antiferromagnetic Materials	26

2.3.1	Structure of Antiferromagnetic Materials	26
2.3.2	Structure of IrMn	27
2.3.3	Interfacial Exchange Coupling	30
2.3.4	Characterisation of Exchange Bias Hysteresis Loops	33
3	Features of Exchange Bias	35
3.1	Early Observations	35
3.1.1	Exchange Field	35
3.1.2	Rotational Hysteresis	36
3.1.3	Enhanced Coercivity	37
3.2	Dynamic Effects	38
3.2.1	Thermal Activation	38
3.2.2	The Training Effect	40
3.2.3	Reversal Asymmetry	41
3.3	Structural Effects	42
3.3.1	Texture	43
3.3.2	Composition	44
3.3.3	Interfacial Doping Effects	46
3.3.4	Effects of Diffusion	48
3.4	Related Phenomena	53
3.4.1	\vec{H}_{set} Dependence	53
3.4.2	Trilayer Experiment	54
3.4.3	Spin Freezing	55
3.4.4	m_s Offset	56
4	Models of Exchange Bias	58
4.1	Early Models	60
4.1.1	Meiklejohn and Bean	60
4.1.2	Fulcomer and Charap	63
4.1.3	Stiles and McMichael	65
4.1.4	Domain State Model	67
4.2	The York Model of Exchange Bias	69
4.2.1	Thermal Processes	69
4.2.2	The York Protocol	73
4.2.3	Measurement of the Blocking Temperature	76
4.2.4	Measurement of Antiferromagnetic Anisotropy	78
4.2.5	Setting Limitations	82
4.2.6	Grain Volume Dependence of Exchange Bias	84

4.2.7	Magnetic Viscosity	86
4.2.8	Limitations of the York Model of Exchange Bias	89
4.3	Proposed Extensions to Exchange Bias Models	91
5	Characterisation	96
5.1	Sample Preparation	96
5.1.1	HiTUS System	96
5.1.2	Sputtering Procedure	99
5.1.3	Film Thickness	100
5.2	Structural Characterisation	102
5.2.1	X-ray Crystallography	102
5.2.2	Grain Size Analysis	111
5.3	Magnetic Characterisation	117
5.3.1	Vibrating Sample Magnetometer	117
6	High-Temperature Behaviour	122
6.1	Irreversibility of Exchange Bias	123
6.1.1	Setting and Resetting	123
6.1.2	Time Dependence of Setting	127
6.1.3	Origin of Magnetic Irreversibility	130
6.1.4	Origin of Compositional Irreversibility	133
6.2	Thermal Activation	137
6.2.1	Blocking Temperature for Films with Manganese-Doped Interfaces	137
6.2.2	Effect of Interfacial Mn on Maximum Exchange Bias	139
6.2.3	Effect of Interfacial Mn on the Median Blocking Tempera- ture and Anisotropy	142
7	Low-Temperature Behaviour	149
7.1	Spin Freezing	150
7.1.1	Spin Freezing of Exchange Bias	151
7.1.2	Spin Freezing of Coercivity and Training	153
7.2	Magnetisation Offset	156
7.2.1	Temperature Dependence of m_s Offset	156
7.2.2	Effect of Training on m_s Offset	164
7.2.3	Effect of Interfacial Mn on m_s Offset	170
7.2.4	Ferromagnetic-Antiferromagnetic Coupling	180
8	Conclusions and Further Work	182

<i>CONTENTS</i>	vi
8.1 Further Work	185
List of Acronyms and Abbreviations	187
List of Symbols and Units	189
References	198
List of Publications	207

List of Tables

5.1	The nominal values and modelling parameters used in the fit of fig. 5.8 showing film thickness d_f , density ρ_f and interfacial roughness σ_f . . .	110
6.1	Loop parameters for the loops shown in fig. 6.2 given for (A) a film set in a positive field and (B) the film set in the opposite direction.	126
6.2	Summary of H_{ex} , $\langle T_B \rangle$ and K_{AF} results for varied thickness of interfacial Mn.	144
7.1	Summary of the exchange bias, coercivity and training at 5.5 and 300 K showing the effect of spin freezing.	152
7.2	Summary of $\Delta m_s(T)$ for films with different values of d_{Mn} (i) before and (ii) after training.	173

List of Figures

2.1	Schematic of the Bethe-Slater curve.	7
2.2	At 4.5 K the saturation field of a multilayer oscillates as d_{Cr} increases.	8
2.3	Three families of crystal directions labelled in (a) a bcc Fe unit cell with (b) their corresponding magnetisation curves.	11
2.4	The stages of magnetising a F material in the hard direction.	14
2.5	The vector diagram for the Stoner-Wohlfarth model for the magnetisation curve of a single-domain particle.	15
2.6	Calculated hysteresis loops for a uniaxial particle in the Stoner-Wohlfarth model at an angle to an applied field.	16
2.7	Calculated hysteresis loops for an assembly of non-interacting and randomly oriented uniaxial particles in the Stoner-Wohlfarth model.	17
2.8	The sublattice magnetisations of a AF material in (a) low field, (b) a field sufficient to induce spin-flopping and (c) a field sufficient to induce metamagnetism.	19
2.9	Hysteresis loop of oxide-coated Co particles at 77 K as presented by Meiklejohn and Bean.	23
2.10	A sheet AF material with sublattices A and B.	26
2.12	The spin structure of IrMn_3 according to neutron diffraction studies of bulk samples.	29
2.13	Example hysteresis loops showing the effect of AF anisotropy and the effect of the setting process on H_{ex}	32
2.14	Schematic of an exchange-biased hysteresis loop with H_{ex} , H_{c} and ΔH_{c1} labelled.	33
3.1	Torque curves for exchange-biased Co/CoO nanoparticles for (a) increasing and (b) decreasing $\theta_{\vec{H}}$	37
3.2	Thermal activation for a IrMn/CoFe film set for 5400 s at 500 K in (a) $\vec{H}_{\text{set}} = 20\text{kOe}$ and (b) $\vec{H}_{\text{set}} = -20\text{kOe}$	39

3.3	The first loop training effect and subsequent thermal activation loops for Co/CoO thin films.	40
3.4	The asymmetry of reversal shown (a) schematically, (b) at a temperature above T_{NA} showing thermal activation	41
3.5	The asymmetry of reversal shown before and after training at a measurement temperature of at 5.5 K.	42
3.6	The blocking temperature T_B^{MAX} of an exchange bias material increases with (a) increasing integrated density and (b) decreasing FWHM of the $\{111\}$ IrMn diffraction peak.	43
3.7	Hysteresis loops for a film with (a) weak texture on a Cu seed layer and (b) strong texture on a NiCr seed layer.	44
3.8	The dependence of H_{ex} on the composition of IrMn.	45
3.9	The value of H_{ex} increases and goes through a peak with the addition of an ultra-thin layer of Mn with thickness d_{Mn}	46
3.10	Diffusion in a IrMn/Co/Cu thin film measured using atom-probe tomography before and after annealing.	50
3.11	The effects of diffusion on the hysteresis loops of an IrMn/Co thin film.	51
3.12	The concentrations of atomic species as function of depth through a IrMn/Co/chCu thin film.	52
3.13	The \vec{H}_{set} dependence of (a) H_{ex} and (b) normalised H_{ex} for films with varied median grain size.	54
3.14	The increase in exchange bias H_{ex} with setting field \vec{H}_{set} for samples with d_{Mn} at the F/AF interface.	54
3.15	The thermal activation of a F/AF/F system carried out at (a) negative saturation and (b) -150 Oe.	55
3.16	Measurement of exchange bias with T for CoFe/IrMn showing an increase in H_{ex} below 50 K attributed to spin freezing.	56
3.17	The magnetisation offset of (a) hysteresis loops as (b) a function of cooling field.	57
4.1	Schematic of (a) the F/AF interface with a small applied field and (b) vector diagram of the Meiklejohn and Bean model of exchange bias.	61
4.2	Schematic of (a) vector diagram and (b) an example of c_I having a value less than 1 in the Fulcomer and Charap model of exchange bias.	63
4.3	The Fulcomer and Charap model compared to experimental results for Co/CoO film.	65
4.4	The magnetisation of an AF sublattice rotates from parallel to the \vec{M}_F direction to parallel to $\pm \hat{u}$ forming a partial domain wall.	65

4.5	Schematic of a domain state with a spin imbalance.	67
4.6	The function $\ln(t)$	69
4.7	The York Protocol measurement shown (a) schematically and (b) as a list of steps.	75
4.8	The standard measurement of a blocking curve compared to the York Protocol.	77
4.9	$H_{\text{ex}} = 0$ at $\langle T_B \rangle$ because equal volumes of the AF film are set in two opposing directions.	80
4.10	Progressive thermal activation was used to find the dependence of d_{AF} on (a) $\langle T_B \rangle$, which was used to calculate (b) K_{AF}	81
4.11	Schematic of the grain volume distribution of AF grains after setting at T_{set} in a magnetic field and then cooling to a temperature at which a fraction of the AF is (a) thermally unstable, (b) the grains between V_c and V_{set} contribute to H_{ex} and a fraction of the grains are (c) unset.	82
4.12	Experimental measurements of the dependence of H_{ex} on grain volume match the forms predicted by eq. (4.22) for (a) AF grain diameter and (b) AF layer thickness.	85
4.13	The decay of H_{ex} for a given temperature is (a) linear with time and (b) when plotted as a function of T_{al} are shown to go through a peak.	87
4.14	Thermal activation measurements for an IrMn layer doped with Cu. The curves are calculated based on the set fractions of the grain volume distribution.	89
4.15	Simulated (a) thermal activation of exchange bias and (b) blocking temperature distribution using a spin-glass-like region at the interface.	92
4.16	A schematic of a F/AF interface showing the spin clusters through one magnetic reversal. The training effect is attributed to the change in magnetic order between the initial and final states.	94
5.1	Schematic of HiTUS system.	97
5.2	The surface of the IrMn target showing (a) the drilled holes which can be filled with material to adjust the effective target composition and (b) Ir crystals on the target surface.	98
5.3	Highlighted planes with their corresponding Miller Indices in a unit cube for (a) the family of $\{100\}$ planes, (b) the (110) plane and (c) the (111) plane.	103
5.4	(a) X-ray diffraction in θ - 2θ geometry and (b) schematic of a two bounce Ge(220) monochromator which uses the Bragg condition to eliminate all but one wavelength.	104

5.5	Example of typical θ - 2θ XRD data for a sample with a polycrystalline thin film and a single-crystal substrate.	104
5.6	X-ray diffraction in 2θ - χ - ϕ geometry.	106
5.7	Examples of pole figure measurements at the Bragg angle for IrMn (1 1 1).	107
5.8	Example of typical XRR data.	109
5.9	Schematic of a TEM.	112
5.10	Mass-thickness contrast for a wedge-shaped film prepared by focused ion beam milling.	113
5.11	Ray diagrams for (a) BF and (b) DF imaging modes.	114
5.12	A film region imaged in (a) BF and (b) its corresponding DF image.	115
5.13	Example of a grain size distribution in terms of (a) D_g and (b) V_g for a 10 nm thick IrMn layer.	116
5.14	Example of data from the Microsense Model 10 VSM for thin layers of CoFe.	118
5.15	Coil arrangement for the Microsense Model 10 VSM.	120
6.1	The portions of a grain size distribution that contribute to H_{ex} at (a) a temperature greater than T_{NA} and (b) T_{NA}	124
6.2	An example of irreversible exchange bias for a sample set in (A) 20 kOe and then (B) -20 kOe.	125
6.3	(a) The time dependence of H_{ex} for a film with (b) structure shown schematically.	128
6.4	In a magnetic viscosity measurement the grains between (a) and (b) activate earlier than the grains between (c) and (d), resulting in a rapid change in H_{ex} followed by a slow change.	129
6.5	The time dependence of (a) H_{ex} and (b) H_c plotted on a logarithmic axis.	134
6.6	(a) York Protocol blocking curves for films with (b) structure shown schematically (thicknesses in nm).	138
6.7	The exchange bias of films with interfacial Mn layers.	140
6.8	The magnetic phase diagram of CoMn alloys.	141
6.9	The median blocking temperature of films with interfacial Mn layers.	143
6.10	Schematic of the energy barrier distribution for two films with the same grain size distribution and different K_{AF}	145
7.1	(a)(i) The first hysteresis loop and (ii) the second hysteresis loop at 5.5 and 300 K for film with (b) structure shown schematically (thicknesses in nm).	151
7.2	H_{ex} for low-temperature measurements.	152

7.3	The temperature dependence of (a) H_c and (b) ΔH_{c1} . The film structure is shown schematically in fig. 7.1(b).	154
7.4	The normalised H_{ex} , H_c and ΔH_{c1} show a similar dependence on T	155
7.5	The measurement protocol to measure m_s^+ and m_s^- shown (a) schematically and (b) as a series of steps.	156
7.6	(a) The temperature dependence of Δm_s for the (i) first and (ii) second hysteresis loop for film with (b) structure shown schematically (thicknesses in nm).	157
7.7	Schematic of the F/AF interface of an exchange bias film showing three regions.	159
7.8	Schematic of the F/AF interface showing regions of F and AF order separated by the interface I during measurement of (a) $m_{s,i}^+$, (b) m_s^- and (c) $m_{s,ii}^+$	166
7.9	Schematic of the F/AF interface showing spins that are (i) parallel and (ii) aligned but not parallel.	168
7.10	The measurement protocol to measure $m_{s,i}^+$, m_s^- and $m_{s,ii}^+$ shown (a) schematically and (b) as a series of steps.	171
7.11	(a) The temperature dependence of Δm_s for the (i) first and (ii) second hysteresis loop for three films with (b) structure shown schematically (thicknesses in nm).	172
7.12	Schematic of the F/AF interface with (a) F and (b) AF spin clusters.	177

Acknowledgements

I would like to underline the critical roles played by the people, mentioned or unmentioned, without whom this work would have been impossible and to whom I offer a simple thanks.

I thank my parents and family for being a source of stability during a difficult time. For essential help in the operation and repair of laboratory equipment as well as sharing technical expertise, I would like to thank all the post-graduate research colleagues I have worked alongside, in particular John Sinclair, Will Frost, Ed Jackson, Kelvin Elphick, Ioan Polenciuc, Teo Huminiuc, Rob Carpenter, Jun-young Kim and Ben Murphy. Besides these are the many dear friends whose invisible contributions are not underestimated.

For indispensable work relating to the repair, maintenance, design, operation and functioning of laboratory equipment I owe a great debt to the technical staff of the Mechanical Workshop, Computer and Electronic Workshop and Research Services in the Department of Physics, as well as to the Mechanical Workshop in the Department of Chemistry and the York JEOL Nanocentre. In addition I would like to thank the many non-technical staff who have done great work on my behalf, foremost amongst whom is Susan Remmer. Furthermore, I express gratitude to the institutions which have facilitated this work. These include Seagate Technology, Diamond Light Source, Tohoku University, the University of Manchester and above all the funder of this work, the Department of Physics at the University of York.

I am especially appreciative of the incalculable contribution of my supervisor Kevin O'Grady whose expertise and attention to detail have been indispensable. He got me out a tricky spot for which I am very grateful.

Author Declaration

I declare that this thesis is a presentation of original work and I am the sole author. This work has not previously been submitted for an award at this, or any other, University. All sources are acknowledged as References.

Signed:

Joseph Gompertz

1. Introduction

When the phenomenon of exchange bias was discovered in 1956 it was considered a curiosity [1, 2]. This lack of applications was also expected to apply to anti-ferromagnetism as a whole, which is the material property from which exchange bias, in part, arises [3]. The potential technological applications of exchange bias were recognised in the 1990s [4]. The phenomenon became the subject of intense research and, in the typical fashion of the computer hardware industry, rose from obscurity to ubiquity in less than ten years [5].

Exchange bias is the phenomenon that made the high-capacity hard disk drive (HDD) possible and with it storage densities above 1 Tbit/inch² [6]. In order to operate these high-capacity storage disks at a useful speed a high-speed magnetic sensor is required. These sensors make use of giant magnetoresistance (GMR) or tunneling magnetoresistance (TMR), both of which affect the electrical resistance of a multilayered magnetic film based on the relative magnetic order of the constituent layers. In each case the resistance of the film is lowest when the layers have parallel magnetic order and decreases as the alignment diverges.

Exchange bias shifts the magnetic hysteresis loop away from the symmetrical condition [1, 2]. In effect, exchange bias can fix the magnetisation of a magnetic layer. By containing one free and one fixed layer, a GMR or TMR device can output a voltage that varies with the orientation of the free layer, operating as high-speed and high-sensitivity magnetic sensors [6]. These components make up the read head of the HDD, reading the data stored on the disk.

In the future, exchange bias could be fundamental in emerging areas of computer hardware technology [5]. The emerging area of spintronics promises high-speed and low-power computing in the near future by storing and transmitting in-

formation as spins, without the use of conventional currents [7]. The storage density of HDD has been increased by heat-assisted magnetic recording (HAMR) [8]. HAMR allows the same data stability to be achieved with smaller magnetised regions by raising the required writing temperature of the ferromagnetic layer well above room temperature. In the future, HAMR based on exchange bias could allow data to be written into an antiferromagnetic layer, making the disk immune to stray magnetic fields and further increasing storage density [9]. On the other hand the HDD could be replaced by magnetoresistive random-access memory (MRAM). The read times, write times, storage stability and power requirements of MRAM rivals or improves on current technology while containing no moving parts [10]. This means MRAM has the potential to perform as a universal memory, simultaneously superseding the HDD, capacitor-based dynamic random-access memory (DRAM) and transistor-based flash memory. The core operation of MRAM is the storage of data in an array of TMR junctions where the data is stored in the free layer and read by comparison to the layer fixed by exchange bias.

The design of the GMR and TMR read head prompted a focus on exchange bias in research. This improved our understanding of exchange bias which led to further manufacturing improvements and more widespread use of exchange bias technologies. However, despite this research interest and commercial success the physical understanding of exchange bias has not developed at the same rate. There is currently no complete theory of exchange bias and its related effects. Various models of exchange bias have been proposed and risen to prominence. While some of these models are mutually compatible, no model or synthesis of models have achieved a significant consensus. This lack of consensus is heightened by the disparate systems in which exchange bias occurs and the many different exchange bias effects which have been described. These systems vary by geometry, crystallinity and material. As such it is controversial to state that any exchange bias effect occurs in all systems generally, other than the most basic observations.

This study is concerned only with exchange bias in polycrystalline thin films and will not discuss exchange bias as it appears in epitaxial thin films or core-shell nanoparticles. This is because polycrystalline thin films are the preferred system in HDDs since they are easier to produce than single-crystal films. Exchange bias is critically dependent on the interface between a ferromagnetic (F) and an antiferromagnetic (AF) material. Due to the different conditions of the interface, exchange bias and exchange bias effects will not be the same for single-crystal films or core-

shell nanoparticles. This is why the application of a single model to all systems has not succeeded. Furthermore, this study will only discuss CoFe/IrMn systems. IrMn is the dominant antiferromagnetic material used in HDDs and commonly paired with ferromagnetic CoFe. The behaviour of different F and AF materials are diverse and a full discussion would be outside the scope of this work.

When focus is narrowed to polycrystalline thin films The most complete model to date is the York Model of Exchange Bias which was formalised in 2010, more than a decade after the first GMR HDD read heads were produced [11]. The York Model of Exchange Bias successfully predicted the dependence of exchange bias on the antiferromagnetic layer thickness and grain diameter. It was also corroborated by the temperature dependence of the logarithmic rate of setting. For this reason Seagate Technology and Western Digital have both publicly acknowledged that the York Model of Exchange Bias is used in the design and production of their HDD read heads.

However, the York Model of Exchange Bias is not complete. In particular, the behaviour of interfacial spins and their role in exchange bias has been unclear and controversial [12]. The York Model of Exchange Bias has one floating parameter, the interfacial stiffness parameter C^* which has been treated as a constant.

This work aims to observe and describe the behaviour of interfacial spins in an exchange bias system. This will be done in two important temperature regimes. The exact temperature ranges these represent vary between systems. However, the important distinction is that in the high-temperature regime the bulk of the antiferromagnetic layer has sufficient energy to reorder while in the low-temperature regime it does not. In the first case this allows the effect of the interface on the antiferromagnetic bulk to be observed. In the second case the bulk is constant and therefore the interface can be observed in isolation. These observations will be made using conventional magnetometers. However, the experimental procedures require and allow the control of the film's magnetic order using methods from and derived from the York Model of Exchange Bias [11]. By considering these phenomena in the context of earlier measurements a hypothetical interfacial spin structure will be proposed.

To establish the framework for this discussion, the relevant physics of magnetic thin films is established in chapter 2. While this chapter will discuss many aspects

of fundamental physics that are generally applicable, the context will be limited to polycrystalline thin films. Where this chapter goes into specifics will include a description of the structure of IrMn and the fundamentals of exchange coupling across interfaces.

Since there is no universally accepted model of exchange bias and because of the wide variety of exchange bias systems that have been studied there is potential for misunderstanding when exchange bias phenomena are discussed. Terms are not always consistently applied between different models and not all exchange bias phenomena exist in all systems. For clarity, the features of polycrystalline, thin-film exchange bias are discussed in chapter 3. This chapter will also serve as an introduction to exchange bias and the current state of knowledge on the subject.

This work is designed to build on and complement the York Model of Exchange Bias. For this reason the York Model of Exchange Bias is discussed in detail in chapter 4. This will include a discussion of the model's strengths and limitations and a description of the experimental procedures it requires. Of course, the York Model of Exchange Bias builds on and was influenced by earlier models. While it is not possible to explore the wide range of exchange bias models, this chapter will highlight a number of models which were proposed before the York Model of Exchange Bias and achieved some degree of orthodoxy.

This work is experimental in nature and therefore makes use of specialist equipment and techniques. In chapter 5 the production of polycrystalline thin films by plasma sputtering and structural analysis using X-ray diffractometer (XRD) and transmission electron microscope (TEM) is described. This is followed by a discussion of the equipment used to make magnetic measurements of the films. However, the magnetic treatment that occurs before and during the measurements vary significantly based on the measurement being performed. In all cases they require an application of the techniques described in section 4.2. For clarity, magnetic treatment before and during the measurements will be discussed alongside the results.

Observations and results will be described in two chapters, divided according to the temperature regime of the phenomena being investigated. The division between high and low temperature paradigms will vary for different systems. The systems discussed in this study are all CoFe/IrMn thin films with a temperature of non-activation (T_{NA}) of 300 K. The physical origin of T_{NA} and its importance in ex-

change bias measurements will be discussed in section 4.2. Phenomena occurring above this temperature will be discussed in chapter 6 and must consider both the antiferromagnetic bulk and the interface. On the other hand, below T_{NA} changes to the antiferromagnetic bulk are not possible, so the behaviour of the interface is isolated. These observations will be described in chapter 7. As observations are described, their consequences for a model of interfacial spins will be discussed.

A summary of this work appears in chapter 8. This includes a summary of observations and a hypothesis for the arrangement and role of interfacial spins in polycrystalline exchange bias systems. Finally, an outline of future work will be given.

1.1 Note on Units and Errors

No unit system dominates in the field of spintronics and in exchange bias research. There has been a general increase in the prevalence of the international system of units (SI). However, the older gram-centimetre-second unit system (cgs) is still firmly entrenched and well used. For this reason both SI and cgs appear in this work. That said, the majority of this work will be discussed in the cgs system in keeping with its prominence in the field. A full discussion of cgs units can be found in the standard text by Cullity and Graham [13]. For certain properties it is established that units which do not fit into either the SI or cgs systems are used. This is notably the case for information density which is typically stated in units of bit/inch². This is kept to a minimum in this work.

Where possible the numerical data in this work is quoted with errors calculated using standard Gaussian error techniques [14]. Values from the literature are quoted as they are reported. Thus where the error is not shown the error was not provided and is not known.

2. Magnetism in Thin Films

The discussion of magnetic phenomena must begin with an introduction to magnetism in general. However, it is not desirable or practical to comment on every part of the field. This chapter will cover only the aspects of magnetism which affect metallic polycrystalline ferromagnetic (F) and antiferromagnetic (AF) thin films where both the film thickness and lateral grain diameter are of the order 10 nm. Unless otherwise stated the source of information in this chapter is the standard text by Cullity and Graham [13]. In keeping with practice in the field and as discussed in section 1.1 this chapter will make use of the cgs system. In the cgs system units and in some cases dimensions of quantities differ from SI so care must be taken when converting between them.

2.1 Exchange Interactions

2.1.1 Direct Exchange

The most fundamental consideration of ferromagnetism is the origin of interatomic and intermolecular ordering. For ferromagnetism to occur there must be an interaction that causes a coherent overall arrangement of atomic magnetic moments. A calculation of magnetostatic forces due to dipole-dipole interactions shows that they are orders of magnitude too small to account for ferromagnetism. Instead this ordering comes from non-classical exchange forces.

The simplest example of exchange forces occurs in the diatomic hydrogen molecule. For two hydrogen atoms there will be a combination of attractive and re-

pulsive electrostatic forces in accordance with Coulomb's law due to the positively charged protons and negatively charged electrons. In addition, there is a probability that electrons can be exchanged between the two atoms which increases as the distance between the atoms reduces. As a consequence of the Pauli exclusion principle the electrons cannot have the same energy and the same four quantum numbers. Since the first three quantum numbers determine the electron's atomic shell the fourth, spin, must be different for the two electrons if they are to exchange between the hydrogen atoms. Thus the Pauli exclusion principle modifies the effect of the Coulomb interaction. If the electrons have parallel spins then they will tend to stay far apart, while if they have opposite spins they can occupy a single energy shell around both atoms. The exchange force due to this binds the hydrogen molecule only if the electrons have opposite spins.

The exchange energy E_{ex} is the additional energy of the two atoms due to the exchange force between them. For two atoms i and j with spin angular momentum $\vec{S}_i\hbar$ and $\vec{S}_j\hbar$ respectively, the exchange energy is given by

$$E_{\text{ex}} = -2J_{\text{ex}}\vec{S}_i \cdot \vec{S}_j \quad (2.1)$$

where J_{ex} is the exchange integral and \hbar is the reduced Planck's constant. If J_{ex} is positive, E_{ex} is minimised when the spins are parallel and maximised when they are antiparallel. Conversely, a negative J_{ex} means that E_{ex} is lowest for antiparallel spins and highest for parallel spins. Thus in principle it can be concluded that in a ferromagnetic (F) material J_{ex} is positive. In practice the sign of J_{ex} cannot be computed for a three-dimensional (3-D) lattice the way it can for a pair of hydrogen atoms.

For the metallic elements Fe, Co and Ni the ferromagnetically active electrons occupy the $3d$ electron shell. The expected value of J_{ex} is thus a function of the ratio of the atomic radius r_a to the radius of the $3d$ shell electrons r_{3d} . This is plotted on the Bethe-Slater curve shown in fig. 2.1. Atoms in a material with a positive J_{ex} align ferromagnetically, while those with a negative J_{ex} align antiferromagnetically. The value

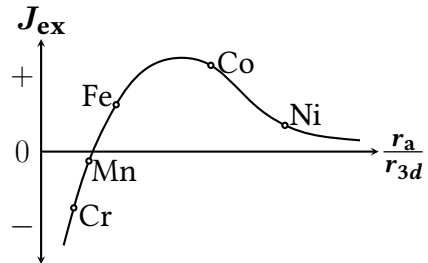


Figure 2.1: Schematic of the Bethe-Slater curve showing AF materials with negative values of J_{ex} and F materials with positive values of J_{ex} [13].

of J_{ex} is proportional to the magnetic ordering temperature. For a ferromagnetic material this temperature is known as the Curie temperature T_C , while for an antiferromagnetic material it is called the Néel temperature T_N . The thermal energy at T_C and T_N is sufficient to overcome the aligning effect of the exchange force. T_C and T_N are discussed in more detail in section 2.3.3 and section 6.1.3.

2.1.2 Indirect Exchange

Direct exchange can be used to explain the simplest magnetic materials. However, the exchange interaction is very short range and is often approximated as affecting only nearest-neighbour atoms. In addition, it has many limitations when applied to more complicated structures such as ordering across non-magnetic or frustrated barriers. The coupling across a non-magnetic barrier alternates between parallel and antiparallel as the thickness of the barrier increases [15]. This is shown in fig. 2.2 for a superlattice of Fe and Cr. Since a larger field is required to align films which are antiparallel compared to films which are parallel, the saturation field corresponds to the tendency of alternating layers to align antiparallel. This alternation rate is dependent on the material of the barrier layer [16, 17].

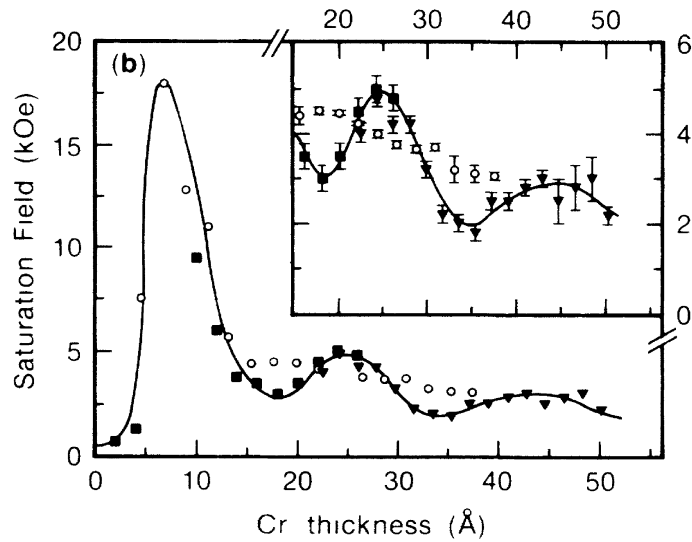


Figure 2.2: At 4.5 K the saturation field of an $[\text{Fe} (2 \text{ nm})/\text{Cr} (d_{\text{Cr}})]_N$ multilayer oscillates as d_{Cr} increases as a consequence of alternating parallel and antiparallel coupling [15].

Thus a second exchange interaction is used to explain long-distance ordering and magnetic ordering across non-magnetic materials. This indirect exchange force is mediated by the conduction electrons. The theory was initially developed

by Ruderman, Kittel, Kasuya and Yoshida to explain the F ordering of rare earth metals in which unpaired, highly localised $4f$ electrons are ordered despite lacking the overlapping wave functions required for direct exchange [18–20]. This Ruderman-Kittel-Kasuya-Yosida (RKKY) interaction arises from the polarisation of conduction electrons by inner shell electrons via the hyperfine interaction. The conduction electrons are free to move to other atoms, especially in a metal. The polarised electrons can then in turn polarise the valence electrons of another atom. In a F material the indirect interaction has a range limited by the scattering length of electrons in the material. However, in an AF material there is no net moment acting on the conduction electrons which results in no polarisation of conduction electrons. It has been shown that a sheath of AF material around F grains reduces the RKKY interaction [21]. This results in AF grains being uncoupled. The consequences of this will be discussed in section 4.2.4.

2.1.3 Superexchange

Superexchange is a mechanism for indirect exchange in ionic materials such as oxides. In materials which exhibit superexchange positively charged transition metal ions are separated by negatively charged ions, usually of oxygen. The $3d$ orbitals of the transition metals overlap the p orbital of the oxygen ion. Due to the Pauli Exclusion Principle the electrons in the p orbital of the oxygen ion must have opposite spins. Also due to the Pauli Exclusion Principle the spin of the electron in the transition metal orbital must be opposite that of the electron in the p orbital of the oxygen. Thus it must be the case that the transition metal ions have opposite spins due to overlapping the p orbital of the oxygen ion. In this way the spin ordering between the metal ions is coordinated without the need for electrons to be exchanged. Superexchange is a critical effect in antiferromagnetic oxides such as CoO and MnO. This study is concerned only with metallic materials in which superexchange does not play a role.

2.1.4 Dzyaloshinskii-Moriya Interaction

The Dzyaloshinskii-Moriya interaction (DMI) or asymmetric exchange results in a canting of AF spins away from antiparallel [22]. This results in a small F

moment perpendicular to the AF easy axis. The DMI is caused by spin-orbit coupling [23]. To observe the DMI highly ordered systems are required. Since the systems in this study are chemically disordered and polycrystalline, the effect of the DMI is negligible.

2.1.5 Ferrimagnetism

Ferrimagnetic materials were not distinguished from ferromagnetic materials until 1948 [24]. Like ferromagnetic materials, ferrimagnetic materials have a net magnetisation at room temperature, magnetically saturated domains and exhibit hysteretic magnetisation curves. On the other hand, their magnetic structure resembles that of antiferromagnetic materials. In a ferrimagnetic material there are ions with opposing magnetic moments. However, unlike in an antiferromagnetic material where these opposing moments are equal and thus cancel, the opposing moments in a ferrimagnetic material are not equal. Thus they do not cancel and the material has an overall magnetisation. The moments are not equal because a ferrimagnetic material is composed of two populations of elements or ions with different magnetic moments, such as Fe^{2+} and Fe^{3+} which both occur in magnetite. In addition, these populations are arranged in the lattice in a way that ensures that there is ferromagnetic-like, parallel alignment for ions of the same type but an antiferromagnetic-like, antiparallel alignment between the two types. In some ways ferrimagnetism can be considered a sort of ferromagnetism or as an incomplete form of antiferromagnetism. A full description of ferrimagnetism is not relevant to this work as no ferrimagnetic materials were studied.

2.2 Anisotropy

2.2.1 Magnetocrystalline Anisotropy

A material that is magnetically isotropic has magnetic properties that are the same when measured in all directions. Magnetic anisotropy is more common, meaning there are particular axes along which a material is easier to or harder to magnetise. Magnetocrystalline anisotropy is the anisotropy that arises from

the crystal structure of a material. In a F material it occurs only below the Curie temperature T_C . The body-centred cubic (bcc) unit cell of Fe is shown in fig. 2.3(a), labelled with three crystal directions. These directions are each representative of a family of directions related to each other by the symmetry of the lattice. The magnetisation curves measured along different crystal axes of Fe are shown schematically in fig. 2.3(b). The $\langle 100 \rangle$ direction is the magnetic easy axis because it saturates in the lowest field.

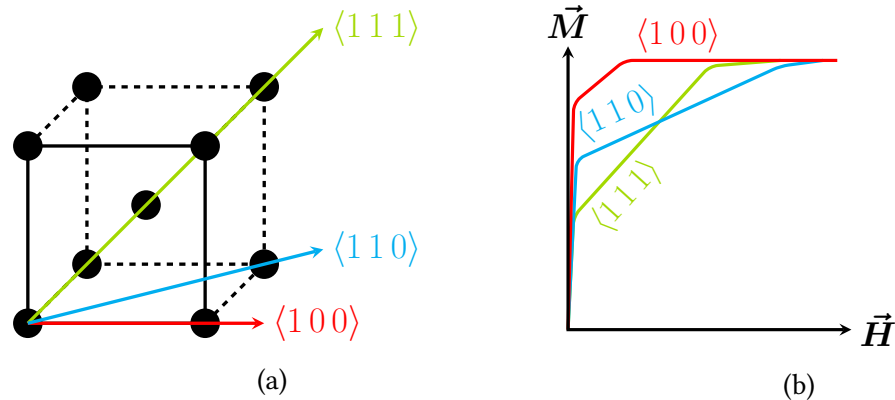


Figure 2.3: Three families of crystal directions labelled in (a) a bcc Fe unit cell with (b) schematics of corresponding magnetisation curves measured in those crystal directions [13].

Direct exchange was discussed in section 2.1.1. It depends on the relative alignments of spins with no consideration of a crystal lattice. Spin-spin coupling is a function of distance and is independent of crystallographic orientation. Direct exchange therefore does not contribute to the magnetocrystalline anisotropy energy. On the contrary, the atomic orbitals are strongly confined by the crystal lattice. However, it is possible to saturate a material in its hard direction. Thus the coupling between the lattice and the orbitals cannot be the origin of anisotropy as this coupling is too strong to overcome.

At the same time, there is a coupling between the spins and the orbitals. An external field that reorients the spin of an electron will also exert a moment on the orbitals to reorient them. Because of the strong lattice-orbit coupling the orbitals will not be reoriented and so will tend to hold the spin-orbit alignment. In other words, the energy required to reorient the spins is the energy required to overcome the coupling between the spins and the orbital. The origin of the magnetocrystalline anisotropy energy is therefore spin-orbit (L-S) coupling.

Magnetocrystalline anisotropy can therefore be regarded as a force which tends to hold the magnetisation in certain equivalent crystallographic directions in a crystal. The applied field therefore does work against this force to bring the magnetisation out of the easy direction. This work can be calculated if we assume the magnetisation \vec{M} of the crystal makes angles with the crystal lattice which have direction cosines α_1 , α_2 and α_3 . This energy density is expressed as a series expansion of the direction cosines such that

$$K = K_0 + K_1 (\alpha_1^2 \alpha_2^2 + \alpha_2^2 \alpha_3^2 + \alpha_3^2 \alpha_1^2) + K_2 (\alpha_1^2 \alpha_2^2 \alpha_3^2) + \dots \quad (2.2)$$

where K is the crystal anisotropy energy density and K_0 , K_1 and K_2 are constants for a given material at a given temperature with units of erg/cm^3 . The value of K_0 does not vary with the angle of \vec{M} and is usually therefore usually neglected, since only the difference in energy associated with different orientations is of interest. Terms of the series higher than K_2 are too small to be relevant and often K_2 itself is negligible.

When the angle between the magnetisation and the easy axis is small, the anisotropy acts like a magnetic field. This field holds the magnetisation parallel to the easy axis [13]. The torque exerted by this field on \vec{M} is equal to the torque exerted by the magnetocrystalline anisotropy. This model assumes the field and the spins are aligned. For this to be valid there must be no thermal motion and therefore $T = 0$. The anisotropy field can be expressed as

$$H_K = \frac{2K_u}{M_s} \quad (2.3)$$

where K_u is the anisotropy constant of a uniaxial crystal [13].

As shown in fig. 2.3, Fe saturates at the lowest field when magnetised in the $\langle 100 \rangle$ direction. for this reason the $\langle 100 \rangle$ direction is called the easy direction, whereas the $\langle 110 \rangle$ and $\langle 111 \rangle$ directions are increasingly hard. Different materials will have different easy and hard axis alignments. In Ni which has a face-centred cubic (fcc) structure the easy direction is $\langle 111 \rangle$, while the hardest direction is $\langle 100 \rangle$. Face-centred cubic structure is also known as cubic close-packed structure. The dependence of the easy and hard axes on the crystal structure is not known. In fact, Fe and Ni form a continuum of solid solutions where the easy direction is $\langle 111 \rangle$ below 25 at.% Fe and changes to $\langle 100 \rangle$ when the Fe concentration is above that amount. This is despite the fact that there is no change in crystal structure.

On the other hand non-cubic lattices can have predictable easy axes. For example the hexagonal close-packed (hcp) structure seen in Co has an easy axis along the axis of the hexagonal prism and a hard axis across the prism.

For this study the F material used was $\text{Co}_{70}\text{Fe}_{30}$. Binary CoFe alloys form a continuum of solid solutions up to 75 % Co [13]. Alloys up to 65 % Co have higher M_s than pure Fe [13, 25]. In particular M_s of iron-rich $\text{Co}_{30}\text{Fe}_{70}$ is (240 ± 1) emu/g, the highest room-temperature M_s of any known material [13, 25]. Cobalt-rich $\text{Co}_{70}\text{Fe}_{30}$ was chosen for this study because of its commercial relevance which is itself due to the material's relatively high M_s equal to (210 ± 1) emu/g, low H_c , high T_C equal to (1040 ± 10) K, bulk fcc structure and resistance to corrosion [26–28]. The easy axes of $\text{Co}_{70}\text{Fe}_{30}$ are in the $\langle 100 \rangle$ directions and the hard axes are in the $\langle 111 \rangle$ directions [25].

2.2.2 Anisotropy and Domains

Due to the exchange interaction F materials below T_C are magnetically ordered at the atomic level. However, not all F samples will have an overall magnetic moment. This is because the sample will be divided into distinct magnetic regions called domains. Each domain is magnetically ordered. In the absence of an external field the magnetisation within a domain is parallel to the easy direction. However there is no particular order between domains. In the ideal case there is no overall moment because the individual moments of the domains all cancel. A ferromagnetic material with two domains each with a magnetisation M_s but with no net magnetisation is shown in fig. 2.4(a)

The edge of a domain is marked by domain walls, where the magnetisation rotates from parallel with one domain to parallel with the other. A material can be saturated in the easy direction using a small field because the field only needs to facilitate domain wall motion. When a field is applied the domain walls move, meaning a larger proportion of the material is magnetised parallel to the external field and in an easy direction. This is shown in fig. 2.4(b) where the domain wall is marked as a dashed line. An external field \vec{H} has caused the domain wall to move, increasing the size of one domain and resulting in a net magnetisation $\vec{M} > 0$. When \vec{H} is applied parallel to the easy direction the material becomes saturated when it contains only a single domain, all others having been eliminated.

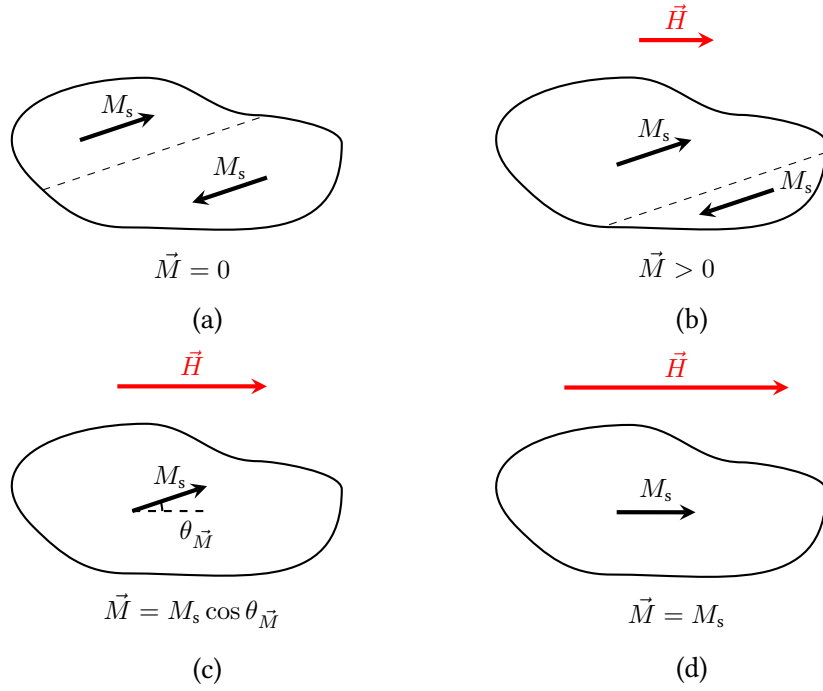


Figure 2.4: The stages of magnetising a F material in the hard direction where (a) is the demagnetised state, (b) is a magnetised state caused by domain wall motion due to the application of an external field \vec{H} , (c) is a single-domain state and (d) is the saturated condition [13]. The domain wall is shown as a dashed line.

However, a larger field is required to saturate a magnetic material in a hard direction. This is because the final state of saturation requires rotation of the atomic moments away from the easy direction and into the external field direction. In fig. 2.4(c) the external field \vec{H} has produced a single-domain state in the F material. The magnetisation of the material is in the easy direction which makes an angle to the external field of $\theta_{\vec{M}}$. The magnetisation of the F material measured parallel to the direction of \vec{H} is given by

$$\vec{M} = M_s \cos \theta_{\vec{M}} \quad (2.4)$$

by trigonometry. The F material is shown saturated in fig. 2.4(d) where \vec{M} and \vec{H} are parallel. A field applied in a hard direction is acting against the crystal anisotropy and forces the magnetisation out of the easy direction.

The F material discussed in this study is sputtered polycrystalline thin-film CoFe. The domain wall processes in this material are affected by the strong exchange coupling of the film. This exchange coupling means that the reversal process in the easy axis direction occurs by domain nucleation followed by rapid domain growth resulting in a highly square loop [13]. Typical coercivities for CoFe

are on the order of 50 to 100 Oe. However, coercivities on the order of 10 Oe are observed when the grain size is reduced below the exchange length [29].

2.2.3 The Stoner-Wohlfarth Model

The Stoner-Wohlfarth model addresses the variation in magnetic switching with angle between the easy axis and the applied field in a uniaxial particle [30]. To do this three core assumptions are required. Since the angle is measured between the easy axis of the particle and the applied field, the particle must be uniaxial. Secondly, the magnetisation of the particle is represented by a single vector which derives from the sum of the spin moments and which remains parallel at all points in the magnetisation switching process. This condition is known as coherent rotation. Finally, the model does not consider thermal effects so can only be considered to apply at $T = 0$.

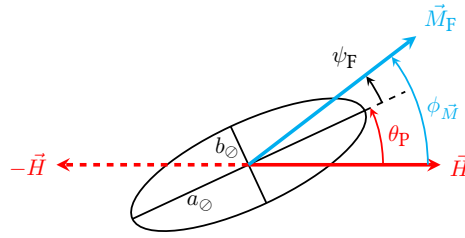


Figure 2.5: The vector diagram for the Stoner-Wohlfarth model for the magnetisation curve of a single-domain particle [30].

The vector diagram of the Stoner-Wohlfarth model is shown in fig. 2.5. \vec{H} is the applied field which varies between a value of $+\vec{H}$ and $-\vec{H}$ without rotating. The particle is a prolate spheroid of rotation and is free to rotate. The angle between the long axis of the particle and the applied field is given by θ_P . The magnetisation of the particle \vec{M}_F is represented by a single vector and reverses by coherent spin rotation. The angle between \vec{M}_F and the long axis of the particle is given by ψ_F . The angle between the particle magnetisation and the applied field is given by $\phi_{\vec{M}}$, which is equal to the sum of θ_P and ψ_F . The semi-major axis of the particle and the axis of rotation is a_0 , while the semi-minor axis is b_0 . Thus the axial ratio of the particle is given by $\frac{a_0}{b_0}$ [30]. The semi-major axis of the particle is parallel to the easy direction. The reason for this is shape anisotropy which will be discussed in section 2.2.5.

The Stoner-Wohlfarth model simplifies magnetic switching by considering particles which are single-domain. Thus there is no need to consider domain wall motion. In addition, thermal effects are not considered. The model also considers either a single F particle or a collection of non-interacting F particles. This assumption will not hold when applied to the crystallites of a polycrystalline F film as the crystallites interact via indirect exchange. In contrast, the AF crystallites can be considered to be non-interacting as will be discussed in section 4.2.

When $\phi_{\vec{M}} > 0$, \vec{M} for a single particle will be a non-linear function of \vec{H} [13]. This rotation of \vec{M} is caused by the torque exerted by the applied field. However, when $\phi_{\vec{M}} = 0$ the magnetisation and applied field will be parallel. Thus there will be no torque exerted on \vec{M} . The magnitude and direction of \vec{M} will be unchanged until \vec{H} reaches a sufficiently large negative value to abruptly reverse \vec{M} . This results in a rectangular hysteresis loop, in contrast to the continuously varying \vec{M} in the $\phi_{\vec{M}} > 0$ case. The coercivity of the rectangular hysteresis loop will be proportional to the anisotropy of the particle. The reversal of a single, uniaxial particle is shown in fig. 2.6 for different values of $\phi_{\vec{M}}$. h is the normalised field $\frac{\vec{H}}{H_K}$ and m is the normalised magnetisation $\frac{\vec{M}}{M_s}$.

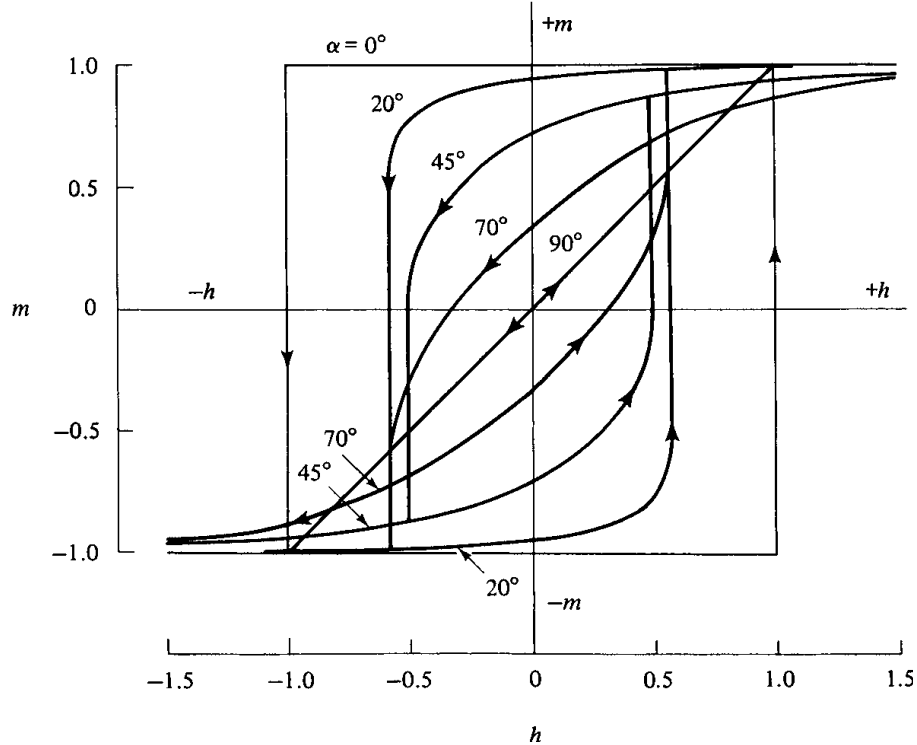


Figure 2.6: Calculated hysteresis loops for a uniaxial particle in the Stoner-Wohlfarth model at an angle $\alpha = \phi_{\vec{M}}$ to an applied field. h is the normalised field $\frac{\vec{H}}{H_K}$ and m is the normalised magnetisation $\frac{\vec{M}}{M_s}$ [13].

The energy of a single-domain, uniaxial particle in a field \vec{H} is given by the sum of the anisotropy energy and the magnetostatic energy by

$$E_u = V_g (K_u \sin^2 \phi_{\vec{M}} + \vec{H} M_s \cos \phi_{\vec{M}}) \quad (2.5)$$

where V_g is the particle volume, K_u is the uniaxial anisotropy and $\phi_{\vec{M}}$ is the angle between the particle magnetisation \vec{M} and the applied field [13]. The energy barrier to reversal is the difference between the maximum and minimum values of E_u [13]. Therefore the energy barrier is given by

$$\Delta E = K_u V_g \left(1 - \frac{\vec{H} M_s}{2K_u} \right) \quad (2.6)$$

which can be combined with eq. (2.3) to give

$$\Delta E = K_u V_g \left(1 - \frac{\vec{H}}{H_K} \right) \quad (2.7)$$

expressed in terms of the anisotropy field $H_K = \frac{2K_u}{M_s}$. This energy barrier to reversal will be discussed in section 4.2 as part of the York Model of Exchange Bias [11].

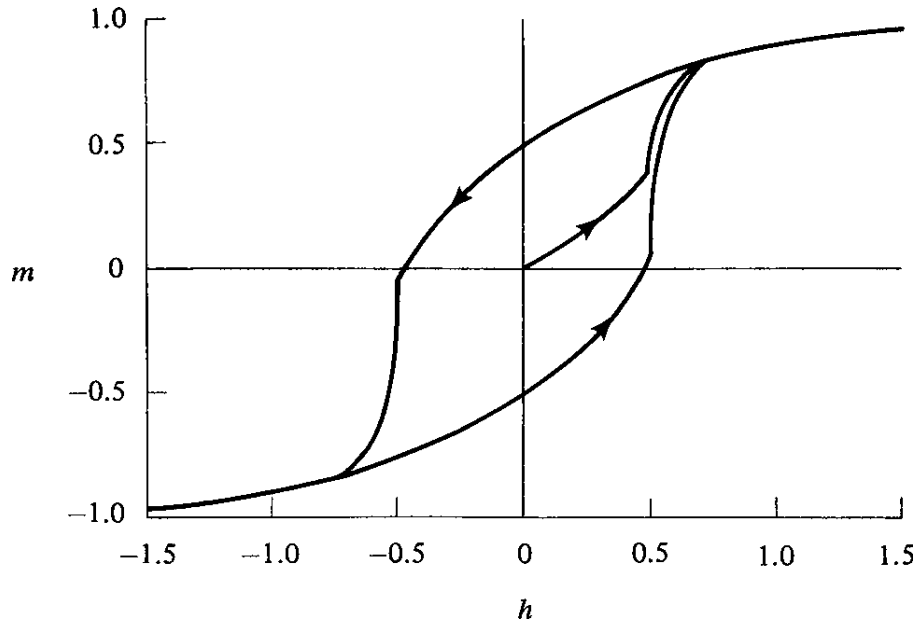


Figure 2.7: Calculated hysteresis loops for an assembly of non-interacting and randomly oriented uniaxial particles in the Stoner-Wohlfarth model. h is the normalised field $\frac{\vec{H}}{H_K}$ and m is the normalised magnetisation $\frac{\vec{M}}{M_s}$ [13].

The hysteresis loop shown in fig. 2.7 shows the magnetisation and reversal of an assembly of randomly-oriented particles in the Stoner-Wohlfarth model. The particles do not interact meaning the external field of a particle has no effect on

neighbouring particles. Since the particles are randomly oriented their easy axes are isotropically oriented in 3-D. In this scenario the hysteresis loop has a remanence of $\frac{M_s}{2}$ and a coercivity that is $0.479 \times H_K$ of a single particle with $\phi_{\vec{M}} = 0$ [30]

In the uniaxial, aligned case the switching field is equal to the anisotropy field H_K given by

$$H_K = \frac{2K_u}{M_s} \quad (2.8)$$

where K_u is the uniaxial anisotropy and M_s is the saturation magnetisation. However, if the particles have an isotropic distribution of easy axes the anisotropy field is reduced to

$$H_K = 0.96 \times \frac{K_u}{M_s} \quad (2.9)$$

and the coercivity and squareness are also reduced [30]. It should be noted that anisotropy in nanoparticles is not generally magnetocrystalline in origin but is usually due to shape anisotropy. Shape anisotropy will be discussed in section 2.2.5. However, similar uniaxial magnetocrystalline anisotropy is seen in certain bulk and film materials. For example the easy axis in hexagonal close-packed (hcp) Co is along the hexagonal prism axis and all the directions in the perpendicular plane are equally hard.

Since this model only applies to non-interacting uniaxial particles it cannot be applied to a polycrystalline F film because the crystallites interact via indirect exchange. However, as will be discussed in section 4.2 the AF film used in this work is composed of non-interacting, uniaxial particles [11]. Thus a modified form of the Stoner-Wohlfarth model can be applied to the AF film. The effective anisotropy of such a film will be dependent on texture. Texture is a preference in the crystallographic orientation of the particles in a polycrystalline material and in thin films is usually controlled by the use of a seed layer.

The Stoner-Wohlfarth model for an assembly of random particles can be considered analogous to a film with 3-D random texture. On the other hand the Stoner-Wohlfarth model for a single particle with $\phi_{\vec{M}} = 0$ can be considered analogous to a film with fully aligned easy axes. These two extremes of texture represent the highest and lowest effective anisotropy values that can be modified only by changes in texture. Most real films will have a texture intermediate between these extremes and therefore have an intermediate effective anisotropy. The method used to measure the effective anisotropy of an AF will be discussed in section 4.2.

2.2.4 AF Anisotropy

The above discussion is concerned mainly with F materials. However, with some modification most of the principles apply equally well to antiferromagnetic (AF) materials. One aspect of magnetocrystalline anisotropy that applies to AF materials but not to F materials is spin-flopping. The magnetic susceptibility of an AF material is greater when a field is applied perpendicular to the magnetisation directions of the sublattices. Thus there is a tendency for AF spins to align perpendicular to an applied field. Above a threshold value, an applied field will re-orient the AF spins until they are perpendicular to the applied field. This is called spin-flopping and is shown schematically in fig. 2.8(a) and (b). However, this tendency is resisted by the anisotropy of the material, which acts to maintain the direction of the AF sublattice magnetisations in the easy direction of the AF. As \vec{H} increases, there comes a point where the spin-orbit coupling energy is overcome. At this field value the AF spins rotate to being perpendicular to \vec{H} .

In fig. 2.8(b) the sublattice magnetisations remain antiparallel since the field has overcome the spin-orbit coupling responsible for anisotropy, but has not overcome the spin-spin direct exchange responsible for AF order. This critical field is associated with an abrupt increase in the susceptibility of the AF at the onset of spin-flopping. Further increases in \vec{H} cause the spins to become parallel to \vec{H} , eventually overcoming the AF order. This is shown in fig. 2.8(c). This state where F order is induced in an AF material only by application of \vec{H} is called metamagnetism.

The field required for metamagnetism is large. Typically a field of larger than 1 kOe is required to observe any change in antiferromagnetic spin alignment. For this reason metamagnetic effects can usually be ignored.

The AF alloy used in this study was IrMn. IrMn is widespread in industrial applications of exchange bias. It replaced an earlier AF material FeMn because of its higher corrosion resistance. In addition, a system containing IrMn and a 2 nm thick CoFe layer has achieved exchange bias of 3.7 kOe, larger than any other system measured at room temperature [31]. This is possible due to the high effective

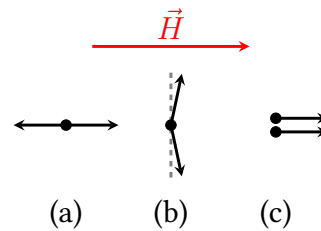


Figure 2.8: The sublattice magnetisations of a AF material in (a) low field, (b) a field sufficient to induce spin-flopping and (c) a field sufficient to induce metamagnetism [13].

anisotropy of IrMn which is $(3.3 \pm 0.4) \times 10^7 \text{ erg/cm}^3$ at 295 K [32]. The protocol used to measure the anisotropy of an AF material will be discussed in section 4.2.4.

Effective anisotropy is the anisotropy of a polycrystalline sample that is modified from the ideal single-crystal anisotropy. Magnetocrystalline anisotropy measurements are typically performed on single crystal samples. Given that magnetocrystalline anisotropy is dependent on crystalline orientation, the overall magnetocrystalline anisotropy of a sample is dependent on its overall crystallographic order. For a polycrystalline material a preferred crystallographic orientation is known as texture. If a sample has 3-D random texture then when observed as a whole the crystalline axes are distributed isotropically. It is therefore not possible to measure along any particular axis and instead an effective anisotropy will be measured. If the crystallite size is large then the crystallites will each contain a multi-domain structure. On the other hand below a certain critical size, the crystallites will contain a single domain.

The previously stated effective anisotropy of IrMn is $(3.3 \pm 0.4) \times 10^7 \text{ erg/cm}^3$ at 295 K [32]. This is an effective value of anisotropy for a thin film with out-of-plane fibrous $\langle 111 \rangle$ texture, meaning with a (111) plane parallel to the surface and the F/AF interface [13]. The easy axis of the IrMn is in the $\{111\}$ planes [32–36]. Thus in IrMn systems out-of-plane fibrous $\langle 111 \rangle$ texture is also known as in-plane easy-axis texture with the same meaning [11, 37]. For an IrMn film with 3-D random texture $K_{\text{AF}} = (5.5 \pm 0.5) \times 10^6 \text{ erg/cm}^3$ at 295 K [11]. This reduction is because the easy-axes do not lie in the plane of the film but are distributed randomly [37]. The method for determining the anisotropy of an AF material by consideration of exchange bias will be discussed in section 4.2.4 [38]. This high anisotropy is also reflected in the value of Néel temperature of IrMn which is $T_{\text{N}} = 690 \text{ K}$ [4]. The effect of texture on exchange bias will be discussed in section 3.3.1.

2.2.5 Other Anisotropies

Magnetocrystalline anisotropy is the only anisotropy that is inherent to a material. Other anisotropies arise from the condition of a particular sample. The important factors for consideration of anisotropy are shape and environment.

The demagnetising field \vec{H}_d is present in all magnetised materials. \vec{H}_d acts in the opposite direction to the magnetisation \vec{M} which causes it. In a bar magnet \vec{H}_d is strongest near the poles and weakest in the middle of the magnet. If the magnet is ellipsoidal then it can be uniformly magnetised throughout, and therefore \vec{H}_d is uniform inside the magnet. The demagnetising field of a body is proportional to the magnetisation that creates it

$$\vec{H}_d = -N_d \vec{M} \quad (2.10)$$

where N_d is the demagnetising factor which is dependent on the shape of the body. \vec{H}_d is minimised when the sample is magnetised parallel to its longest axis. Therefore due to shape anisotropy the long axis is the magnetically easy axis, since along the short axis a larger applied field is required to contract the enhanced demagnetising field.

The magnetostatic energy E_{ms} of a magnetised material is the energy of a magnet in its own field. It can be expressed as

$$E_{ms} = -\frac{1}{2} \vec{H}_d \cdot \vec{M} \quad (2.11)$$

where \vec{H}_d and \vec{M} are antiparallel by definition. This can be expressed using N_d by combining eq. (2.10) and eq. (2.11) to give

$$E_{ms} = \frac{1}{2} N_d \vec{M} \cdot \vec{M} \quad (2.12)$$

which shows that the magnetostatic energy is proportional to the magnetisation squared. When a field is removed from a sample it demagnetises either by the rotation of magnetisation or by the formation of domains. The magnetisation rotation is caused by anisotropy which rotates the magnetisation into the easy direction. The demagnetising field causes the formation of domains.

Since \vec{H}_d occurs only in magnetised materials it does not occur in AF materials since they have no free poles. The F material used in this study is sputtered, polycrystalline CoFe thin films. The grains of CoFe are coupled and therefore there are no free poles on the surface of the grains. In the absence of free poles shape anisotropy cannot have a significant effect.

Stress anisotropy results from the displacement of atoms by strain [39, 40]. In the case of thin film heterostructures it can also arise from a difference between the lattice parameters of adjacent layers. This condition is known as lattice mismatch. The lattice parameters of CoFe and IrMn are

$$\begin{aligned} a_{\text{CoFe}} &= 0.286 \text{ nm} \quad [41] \\ a_{\text{IrMn}} &= 0.378 \text{ nm} \quad [42] \end{aligned} \tag{2.13}$$

and thus a_{IrMn} exceeds a_{CoFe} by 32 %. Stress anisotropy is typically on the order of 10^4 to 10^5 erg/cm³ [13, 43]. This is small compared to the AF anisotropy for IrMn used in this study which is on the order of $\sim 10^7$ erg/cm³ [11]. The effects of stress anisotropy were not considered in this study for that reason.

2.2.6 Exchange Anisotropy

Exchange anisotropy was first observed by Meiklejohn and Bean in Co/CoO core-shell nanoparticles produced by electrodeposition in mercury (Hg) with diameters ~ 20 nm [1, 2]. A shifted, asymmetric hysteresis loop was observed when the particles were cooled in positive field to 77 K. Figure 2.9 shows the \vec{M} - \vec{H} loop of a compact of nanoparticles has been shifted to a negative field. In addition, the particles displayed unusual rotational hysteresis behaviour. Rotational hysteresis is the difference in magnetic state as a material is rotated in a constant field. In F materials rotational hysteresis loss reduces to zero at high fields because the material is saturated. However in the Co/CoO particles the rotational hysteresis loss remained high up to at least 16 kOe. This is discussed in more detail in section 3.1.2. Rotational hysteresis is of historical interest but is not measured in this work.

Shape and stress anisotropies are uniaxial. For uniaxial anisotropies the magnetisation is held in one of two antiparallel directions. For these the anisotropy energy has the form $\cos^2 \phi_F$ where ϕ_F is the angle of the F magnetisation to the easy axis. Exchange anisotropy is distinct because it is unidirectional. The anisotropy energy is thus proportional to $\cos \beta_{\vec{M}}$ where $\beta_{\vec{M}}$ is the angle between the magnetisation and the direction of the field during field cooling.

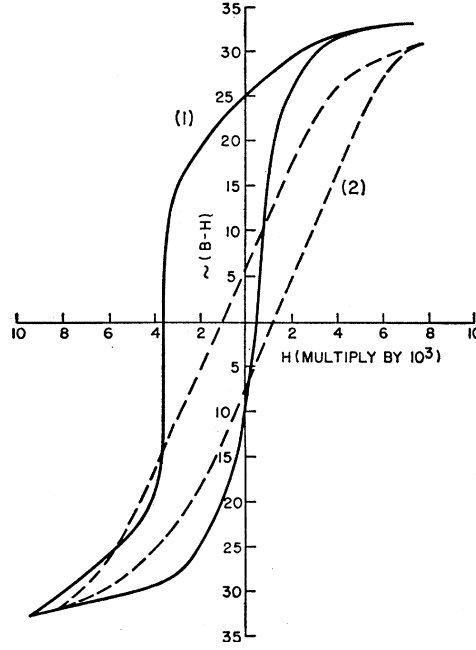


Figure 2.9: Hysteresis loop of oxide-coated Co particles at 77 K as presented by Meiklejohn and Bean [1].

The hysteresis loop shift H_{ex} is called the exchange bias or exchange field. Exchange bias has applications in giant magnetoresistance (GMR) and tunneling magnetoresistance (TMR) devices. In these the change in relative orientation of two magnetic layers in a thin film changes the resistance of the stack [44, 45]. Using exchange anisotropy the orientation of one magnetic film can be maintained which allows the orientation of the other film to be inferred from the changes in resistance. GMR and TMR are the principles that underlie the operation of high speed and high sensitivity magnetic sensors required for hard disk drives (HDDs) [6].

The original calculation of the magnitude of exchange bias H_{ex} by Meiklejohn and Bean was given to be

$$H_{\text{ex}} = \frac{J_K}{|\vec{M}|d_F} \quad (2.14)$$

where J_K is the interfacial coupling constant, \vec{M} is the magnetisation of the F material and d_F is the thickness of the F layer [2]. This calculation results in a values of H_{ex} typically two orders of magnitude higher than for any system measured [46]. From this, the AF anisotropy was estimated to be

$$K_{\text{AF}} \approx 5 \times 10^6 \text{ erg/cm}^3 \quad (2.15)$$

for CoO at 77 K [1, 2]. This model is discussed more fully in section 4.1.1.

Since exchange anisotropy and exchange bias are central to this study, the experimental features of exchange bias are discussed in detail in chapter 3. Modern and historic theories of exchange bias will be discussed and compared in chapter 4. In section 4.2.4 the method for measuring and calculating the AF anisotropy will be discussed.

2.2.7 Temperature Dependence of Anisotropy

Below the Curie temperature T_C a ferromagnetic material is ordered at the atomic level. This is known as spontaneous magnetisation. However, a macroscopic F sample is not necessarily magnetised since under the influence of the demagnetising field the material can separate into domains which, in the ideal case, would eliminate all net magnetisation. A ferromagnetic sample can be magnetised by cooling it in a magnetic field to below T_C . This is because above T_C the spins are free to rotate to align with the applied field. The temperature dependence of anisotropy of a CoFe thin film is given by

$$K_F(T) = K_F(0) \cdot \left(1 - \frac{T}{T_C}\right)^{\frac{1}{3}} \quad (2.16)$$

where K_F is the anisotropy constant of the F material, T is the temperature and T_C is the Curie temperature. The exponent of $\frac{1}{3}$ originates from the ordering temperature for the total angular momentum being proportional to the cube of the ionic moments such that

$$K_F \propto \left[\frac{\vec{m}(T)}{\vec{m}(0)}\right]^3 \quad (2.17)$$

where \vec{m} is the moment of the ions [43]. Once the material is cooled through T_C magnetocrystalline anisotropy dominates. Since the spins were aligned above T_C a spin imbalance results and the sample has a net magnetisation.

Due to intergranular exchange coupling the reversal process in CoFe thin films is by domain nucleation and rapid domain growth. This results in a highly square hysteresis loop as was discussed in section 2.2.2 [13]. At room temperature the value of K_F for CoFe is on the order of $\sim 10 \times 10^5$ erg/cm³ [13]. This is much lower than the room temperature value of K_{AF} for IrMn which is on the order of $\sim 10 \times 10^7$ erg/cm³ [11]. For this reason in a CoFe/IrMn thin film the anisotropy of the AF layer will dominate.

Other than in cases of metamagnetism which occurs only for very high fields, an AF material does not align under the influence of an external field. Thus the alignment of an AF material is by means of the direct exchange across an interface with an ordered F material. As will be discussed in section 2.3.1, the magnetisation of an AF material is made up of the magnetisations of two antiparallel sublattices with moment \vec{m}_{AF} . The temperature dependence was shown by Stiles and McMichael to be

$$\vec{m}_{\text{AF}}(T) \propto (T - T_{\text{N}})^{\frac{1}{3}} \quad (2.18)$$

where T is the temperature and T_{N} is the Néel temperature [47]. The exponent from eq. (2.18) cancels the cubic relationship between anisotropy and sublattice magnetisation given by

$$K_{\text{AF}} \propto \left[\frac{\vec{m}_{\text{AF}}(T)}{\vec{m}_{\text{AF}}(0)} \right]^3 \quad (2.19)$$

where K_{AF} is the AF anisotropy constant [48]. Thus the anisotropy of an AF material was shown to be

$$K_{\text{AF}}(T) = K_{\text{AF}}(0) \cdot \left(1 - \frac{T}{T_{\text{N}}} \right) \quad (2.20)$$

by Stiles and McMichael where K_{AF} is the AF anisotropy constant, T is the temperature and T_{N} is the Néel temperature [11, 32, 38, 47, 48]. Because of this K_{AF} reduces as T_{N} is approached and is zero at $T_{\text{N}} = T$. This relationship differs from that for a ferromagnet only in the exponent because in an AF material there are two sublattices with opposite magnetisation \vec{m}_{AF} . The veracity of eq. (2.20) is shown by the quality of the fit of the temperature dependence of AF setting as will be discussed in section 4.2.7 as part of the York Model of Exchange Bias [11, 48].

An AF material cooled to below T_{N} will have antiparallel spin sublattices. However, if it is coupled to a F material the direct exchange across the interface will tend to induce a surface magnetisation in the AF layer adjacent to the interface. This means that once AF order begins to dominate the sublattice structure will tend to conform to this initial surface magnetisation, so that the AF sublattice closest to the F layer will be parallel to it and then the sublattices will occupy alternate layers.

Note that this discussion is concerned with the magnetic properties of a material and does not consider the effects of temperature on intergranular order. This ordering will be discussed in chapter 4. Thermal effects can dominate when the crystallite size is reduced below 20 nm [47].

2.3 Antiferromagnetic Materials

2.3.1 Structure of Antiferromagnetic Materials

When an antiferromagnetic (AF) material is cooled below a particular temperature the atomic moments have a tendency to align antiparallel to their neighbours. This critical temperature is called the Néel temperature T_N . When heated above T_N an AF material will behave paramagnetically, just as is the case for a F material heated above T_C . The antiparallel alignment of the moments in an AF material arises from the exchange interaction discussed in section 2.1.1. In an AF material the exchange integral J_{ex} is negative, unlike in a F material where it is positive. In one dimension this results in an alternating pattern of spin orientations where each adjacent atom's spin is opposite to its two neighbours. This is known as an atom-by-atom antiferromagnetism. Antiferromagnetic materials containing only a single atomic species include Cr and Mn, although T_N for Mn is 97 K.

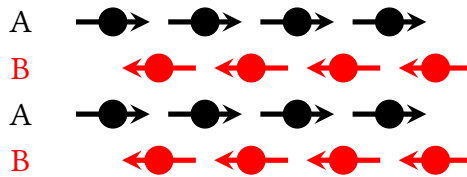


Figure 2.10: A sheet AF material with sublattices A and B [13].

An atomic lattice is an array of atoms with periodic translation symmetry. An AF material can be thought of as being composed of two spin sublattices. Each sublattice is an array of spins with periodic translation symmetry. In addition, each sublattice occupies half of the lattice sites in the atomic lattice. The spins within a sublattice are parallel while the spins between sublattices are antiparallel. In three-dimensional lattices the spin lattices can be aligned to alternating two-dimensional planes in an arrangement known as sheet antiferromagnetism. This arrangement is shown schematically in fig. 2.10 where sublattices A and B have opposite spin orientations but the same translation symmetry.

Many AF materials are metal oxides. However these will not be discussed in detail because they were not used in this work. Superexchange is important in AF oxides such as MnO. Superexchange is an exchange mechanism by which the spin ordering in metal oxides is coordinated by the p orbital of the oxygen ions.

This was discussed in section 2.1.3. In this study, the AF material used was IrMn. Superexchange does not play a role in IrMn due to the lack of oxygen ions. In fact, IrMn is highly resistant to corrosion and oxidation. For this reason oxygen is unlikely to be present in IrMn above trace amounts.

2.3.2 Structure of IrMn

The AF material used in this study is IrMn due to its commercial relevance. IrMn is used in GMR and TMR read-heads due to its high anisotropy, high T_N and resistance to corrosion. A film of IrMn/CoFe where the thickness of the F layer was 2 nm as been measured to have $H_{ex} = 3.7$ kOe at room temperature, which is the highest value of H_{ex} yet recorded [31]. IrMn was the AF material that replaced FeMn due to the tendency of FeMn to oxidise readily. Although Ir is expensive, the quantity required is small which prevents the cost from being prohibitive. That said, there is increasing research interest in AF alloys that do not contain Ir [49, 50].

The degree of exchange bias attainable using IrMn is strongly dependent on the relative amounts of constituent iridium and manganese ions. This presents a challenge as the composition of IrMn cannot easily be measured. Typical chemical analysis techniques require the material to be dissolved into its constituent ions. However, Ir does not dissolve in any acid, making conventional chemical analysis impossible [51]. The effect of the composition of IrMn on exchange bias will be discussed in more detail in section 3.3.2.

The effect of IrMn composition of J_{ex} was calculated by Tsunoda et al. using measurements of H_{ex} and the Meiklejohn and Bean model of exchange bias [1, 2, 52]. This model will be discussed in section 4.1.1. It was found that there is a flat peak in J_{ex} from 22 to 32 at.% Ir above and below which J_{ex} rapidly falls [52]. This J_{ex} peak is correlated with a measured increase in the integral of the X-ray diffraction (XRD) peak which corresponds to an increase in the crystallographic order. X-ray diffraction will be discussed in detail in section 5.2.1. It should be noted that crystallographic order does not necessarily correspond to chemical order. In addition, this data was obtained for single-crystal samples produced in an ultraclean film deposition system and not necessarily representative of the systems used in this work.

This calculation based on early models has been superseded by measurements of K_{AF} based on the York Model of Exchange Bias [11]. The York Model of Exchange Bias will be discussed in section 4.2. The effect of IrMn composition of K_{AF} is shown in fig. 2.11 in the range of 13 to 22 at.% for sample grown in a high target utilisation sputtering (HiTUS) system [53]. This system will be described in section 5.1.1. Figure 2.11 shows that K_{AF} decreases as the Ir concentration increases. It should be noted that an increase in K_{AF} does not directly correspond to an increase in H_{ex} . The effect of IrMn composition on H_{ex} will be discussed in section 3.3.2 while the effect of K_{AF} on H_{ex} will be discussed in section 4.2.4 as part of the York Model of Exchange Bias. The observation that K_{AF} increases as the order of IrMn decreases is not understood and is the subject of ongoing research [54].

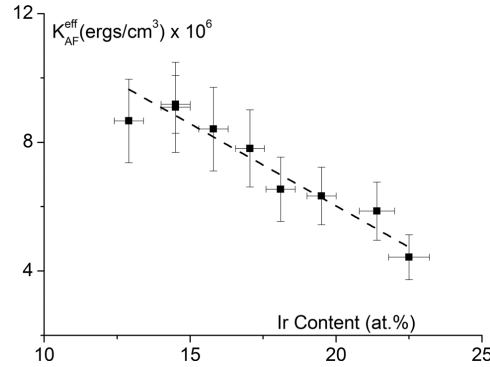


Figure 2.11: The composition of IrMn has a strong effect on the anisotropy constant [53].

To prepare samples for the measurement of K_{AF} , IrMn was sputtered from a target with 25 at.% Ir which is equivalent to IrMn_3 [53]. The target was a stoichiometric powder-pressed mixture of Ir and Mn metals due to the difficulty in producing an alloy. The film is produced by sputter deposition from the target in high target utilisation sputtering (HiTUS). HiTUS will be discussed in section 5.1.1. The composition of the film is not necessarily the same as the composition of the target due to the different melting points of the two materials. Since the melting point of Ir is expected to be higher than that of Mn the films produced are expected to be iridium-poor compared to the target. Iridium-poor films are commonly used since K_{AF} increases as the Ir content decreases. The sputtering rate across a target in HiTUS is uniform as discussed in section 5.1.1. By drilling holes in the target, Mn pegs or Ir shards can be inserted onto the target surface. This changes the effective composition of the target and subsequently the film. By this method it is possible to fine-tune the composition of the IrMn film.

The increase in J_{ex} corresponds to an increase in crystallographic ordering [52]. The crystallographic ordering parameter used was the integral of the (110) and (200) peaks measured by grazing incidence X-ray diffractometer (XRD). This corresponds to the $L1_2$ structure of IrMn which is chemically and magnetically ordered [52]. Neutron diffraction studies of bulk crystal and 200 nm thick film samples of ordered fcc IrMn have been performed [42, 55]. These show the Mn spin moments lying in a $\{111\}$ plane and containing three sublattices pointing in the $\langle 112 \rangle$ directions, which are separated by 120° . In fig. 2.12(a) the unit cell is shown with this arrangement known as a triangular spin structure [55]. The solid circles represent Ir lattice sites and the open circles represent Mn lattice sites. Note that the unit cell contains three Mn ions and one Ir ion and are chemically ordered such that Mn ions occur only on Mn lattice sites. The dashed lines lie on a $\{111\}$ plane and connect the Mn ions on that plane. The three spin sublattices separated by 120° are shown in a section of one of the $\{111\}$ planes in fig. 2.12(b) [55].

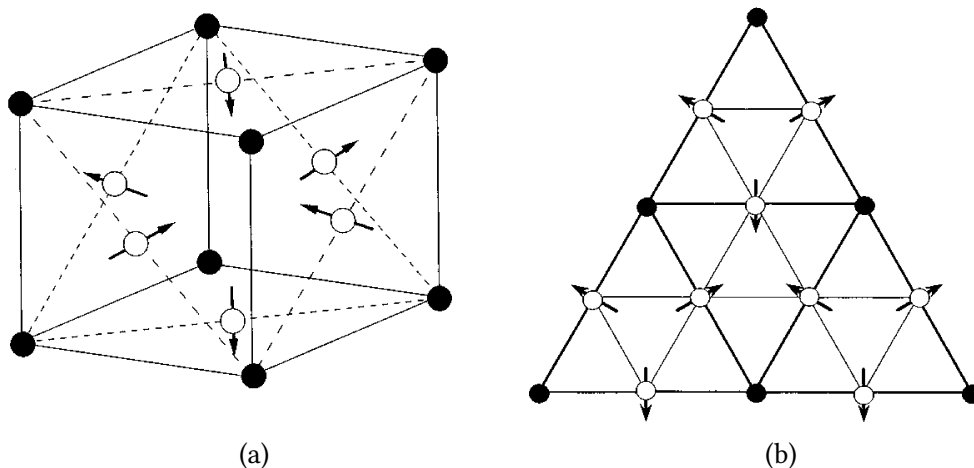


Figure 2.12: The spin structure of IrMn₃ in (a) the unit cell and (b) a section of an $\{111\}$ plane according to neutron diffraction studies of bulk samples where the solid circles represent Ir lattice sites and the open circles represent Mn lattice sites. [55].

These neutron diffraction studies were carried out for annealed IrMn in two form factors, these being a rectangular thin film $10\text{ mm} \times 12\text{ mm} \times 200\text{ nm}$ [42] and a bulk disk 8 mm in diameter and 2 mm thick [55]. As such these single-crystal alloys have a lateral extent greater than the grains in this study by a factor of $\sim 10^6$. When measuring grain volume the difference is even more significant. For the film the crystallite volume is larger by a factor of 10^{11} while the single-crystal disk has a volume 10^{17} times that of the typical grain volume of the samples in this study.

Due to the difference in scale the magnetic order of these single-crystal systems may not be representative of the magnetic order in a polycrystalline thin film. This is both because of the difference in production methods as well as the effect of grain interfaces on the atomic spacing in the crystallites. It should be noted that the triangular spin structure has never been observed in a monocrystalline thin film with median grain diameter and film thickness ~ 10 nm such as is used in this study. Since the atomic spacing will be modified by residual microstress, the exchange interaction in the film will not be the same, due to the strong dependence of exchange on atomic separation. In addition, these measurements were carried out on stoichiometric IrMn_3 , whereas the IrMn films used in this study are expected to be manganese-rich [53, 56]. Due to the additional Mn ions the chemically ordered state of IrMn_3 is unattainable.

Furthermore, in a thin film the maximum value of H_{ex} corresponds to $\langle 111 \rangle$ texture, which is incompatible with the triangular spin structure. This will be discussed in section 3.3.1. It is also the case that the York Model of Exchange Bias is the most complete model of exchange bias in polycrystalline thin films. The York Model of Exchange Bias will be discussed in section 4.2. The York Model of Exchange Bias assumes that the AF grains are uniaxial which is not compatible with the triangular spin structure. The success of the York Model of Exchange Bias in describing the behaviour of films similar to those used in this study indicates that the triangular spin structure is not present in these films.

2.3.3 Interfacial Exchange Coupling

The coupling of AF materials to F materials across an interface is central to the production of exchange bias. This coupling is a result of direct and indirect exchange between the two materials. However, the concept of an interface in CoFe/IrMn thin films is something of a misnomer. Mn, Fe and Co have similar size and chemistry which allows them to intermix readily. Thus the CoFe/IrMn interface is not a sharp division but contains several other phases including CoMn , FeMn and CoFeMn each in different proportions, compositions and median depth. This intermixing will modify the magnetic properties of the film [57–59]. The interfacial layer has been shown to behave independently in the trilayer experiment [60, 61]. The trilayer experiment demonstrates that the interface can reverse separately to the adjacent layers. This will be discussed in section 3.4.2. Thus it

is appropriate to discuss an interface region which has both a non-zero thickness and magnetic behaviour separate to either of the adjacent layers.

The magnetic behaviour of the interface region will be dependent both on the materials which compose it and the materials which border it. As previously discussed CoFe is a F material with $T_C = (1260 \pm 10)$ K, while IrMn is an AF material with $T_N = 690$ K [4, 13]. FeMn is an AF material [62]. On the other hand, at room temperature CoMn is F up to 25 at.% Mn, AF above 42 at.% Mn and paramagnetic (P) between those concentrations [63]. These phases will exist in a mixture at the interface. CoMn has been observed to exhibit exchange bias as a single material which is due to a mixture of F and AF regions, a condition known as mictomagnetism [64, 65]. The magnetic phase diagram of CoMn will be discussed in detail in section 6.2.2 and 7.2.3 [63]. CoFeMn can behave as a F, AF or P material dependent on its composition. In addition, at low temperatures the $\text{Co}_{50}\text{Fe}_{25}\text{Mn}_{25}$ alloy exhibits spin-glass behaviour [66].

The interface therefore is a region of great magnetic complexity. However, it is possible to overlook the precise structure of the interface and its role in H_{ex} . The models of exchange bias discussed in chapter 4 all take a simplified approach to the interface. Despite this, the models have had success in explaining aspects of exchange bias. Thus the role of F/AF coupling can be discussed in general terms without reference to the complexities of the interface. However, these simplified models do not describe all H_{ex} behaviour. A full discussion of the behaviour of the interface will follow in chapter 3. In chapter 6 and chapter 7 the structure of the interface will be discussed.

Proposed models of exchange bias will be discussed in chapter 4. The earliest model of exchange bias was proposed by Meiklejohn and Bean [1, 2]. This model was designed for oxide-coated Co nanoparticles formed by electrodeposition in Hg. The model and its assumptions will be discussed in section 4.1.1. However, the core of the model is the coupling across the ferromagnetic/antiferromagnetic interface. This coupling was taken to be ferromagnetic, meaning that the moments on either side of the F/AF interface were parallel. However, it is now clear that the F/AF interface has magnetic behaviour independent of the adjacent layers [11, 37, 67]. In polycrystalline CoFe/IrMn atomic mixing and diffusion will increase the effective size of the interfacial region.

Figure 2.13 shows hysteresis loops for two thin films, one of Cu/CoFe and a Cu/IrMn/CoFe film in three different conditions [37]. The use of Cu as a seed layer is to control the texture of the other layers which has consequences for exchange bias which will be discussed in section 3.3.1. The Cu/CoFe film has no AF layer and therefore lacks exchange bias. The hysteresis loop is symmetric and not shifted. In addition it has a low coercivity. The enhancement of coercivity with exchange bias will be discussed in section 3.1.3.

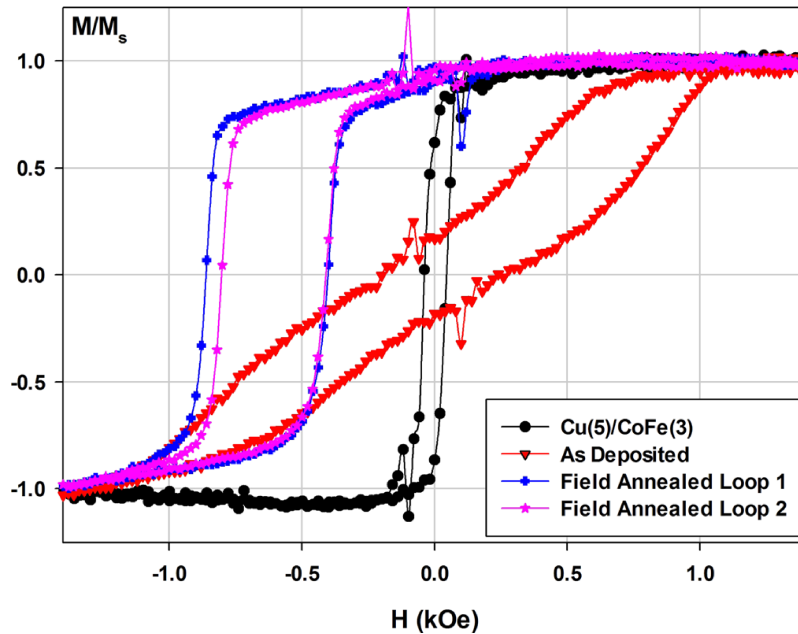


Figure 2.13: Example hysteresis loops showing the effect of AF anisotropy and the effect of the setting process on H_{ex} [37].

In fig. 2.13 the hysteresis loop is shown for the Cu/IrMn/CoFe film in the as-deposited state [37]. The hysteresis loop is not shifted but its character is distinct from the Cu/CoFe hysteresis loop. This is a consequence of the enhanced anisotropy which modifies the switching mechanism. In the Cu/CoFe film the CoFe crystallites are strongly coupled so the switching process occurs by domain nucleation and rapid domain growth resulting in a highly square loop [13]. This was discussed in section 2.2.2. In contrast in the as-deposited Cu/IrMn/CoFe film there are more domain wall pins so the magnetic reversal occurs more gradually in a loop with lower squareness and a higher saturation field [37]. This is a consequence of the high K_{AF} of the IrMn layer.

Figure 2.13 shows two hysteresis loops of the Cu/IrMn/CoFe film after exchange bias has been induced in the film [37]. The method by which exchange bias is induced in the film will be discussed in section 4.2.2 [11, 37]. This shows a

shifted and asymmetric loop with enhanced coercivity. The loop shift, enhanced coercivity and asymmetry will be discussed in section 3.1.1, 3.1.3 and 3.2.3 respectively. The difference between the two measured loops is the training effect which will be discussed in section 3.2.2. After exchange bias has been induced in the film the CoFe crystallites are again strongly coupled and there are fewer domain wall pinning sites which results in increasing squareness more similar to the film without an AF layer. However, the exact loop shape will be affected by the texture of the IrMn layer as will be discussed in section 3.3.1 [37].

2.3.4 Characterisation of Exchange Bias Hysteresis Loops

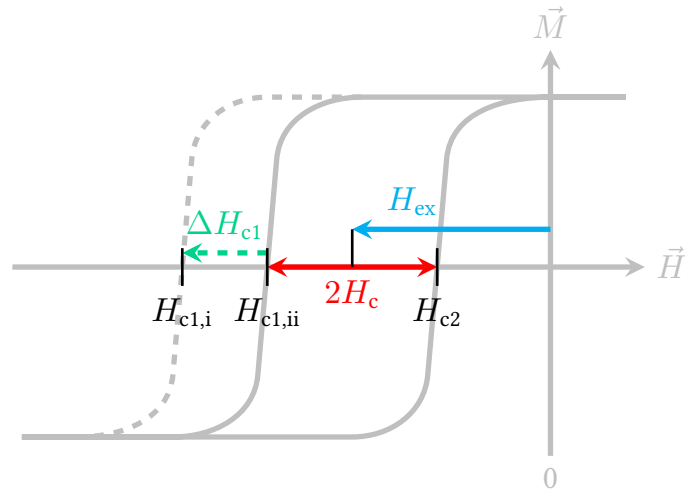


Figure 2.14: Schematic of an exchange-biased hysteresis loop with the intercepts $H_{c1, i}$, $H_{c1, ii}$ and H_{c2} and the values measured from them H_{ex} , H_c and ΔH_{c1} labelled. The physical meaning of these vales will be discussed in chapter 3.

A schematic representation of an exchange bias hysteresis loop is shown in fig. 2.14. The difference between $H_{c1, i}$ and $H_{c1, ii}$ is the athermal training effect and will be discussed in section 3.2.2 [68, 69]. For an exchange bias system $H_{c1} \neq -H_{c2}$, which would be the case for an isolated F material. The coercivity H_c of an exchange bias sample is defined as half the difference of H_{c1} and H_{c2} . Thus

$$H_c = \frac{H_{c2} - H_{c1}}{2} \quad (2.21)$$

in an exchange bias system. The point half-way between H_{c1} and H_{c2} is the exchange field or exchange bias H_{ex} . It is calculated from an \vec{M} - \vec{H} loop using

$$H_{ex} = -\frac{H_{c2} + H_{c1}}{2} \quad (2.22)$$

where the minus sign indicates the convention that loops shifted to the left have positive exchange bias. This was established when exchange bias was first observed and indicates that the preferred magnetisation direction is in the positive field direction [1]. Exceptions to this convention are sometimes made when the exchange bias of a film goes through zero. This can occur in a number of different measurements including the blocking temperature measurement protocol discussed in section 4.2.3 as part of the York Model of Exchange Bias. In a York Model of Exchange Bias blocking curve measurement the initial state of exchange bias is taken to be negative until it goes through zero and becomes positive.

3. Features of Exchange Bias

The shift of the hysteresis loop is the definitive feature of exchange bias. However, systems which have exchange bias have a large number of related phenomena. In this chapter these will be defined and discussed. However, it is not possible to describe phenomena in a wide variety of systems. For this reason, the discussion in the chapter will in general be limited to phenomena which occur in metallic, polycrystalline thin films including CoFe/IrMn. Models of exchange bias will be discussed in chapter 4. However, there is no model of exchange bias that can account for all related phenomena.

3.1 Early Observations

Exchange bias was first observed by Meiklejohn and Bean [1, 2]. They noted a group of fundamental features that define exchange bias. These are the loop shift, high-field rotational hysteresis and the enhancement of coercivity.

3.1.1 Exchange Field

The amount by which a magnetisation loop is shifted is the exchange field H_{ex} , it is shown schematically in fig. 2.14. The exchange field quantifies the exchange bias phenomenon. The loop shift was first observed for a compact of Co/CoO nanoparticles [1, 2]. The shifted hysteresis loop is shown in fig. 2.9 after cooling in a positive field. The loop shift can be calculated from a hysteresis loop using

$$H_{\text{ex}} = -\frac{H_{c2} + H_{c1}}{2} \quad (3.1)$$

where H_{c1} and H_{c2} are the two points of the loop where $\vec{m} = 0$. Thus the exchange field is defined as the average of the two coercivities. The negative sign represents the convention that loops shifted in the negative field direction and which therefore have negative values of H_{c1} and H_{c2} , have a positive exchange field. This is a result of cooling in a positive field. Samples cooled in a negative field have a negative exchange field and the loop is shifted in the positive field direction.

Models of exchange bias relate primarily to explaining the origin of the exchange field. Historical models of exchange bias will be discussed in chapter 4. The dependence of H_{ex} on the grain volume will be discussed in section 4.2. The difference between $H_{c1, i}$ and $H_{c1, ii}$ is the athermal training effect and will be discussed in section 3.2.2 [68, 69].

3.1.2 Rotational Hysteresis

A torque magnetometer measures the torque on a magnetised sample. This torque arises due to the interaction of the sample's magnetic moment and a uniform magnetic field. The torque curves of a compact of Co/CoO particles are shown in fig. 3.1 where $\theta_{\vec{H}}$ is the angle between the exchange bias axis and the applied field [2]. These samples were measured in a field of 7.5 kOe. The torque curves have the form $\sin\theta_{\vec{H}}$ and show a significant rotational hysteresis and unidirectional anisotropy. Samples of fcc Co nanoparticles of a similar size have been found to have relatively weak magnetocrystalline anisotropy or shape anisotropy on the order of 2×10^6 erg/cm³ [70].

In a F material measured in a field sufficient to saturate the sample a torque curve has no hysteresis. This is because the magnetisation follows the external field. However, in the Co/CoO nanoparticle compact rotational hysteresis persisted up to a maximum measurement field 16 kOe, which was twice the value required to saturate the sample. Rotational hysteresis has since been shown in IrMn systems [71]. The unidirectional anisotropy of exchange bias systems has been shown to be brought about by a thermal setting process that will be discussed in section 4.2 [11]. However, while the exchange bias has unidirectional anisotropy the anisotropy of the coercivity in CoFe/IrMn systems has been shown to be uniaxial [72]. Rotational hysteresis is included here for its historical importance but in this work it was not measured.

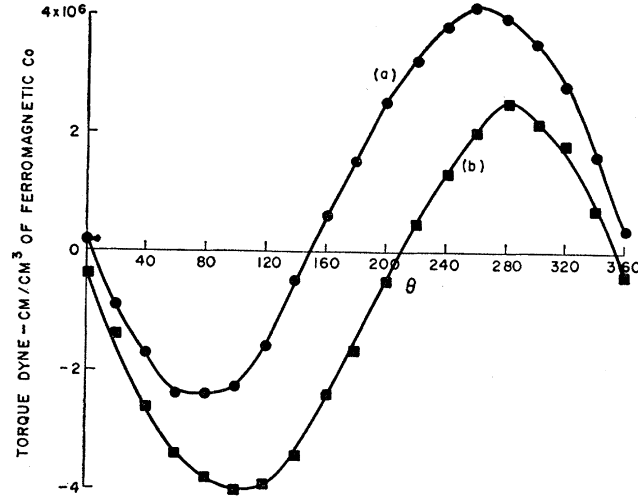


Figure 3.1: Torque curves for exchange-biased Co/CoO nanoparticles for (a) increasing and (b) decreasing $\theta_{\vec{H}}$. The existence of hysteresis in the measurement at high field is indicative of exchange bias [2]. Since the sample is a compact of fcc Co nanoparticles it has relatively weak magnetocrystalline anisotropy or shape anisotropy [70].

3.1.3 Enhanced Coercivity

In a ferromagnetic (F) material the coercivity H_c is the point in the $\vec{M}-\vec{H}$ loop where $\vec{m} = 0$ after the material has been saturated. In a sample with no exchange bias this value is equal in both magnetisation directions and can simply be read from the hysteresis loop. In an exchange-biased system the loop shift causes the magnitude of the coercivity in different magnetisation directions to not be equal. For this reason they are separated into two values called H_{c1} and H_{c2} , where H_{c1} denotes the magnetisation going from positive to negative. Since when measuring from positive saturation the first magnetisation reversal occurs in negative field $H_{c1} < H_{c2}$. The equation

$$H_c = \frac{H_{c2} - H_{c1}}{2} \quad (3.2)$$

is used to calculate H_c for an exchange-biased system. This defines H_c as half the width of the hysteresis loop. For a non-exchange-biased system where $H_{c1} = -H_{c2}$, the same value of H_c will be obtained by either method. H_c is shown schematically in fig. 2.14.

The coercivity of a F material is strongly affected by composition, shape, grain size and measurement time [13]. Exchange bias is also associated with an enhanced coercivity [4]. For the soft magnetic material CoFe, the value of H_c typically in-

creases by an order of magnitude in an exchange bias system. The enhanced coercivity is seen even in F/AF films where $H_{\text{ex}} = 0$ due to thermal activation [37]. The temperature dependence of H_c has been shown to be distinct from that of H_{ex} [69]. It has also been shown to be more interface-dependent than H_{ex} [73].

3.2 Dynamic Effects

As is the case for a ferromagnetic sample, the state of exchange bias system is dependent on the sample's history. The way in which exchange bias changes is indicative of hysteretic changes in the AF layer. As in a ferromagnetic material these effects are brought about by the magnetic history of the sample and are exacerbated with temperature and time.

3.2.1 Thermal Activation

The exchange bias of a F/AF system can change due to the application of heat [11, 74] Thermal activation of the AF film will be discussed in section 4.2. However, a number of historical treatments of exchange bias systems misattributed the change in H_{ex} to other causes. The H_{ex} was seen to reduce as a function of time, field cycles or measurement time. In these contexts it was described as a training effect [75–79]. The decay of H_{ex} was compared to both functions of $1/\ln t$ and $(N_{\bar{H}})^{-1/2}$ where t is time and $N_{\bar{H}}$ is the number of magnetic cycles [80, 81]. After careful observation, the so-called training effect was shown to be a combination of two separate effects, called thermal or type I training and athermal or type II training [68, 82, 83]. Discussion of athermal or type II training will follow in section 3.2.2.

Thermal training was shown to be strongly dependent on temperature [84]. The designation type I described the way that H_{ex} decreased, which was by way of the motion of both legs of the hysteresis loop. This effect is caused by thermal activation and is eliminated when measuring at low temperatures [11]. In the rest of this work it will simply be called thermal activation. An example of thermal activation is shown in fig. 3.2 for a sample with composition Si/Ta (2)/Ru (2)/IrMn (10)/Mn (0.05)/CoFe (5)/Ru (5) (thicknesses in nm). In contrast, athermal or type II

training is not eliminated by measuring a low temperature [11]. Type II indicates that only one leg of the hysteresis loop moves, which is H_{c1} . It will be called the training effect ΔH_{c1} in the rest of this work. To eliminate the training effect it is usual to take measurements of H_{ex} and H_c using the second hysteresis loop [11]. Alternatively, the hysteresis loop can be measured starting at negative field compared to the setting direction. This effectively begins the measurement at negative saturation, avoiding the first magnetic reversal.

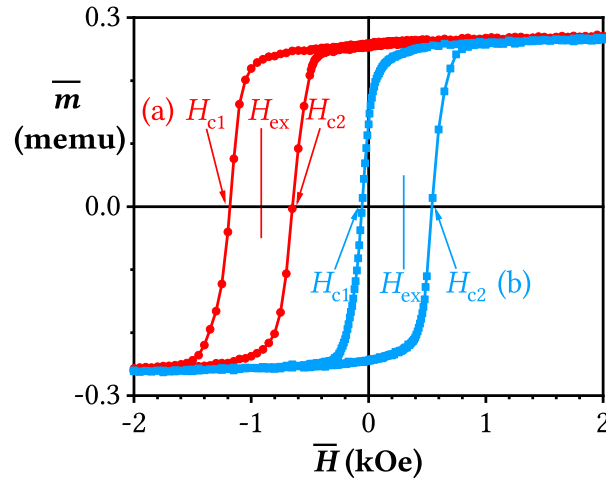


Figure 3.2: Thermal activation changes the value of exchange bias for a CoFe/IrMn film set for 5400 s at 500 K in (a) $\vec{H}_{set} = 20\text{kOe}$ and (b) $\vec{H}_{set} = -20\text{kOe}$. The exchange bias is the average of the x -intercepts H_{c1} and H_{c2} .

Thermal activation is a significant part of models of exchange bias. For this reason it will be discussed in full in chapter 4. However, here blocking temperature will be defined. In conventional magnetism for ferromagnetic particles of a constant size there is a critical temperature below which the magnetisation is stable. This temperature is called the blocking temperature and is distinct from T_C since a magnetic particle can be reversed by thermal action without becoming paramagnetic as it would be above T_C . This reversal occurs over a volume-dependent energy barrier. The definition of stable specifically refers to a particle with a relaxation time longer than the measurement time. An unstable particle has a relaxation time shorter than the measurement time and will therefore be thermally reordered during the measurement process. Stable particles will display ferromagnetic behaviour while unstable grains will display superparamagnetic behaviour. If the particle volumes are distributed then the energy barriers to reversal will be distributed and as a consequence there will be a distribution of blocking temperatures.

In exchange bias systems the blocking temperature is defined differently to the ferromagnetic case [11]. The blocking temperature T_B of an exchange bias material is the temperature at which $H_{ex} = 0$. However, there are two procedures for measuring T_B which result in different values that are both called the blocking temperature. T_B for a sample was conventionally measured by measuring hysteresis loops at elevated temperatures until H_{ex} was reduced to zero. This value of T_B corresponds to a temperature where all the grains are unstable. It is therefore equal to the temperature at which the largest grain becomes unstable [11]. In this work it will be denoted with T_B^{MAX} .

However, the York Protocol method of measuring T_B will be discussed in section 4.2.3. It involves taking measurements at the temperature of non-activation T_{NA} , a temperature sufficiently low to eliminate the effects of thermal activation. The York Protocol allows measurement of the median T_B of the AF grains. In this work this value is denoted $\langle T_B \rangle$. From this the median energy barrier to reversal can be calculated and from that K_{AF} can be found [11]. A full discussion of thermal activation in CoFe/IrMn exchange bias films and T_{NA} will be discussed in section 4.2.

3.2.2 The Training Effect

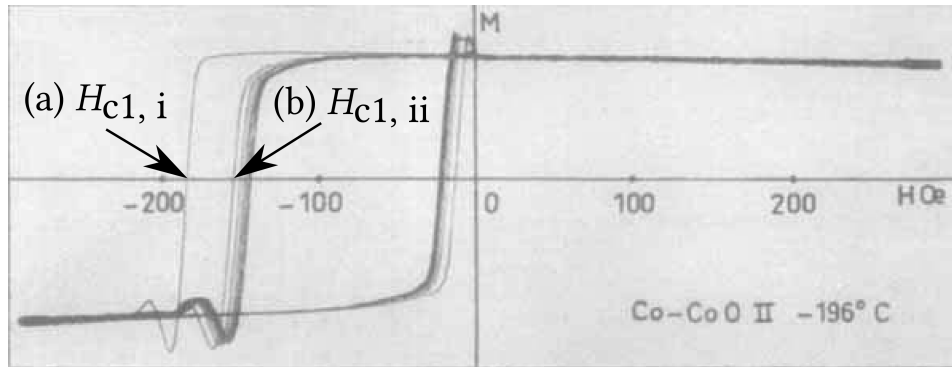


Figure 3.3: The first loop training effect is shown by the difference between (a) and (b) loops for Co/CoO thin films in this historic measurement from 1966 made using a torque balance. The further differences between the subsequent loops are the result of thermal activation. The overshoot is an instrumental artefact [80].

The training effect ΔH_{c1} is a change of an $\vec{M}-\vec{H}$ loop with subsequent measurements first observed in 1966 [80]. It is also known as the athermal training effect to distinguish it from thermal activation with which it had been conflated. The training effect is the movement of H_{c1} between the first and second measurements

of the hysteresis loop. For this reason it is also known as the first-loop training effect. It is defined as

$$\Delta H_{c1} = H_{c1, i} - H_{c1, ii} \quad (3.3)$$

where $H_{c1, i}$ is the first leg coercivity of the first hysteresis loop or training loop and $H_{c1, ii}$ is the first leg coercivity of the second loop. Training has been observed in polycrystalline IrMn systems [4, 85]. The significant asymmetry in the movement of H_{c1} and H_{c2} is shown in fig. 3.3 [80]. The training effect ΔH_{c1} was found to be separate to thermal activation in which both H_{c1} and H_{c2} move [68, 69]. Measuring below T_{NA} does not eliminate the training effect [11, 78]. After the second hysteresis loop, when measured at sufficiently low temperatures there is no change in either H_{c1} or H_{c2} [11]. ΔH_{c1} is shown schematically in fig. 2.14.

Early attempts to explain ΔH_{c1} attributed it to a property of cubic AF materials due to the fact they have orthogonal easy axes along the $\langle 100 \rangle$ directions [68]. However, ΔH_{c1} has been observed in IrMn which has easy axes in the $\langle 111 \rangle$ directions, which are not orthogonal [32, 34]. As discussed in section 3.3.1, IrMn systems have been observed both with and without training depending on the texture of the film [37]. The training effect highlights the asymmetry in the reversal processes in an exchange biased film.

3.2.3 Reversal Asymmetry

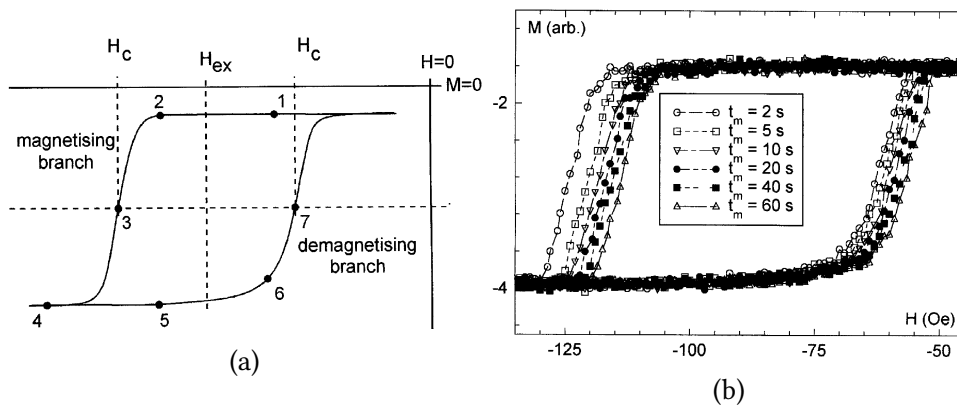


Figure 3.4: The asymmetry of reversal shown (a) schematically [86], (b) at a temperature above T_{NA} showing thermal activation [86].

The reversal process in a F material is symmetrical. This means both that $H_{c1} = H_{c2}$ and that the reversal process proceeds in the same way in both the forwards and backwards directions. However, in an exchange bias film the reversal process

is asymmetric, both being shifted and having noticeably different shapes on the two legs of the loop [86]. For this reason it is necessary to label points on the hysteresis loop for discussion. An example of this is shown in fig. 3.4(a) [86]. In this way the 3 in fig. 3.4(a) labels the part of the hysteresis loop at the point of the first magnetisation reversal. Likewise the 7 in fig. 3.4(a) labels the point where the magnetisation reverses again. It is the loop shape in the region of labels 2 and 6 that is asymmetric. The points labelled 3 and 7 correspond to H_{c1} and H_{c2} respectively.

Figure 3.4(b) shows the asymmetric reversal of an exchange biased layer of a GMR heterostructure. The measurements show H_{ex} and H_c reducing as the measurement time increases [86]. This is due to thermal activation since the measurements were not performed at T_{NA} . As a consequence both legs of the hysteresis loop change. In fig. 3.5 a film with composition Si/Ta (2)/Ru (2)/IrMn (10)/Mn (0.2)/CoFe (5)/Ru (5) (thicknesses in nm) has been set. Two loops (i) and (ii) are shown to demonstrate the training effect. The loops are measured at 5.5 K, which is well below T_{NA} . There is no thermal activation of the loop and the training effect can clearly be seen as the difference between loops (i) and (ii). The loops are both asymmetric and the degree of asymmetry changes before and after training. This has also been observed for Co/CoO thin films [68].

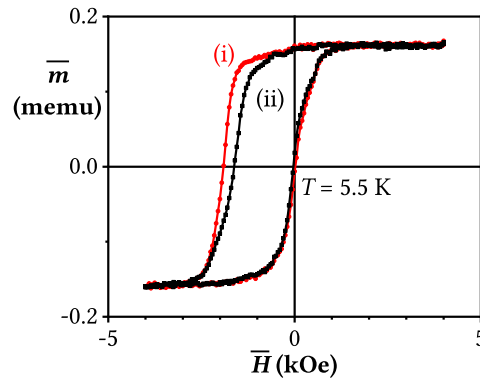


Figure 3.5: The asymmetry of reversal shown before and after training at a measurement temperature of at 5.5 K.

3.3 Structural Effects

This section discusses the effect of the crystallographic order, stoichiometry and interfacial doping on exchange bias. By necessity this section is limited to CoFe/IrMn thin film systems as these effects vary significantly between systems.

3.3.1 Texture

Texture is a preference of an orientation of crystallites in a polycrystalline material [13]. The value of H_{ex} has been observed to depend on texture [37, 87]. This effect is due to the increase in effective anisotropy of the AF layer [11]. The anisotropy is described as effective as it is dependent on the texture. Thus the effective anisotropy can be increased by controlling the texture, while the magnetocrystalline anisotropy of each grain remains constant. When there is a $\{111\}$ plane parallel to the surface of the film but the crystallites are otherwise randomly rotated about that axis, the film is said to have $\langle 111 \rangle$ fibrous texture with the $\langle 111 \rangle$ direction oriented out-of-plane [13]. In IrMn/CoFe systems the largest effective, in-plane, AF anisotropy correlates to an out-of-plane $\langle 111 \rangle$ fibrous texture [32–36]. For this reason in IrMn/CoFe systems out-of-plane $\langle 111 \rangle$ fibrous texture is called in-plane easy-axis texture with the same meaning [11, 37].

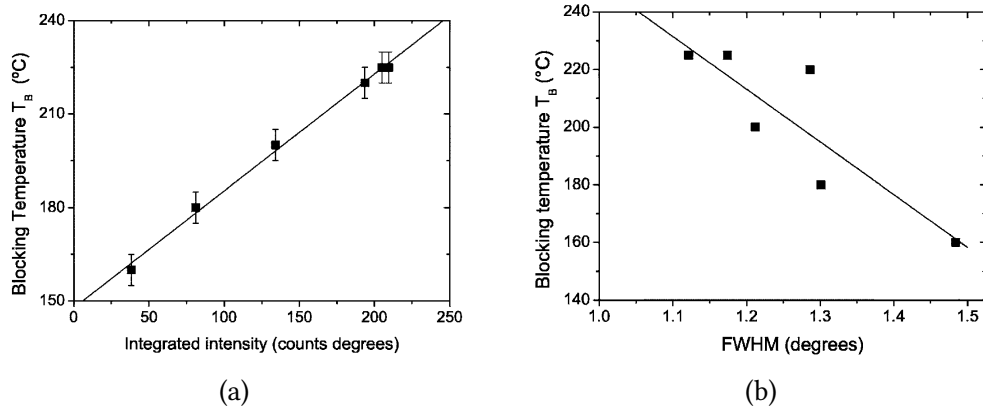


Figure 3.6: The effect of crystallographic order on exchange bias films is shown by the increase in blocking temperature with (a) increasing integrated density and (b) decreasing FWHM of the $\{111\}$ IrMn diffraction peak [36].

Figure 3.6 shows the integrated density and the full-width of half-maximum (FWHM) of the IrMn $\{111\}$ diffraction peak. These have been varied by the thickness of an underlying seed layer. The increasing integrated density and decreasing FWHM are indicators of improving texture. Improvements in the IrMn $\langle 111 \rangle$ texture correlated to a higher value of T_B^{MAX} [36]. It is also correlated with an increase in $\langle T_B \rangle$ which will be discussed in section 4.2 [11].

An increase in grain diameter would result in both an increased integrated density and an increased FWHM. This possibility can therefore be excluded since T_B^{MAX} is shown to decrease with FWHM which is the opposite of would be expected

if increasing FWHM indicated increasing grain diameter [36]. The dependence of T_B^{MAX} on grain diameter will be discussed in section 4.2 [11].

Texture can alter the shape of the hysteresis loop. This is due to the changing pinning energies in the F layer. In addition, the training effect can be altered by different textures. Figure 3.7 shows two F/AF films with different textures. They have composition Si/seed layer (d_{seed})/IrMn (10)/CoFe (3)/Ta (2) (thicknesses in nm) where the seed layer is (a) Cu (5 nm) and (b) NiCr (7.5 nm). The sample grown on a Cu seed layer has 3-D random texture while the sample with a NiCr seed layer has out-of-plane fibrous $\langle 111 \rangle$ texture. Thus for the sample with a NiCr seed layer a $\{111\}$ plane lies parallel to the surface. This is significant as the magnetic easy axis is in-plane. This results in significantly different hysteresis loops. In particular, the sample with poor texture exhibits the training effect, while the sample with strong texture does not [37].

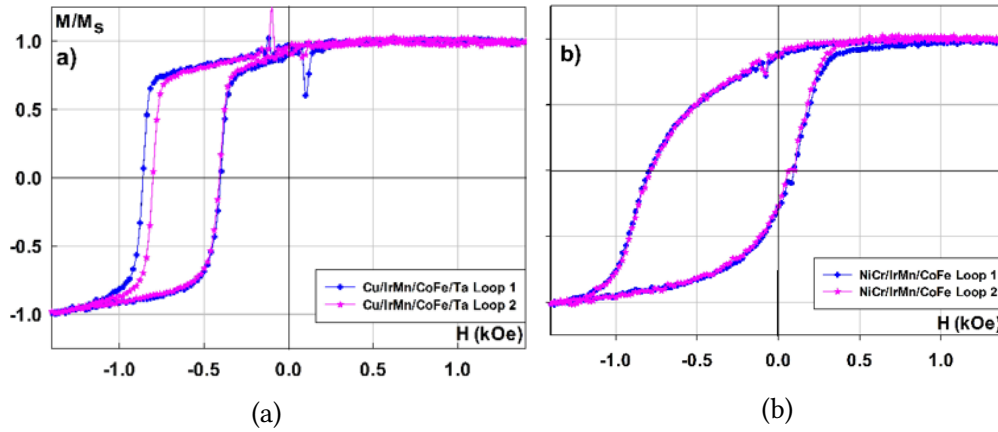


Figure 3.7: Hysteresis loops for a film with (a) weak texture on a Cu seed layer and (b) strong texture on a NiCr seed layer |addedshowing distinct reversal mechanisms [37].

3.3.2 Composition

The stoichiometry of IrMn is crucial for exchange bias as discussed in section 2.3.2. The compositional dependence of the anisotropy is shown in fig. 2.11 based on thermal activation measurements for a film produced in high target utilisation sputtering (HiTUS). The HiTUS system will be discussed in section 5.1.1. The anisotropy of IrMn increases as the proportion of Ir decreases [53]. The maximum anisotropy measured was $(9.2 \pm 1.0) \times 10^6$ erg/cm³ for IrMn₆. The effect of IrMn composition on H_{ex} is shown in fig. 3.8 from on thermal activation measure-

ments. This shows a broad peak from 16 to 20.5 at.% Ir with a sharp reduction outside that range [53]. This corresponds to an Ir content between IrMn_4 and IrMn_5 and excludes the ordered IrMn_3 phase.

A material that is chemically disordered is more chemically isotropic than an ordered material. However, measurements have shown that chemical order does not correspond to magnetocrystalline anisotropy and exchange bias in IrMn [42, 52, 53]. This is demonstrated by the increase in K_{AF} as the Ir content is reduced from the chemically ordered IrMn_3 phase. The origin of anisotropy in AF materials is not yet fully understood and an area of ongoing research [54]. The anisotropy and exchange bias of a sample are not necessarily correlated since the exchange bias is a function of the magnetic order of the AF layer as will be discussed in section 4.2.

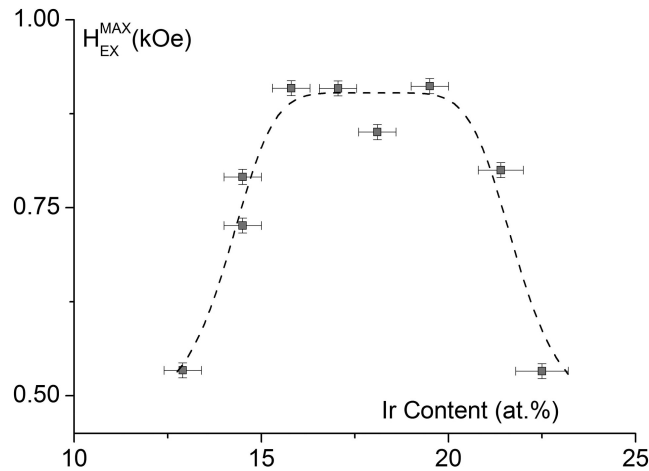


Figure 3.8: The dependence of H_{ex} on the composition of IrMn based on thermal activation measurements shows a broad peak from 16 to 20.5 at.% Ir [53].

The effect of non-magnetic copper impurities in IrMn has also been investigated [88]. This was performed for multi-domain grains with an estimated diameter of ~ 60 nm. The exchange bias at 300 K of a $\text{CoFe}/(\text{IrMn})_{1-x}\text{Cu}_x$ was shown to peak at $x = 0.05$. This resulted in an increase in H_{ex} of 60% compared to the copper-free film. Above $x = 0.1$ the exchange bias is reduced compared to the copper-free film. These results were later re-interpreted using the York Model of Exchange Bias. In this interpretation the Cu impurities act as domain wall pinning sites, effectively reducing the AF grain volume [89].

Neutron diffraction experiments were performed on IrMn with an Ir content between 12.8 and 25.6 at.% [90]. A disordered fcc phase was observed over the whole range of compositions. For disordered IrMn the Ir and Mn can exist in any

lattice site. In the disordered phase Néel temperature T_N increased with increasing Ir content to a maximum of 730 K. In this arrangement there are two antiparallel sublattice magnetisations. An additional ordered phase was observed between 20 and 30 at.% Ir with an enhanced T_N of 930 K, however, the exchange bias of this phase was not investigated [90].

3.3.3 Interfacial Doping Effects

Exchange bias is sensitive to the condition of the F/AF interface since it arises from the exchange interaction over the interface. During deposition, ultra-thin layers can be added to the interfacial region to alter the exchange bias properties. This condition is also known as doping or as the addition of a δ -layer. The changes are sensitive to the thickness and species of the layer. Where the layer thickness is lower than the atomic diameter the ultra-thin layer is in effect an alteration of the composition near the interface. The anisotropy of a CoFe/IrMn system has been shown to increase with the addition of Mn at the interface, reaching a peak at 0.3 or 0.5 nm [91, 92]. This increase is shown in as an increase in H_{ex} in fig. 3.9 for a series of samples with composition Si/Ta (5)/Ru (5)/IrMn (10)/Mn (d_{Mn})/CoFe (2)/Ta (5) (thicknesses in nm) where d_{Mn} is the thickness of the Mn ultra-thin layer.

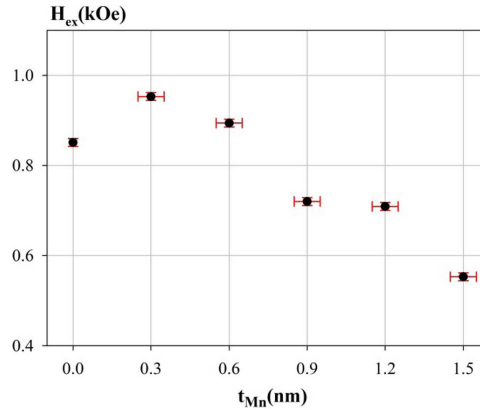


Figure 3.9: The value of H_{ex} increases and goes through a peak with the addition of an ultra-thin layer of Mn at the F/AF interface with thickness d_{Mn} [91].

Other elements that have been observed to increase the exchange bias are Fe, Ni and $Ni_{80}Fe_{20}$ also known as permalloy [93]. For Fe this increase occurred for all the tested thicknesses up to a maximum of 0.45 nm and peaked at a 72 % increase in H_{ex} for a sample with 0.2 nm of Fe at the interface of a Co/IrMn system. In contrast the Ni and permalloy interfacial layers were associated with an enhance-

ment of H_{ex} followed by a reduction below that of the unaltered interface. The thickness below which there is an increase in H_{ex} and above which there was an overall decrease was 4.5 nm for Ni and 3.5 nm for $\text{Ni}_{80}\text{Fe}_{20}$. In the case of Fe and permalloy dopants in Co/IrMn the increase in H_{ex} could be due to the formation of CoFe which has a higher moment than Co. For interfacial Ni the H_{ex} shows a broad peak at 34 % enhancement from 0.1 to 0.3 nm, while for $\text{Ni}_{80}\text{Fe}_{20}$ the peak occurred at 0.1 nm and enhanced H_{ex} by 29 %. A small increase in H_{ex} is shown with an interfacial layer of Pt. This peaked at 10 % when below 0.15 nm [93]. However, a monotonic decrease in J_K with increasing thickness of interfacial Pt layers has also been observed [92]. This was observed for a film with composition $\text{IrMn}_3/\text{Pt}/\text{Co}_{70}\text{Fe}_{30}$.

A reduction in H_{ex} was observed for all thicknesses between 0 and 0.4 nm of Cu and Ta at the interface of a Co/IrMn [93]. Further to this, studies carried on non-magnetic spacer layers at $\text{Ir}_{22}\text{Mn}_{78}/\text{Co}_{84}\text{Fe}_{16}$ interfaces showed a decrease in H_{ex} for thicknesses of Al, Ti, Cu, Ru, Pd, Ag and Au up to 1.0 nm [94]. The rate of H_{ex} reduction was logarithmic for Cu, Ru, Pd, Ag and Au, although Ag had a significantly different rate of reduction. On the other hand the reduction for Al and Ti was neither linear nor logarithmic. For Ti H_{ex} increases between 0.2 and 0.3 nm, although always remains lower than the un-doped case [94].

In the Co/IrMn system an interfacial layer of Au had no effect on H_{ex} up to 0.1 nm thick, with H_{ex} gradually decreasing thereafter [93]. On the other hand an interfacial layer of Gd had no effect on H_{ex} up to 0.25 nm, but this was followed by a rapid decline in H_{ex} such that at 0.35 nm $H_{\text{ex}} = 0$ [93]. This effect has also been seen with Tb interfacial layers in $\text{IrMn}_3/\text{Tb}/\text{Co}_{70}\text{Fe}_{30}$ systems in which a layer up to 0.3 nm thick has no effect on J_K while by 0.5 nm J_K has fallen to less than one third of its initial value. For a system of the segregated F material $\text{CoCrPt}-\text{SiO}_2$ coupled to IrMn, the addition of 0.8 nm of Co at the interface induces perpendicular exchange bias [9]. The strong thickness dependence of these results is indicative of the short range of the relevant exchange forces.

The effects of interfacial layers on H_{ex} are therefore diverse and highly dependent on species and thickness. For this reason this work has undertaken a study in ultra-thin Mn layers at the F/AF interface. However, the scope of these measurements is restricted to interfacial layers of Mn up to 0.6 nm thick. Mn was chosen due to the observed increase in H_{ex} [91, 92].

3.3.4 Effects of Diffusion

Theory of Diffusion

The films discussed in this study are metallic multilayers with thickness of order 10 nm. Because of the thickness of these films, atoms near a surface or interface make up a significant fraction of all the atoms in the film. In addition to this, IrMn and CoFe readily inter-diffuse which leads to complex magnetic behaviour. For this reason, it is necessary to discuss diffusion. In section 3.3.2 and section 3.3.3 the composition of layers and interfaces was discussed. However, both of these will be affected by diffusion of atomic species between layers. Diffusion can change the composition of a layer which has consequences for exchange bias [59]. By definition the surface area of a sphere of root mean square (rms) displacement of material will increase linearly with time t in accordance with

$$A_{\text{rms}} = \mathcal{D}t \quad (3.4)$$

where \mathcal{D} is a diffusion coefficient with dimensions of m^2/s [95, 96].

A polycrystalline solid is made up of two parts, the first of which are the crystalline regions which form each grain and the second is an interconnected network of grain boundaries [97]. In general, diffusion will occur preferentially along the boundaries and dislocations between grains [98–100]. Thus two coefficients of diffusion can be defined where \mathcal{D}_b is the diffusion coefficient in the grain bulk and \mathcal{D}_d is the diffusion coefficient in the dislocation network [96, 98]. In 1961 Harrison established the standard description of diffusion in polycrystalline solids [101].

Three possible diffusion regimes were described based on the relative sizes of \mathcal{D}_b and \mathcal{D}_d [101]. If $\mathcal{D}_b \ll \mathcal{D}_d$, then diffusive changes in composition will be dominated by changes in the composition of the dislocation network. This is called Harrison Type C diffusion. Since the diffusion distance in the bulk is small compared to the thickness of the grain boundaries, material discharged from the bulk will be negligible and so the condition for Harrison type C diffusion is given by

$$\mathcal{D}_b t^2 \ll d_{\text{gb}} \quad (3.5)$$

where t is the time elapsed and d_{gb} is the thickness of the boundary layer around each grain [101].

On the other hand if $\mathcal{D}_b \approx \mathcal{D}_d$, or if the diffusion is allowed to continue for a very long time, then the compositional changes will apply equally to both the crystallite bulk and the dislocations. This is called Harrison Type A diffusion and is equivalent to Fick's Law for fluids [95, 101]. In this case the time t must be much greater than the time taken for a particle to migrate between dislocations. Thus the condition for Harrison Type A diffusion is given by

$$\frac{D_g^2}{4\mathcal{D}_b} \ll t \quad (3.6)$$

where D_g is the grain diameter and \mathcal{D}_b is the bulk diffusion constant [101].

Harrison Type B diffusion is an intermediate regime where $\mathcal{D}_b < \mathcal{D}_d$. It occurs when the conditions for Harrison Type C diffusion and Harrison Type A diffusion are violated simultaneously [101]. Although Harrison's original formulation was applied to the diffusion of anions in an ionic solid it has since been applied to diffusion in metallic solids [102].

Observation of Diffusional Effects

Diffusion in thin films differs from diffusion in bulk due to a number of factors [103, 104]. In a multilayer thin film every volume element is close to a free surface or to an interface. Thus the concentration gradients between layers will be large which will tend to enhance the effects of diffusion. Diffusion across interfaces has the effect of changing an alloy's composition or effectively introduces a new alloy phase at the interfacial region. In addition, the thin films discussed in this work have a grain size ~ 10 nm, which means there is a high density of grain boundaries which, together with the interfaces, will form a dense dislocation network. This will tend to increase the rate of diffusion since diffusion progresses more rapidly through the dislocation network than through the bulk of the grains [105].

Furthermore, the films discussed in this study are grown by sputter deposition with Ar plasma. Although Ar is a non-reactive gas some Ar atoms will be incorporated into the film structure. As well as this the films are exposed to the atmosphere, which is an opportunity for further impurities such as oxygen to be incorporated into the film. For this reason the films are coated in a capping layer made of Ta or a platinum group metal such as Ru. Impurities will diffuse through

the film themselves but can also affect the diffusion of other species as they will cause dislocations. Unlike in a bulk material, thin films are subject to significant stresses in the plane of the film. These stresses can result in dislocations or can enhance diffusion around dislocations [103, 104]. Figure 3.10 shows the distribution of atomic species in a sputtered IrMn/Co/Cu film measured using atom-probe tomography [59]. The solid line indicates the Co/Cu interface and the dashed lines indicate the IrMn/Co interfacial region. The film is shown (a) in the as deposited state as well as after annealing at (b) 400 °C and (c) 500 °C. The annealing process has resulted in significant intermixing of the Co, Mn and Ir atoms into adjacent layers when compared to the as-deposited sample. This has resulted in the creation of an interfacial region with a similar thickness to the sputtered layers where Co, Mn and Ir atoms are all present [59].

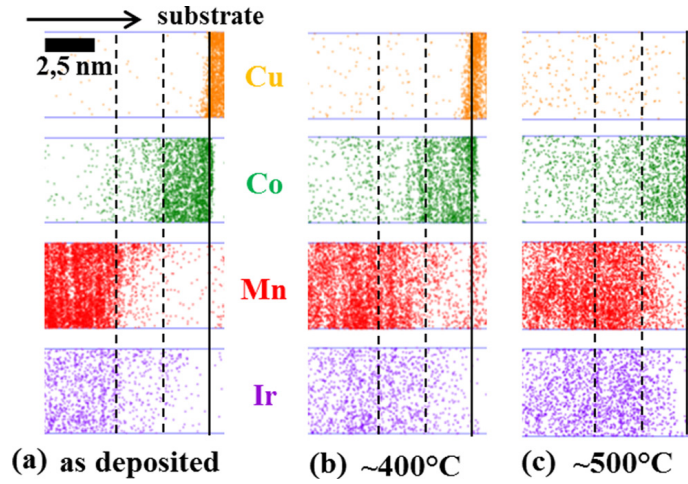


Figure 3.10: Diffusion in a IrMn/Co/Cu thin film measured using atom-probe tomography. The film is shown in the (a) as deposited condition and (b) after annealing at 673 K (400 °C) and (c) 773 K (500 °C) showing that intermixing has occurred following deposition and diffusion progresses as the temperature is increased [59].

In the York Model of Exchange Bias the AF layer is magnetically ordered by the exchange field from the F layer at high temperature. This will be discussed in more detail in section 4.2. Thus the effect of temperature on diffusion must be considered. In general

$$\mathcal{D}_d = \xi a^2 \omega_D \exp\left(-\frac{\Delta E_{\text{diff}}}{k_B T}\right) \quad (3.7)$$

where ξ is a dimensionless factor dependent on the lattice and of order unity, a is the lattice spacing, ω_D is the Debye frequency ΔE_{diff} is the energy barrier to moving an atom between sites, k_B is the Boltzmann constant and T is the temperature [105]. Diffusion will progress with time t . For type-C diffusion where diffusion in the dislocation network dominates, the concentration profile C of a

tracer species with a starting condition of a thin layer will have the form

$$C \propto \frac{1}{\sqrt{\mathcal{D}_d t}} \exp\left(-\frac{\delta^2}{4\mathcal{D}_d t}\right) \quad (3.8)$$

where \mathcal{D}_d is the diffusion coefficient in the dislocation network, t is time and δ is the diffusion depth of the tracer [97].

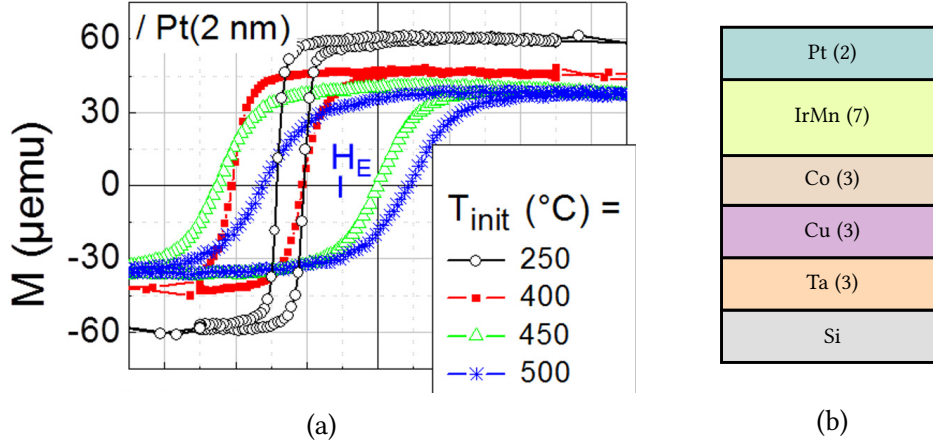


Figure 3.11: The effects of diffusion in an IrMn/Co thin film on (a) the exchange bias and shape of the hysteresis loop where the x -axis spans a range of \vec{H} of -0.7 to 0.7 kOe for a film with (b) structure shown schematically (thicknesses in nm) [59].

The effects of diffusion on the hysteresis loops of an IrMn/Co thin film are shown in fig. 3.11(a) where the x -axis spans a range of \vec{H} from -0.7 to 0.7 kOe. [59]. The film has composition Si/SiO₂/Ta (3)/ Cu (3)/Co (3)/IrMn (7)/Pt (2) (thicknesses in nm) which is shown schematically in fig. 3.11(b). The hysteresis loops shown in fig. 3.11(a) are for films which have been field-cooled in a field of 2.5 kOe. The samples were cooled from an initial temperature $523\text{ K} < T_{\text{init}} < 773\text{ K}$ to room temperature over 60 min. The hysteresis loops show an initial increase in the exchange bias H_{ex} followed by a decrease for high annealing temperatures. This decrease coincides with an increase in the coercivity H_c and a decrease in the saturation magnetisation M_s . The diffusion that occurs at the interface of the Co/IrMn system will be indicative of the diffusion that occurs in CoFe/IrMn systems. However, the presence of Fe will change both the diffusive properties and the effect of diffusion on the magnetic properties. In addition, in Harrison Type C diffusion the diffusion proceeds preferentially through the dislocation network. Therefore all else being equal diffusion will progress more quickly in a film with a lower median grain volume due to the increase in the corresponding dislocation network density. The median grain volume and grain volume distribution of the Co/IrMn is not given but the layer thickness are given as Co (3)/IrMn (7) (thicknesses in nm)

which is of the same order as used in this work [59]. The decrease in M_s will be discussed further in chapter 7.

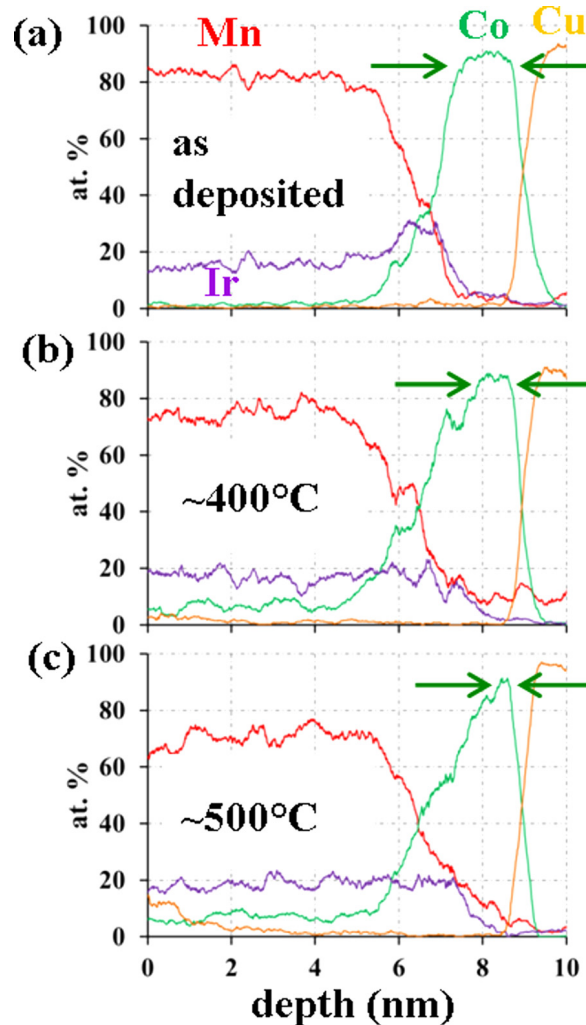


Figure 3.12: The concentrations of atomic species as function of depth through a IrMn/Co/Cu thin film when (a) unannealed and (b) annealed at 673 K (400 °C) and (c) 773 K (500 °C) showing significant intermixing and the change in shape of the Co peak as it diffuses into the IrMn layer at elevated temperature [59].

The effect of diffusion is shown in fig. 3.10 and fig. 3.12 for a film with composition Si/SiO₂/ Ta (3)/[Cu (3)/Co (3)/IrMn (7)]₇/ Pt (80) (thicknesses in nm) measured with a 3-D atom probe. Figure 3.10 shows a distribution maps for each atomic species where the solid line is the abrupt interface between Co and Cu while the dashed lines are the diffuse interfaces between IrMn and Co [59]. Only one representative [Cu (3)/Co (3)/IrMn (7)] sub-repetition is shown, this being the second when counted from the film surface. This shows significant intermixing of the IrMn and Co layers resulting in an ill-defined interface. This will be discussed further in section 5.2.1. Figure 3.12 shows the concentration profiles of each atomic species after different annealing conditions. It shows that an interfacial region ex-

ists with a continuum of Ir, Mn and Co concentrations even in the unannealed state and that the degree of intermixing increases at high annealing temperatures [59].

3.4 Related Phenomena

Despite a great deal of research interest there remain a number of unexplained phenomena that occur in exchange bias systems, including CoFe/IrMn systems. In general these relate to increases or changes in H_{ex} that occur under certain conditions. However, this section also discusses the \vec{m} offset which is a magnetisation shift in the hysteresis loop. These phenomena are indicative of the complexity of the exchange bias mechanism and the F/AF interface.

3.4.1 \vec{H}_{set} Dependence

Exchange bias arises after the setting of an AF film. This is brought about by the direct exchange interaction from the F layer and will be discussed in detail in section 4.2. For this to result in a net exchange bias the F film must be ordered, which is achieved by use of a saturating external field \vec{H}_{set} [1, 2]. Once saturated, there is by definition no further increase in F order with increasing field strength [13]. However, increasing the field strength during setting has been observed to increase the maximum H_{ex} [11, 67, 91]. This indicates an increase in the set fraction of the AF film without a corresponding increase in order in the F film.

An example of the \vec{H}_{set} dependence of H_{ex} is shown in fig. 3.13 for a series of films with composition Si/Ta (5)/Ru (5)/IrMn (10)/CoFe (3)/Ta (5) (thicknesses in nm) and a median grain diameter between 6.6 and 7.6 nm [67]. In the figure this is denoted D_m . A further example is shown in fig. 3.14 for a series of films with composition Si/Ta (5)/Ru (5)/IrMn (10)/Mn (d_{Mn})/CoFe (2)/Ru (5) (thicknesses in nm) where d_{Mn} is the thickness of the ultra-thin interfacial Mn layer. In the figure this is denoted t_{Mn} . These films were produced by high target utilisation sputtering (HiTUS). Note that the AF grain diameter and the addition of Mn at the F/AF interface affects both the total exchange bias of the film and the form of the setting field dependence of exchange bias. Figure 3.14 shows that the dependence is weakest when $d_{\text{Mn}} = 0$ nm.

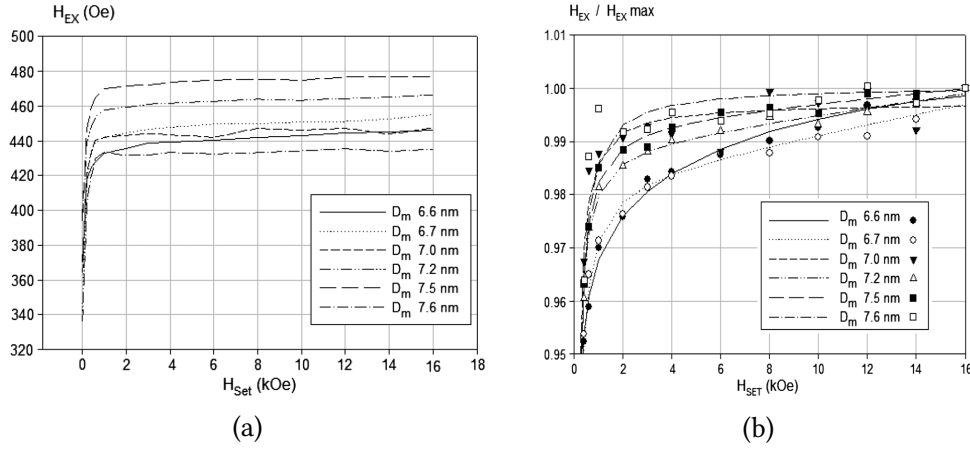


Figure 3.13: The \vec{H}_{set} dependence of (a) H_{ex} and (b) normalised H_{ex} for for a series of films with composition Si/Ta (5)/Ru (5)/IrMn (10)/CoFe (3)/Ta (5) (thicknesses in nm) and a median grain diameter between 6.6 and 7.6 nm [67].

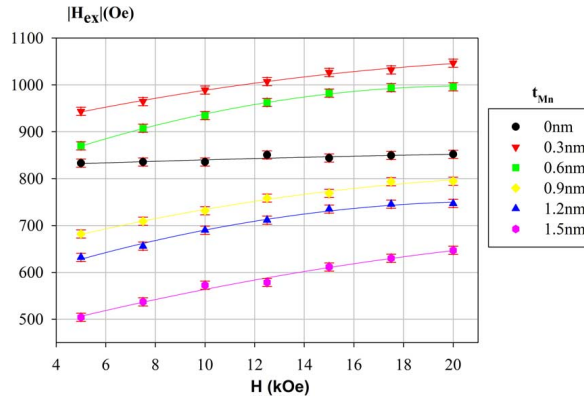


Figure 3.14: The setting field dependance is shown by the increase in exchange bias H_{ex} with setting field \vec{H}_{set} for samples with composition Si/Ta (5)/Ru (5)/IrMn (10)/Mn (t_{Mn})/CoFe (2)/Ru (5) (thicknesses in nm) where t_{Mn} is the thickness of the ultra-thin interfacial Mn layer [91].

3.4.2 Trilayer Experiment

In this work the F layer is sputtered after the AF layer and is therefore described as being above the AF layer. Such an arrangement of F and AF layers is also called bottom-biasing. However, it is also possible to have the F layer below the AF layer, which is known as a top-biased stack. In the trilayer experiment a heterostructure is sputtered with a layer order of F/AF/F. In this way there is a F layer both above and below the AF layer. In this arrangement the AF induces exchange bias in both F layers [60]. A trilayer sample was prepared with composition Si/NiCr (5)/CoFe (12)/IrMn (5)/CoFe (8)/Ta (5) (thicknesses in nm) by Seagate Technology at their facility in Northern Ireland. After setting the two CoFe layers have different values of H_{ex} and H_c , due to their different thicknesses [61]. This results in a

hysteresis loop with two separated sub-loops. The 8 nm loop has a higher value of H_{ex} and H_c than the 12 nm loop. The combined hysteresis loop for the whole sample is shown in fig. 3.15, showing a plateau region between the two sub-loops.

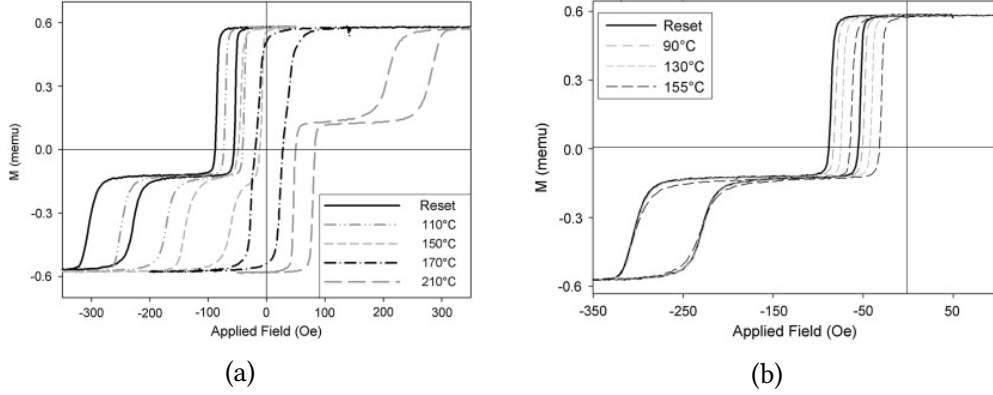


Figure 3.15: The thermal activation of a F/AF/F system carried out at (a) negative saturation and (b) -150 Oe. In the case of (a) the exchange bias of both sub-loops changes whereas for (b) this is only true of one sub-loop [60].

In fig. 3.15(a) thermal activation is carried out at negative saturation, resulting in both loops moving to the right. This occurs because of the changing order of the AF layer as will be discussed in section 4.2. In fig. 3.15(b) thermal activation is carried out in a field that falls in the plateau region at $\vec{H} = -150$ Oe. This results in a change in H_{ex} of only the low-coercivity 12 nm loop which is the rightmost loop in fig. 3.15(b). This difference in the change in H_{ex} is despite the fact that the two F layers are coupled to the same 5 nm thick AF layer. Thus there must exist spins at the F/AF interface that moderate the exchange interaction between the AF layer and the two F layers. Some portion of the H_{ex} is due to the AF bulk while another portion is due to the interfacial regions between the AF layer and the F layers. These interfacial regions have magnetic behaviour that is not identical to the AF bulk and independent of the other interface.

3.4.3 Spin Freezing

A low temperature measurement of the conventional blocking temperature T_B^{MAX} is shown in fig. 3.16 for a CoFe/IrMn thin film [106]. In a measurement of T_B^{MAX} a hysteresis loop of an exchange bias sample is measured at increasing temperatures. As will be discussed in section 4.2.3 it is possible to measure $\langle T_B \rangle$ while making all measurements at the same temperature [11]. This eliminates the effect of thermal activation during the measurement.

The measurement of T_B^{MAX} shows an increase in H_{ex} that occurs when the film is measured below 50 K [106]. This increase in H_{ex} is called spin freezing. This enhancement of H_{ex} occurs below the temperature of non-activation T_{NA} and therefore does not originate from changes in the AF bulk. The meaning and importance of T_{NA} will be discussed as part of the York Model of Exchange Bias in section 4.2. A study in spin freezing was undertaken as part of this work and will be discussed in section 7.1. Spin freezing has also been observed in Co/IrMn systems [107].

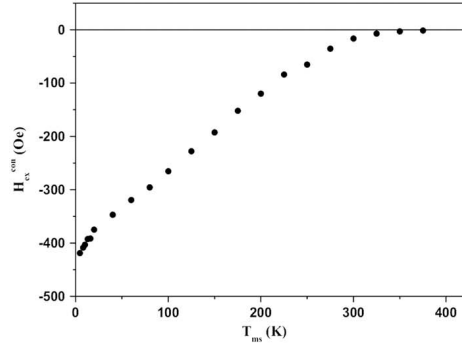


Figure 3.16: Measurement of exchange bias with T for CoFe/IrMn showing an increase in H_{ex} which is further enhanced below 50 K attributed to spin freezing [106]. The point where $H_{\text{ex}} = 0$ is the maximum blocking temperature T_B^{MAX} [11].

3.4.4 m_s Offset

While the field shift of the hysteresis loop is the earliest known and most-studied aspect of exchange bias, the magnetisation shift has only recently attracted attention. In a traditional F material M_s is constant independent of the direction in which it is measured. This differentiates exchange bias materials from all other F materials. This has been observed in thin films of Co/CoO and Fe/Fe₂O₃ [108, 109]. In addition the magnetisation offset has been observed in exchange biased nanoparticles of Fe/Fe₂O₃ and granular systems of Fe/MnO₂ [110–112]. It has also been observed for oxide multilayers, cobalt-doped ZnO and mixed-phase ferrimagnetic systems such as La_{0.3}Sr_{0.7}FeO₃/SrRuO₃ and Bi_{0.84}La_{0.16}Fe_{0.96}Ti_{0.04}O₃ [108, 113–115]. The shift was shown to correlate to H_{ex} in FeF₂/Fe and MnF₂/Fe thin films and in simulations of Co/CoO bilayers [116, 117].

For the purposes of calculation the m_s or M_s offset is defined by two values, these being the magnetic moment of magnetisation in the positive field direction m_s^+ or M_s^+ , and the magnetic moment or magnetisation in the negative field direc-

tion m_s^- or M_s^- . The measurements of m_s^+ and m_s^- must be made at a field value when the hysteresis loop is saturated.

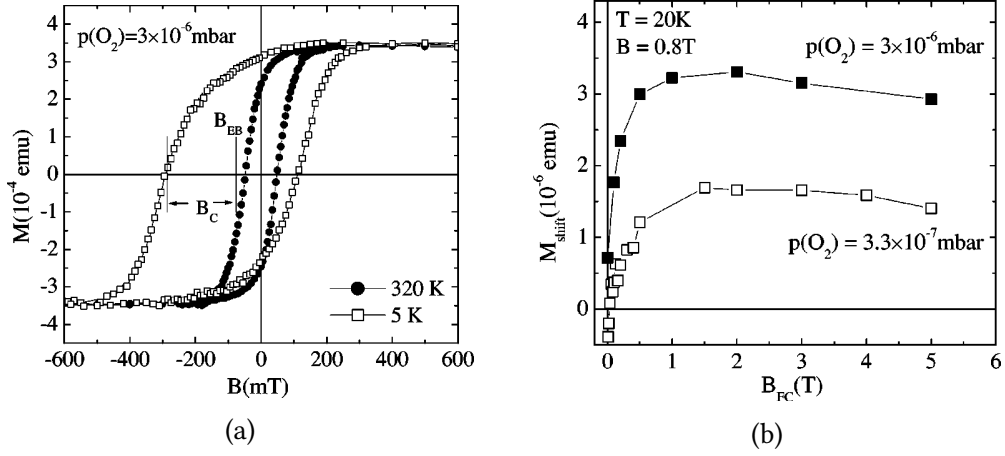


Figure 3.17: The magnetisation offset of (a) hysteresis loops as (b) a function of cooling field [108].

An example of the M_s offset for a film with composition Co/CoO prepared by reactive sputtering is shown in fig. 3.17 [108]. Figure 3.17(a) shows the hysteresis loops taken at 5 and 320 K. The offset ΔM_s is two orders of magnitude lower than the saturation magnetisation M_s . The values of M_s^+ and M_s^- were taken at ± 0.8 T and $T = 20$ K. The shift was defined as

$$\Delta M_s = M_s^+ + M_s^- \quad (3.9)$$

where ΔM_s has dimensions of emu/g or emu/cm². The offset can also be expressed in terms of moment

$$\Delta m_s = m_s^+ + m_s^- \quad (3.10)$$

where Δm_s has dimensions of emu which are equivalent to erg/G, m_s^+ is the magnetic moment at positive saturation and m_s^- is the moment at negative saturation. Since both M_s^- and m_s^- are negative, this definition amounts to the difference in magnetisation or magnetic moment when measured in the positive and negative directions. For a loop shifted in the same direction as the setting field $M_s^+ > -M_s^-$ and $m_s^+ > -m_s^-$. Therefore both ΔM_s and Δm_s are positive.

4. Models of Exchange Bias

There has been significant research interest in exchange bias since its discovery in 1956 [1]. This has been partially motivated by its use in the read head of the hard disk drive (HDD) since the 1990s. This work excludes consideration of exchange bias in nanoparticles and epitaxial single-crystal systems, focusing only on exchange bias in polycrystalline thin films using IrMn/CoFe. This is both because these are the most relevant for applications in HDDs and because these films achieve the largest room-temperature exchange bias.

Even narrowing the discussion in this way, there is no complete theory that fully explains all aspects of exchange bias in polycrystalline IrMn/CoFe thin films. For this reason, it is worthwhile to discuss historical models of exchange bias, including some which use different systems. A great deal of exchange bias models have been proposed with varying degrees of success. In this chapter four will be discussed in some detail either because of their prominence when they were proposed or because of the influence they had on later models, in particular the York Model of Exchange Bias.

However to be concise, a number of models will not be discussed. These are the models of Néel [118], Xi [119], Mauri et al. [120], Malozemoff [121, 122], Koon [123], Schultness and Butler [124], Stamps and Camry [125, 126], and Saha and Victoria [127]. However, they will be briefly addressed here.

The model proposed by Néel considered a F/AF interface with realistic roughness, leading to both AF sublattices being present at the interface [118]. However, it failed to predict realistic values of H_{ex} .

The thermal fluctuation model was proposed by Xi [119]. It described an increase in H_{ex} with the thickness of the AF layer for large grain systems and a decrease in T_{B} with the measurement time. However, the model does not consider the effects of a distribution of grain sizes. In the model proposed by Mauri et al. domain walls parallel to the interface reduced the predicted H_{ex} to realistic values [120]. However, a thick AF layer is required to support this domain structure, while H_{ex} has been observed in systems with AF thickness of a few atoms [11].

The Malozemoff model also made use of interfacial domain walls [121, 122]. However, the model strictly applies only to simple cubic single-crystal AF layers with interfacial roughness, and thus cannot explain H_{ex} in polycrystalline systems or in single-crystal systems with flat interfaces. The model of Koon proposed that the interfacial AF spins are coupled to the F layer through spin-flop coupling [123].

By assuming a flat interface between single-crystal and single-domain F and AF layers, Schultness and Butler were able to solve the Landau-Lifshitz-Gilbert equation at the interface [124]. In this model interfacial spin-flop coupling results in the increase in H_{c} while interfacial defects results in H_{ex} . However, this model is not applicable to polycrystalline systems with rough interfaces. In addition the Landau-Lifshitz-Gilbert equation is only valid at $T = 0$. In the model proposed by Stamps two separate mechanisms of exchange bias are suggested [125]. The first is reversible domain walls in the AF layer and the second is irreversible processes take place during the hysteresis measurement. A thermal activation mechanism was proposed to describe the rate at which equilibrium was approached [126].

The micromagnetic model proposed by Saha and Victora successfully predicted the increase in H_{ex} with the thickness of the antiferromagnetic layer d_{AF} and the dependence of H_{ex} and H_{c} on the thermal energy supplied [127]. This model assumed non-interacting AF grains coupled to F grains through rough interfaces. In this model the AF micromagnetic regions were considered to have easy-axes distributed in the plane of the film. The AF regions had a net moment due to uncompensated spins at the rough F/AF interface. The coupling between the F and AF regions was through the coupling of their net moments. The reversal of the AF moments is by in-plane coherent rotation. The net moment of the AF region points either in the direction of a local or global energy minimum, dependent on the supplied thermal energy [127].

The York Model of Exchange Bias is currently the most complete model of exchange bias systems and its associated phenomena. In this chapter its advantages over other models will be discussed. While the York Model of Exchange Bias is extremely successful it does not fully explain all exchange bias related phenomena. The limitations of the York Model of Exchange Bias will be discussed.

Since there remain aspects of exchange bias that have not been explained, there exist a number of contemporary models that attempt to explain these phenomena. These extended models typically build on earlier incomplete models. In this chapter some extended models will be outlined, including an extension to the York Model of Exchange Bias. It should be noted that there is significant mutual compatibility between many of these models.

4.1 Early Models

4.1.1 Meiklejohn and Bean

The earliest model of exchange bias was proposed by its discoverers Meiklejohn and Bean in the 1950s [1, 2]. This model was applied to a compact of partially-oxidised Co particles. Since the particles were not fully oxidised, F Co and AF CoO coexist in each particle. An example of a hysteresis loop they measured is shown in fig. 2.9 on page 23. In this model it was assumed that the interface between the F and AF materials was flat and that each material was single-domain. The F and AF interact only via direct exchange across this uncompensated (1 1 1) interface. For both the F and AF the coupling within the material was assumed to be stronger than the coupling between the materials. This situation is shown in fig. 4.1(a).

The model assumes that the F material is ordered. Thus if there is exchange coupling as the sample is cooled through T_N , then there will be a preferential alignment of the interfacial AF spins. This arises due to the paramagnetic ordering of the AF material at T_N . The direct exchange within the AF will result in the entire material being ordered. Thus if the sample is cooled to a low temperature at which the anisotropy of the AF material is large, then the direct exchange interaction will align the F spins in one direction. This can then be observed as the shift

in the hysteresis loop. This unidirectional anisotropy will be maintained unless it is overcome by the torque exerted by the F material over the interface.

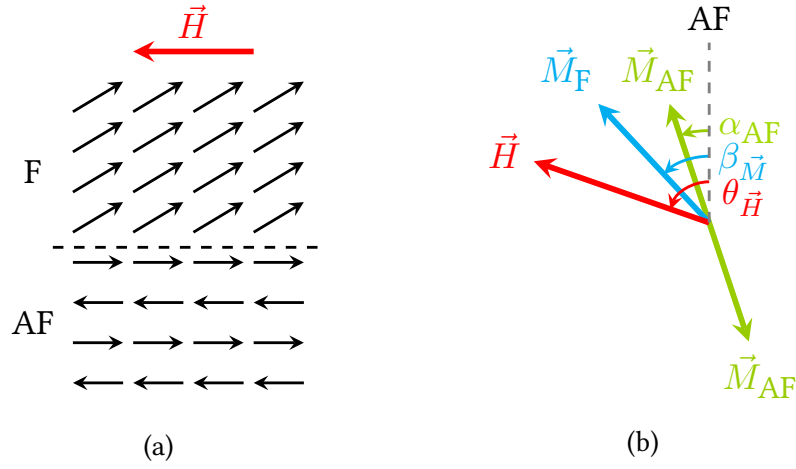


Figure 4.1: Schematic of (a) the F/AF interface with a small applied field and (b) vector diagram of the Meiklejohn and Bean model of exchange bias [2, 128].

However, if the sample is cooled through T_N without an applied external field then exchange bias will not be observed. The external field aligns F material in all the particles. Thus when cooled through T_N in an external field all the particles have the same AF order. When no external field is used each particle has a unidirectional exchange anisotropy, but this cannot be observed in the compact because of the random distribution of directions of the anisotropy axes.

The model gives the interfacial energy E_I as the sum of misalignments such that

$$E_I = -|\vec{H}||\vec{M}|\cos(\theta_{\vec{H}} - \beta_{\vec{M}}) + K_{AF}\sin^2(\alpha_{AF}) - J_K\cos(\beta_{\vec{M}} - \alpha_{AF}) \quad (4.1)$$

where \vec{H} is the applied external field, \vec{M} is the magnetisation of the F material, $(\theta_{\vec{H}} - \beta_{\vec{M}})$ is the angle between \vec{H} and \vec{M} , K_{AF} is the anisotropy constant of the AF material, α_{AF} is the angle between K_{AF} and the sublattice magnetisation, J_K is the interfacial coupling constant and $(\beta_{\vec{M}} - \alpha_{AF})$ is the angle between the F and AF sublattice magnetisations [2]. The relative alignments of these quantities are shown in fig. 4.1(b).

This model can be used to calculate theoretical values of H_{c1} and H_{c2} from which H_c and H_{ex} can be found. This is done by assuming that \vec{M} is constant and both it and \vec{H} are aligned to the easy axis of the F. In addition the AF is also aligned to its easy axis, which is also parallel to the F easy axis [128]. Finally, the F film

thickness d_F is also included. This simplifies eq. (4.1) to

$$E_1 = -|\vec{H}||\vec{M}|d_F \cos(\beta_{\vec{M}}) + K_F \sin^2(\beta_{\vec{M}}) - J_K \cos(\beta_{\vec{M}}) \quad (4.2)$$

Thus E_1 is minimised at $\beta_{\vec{M}} = 0$ where $J_K + \vec{H} + 2K_F > 0$ and maximised at $\beta_{\vec{M}} = \pi$ where $2K_F - J_K - \vec{H} > 0$. These conditions allow the bounds for the coercive fields H_{c1} and H_{c2} to be given by

$$H_{c1} = -\frac{J_K - 2K_F}{|\vec{M}|d_F} \quad (4.3)$$

$$H_{c2} = -\frac{J_K + 2K_F}{|\vec{M}|d_F}$$

where H_{c1} is the field when the film first reaches zero magnetisation when going from positive to negative saturation while H_{c2} is the field when the film returns to positive saturation. Half of the difference between these fields gives H_c , while the average of them gives H_{ex} . These fields not being equal in magnitude results in an overall shift in the hysteresis loop [128]. Thus H_{ex} is the midpoint of the loop directly proportional to the interfacial coupling, given by the average of the expressions in eq. (4.3) so that

$$H_{ex} = \frac{J_K}{|\vec{M}|d_F} \quad (4.4)$$

This calculation results in a values of H_{ex} typically two orders of magnitude higher than for any system measured [46]. These extremely high values arise due to a number of central assumptions, such as the flat interface and lack of defects of any kind. In addition, it also predicts that $H_{ex} = 0$ for a fully compensated interface which is not observed experimentally. The model can also not account for the many exchange bias phenomena discovered, including changes in H_{ex} occurring below T_N . Despite the problems with this model, the conclusion that $K_{AF}d_{AF} \geq J_K$ is a necessary condition for exchange bias is reasonable. Were this not the case the interfacial coupling constant would overcome the AF anisotropy, meaning the AF would simply rotate with the F layer.

4.1.2 Fulcomer and Charap

The first significant model to address the changes seen in H_{ex} below T_N and to consider the effect of distributed particle size was the 1972 model of Fulcomer and Charap [129]. This model was applied to a partially-oxidised NiFe film. The oxide NiO formed a discontinuous AF layer with a typical grain diameter of 30 nm on top of a continuous F film. The AF was treated as an assembly of non-interacting particles exchange coupled to the moment of the adjacent F film. The total energy of an AF particle E_{AF} is thus given by

$$E_{\text{AF}} = K_{\text{AF}} A_{\text{AF}} d_{\text{AF}} \sin^2(\theta_{\text{AF}} - \psi_{\text{AF}}) - J_K c_I A_{\text{AF}} \cos(\theta_{\text{AF}} - \phi_{\text{F}}) \quad (4.5)$$

where K_{AF} is the uniaxial anisotropy constant, A_{AF} is the area of the AF grain in contact with the F, d_{AF} is the thickness of the AF grain, θ_{AF} is the angle between the surface AF moment and the F easy axis, ψ_{AF} is the angle between the F and AF easy axes, ϕ_{F} is the angle between the F magnetisation and easy axis, J_K is the interface coupling constant and c_I is the interfacial contact fraction [129]. The relative alignment of these quantities are shown in fig. 4.2(a).

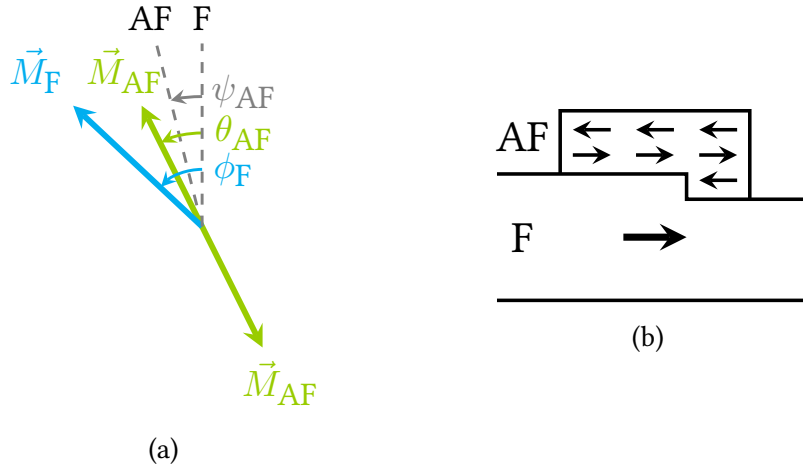


Figure 4.2: Schematic of (a) vector diagram and (b) an example of c_I having a value less than 1 due to a stepped interface in the Fulcomer and Charap model of exchange bias [129].

Note that unlike the Meiklejohn and Bean model shown in fig. 4.1(b), this model measures angles from the F easy axis and does not require that the F and AF easy axes are parallel. However, considering the case where they are parallel, and thus $\psi_{\text{AF}} = 0$, allows calculation of energy minima of eq. (4.5) and the energy barrier between these states [129]. The contact fraction c_I accounts for the fact that AF

grains with the same area can have unequal surface moments. This is due to different proportions of each AF sublattice being present at the surface, for example due to a step defect. An example of such a situation is shown in fig. 4.2(b).

By considering a population of AF grains with a distribution of sizes and shapes, Fulcomer and Charap modelled a system with distributed anisotropy and coupling energies, E_K and E_J respectively. The maximum exchange field is calculated from

$$H_{\text{ex}} = \pm H_c - \frac{N_{\text{AF}}}{M_s V_f} \int_0^\infty \int_0^\infty \vec{m}(t) E_J G(E_K, E_J) dE_K dE_J \quad (4.6)$$

where N_{AF} is the number of AF particles, M_s and V_f are the saturation magnetisation and volume of the F film, $\vec{m}(t)$ is the time-dependent surface moment of the F layer, $G(E_K, E_J)$ is the joint distribution function of anisotropy energy E_K and coupling energy E_J .

Since the AF switching is dependent on thermal activation, $\vec{m}(t)$ is the term that introduces temperature-dependent behaviour. The function $G(E_K, E_J)$ is determined by three independent physical properties of the grains, these being the area A_{AF} , thickness d_{AF} and contact fraction c_f . In the model's original formulation it is assumed that all values of grain area between zero and some maximum value are equally likely. The distributions for thickness and contact fraction were also assumed to have the same form. While the model requires that $G(E_K, E_J)$ be distributed, it also concludes that knowledge of the precise shape of this distribution is unnecessary. However, as will be discussed in section 4.2: The York Model, the shape of the distribution is critical for understanding exchange bias properties. However, for this model a flat distribution is justified as being physically plausible, intuitive and maximally simplistic.

Using this model analogous to a Stoner-Wohlfarth system, numerical modelling based on a granular reversal model gave some agreement to experimental observations, as shown in fig. 4.3. This model was able to predict the temperature dependence of H_{ex} over a wide range of temperatures and had reasonable agreement with H_c near T_B [129, 130]. The success of this distributed and thermal model meant it influenced many later models including the York Model of Exchange Bias. Similar models were used to analyse the dependence of H_{ex} and T_B on d_{AF} [119].

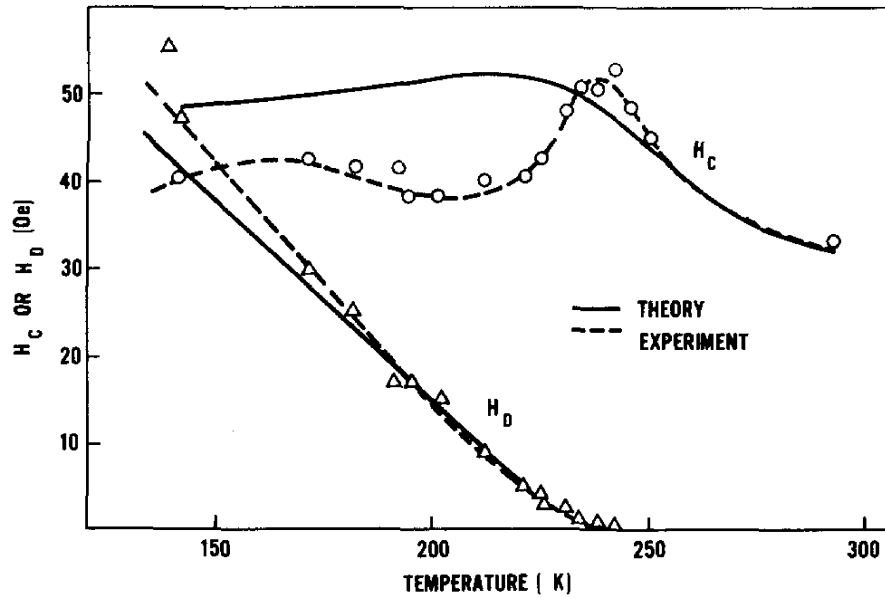


Figure 4.3: The Fulcomer and Charap model compared to experimental results for Co/CoO film. The total film thickness was 1000 Å before a 1 h oxidation at 200 °C. Exchange bias is shown as H_D . There is good agreement between experiment and theory for exchange bias but not for coercivity H_c [129].

4.1.3 Stiles and McMichael

The model outlined by Stiles and McMichael in 1999 consists of a polycrystalline layer of F coupled to independent, randomly oriented and randomly sized AF grains by direct exchange [47]. The interface is frustrated because both AF sublattices are present at the interface. As the F magnetisation rotates, the interfacial magnetisation of the grain adjusts to minimise the exchange energy at the interface by aligning parallel to the F magnetisation \vec{M}_F . However, the sublattice magnetisation of each layer from the interface is incrementally more aligned with the AF easy axis direction $\pm \hat{u}$. In fig. 4.4 a single sublattice is shown in two arrangements, either rotating to $-\hat{u}$ or $+\hat{u}$. For clarity, the corresponding sublattice with opposite spins is not shown.

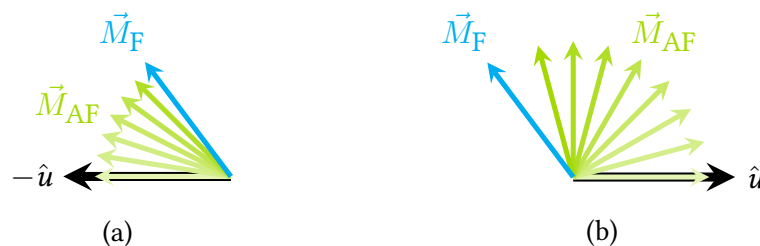


Figure 4.4: The magnetisation of an AF sublattice rotates from parallel to the \vec{M}_F direction to parallel to $\pm \hat{u}$ forming a partial domain wall [131].

This rotation of magnetisation through the AF constitutes a partial domain wall and the deviation from $\pm \hat{u}$ has an associated energy which at the interface is given by

$$E_I = -N_S J_{\text{net}} \frac{\vec{M}_F}{|\vec{M}_F|} \cdot \frac{\vec{m}_I}{|\vec{m}_I|} + \frac{N_S a^2 \sigma_{\text{DW}}}{2} \left[1 - \frac{\vec{m}_I}{|\vec{m}_I|} \cdot (\pm \hat{u}) \right] \quad (4.7)$$

where N_S is the number of spins at the interface, J_{net} is the effective interfacial coupling per spin, $\frac{\vec{M}_F}{|\vec{M}_F|}$ and $\frac{\vec{m}_I}{|\vec{m}_I|}$ are the unit vectors in the direction of the F magnetisation and interfacial moment respectively, a is the lattice constant and thus a^2 is the area of the interface spin, σ_{DW} is the domain wall energy per unit area of the AF and \hat{u} is the unit vector in the AF easy axis direction [47]. These two energy states are separated by an energy barrier.

When the AF is isolated it has two degenerate ground states, one with sublattice magnetisation along \hat{u} and the other along $-\hat{u}$. However, the energy levels of these states are not equal when the AF film is coupled to a F layer. This is a result of the partial domain wall energy shown in eq. (4.7).

The model distinguishes two separate timescales for AF grains, a short timescale responsible for the antiparallel order of AF sublattices within each ground state and a long timescale responsible for the switching of sublattices between the two ground states. These timescales are classified as long or short dependent on the length of the measurement [47]. The short timescale is on the order of seconds to minutes and refers to changes that occur during the measurement. The long timescale is on the order of hours to days and refers to changes that occur between repeated measurements. The short timescale sets in at T_N and is responsible for the antiparallel ordering of the two sublattices, as opposed to the paramagnetic P order observed above T_N . On a longer timescale, the AF order can switch between the two states so that the sublattice magnetised in the \hat{u} direction switches to the $-\hat{u}$, while the other sublattice switches from $-\hat{u}$ to \hat{u} . The long timescale results in the reduction in H_{ex} with time and with repeated field cycling [84, 132].

For a given temperature and measurement time these two timescales can be used to categorise the AF grains into three populations with characteristic behaviours. A stable grain will remain in its initial state throughout the measurement, being affected by neither the short or long timescales. An unstable grain is unstable on the short timescale and so will flip from one state to the other at a rate much faster than the measurement time. A partially stable grain is affected by the

long timescale but not the short one. Therefore a partially stable grain will remain in the lowest energy state and not any other. This is because there is sufficient thermal energy to overcome the energy barrier to reversal, as is the case for the unstable grains, but not so much thermal energy that the grain is continuously reoriented. Consideration of thermal activation of AF grains explains why there is a difference between T_N and T_B , which is due to the condition for partial stability being reached at a lower temperature than the condition for instability [133].

The model overestimates the value of H_{ex} and predicts it will decrease with d_{AF} [131]. The model successfully describes the effect of thermal activation on magnetic measurements of exchange bias grains. However, it does not consider the combined effect of grains of different sizes nor does it describe any grain volume dependence. The model also does not describe a measurement protocol to control the effects of thermal activation.

4.1.4 Domain State Model

In 2002 the Domain State model proposed that exchange bias arises from domain formation in the AF layer [117]. In the model, domain walls form perpendicular to the interface and extend through the volume of the AF film. This model is applicable for a single-crystal AF layer, but was also applied to polycrystalline systems. However, the AF is described as diluted, meaning impurities are present either in the form of vacant lattice sites or sites occupied by non-magnetic ions. In the model, domain states in the AF layer are formed during field cooling. This metastable state forms due to the statistical imbalance of impurities. Within any finite region, the impurities of the two AF sublattices will not be equal. This results in a net spin imbalance in the AF, as shown in fig. 4.5. The net magnetisation of the domain can couple to an external field forming a domain. The domain wall energy is minimised by passing through the non-magnetic impurities. Since the AF domain has a net magnetisation it can couple to the F layer, which results in exchange bias.

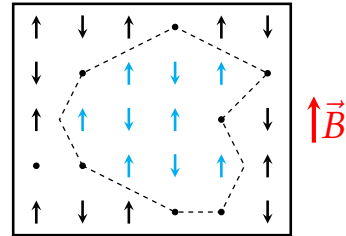


Figure 4.5: Schematic of a domain state with a spin imbalance where \vec{B} is the magnetic flux density and the dashed line is a domain wall which preferentially forms through magnetic impurities shown as solid circles [117].

The Domain State model correctly predicts the temperature dependence of H_{ex} . It was also predicted that H_{ex} would depend on the level of dilution, going through a peak at 60 % dilution. The initial increase in H_{ex} was attributed to the availability of impurities, which allow for more domains with lower domain wall energy. This would then be followed by a decrease in H_{ex} as AF ordering is disrupted. Accompanying experiments showed that H_{ex} did go through a peak but at 15 % dilution [108]. This reduction was attributed to grain boundaries in the polycrystalline AF layer. Grain boundaries are crystal defects by definition and can therefore take the place of dilution in the model.

The model described the reduction in H_{ex} with field cycling. Cycling the external field resulted in a reduction in H_{ex} of 50 % after one cycle. This was attributed to a 10 % reduction in M_{s} , which prevents the hysteresis loop from closing. For AF layers thinner than four monolayers, the domain state model predicts H_{ex} increases with thickness due to the increasing stability of the domain state. For thicker AF layers, the domain state model predicts a reduction in H_{ex} . This was explained as being due to a reduction in the number of domains that form, which is itself due to the increased energy requirement to form a domain that passes through the whole AF layer. These features of the dependence of H_{ex} on d_{AF} were observed experimentally, although at much larger values of d_{AF} [134].

The model works best for single crystal AF layers, which are difficult to produce and have limited practical use. In a polycrystalline film the F/AF coupling in each crystallite will depend on the crystal orientation. However, the model does not consider the effect of texture. Additionally, in a polycrystalline material with well-crystallised grains, there will be few impurities in the grain, while at the grain boundary the dilution fraction will be very large. Therefore in real systems the domain walls will preferentially form in grain boundaries. However, the volume of the single-domain grains was not considered. The model assumes an infinite value of AF anisotropy, such that there are only two possible states for the AF spins and the domain wall width is zero. Attempts to extend the model to systems with realistic K_{AF} have had limited success [135]. The model also does not address the increase in H_{c} which accompanies exchange bias.

4.2 The York Model of Exchange Bias

When it was proposed in 2010, the York Model of Exchange Bias was not the first model to conceive of thermal effects in exchange bias systems. In earlier models already discussed, thermal activation was observed, but attempts to control it were limited. The York Model of Exchange Bias departs from older models by controlling thermal activation both during measurement and prior to them. By controlling the initial state of the AF film, the York Model of Exchange Bias allows for highly reproducible measurements to be made [11]. Measurements of the effect of d_{AF} , the AF layer thickness, on H_{ex} had shown a $\frac{1}{d_{\text{AF}}}$ dependence [136, 137]. However, this dependence had not been explained. On the other hand, measurements of the effect of increasing lateral grain size reported apparently contradictory findings where H_{ex} was shown either to increase [138] or decrease [139]. The York Model of Exchange Bias established a framework where the grain size distribution in the AF is considered, from which the magnetic and thermal properties of the film can be predicted. A grain is a crystallographically ordered unit of a polycrystalline film. For the films under discussion a grain has a typical diameter and thickness on the order of 10 nm.

4.2.1 Thermal Processes

Early work on thermal processes focused on the decay of magnetisation in ferromagnetic (F) materials. This can be expressed by

$$\vec{M}(t) = \vec{M}_0 \pm S_{\text{F}}(\vec{H}, T) \ln t \quad (4.8)$$

where \vec{M} is the magnetisation, \vec{M}_0 is the initial state of the magnetisation, $S_{\text{F}}(\vec{H}, T)$ is the time dependence coefficient which is

dependent on the field \vec{H} and temperature T and t is time [140]. The temperature dependence of S_{F} on T is shown in eq. (4.10) [141]. It is worth noting the form of the function $\ln(t)$ which is shown in fig. 4.6. This function is central to thermal effects due to the probabilistic nature of thermal activation. The function $\ln(t)$ is characterised by rapid change for low t , and slower change thereafter [142].

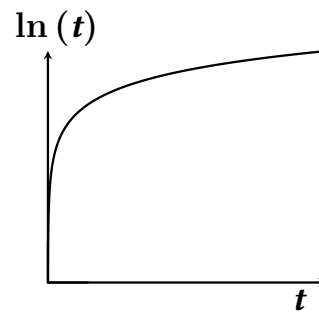


Figure 4.6: The function $\ln(t)$.

Fundamentally, the York Model of Exchange Bias adapts the Stoner-Wohlfarth model of reversal in F fine particles to AF polycrystalline thin films [30, 143]. It is therefore similar to the work of Street and Woolley, in which the Stoner-Wohlfarth model was applied to a F alloy, and the Fulcomer and Charap model of exchange bias which was discussed in section 4.1.2 [129, 142, 144].

The factor S_F is known to be a function of both temperature T and applied field \vec{H} . Assuming that the decay in magnetisation is not due to structural changes in the F, it must be due to changes in the domain structure. These changes are caused by thermal activation of domains or domain walls over free energy barriers [142]. If we assume the energy barriers to reversal are given by ΔE then the relaxation time τ^{-1} , which is the mean time required before the energy barrier is exceeded, is given by the Néel-Arrhenius law

$$\tau^{-1} = f_0 \exp\left(-\frac{\Delta E}{k_B T}\right) \quad (4.9)$$

where f_0 is the attempt frequency, k_B is Boltzmann's constant and T is the temperature [141, 143]. The value of f_0 is usually taken to be equal to that of Fe, which has been calculated to be $\sim 10^9$ s [145]. The reasoning is that an energy $k_B T$ 'attempts' to exceed the energy barrier ΔE with a frequency equal to f_0 [129, 145]. The measurement of f_0 in IrMn will be discussed in section 4.2.4 [146]. Using this reasoning the form of the time dependence coefficient can be shown to be

$$S_F = 2k_B T M_s f(\Delta E) \quad (4.10)$$

where $f(\Delta E)$ is the energy barrier distribution [141].

If the measurement time is much longer than the relaxation time then the magnetisation will flip several times during the measurement, which in a F material leads to superparamagnetic behaviour. On the other hand, if the measurement time is much less than the relaxation time then the magnetisation will not change during the measurement and so the final state will be the same as the initial state. Such a particle is said to be blocked in its initial state. A particle being blocked or superparamagnetic is therefore dependent on the measurement time or, since the particle will reverse much more frequently at higher temperatures, a function of T . The blocking temperature T_B is thus the temperature at which the relaxation time equals the measurement time. Rearrangement of eq. (4.9) gives an expression

for T_B of

$$T_B = \frac{\Delta E}{k_B \ln(t_m f_0)} \quad (4.11)$$

where t_m is the measurement time. t_m is on the order of seconds, so

$$\begin{aligned} \frac{\Delta E}{k_B T_B} &= \ln(t_m f_0) \\ &\approx 25 \end{aligned} \quad (4.12)$$

for typical measurements [11]. Later measurements made on AF materials found $f_0 \sim 10^{12}$ s [146]. This is discussed further in section 4.2.4.

The magnetisation \vec{M} of a F material is an order parameter. For an AF material an analogous AF order parameter \vec{P} can be defined such that

$$\vec{P}(t) = \vec{P}_0 \pm S_{AF} \ln t \quad (4.13)$$

where S_{AF} is the antiferromagnetic time dependence coefficient. This implies that an AF material will logarithmically approach an ordered state in the presence of an ordering effect.

To be clear, the different kinds of order in a polycrystalline AF film must be distinguished. Firstly, crystalline order relates to the symmetry of the placement of constituent atoms of a material. This study focuses on polycrystalline thin films in which there is no change in crystallinity. Thus that is not a changing order parameter. Secondly, in an AF material the constituent atoms have an antiparallel magnetic alignments in a pair of magnetic sublattices. This is due to the negative exchange integral. This order exists below the Néel temperature (T_N) which is 690 K for IrMn [4]. In this study T_N of IrMn is not exceeded. Therefore the antiparallel alignment of adjacent atoms will be maintained. In a polycrystalline AF material below T_N , order is to be understood as the orientation of the magnetic sublattices in a grain with those of other grains. This only applies when the grain size is ~ 10 nm and therefore a grain contains a single domain. Each grain has an alignment axis which is parallel to the magnetic sublattices and in an AF easy direction. When this aligns with the axes in other AF grains, the material is said to be ordered. In addition, a grain is said to be stable when this orientation does not change and unstable when it does.

The logarithmic ordering indicated by eq. (4.13) has been observed for an AF film exchange coupled to a F layer where the ordering effect is the exchange across the F/AF interface [129, 144]. Therefore, finding the factors that control S_{AF} will describe the ordering behaviour of a AF material.

The York Model of Exchange Bias is based on the application of the Stoner-Wohlfarth model to an AF system. The Stoner-Wohlfarth model describes the magnetic reversal of F nanoparticles and was discussed in section 2.2.3 [30]. In the model, the particles are modelled as prolate ellipsoids. This gives them an overall shape anisotropy. However, in principle the model can be generalised regardless of the origin of the magnetic anisotropy.

In the Stoner-Wohlfarth model the reversal process is controlled by spin rotation rather than by nucleation and domain wall motion, as would be the case for multi-domain particles. For a multi-domain particle there is an activation volume which, once switched, will allow the rest of the domain to switch by domain wall motion [147]. However, for particles small enough to always be single domain the effective activation volume is the same as the particle volume. In both the Stoner-Wohlfarth model and the York Model of Exchange Bias, the magnetic rotation is assumed to be coherent.

For a single-domain grain in the Stoner-Wohlfarth model where the activation volume and the grain volume are equal, the energy barrier to reversal can be expressed as

$$\Delta E = K_F V_g \quad (4.14)$$

where K_F is the F anisotropy and V_g is the grain volume [148, 149]. Since V_g is distributed each grain has a different energy barrier to reversal. Thus for a given temperature thermal energy will be sufficient to overcome the energy barrier to reversal. By combination with the Néel-Arrhenius law, the thermal stability of a particle can be expressed as

$$\frac{K_F V_g}{k_B T} = \ln(t_m f_0) \quad (4.15)$$

where the size of $\ln(t_m f_0)$ indicates the thermal stability and t_m is the measurement time. The behaviour of AF grains which reverse over volume-dependent energy barriers has been modelled using a micromagnetic Monte Carlo approach [150].

Due to its applicability to recording media, eq. (4.15) is usually computed for room temperature. However, it also implies that a large grain will remain stable even at elevated temperatures and that a small grain will remain thermally unstable until cooled to a sufficiently low temperature. When applied to an AF material K_F is replaced by K_{AF} . Thus an AF grain will have a blocking temperature higher than 0 K and lower than T_N , above which it is thermally active and below which it is stable for a given timescale. Since in an AF film the grain sizes are distributed, this temperature will be distributed. However, not all grain sizes are equally likely and there will exist a maximum and a minimum grain size. If a minimum size exists then a minimum critical temperature exists. This temperature, T_{NA} , is the temperature of non-activation. At and below T_{NA} none of the AF grains are thermally active on relevant timescales. The spin order of the AF film can then be considered to be fixed.

The existence of T_{NA} has two important consequences. Firstly, since at T_{NA} the AF film is free of thermal activation, measurements made at T_{NA} are reproducible. Early measurements of exchange bias made above T_{NA} showed H_{ex} changing between measurements and dependent on the duration of the measurement [84, 132]. However, these effects are removed when measuring at T_{NA} [78]. Secondly, the reproducibility of the measurements at T_{NA} allow thermal activation to be controlled. By performing thermal activation at temperatures above T_{NA} , but always measuring at T_{NA} , thermal activation occurs before the beginning of the measurement. Procedures of this nature are discussed in the rest of this section.

4.2.2 The York Protocol

IrMn is the most common and highest-performing AF alloy. It has become widely used in HDD technology due to having the highest potential H_{ex} of any AF material [31]. There are two main challenges to measurement of IrMn films. The first is that T_N of IrMn is 690 K [4]. Heterostructures heated to this temperature are susceptible to diffusion of atoms between layers [59, 101, 103]. For high performance technological applications this would be unacceptable and diffusion also reduces the maximum H_{ex} achievable [59]. The model of Fulcomer and Charap described the magnetic disordering of an AF film within a grain by thermal activation. In contrast, the York Model of Exchange Bias takes advantage of the potential of thermal activation to magnetically order an AF film by thermal activation of AF

grains. Fulcomer and Charap also note that the AF layer can change during the measurement which has an effect on the measurement of H_{ex} and H_c . To counteract this the thermal and magnetic history of the film must be controlled.

The second challenge to overcome is that the AF layer cannot itself be directly measured. However, the behaviour of the AF layer can be observed by indirect means. Namely, control of the thermal and magnetic history of the film allows the state of the AF layer to be inferred. The state of the AF layer then influences the F layer which can be measured.

The York Protocols are systematic procedures for the measurement of metallic, polycrystalline AF thin films coupled to an F layer, having a grain size ~ 10 nm and therefore containing a single domain. They allow the determination and control of the AF state prior to and throughout the measurement. This control allows the systematic determination of the film properties.

Before measurement, the state of the AF is generally unknown. Polycrystalline thin films are usually produced by sputtering which alone does not confer any particular magnetic state. Thus the first stage of the York Protocol is to set the AF film in a reproducible manner. This is achieved by applying an external field sufficient to saturate the F layer and raising the temperature of the sample. The temperature chosen is as high as possible without resulting in a decrease in exchange bias due to diffusion [59]. This temperature is called T_{set} and will produce the highest H_{ex} . The film is held at this temperature for 90 min. After 90 min changes in H_{ex} are $<1\%$ since changes in H_{ex} are proportional to $\ln(t)$ [11].

The second stage of the York Protocol ensures that there is no thermal activation of AF grains during the measurement. To achieve this, the film is cooled in a positive field to a temperature at which no thermal activation of AF grains occurs. This temperature is defined as T_{NA} , the temperature of non-activation. To find T_{NA} the film is cooled to a trial T_{NA} . The field is reversed for 1 min and two hysteresis loops are measured. After this the film is left in reverse field for 30 min before another two loops are taken. A change in H_{ex} between the second and fourth measurements indicates that thermal activation has occurred and the trial T_{NA} was too high. It is essential that two loops be measured at each step and only the later used to calculate H_{ex} . This removes the first loop training effect which has been known to not be part of thermal activation for many years, as discussed in

section 3.2.2 [68]. Changes between the second and following loops are the result of thermal activation [78].

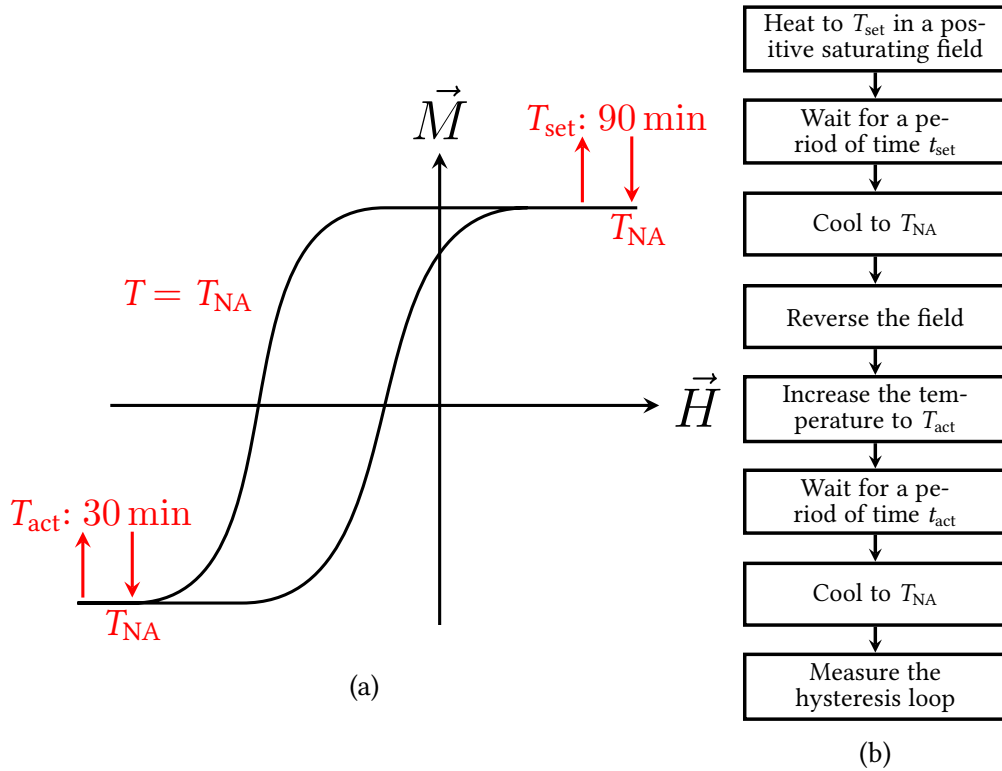


Figure 4.7: The York Protocol measurement shown (a) schematically and (b) as a list of steps [11].

The two steps outlined prepare the film for controlled and reproducible measurements. One such measurement is controlled thermal activation which is detailed here. Controlled thermal activation is achieved first by following the two steps already outlined. Following these the sample is heated in appropriate steps in a negative field to activation temperatures T_{act} . The film is cooled to T_{NA} before measuring. The measurement at T_{NA} ensures no thermal activation occurs during the loop measurement. The film is held at T_{act} for the activation time t_{act} which is typically 30 minutes. This duration was assumed to be sufficient due to the dependence of H_{ex} on $\ln(t)$. This will be discussed further in chapter 6. Figure 4.7 shows the procedure for thermal activation measurements. Since the sample is measured at T_{NA} no thermal activation takes place during the measurement. Instead the thermal activation at T_{act} causes a reduction in H_{ex} .

4.2.3 Measurement of the Blocking Temperature

The blocking temperature T_B is defined as the temperature at which $H_{\text{ex}} = 0$. Historically, this was measured by increasing the measurement temperature until H_{ex} reduced to zero [151]. However, in that procedure the AF is changing logarithmically during the measurement. These changes during the measurement reduce the reproducibility of the measurements as the value of T_B depends on the time taken to measure it [74].

In fact, each AF grain has its own blocking temperature so the overall blocking temperature for the film will be distributed. If the film is heated during measurement, the blocking temperature measured is the maximum blocking temperature of any grain, denoted by T_B^{MAX} . The maximum blocking temperature will be associated with the largest grain since the energy barrier to reversal is proportional to V_g as stated in eq. (4.14) [142]. During the York Protocol the film is measured at T_{NA} and it is therefore not subject to any time-dependent effect. Because of this it gives reproducible data. In principal, thermal activation during the York Protocol allows reversal of H_{ex} to be achieved [152].

In the York Protocol the film is heated in reverse field to T_{act} for t_{act} . It is then cooled to T_{NA} before measurement of the hysteresis loop. T_{act} is increased for each measurement, which results in progressive thermal activation of the AF layer.

Using the York Protocol, the blocking temperature measured is the median blocking temperature for set grains, $\langle T_B \rangle$. An example of a York Protocol blocking curve where the sample is measured at T_{NA} is shown in fig. 4.8 with square, blue points. It is compared to a conventional measurement where the measurement temperature is higher for each subsequent measurement which is shown with circular, red points. In each case the sample measured has structure IrMn (3)/ CoFe (10) (thicknesses in nm). The increase in H_{ex} that occurs below 50 K is an example of spin freezing, which was discussed in section 3.4.3. An investigation into spin freezing is discussed in section 7.1.

Heating the film while the F layer is reversed causes the AF order to reverse grain-by-grain. The amount of AF that reverses is a function of T_{act} and H^* , the

exchange field from the F. The value of H_{ex} is thus given by

$$H_{\text{ex}}(T_{\text{act}}) \propto \int_{T_{\text{act}}}^{\infty} f(T_{\text{B}}) dT_{\text{B}} - \int_0^{T_{\text{act}}} f(T_{\text{B}}) dT_{\text{B}} \quad (4.16)$$

which is simply the fraction of grains oriented in different directions [11].

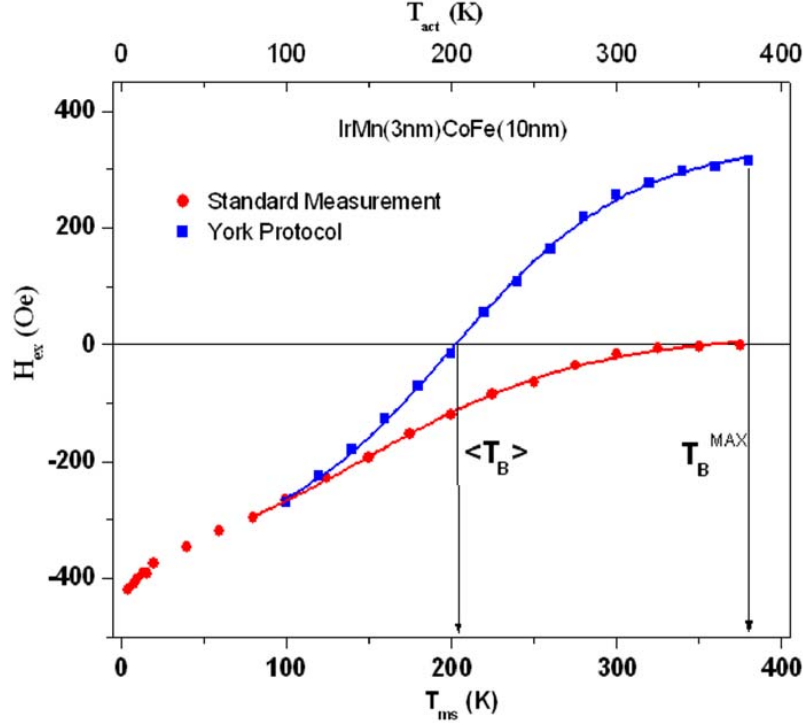


Figure 4.8: In the standard measurement H_{ex} is measured at increasing temperatures until $H_{\text{ex}} = 0$, which is at the maximum blocking temperature $T_{\text{B}}^{\text{MAX}}$. In a York Protocol measurement the film is measured at T_{NA} , which allows the median blocking temperature $\langle T_{\text{B}} \rangle$ and the distribution of blocking temperatures $f(T_{\text{B}})$ to be found [11].

Equation (4.16) assumes that the AF is thin enough that the size of the grains does not effect the F/AF coupling. The relation given in eq. (4.16) shows that when $T_{\text{act}} = T_{\text{B}}$ then equal proportions of the volume of the AF grains are set in opposite directions. Thus the value of T_{B} obtained at $H_{\text{ex}} = 0$ is the median blocking temperature $\langle T_{\text{B}} \rangle$, at which point the grains being reversed are those having the median volume $\langle V_{\text{g}} \rangle$.

4.2.4 Measurement of Antiferromagnetic Anisotropy

The median blocking temperature $\langle T_B \rangle$ can be used to calculate the anisotropy K_{AF} of the AF layer. The model assumes that the AF film is composed of grains of distributed size of order 10 nm. This size results in the grains containing a single AF domain. Like F grains, AF grains are subject to thermal activation leading to a magnetic transition over an energy barrier given by

$$\Delta E = K_{AF} V_g \quad (4.17)$$

where ΔE is the energy barrier to thermal activation, K_{AF} is the AF anisotropy constant and V_g is the volume of the AF grain [129, 142, 144]. When applied to F fine particles the anisotropy arises from the shape of the particles. However, in an AF thin film K_{AF} is dominated by the magnetocrystalline anisotropy.

The relevant timescale for the reversal depends on the temperature and grain volume. The relaxation time is given by the Néel-Arrhenius law

$$\tau^{-1} = f_0 \exp \left[- \frac{K_{AF} V_g \left(1 - \frac{H^*}{H_K^*} \right)^2}{k_B T} \right] \quad (4.18)$$

where τ^{-1} is the relaxation time, f_0 is the attempt frequency which has a value of $(2.1 \pm 0.4) \times 10^{12} \text{ s}^{-1}$ [146]. K_{AF} is the AF anisotropy, V_g is the AF grain volume calculated as a cylinder with volume equal to $\pi D_g^2 d_{AF} / 4$ where D_g is the grain diameter, H^* is the exchange field from the F layer, H_K^* is a pseudo-anisotropy field, k_B is the Boltzmann constant and T is the temperature. The values of H^* and H_K^* are not known, but the ratio H^* / H_K^* has been shown to be small [152]. This is the case even for small values of F moment \vec{m} , since although the overall magnetic moment of the F film varies continuously, the \vec{m} and thus H^* of an individual F crystallite is always in one of two antiparallel and non-zero magnetisation states. K_{AF} is magnetocrystalline in origin and thus varies with temperature such that

$$K_{AF}(T) = K_{AF}(0) \cdot \left(1 - \frac{T}{T_N} \right) \quad (4.19)$$

and therefore $K_{AF}(T_N) = 0$ [11, 32, 38, 47, 48].

There is no intergranular exchange coupling between AF grains. This is relevant to the York Model of Exchange Bias since the activation of AF grains is over volume-dependent energy barriers. Direct exchange between AF grains is prevented due to the incorrect lattice spacing that occurs at the grain boundaries. In ferromagnetic polycrystalline metallic materials intergranular exchange occurs via the RKKY interaction which is mediated by conduction electrons. In a F film conduction electrons are polarised by the grain moment. In an AF crystallite there is no overall moment so the conduction electrons are not polarised. When a spin imbalance does occur at the edge of an AF grain the resulting polarisation is much less than that seen in a F grain, since the grain is much larger than the grain boundary. It is also the case that conduction electrons are scattered as they move over grain boundaries, which would weaken the indirect exchange even if the electrons were polarised. It has been shown that a sheath of AF material around F grains reduces the RKKY interaction [21].

The most likely source of AF intergranular coupling is coupling via the F layer. However, if the intergranular coupling was significant then it would increase the effective AF grains volumes for the purpose of calculating the energy barriers to reversal. For the samples described in this study the polycrystalline nature of the films and the distribution of grain volumes has been established by TEM imaging and are shown in section 5.2.2. The use of bright-field (BF) and dark-field (DF) imaging techniques show that the grains are crystallographically ordered. Since the York Model of Exchange Bias successfully describes the magnetic behaviour of the films based on the AF grain volume distribution, measured either through varying the layer thickness d_{AF} or grain diameter D_g , it is reasonable to conclude that the intergranular coupling must be insignificant. Due to their size and anisotropy the AF grains are proposed to be single-domain as in the model of Fulcomer and Charap.

Measurement of K_{AF} requires controlling how much of the AF layer is contributing to H_{ex} and accounting for the interface coupling. In the York Model of Exchange Bias both of these requirements are fulfilled when at the point on the blocking curve where $H_{ex} = 0$. Of the film volume that contributes to exchange bias, when $H_{ex} = 0$ exactly half is set in each opposite direction. This is shown in fig. 4.9. In fig. 4.9 the grain size distribution is shown to be log-normal. This is a consequence of particle coalescence by Ostwald ripening [153, 154]. This distribution is typical for thin films [9, 11, 31, 73, 91, 146, 152, 155]. For the films used

in this work the log-normal distribution was confirmed by analysis of BF TEM images as will be described in section 5.2.2.

Since the grains are set in order of their energy barriers and thus volume, at $\langle T_B \rangle$ the largest reversed grain has a volume equal to the median grain volume $\langle V_g \rangle$. Thus the interfacial coupling parameter C^* can be extracted from eq. (4.16), producing

$$H_{\text{ex}}(\langle T_B \rangle) \propto C^* \left[\int_0^{\langle T_B \rangle} f(T_B) dT_B - \int_{\langle T_B \rangle}^{\infty} f(T_B) dT_B \right] = 0 \quad (4.20)$$

where $\langle T_B \rangle$ is the median blocking temperature of the AF grain size distribution. Thus when $H_{\text{ex}} = 0$ the effect of C^* is negated. However, this assumes there is no grain size dependence to interfacial spin order.

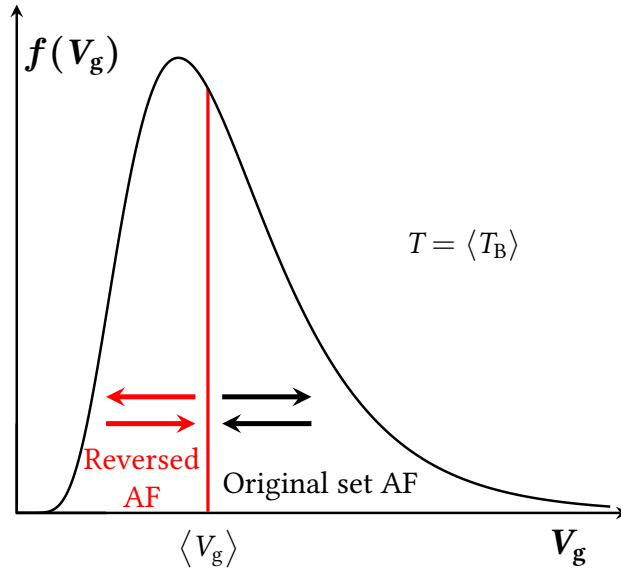


Figure 4.9: $H_{\text{ex}} = 0$ at $\langle T_B \rangle$ because equal volumes of the AF film are set in two opposing directions.

By taking $H^*/H_K^* = 0$ it is possible to evaluate eq. (4.18) for the median T_B and V_g which gives

$$K_{\text{AF}}(\langle T_B \rangle) = \frac{\ln(t f_0)}{\langle V_g \rangle} k_B \langle T_B \rangle \quad (4.21)$$

where t is the activation time which is typically 1800 s and f_0 is the attempt frequency. The samples were grown in a high target utilisation sputtering (HiTUS) system which will be discussed in section 5.1.1 and the lognormal grain size distribution was measured from BF TEM images as will be described in section 5.2.2.

Progressive thermal activation has been used by O'Grady et al. to calculate the value of K_{AF} at 295 K for samples with composition Si/Cu (10)/CoFe (5)/IrMn (d_{AF})/Ta (10) (thicknesses in nm) where $d_{AF} = 4$ to 12 nm [11]. This was $K_{AF}(295\text{ K}) = (5.5 \pm 0.5) \times 10^6 \text{ erg/cm}^3$ which was reduced by 15 % when $d_{AF} = 3$ nm. The results are shown in fig. 4.10, the lines shown are a guide to the eye and in the case of $d_{AF} > 3$ nm show that K_{AF} is constant. Note that the error bars in fig. 4.10(b) appear large because of the fine scale of the y -axis. However, they represent a systematic error due to the setting process which will be discussed in section 4.2.5.

Above 4 nm the value of K_{AF} is constant. It should be noted that this calculation used a value of f_0 three orders of magnitude lower than was later shown to be the case [146]. This does not significantly affect the value of K_{AF} found due to the $\ln(f_0)$ dependence of K_{AF} . It was also assumed that T_N for the film was 690 K, the same as the bulk value [4]. The reduced K_{AF} for $d_{AF} = 3$ nm was attributed to low crystallisation of the film as a consequence of the film's low thickness.

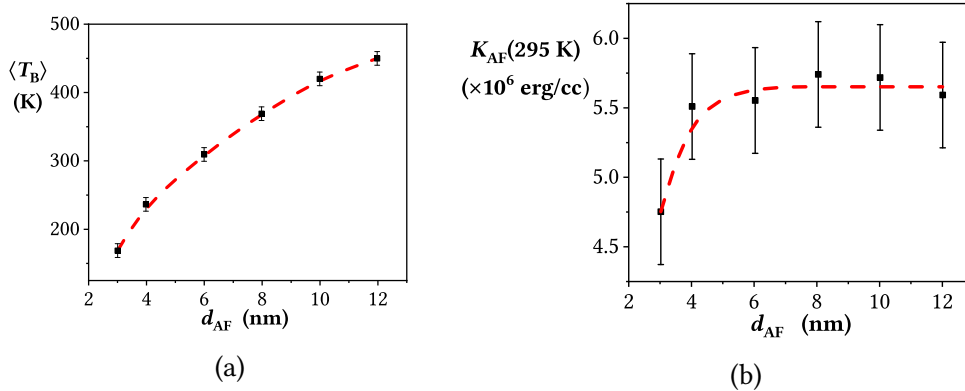


Figure 4.10: Progressive thermal activation was used to find the dependence of d_{AF} on (a) $\langle T_B \rangle$, which was used to calculate (b) K_{AF} . In each case the line is a guide to the eye. After O'Grady et al. [11].

Using this method K_{AF} was found to be higher than earlier measurements [156]. This was attributed to control of the activation process which resulted in the AF film being fully set. The consistent value of K_{AF} at 295 K above $d_{AF} = 4$ nm is shown in fig. 4.10(b) and suggests that the use of $\langle T_B \rangle$ has removed the influence of interfacial coupling. Since $\langle T_B \rangle$ increases while K_{AF} is constant, this method showed that the value of $\langle T_B \rangle$ is not simply a function of K_{AF} but is in fact dependent on the thermal activation process.

Strictly speaking the Néel-Arrhenius law eq. (4.18) only applies to a system with aligned easy axes. Thus K_{AF} can be improved further by improving the poly-

crystalline order, also known as texture. For this reason the K_{AF} found should be considered an effective value.

4.2.5 Setting Limitations

In a material such as IrMn the Néel temperature T_N is high enough that the sample cannot be heated to T_N without causing damage to the structure, such as by destructive diffusion of material into adjacent layers. Hence, setting IrMn must be done below T_N and is achieved by thermal activation. Since $\Delta E = K_{AF}V_g$, the distribution of energy barriers and grain volumes have the same form.

Figure 4.11 shows the distribution of grain volumes after the sample has been set and is subsequently at $T > T_{NA}$. The region labelled (c) contains the grains that were not set during the setting process due to T_{set} being lower than T_N . These grains did not align to the direction of the F magnetisation because the energy barriers to reversal were too large to overcome during the setting time. Thus the fraction of grains with volume larger than the set volume V_{set} shown in region (c) do not contribute to H_{ex} .

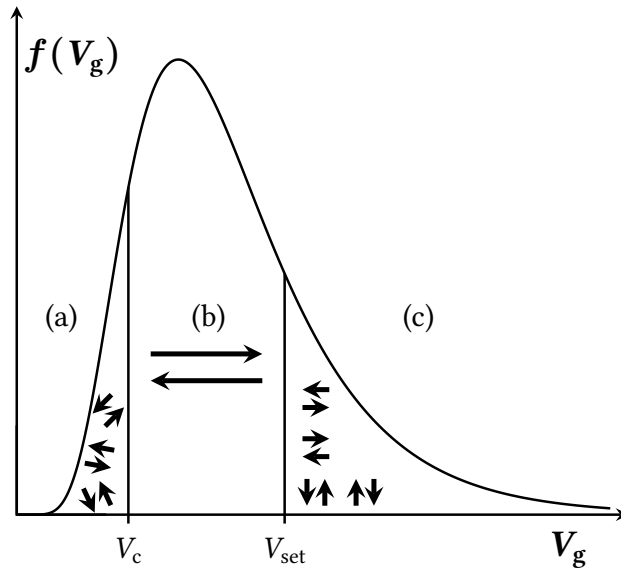


Figure 4.11: Schematic of the grain volume distribution of AF grains after setting at T_{set} in a magnetic field and then cooling to a temperature at which a fraction of the AF is (a) thermally unstable, (b) the grains between V_c and V_{set} contribute to H_{ex} and a fraction of the grains are (c) unset.

The region labelled (a) includes the fraction of grains which are not thermally stable. For the fraction of grains with a volume lower than the critical volume V_c , the energy barriers to reversal are sufficiently low that the grains are thermally active. The grains with $V_g < V_c$ are thermally disordered as in the Fulcomer and Charap model. This means that although AF order persists in each grain, the direction of the order changes due to thermal processes and there is no relative order between grains. The grains in regions (a) and (c) do not contribute to H_{ex} .

Thus only the grains in the region labelled (b) contribute to exchange bias, these being the grains with a volume between V_c and V_{set} . The exchange bias can therefore be expressed as proportional to the integral of the grain volume distribution between these two critical volumes

$$H_{\text{ex}}(T) \propto \int_{V_c(T)}^{V_{\text{set}}(T)} f(V_g) dV_g \quad (4.22)$$

where $H_{\text{ex}}(T)$ is the exchange bias, $V_c(T)$ is the critical volume below which grains are thermally active and $V_{\text{set}}(T)$ is the largest grain volume that was set during the setting process.

Under ideal conditions the exchange bias will equal the intrinsic exchange bias $H_{\text{ex}}^{\text{INT}}$. These conditions would be $T_{\text{set}} > T_{\text{B}}^{\text{MAX}}$ so that the largest grains will be set during the setting process and during the measurement $T < T_{\text{NA}}$ so that the smallest grains will be stable. However, in a real measurement H_{ex} will be modified by the interfacial coupling parameter C^* and reduced due to the incomplete setting of the AF layer. As discussed in section 3.4.1 the exchange bias is dependent on the setting conditions, in particular the setting field \vec{H}_{set} and the setting temperature T_{set} [11]. Thus the total exchange bias at T_{NA} for a given setting condition is given by

$$H_{\text{ex}}(\vec{H}_{\text{set}}, T_{\text{set}}) = H_{\text{ex}}^{\text{INT}} C^*(\vec{H}_{\text{set}}, T_{\text{set}}) \int_{V_c(T_{\text{NA}})}^{V_{\text{set}}(T_{\text{set}})} f(V_g) dV_g \quad (4.23)$$

where $C^*(\vec{H}_{\text{set}}, T_{\text{set}})$ is treated as a constant. As will be discussed in section 4.2.6 and section 4.2.7, the use of a constant value for C^* is appropriate given that H_{ex} is shown to depend on the grain size distribution [11].

4.2.6 Grain Volume Dependence of Exchange Bias

The York Model of Exchange Bias was used by Vallejo-Fernandez et al. to determine the dependence of H_{ex} on the AF grain volume, considering the combined effect of the grain diameter distribution and the thickness of the AF layer (d_{AF}) [155]. This study used samples with composition Si/Cu (10)/CoFe (2.5)/IrMn (d_{AF})/Ta (10) (thicknesses in nm) where $d_{\text{AF}} = 3$ to 12 nm and each value of d_{AF} was prepared with four different median grain diameters [155]. Control of the median grain diameter is achieved by controlling the sputtering parameters in high target utilisation sputtering (HiTUS) as will be discussed in section 5.1.1 [157]. The median grain diameters and grain size distribution was measured using TEM images as will be discussed in section 5.2.2 [158].

Using the techniques discussed in section 4.2.3 to measure $\langle T_{\text{B}} \rangle$, eq. (4.21) was used to find K_{AF} . The value of K_{AF} thus found can be used to calculate the critical volumes V_{c} and V_{set} . Since V_{c} is the smallest grain volume that is thermally stable and the measurements were made at $T_{\text{NA}} = 293\text{K}$ it can be found using a rearranged form of eq. (4.18)

$$V_{\text{c}}(T_{\text{NA}}) = \frac{\ln(t_{\text{m}}f_0)k_{\text{B}}T_{\text{NA}}}{K_{\text{AF}}(T_{\text{NA}})} \quad (4.24)$$

where the relaxation time is equal to the measurement time of 100 s [11]. Using the same logic V_{set} can be found using the setting time $t_{\text{set}} = 5400\text{s}$ and the setting temperature $T_{\text{set}} = 498\text{K}$, which gives

$$V_{\text{set}}(T_{\text{set}}) = \frac{\ln(t_{\text{set}}f_0)k_{\text{B}}T_{\text{set}}}{K_{\text{AF}}(T_{\text{set}})} \quad (4.25)$$

as the volume of the largest active grain. Using the critical volumes and the grain volume distribution eq. (4.22) can be used to predict the dependence of H_{ex} with grain volume.

Experimental measurements of H_{ex} as a function of $\langle V_{\text{g}} \rangle$ are shown for three films with different values of d_{AF} in fig. 4.12(a). H_{ex} increases with $\langle V_{\text{g}} \rangle$ except for the film with the greatest thickness, which shows a decreasing trend at the largest grain sizes. For films with low d_{AF} many grains are thermally unstable due to their low volume, which results in a decrease of H_{ex} . For films with high d_{AF} and $\langle V_{\text{g}} \rangle$ grains could not be set during the setting process, which also results

in a decrease in H_{ex} . This explains why H_{ex} first increases and then decreases with increasing AF grain diameter. This unites earlier measurements which had found apparently incompatible results for the dependence of H_{ex} on grain size [138, 139]. The maximum H_{ex} is achieved when the maximum fraction of the grains are between V_c and V_{set} in size, as they are neither too small to be thermally stable nor too large to be impossible to set. The lines shown in fig. 4.12(a) were calculated using eq. (4.23) and therefore represent the integral of a volume distribution. The fits have been vertically scaled using C^* as a fitting parameter since eq. (4.22) gives only a proportional relationship rather than an exact value.

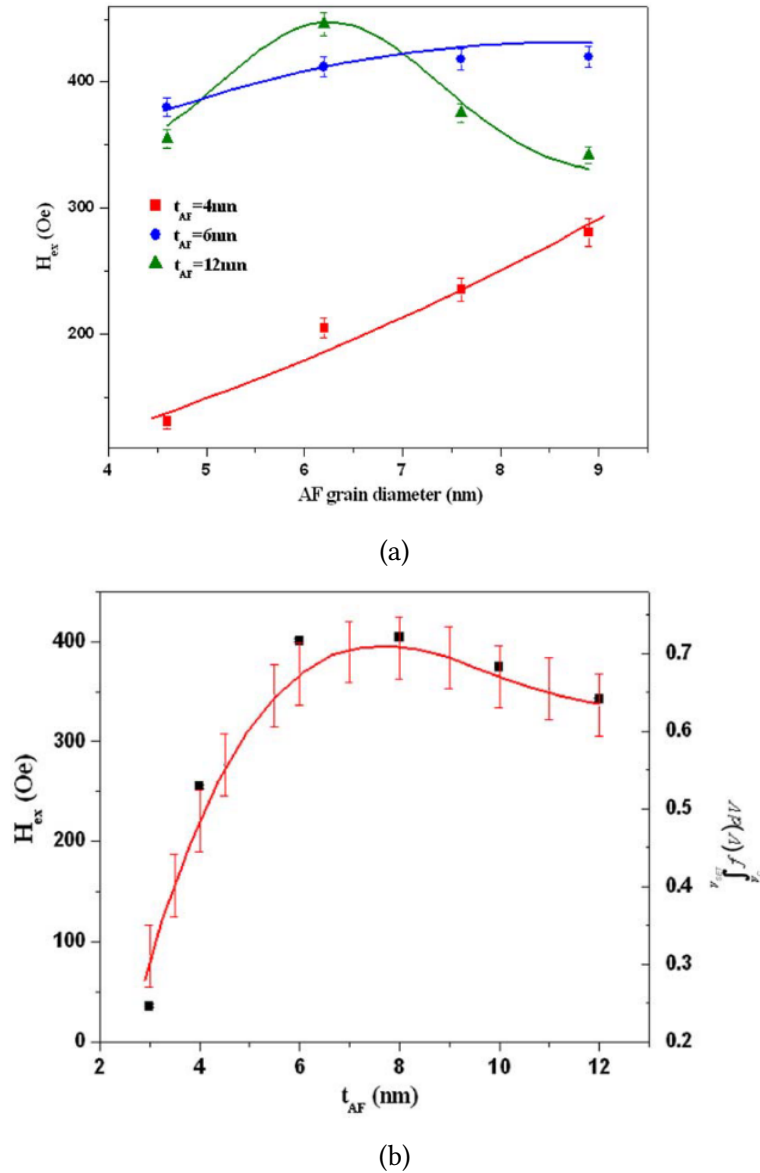


Figure 4.12: Experimental measurements of the dependence of H_{ex} on grain volume match the forms predicted by the York Model of Exchange Bias in eq. (4.22) for (a) AF grain diameter and (b) AF layer thickness which is here denoted t_{AF} [11].

The effect of d_{AF} on H_{ex} is shown in fig. 4.12(b) for a film where $\langle D_g \rangle = 7.6$ nm. This shows a sharp increase in H_{ex} followed by a slow decline. This decrease is approximately of the form $1/d_{AF}$ which has been seen in earlier measurements [136, 137]. This apparent $1/d_{AF}$ dependence arises from the long tail of the distribution of grain volumes, which approximates to a $1/d_{AF}$ form [11, 159]. The fit shown in fig. 4.12(b) is calculated from eq. (4.22). The fit has been vertically scaled using C^* as a fitting parameter. The assumption that C^* is constant is supported by the quality of the fits. The error bars of the theoretical fit arise from the uncertainty inherent in integrating over a distribution. They do not come from an error in $\langle D_g \rangle$ as that was calculated from measurement of > 800 grains as will be described in section 5.2.2.

The theoretical fits in fig. 4.12 match the experimental trends within error. The vertical scaling of the fits has been adjusted to the value of H_{ex} , however the form of the curves derives from eq. (4.22). The correspondence of the trends imply the validity of the York Model of Exchange Bias which uses a consideration of the grain volumes to explain both trends in both d_{AF} or $\langle D_g \rangle$ [11]. The fits shown represent the first time the dependence of H_{ex} with grain volume had been theoretically determined and united earlier measurements which had been assumed to be incompatible [138, 139].

4.2.7 Magnetic Viscosity

By consideration of the two critical volumes from eq. (4.22) the York Model of Exchange Bias allowed the magnetic viscosity of a AF to be measured by O'Grady et al., which as previously been measured in ferromagnetic materials [11, 140, 159]. In a F material the magnetisation process is associated with a time dependence of \vec{M} , which is an ordering parameter. This ordering increases following a $\ln(t)$ law. For an AF material the setting process ordering parameter should also follow a $\ln(t)$ dependence.

A sample with composition Si/Ru (5)/IrMn (10)/CoFe (3)/Ta (10) (thicknesses in nm) with a median grain diameter of (6.0 ± 0.4) nm was heated to $T_{set} = 498$ K in the presence of a field $\vec{H}_{set} = -1$ kOe, which is sufficient to saturate the F layer, where it remained for $t_{set} = 5400$ s. If T_{set} is large enough all the AF grains will reverse. This allows the state of the AF to be known. The AF being fully set at

$T_{\text{set}} = 498\text{K}$ was confirmed by the full reversal of H_{ex} . This sample was chosen as it is possible to set the entire film in a reasonable time and at a reasonable temperature. Increasing T_{set} or t_{set} increased H_{ex} by $<1\%$.

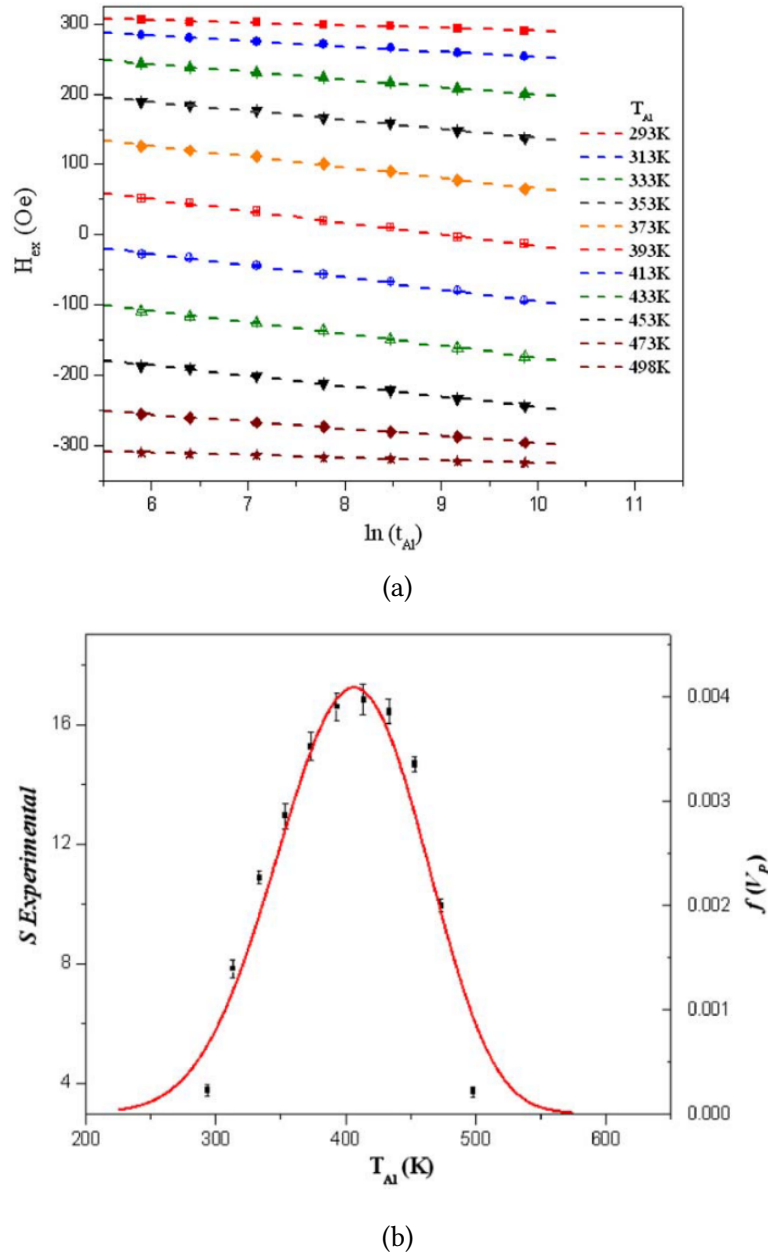


Figure 4.13: The decay of H_{ex} for a given temperature is (a) linear with time and (b) when plotted as a function of T_{al} are shown to go through a peak which matches the form predicted by the York Model of Exchange Bias [11].

In a reverse field the film was then heated to the aligning temperature T_{al} . At T_{al} the AF grains are thermally activated and align in the opposite sense to how they were aligned during the setting process. This was done several times sequentially for a cumulative aligning time t_{al} . At intervals the film was cooled to T_{NA} and H_{ex} was measured. This allowed the dependence of H_{ex} with t_{al} to be measured

for several values of T_{al} . When H_{ex} was measured care was taken to exclude the training effect by measuring the second loop.

The time dependence of H_{ex} is shown in fig. 4.13(a) for several values of T_{al} . For all values of T_{al} the variation of H_{ex} is linear with $\ln(t_{\text{al}})$. Note that the value of H_{ex} after aligning at 498 K is the same as the initial value although in the opposite direction. This is evidence that the whole distribution was set during the setting process and reset during the alignment process. Figure 4.13(a) shows that at T_{al} a fraction of the AF film is thermally activated, meaning it realigns with a $\ln(t)$ dependence.

The gradients of the linear fits in fig. 4.13(a) are not invariant, nor do they increase monotonically with T_{al} . The gradients are plotted as a function of T_{al} in fig. 4.13(b). There is a peak at 413 K which is within 5 K of the median blocking temperature $\langle T_{\text{B}} \rangle$. This is shown alongside a theoretical fit from the consideration of the grain volume distribution and the two critical volumes. This fit has been scaled vertically to account for the effect of C^* . The agreement between the experimental results and the theoretical fit is excellent. The largest deviation is found at the edges of the distribution. However, this can be explained as the error bars on the data points are only from the error in measuring the gradients and do not take into account errors in measuring $\langle V_{\text{g}} \rangle$ or K_{AF} . The error in V_{g} is expected to be largest at the edges of the distribution as, although > 500 grains are measured, only a fraction of those will be the very largest and smallest grains. The distribution shown in fig. 4.13(b) is symmetric due to the temperature dependence of K_{AF} . The correspondence between the experimental data and theoretical curves in fig. 4.13(b) is further evidence of the validity of the York Model of Exchange Bias, which was the first model to correctly predict this effect [11]. The calculation of K_{AF} , the grain volume dependence of exchange bias and the magnetic viscosity of an AF material constitute three independent corroborations of this model.

4.2.8 Limitations of the York Model of Exchange Bias

The York Model of Exchange Bias is nominally only valid for sputtered, granular AF films. In addition, the grain sizes must be of the order of 10 nm so that the grains contain only a single AF domain. The York Model of Exchange Bias does not apply to systems with large grain sizes as the activation volume necessary to nucleate a domain will not necessarily be equal to the grain volume, and as a consequence $\Delta E \neq K_{AF} V_g$. In addition, the model is not designed for epitaxial, single-crystal systems or for core-shell nanoparticles. The magnetocrystalline anisotropy of an AF single crystal cannot be measured. Instead only the effective anisotropy of the film can be measured, which is dependent on texture.

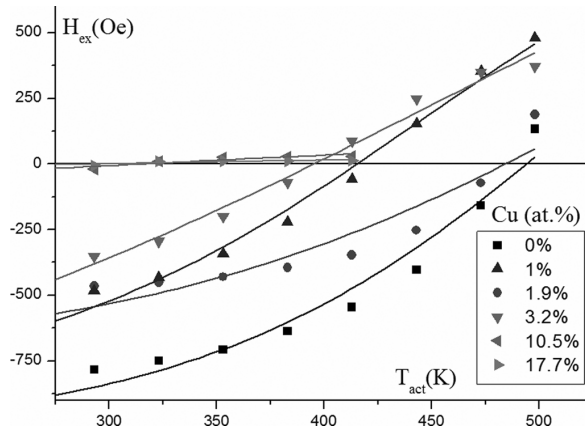


Figure 4.14: Thermal activation measurements for an IrMn layer doped with Cu. The curves are calculated based on the set fractions of the grain volume distribution as in the York Model of Exchange Bias [89].

Despite this the York Model of Exchange Bias has been applied to polycrystalline films with grain diameters of 43 to 65 nm. In these large-grain systems Cu was added as a non-magnetic impurity. Cu is an ideal material for substitution defects in IrMn since it has a lattice constant of 0.3615 nm, which is close to that of IrMn which is 0.371 nm [41, 42]. In addition both IrMn and Cu have an fcc structure. These two factors allow Cu to occupy lattice sites in IrMn without inducing extra strain. In the systems studied H_{ex} was observed both to rise when the Cu dilution was increased from 0 to 5%, and to fall when increased further to 30% [88]. The data was reinterpreted according to the York Model of Exchange Bias, considering the defects as strong pinning sites. These strong pinning sites behave like grain boundaries, such that increasing the Cu dilution fraction has the same effect as reducing the grain size. However, the reversal process changes from domain wall motion to rotation over the anisotropy barrier [88]. By considering

the effective grain size of the doped films, the results could be explained using a York Model of Exchange Bias approach [89]. The thermal activation measurements are shown in fig. 4.14. The curves are calculated based on eq. (4.16).

In large-crystal systems, ion bombardment was shown both to increase [160] and decrease [161] the exchange bias. The increase in exchange bias was attributed to the energy supplied by the ions activating the AF film over energy barriers in a mechanism analogous to heating [160]. On the other hand the decrease in H_{ex} was attributed to the ion bombardment modifying the interface in such a way as to decrease the interfacial coupling [161]. However, both these results coincided with a decrease in T_{B} . The changes to H_{ex} and decrease of T_{B} were reinterpreted using the strong domain wall pinning modification to the York Model of Exchange Bias [162]. In this interpretation the ion bombardment introduced non-magnetic impurities into the AF layer. These non-magnetic impurities act as pinning sites which reduce the effective size of the AF grains. The reduced AF grain size results in a lower $\langle T_{\text{B}} \rangle$. This is a consequence of eq. (4.21) which can be rearranged to give

$$\langle T_{\text{B}} \rangle = \frac{K_{\text{AF}}(\langle T_{\text{B}} \rangle) \langle V_{\text{g}} \rangle}{k_{\text{B}} \ln(t_{\text{act}} f_0)} \quad (4.26)$$

where $\langle T_{\text{B}} \rangle$ is the median blocking temperature $K_{\text{AF}}(\langle T_{\text{B}} \rangle)$ is the AF magnetocrystalline anisotropy constant at $\langle T_{\text{B}} \rangle$, $\langle V_{\text{g}} \rangle$ is the median grain size, k_{B} is the Boltzmann constant, t_{act} is the activation time and f_0 is the attempt frequency. In this interpretation the changes in H_{ex} are explained by the different proportions of the grain volume distribution that are set, unset and unstable as a result of the differences in effective grain volume.

The York Model of Exchange Bias was not designed to be applicable to large grain systems. However, it has been shown to be suitable when discussing AF layers doped with non-magnetic impurities and to thin films which have undergone ion bombardment [89, 162]. This is in addition to the good agreement the model has between experiment and theory [11]. This applicability across diverse systems reinforces the validity of the model.

As discussed in previous sections the York Model of Exchange Bias successfully predicted the form of the dependence of H_{ex} on $f(V_{\text{g}})$. However, the model does not predict the value of H_{ex} due to the unknown value of the interfacial stiffness constant C^* , which is used as a fitting parameter.

As with older models of exchange bias the York Model of Exchange Bias cannot account for the increase in coercivity H_c that occurs in F/AF coupled systems as opposed to an uncoupled F film. CoFe is a soft magnetic material with a typical coercivity < 100 Oe [29]. When coupled to an AF material the coercivity typically increases by a factor of between 2 and 10 to 200 to 1000 Oe [11]. A value of $H_c > 0$ is the result of irreversible processes occurring in the F material such that $H_{c1} \neq H_{c2}$. In a F film the non-reversible processes occur during domain wall motion. However, in an exchange-biased film these processes are occurring in fields large enough to saturate an uncoupled F film. On the other hand, the increase in H_c does not disappear at T_{NA} , where the AF film is not thermally active. Thus the increase in coercivity cannot derive from changes in the AF layer.

The use of T_{NA} succeeds in preventing thermal activation of the AF film, as shown by the reproducibility of measurements made at T_{NA} and the fact that H_{ex} does not change when $T_{act} = T_{NA}$. However, as discussed in section 3.2.2 care must still be taken to remove the first loop which has an enhanced H_{ex} , even when subsequent loops have the same value of H_{ex} . While the changes in subsequent loops are shown to be thermal in nature due to their disappearance at T_{NA} , the first loop training effect ΔH_{c1} is athermal [68, 69]. The discussion of the interfacial origin of H_c and ΔH_{c1} follows in chapter 6 and chapter 7.

4.3 Proposed Extensions to Exchange Bias Models

Models of exchange bias are primarily concerned with explaining the loop shift. Nevertheless, there have been a number of proposals which attempt to explain other exchange bias phenomena by building on earlier models. The aim of these proposals is to explain phenomena such as spin freezing, athermal training and the \vec{m} offset in a coherent framework that also explains the loop shift. However, none of these proposed extensions to exchange bias models have provided a comprehensive explanation of all exchange bias phenomena, or achieved consensus.

As discussed in section 4.2, the loop shift depends on the order of the AF bulk. However, the role and effects of the interface has not been conclusively established. In the York Model of Exchange Bias the interfacial contribution is represented by the interfacial coupling parameter C^* and the interfacial exchange field H_I . On

the other hand the factor $H_{\text{ex}}^{\text{INT}}$ represents the maximum potential H_{ex} that can be produced by ordering the bulk of the AF layer, which is reduced by the integral of the grain volume distribution of the set grains. This distinction between the bulk of the AF and the interfacial region is central to the proposed extensions to models of exchange bias. This separation is demonstrated by the trilayer experiment discussed in section 3.4.2. The success of the York Model of Exchange Bias suggests that it is appropriate to treat C^* and H_{I} as constants. Incorporating disordered interfacial spins into C^* has been shown to be effective by the excellent fit between the data and the predictions of the model [11]. However, York Protocol measurements are performed after removing the training effect, a phenomenon that the York Model of Exchange Bias cannot explain. Furthermore, the existence of spin freezing suggests that C^* and H_{I} are not constant but functions of T and V_{g} .

In general, proposed extensions postulate the existence of disordered spins at the F/AF interface. The behaviour of these spins is then described. Various descriptions are called disordered interfacial spins, low freezing temperature spins, spin-glass regions and spin clusters the overlapping descriptions describe substantially similar phenomena, although not by identical mechanisms [12]. In the Domain State Model discussed in section 4.1.4 the F/AF interface contains non-magnetic impurities and crystalline defects which act as the pinning sites of AF domain walls. The reduction in magnetisation of the domain states is correlated with the training effect [117]. However, this mechanism does not have sufficient magnitude to induce the large training effect observed and does not account for thermal activation. A terraced interface has also been proposed in order to explain the spin freezing effect [107, 121, 122, 163]. However, this applies only to single-crystal systems.

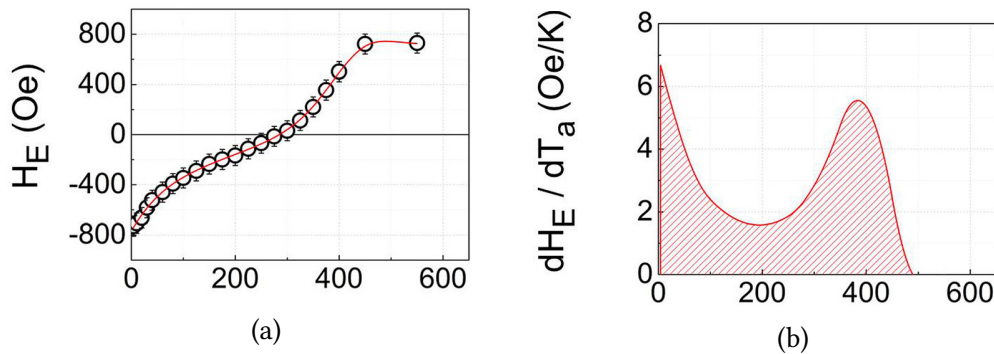


Figure 4.15: Simulated (a) thermal activation of exchange bias and (b) blocking temperature distribution using a spin-glass-like region at the interface. The x -axis is similar to T_{act} and has units of K [12].

A spin-glass-like interface has been proposed to explain spin freezing by Baltz et al. [107]. In this model the change in H_{ex} around $\langle T_{\text{B}} \rangle$ is due to the thermal activation of the bulk of the AF layer. This thermal activation is distributed due to the lognormal distribution of the AF grain volumes. At the interface, there is a distribution of the exchange coupling due to interface roughness. This results in disordered interfacial spins. Where the spins are particularly frustrated, spin-glass behaviour will be observed. The spin-glass-like interface will be further subdivided due to the distributed conditions from which it arises. Thus the interface will have a distributed spin-freezing temperature. This will enhance the temperature-dependence of the coupling between the F and AF bulk, since the layers will be effectively decoupled above the spin freezing temperature. It is this spin freezing temperature distribution that results in the increase in H_{ex} seen below 50 K [107]. Monte Carlo simulations of this model resulted in a good agreement with experiment [12, 164]. An example of simulated spin freezing is shown in fig. 4.15. Note that the x -axis is to similar $T_{\text{act}}(\text{K})$ albeit with $t_{\text{set}} = t_{\text{act}} = 0$. In these simulations there are spin-glass-like regions across 75 % of the interface. For the remainder of the interface, the AF and F layers are in direct contact.

A spin cluster is a collection of cooperatively acting spins at the F/AF interface. They have been proposed as a potential extension to the York Model of Exchange Bias [11, 37, 67]. A schematic of the spin clusters at the F/AF interface is shown in fig. 4.16 [37]. In section 3.4.1 the increase in H_{ex} with increasing setting field was discussed. This implies that the ordering of the interfacial spins is ferromagnetic and that their ferromagnetic order is increased by an applied field. It is proposed that the ordering follows a Langevin function and that the F/AF coupling depends linearly on the order of the interfacial spins. Thus a variation of the form

$$H_{\text{ex}}(\vec{H}_{\text{set}}, T_{\text{set}}) \propto H_{\text{ex}}^{\text{INT}} L(\vec{P}_1) \quad (4.27)$$

is expected where H_{ex} is the exchange bias, \vec{H}_{set} is the setting field, T_{set} is the setting temperature $H_{\text{ex}}^{\text{INT}}$ is the intrinsic exchange bias and $L(\vec{P}_1)$ is a Langevin function of \vec{P}_1 , the interfacial ordering parameter. \vec{P}_1 is given by

$$\vec{P}_1 = \frac{N_S \mu_B (\vec{H}_{\text{set}} + H_I)}{k_B T_{\text{set}}} \quad (4.28)$$

where N_S is the number of spins, μ_B is the Bohr magneton and H_I is the interfacial exchange field due to the F, AF and spin cluster interactions [11].

This form of the Langevin function has two unknowns, N_S and H_I . Thus a unique solution cannot be found. However, the values of one can be used to constrain the other. If the value of the interfacial exchange field is taken to be half the value of the exchange field of Fe then $H_I = 0.5 \times 10^4$ kOe. This value of H_I constrains the number of cooperating spins to between 10 and 50 [11]. This corresponds to spin clusters with internal F order and with a size distribution similar to the grain diameter distribution.

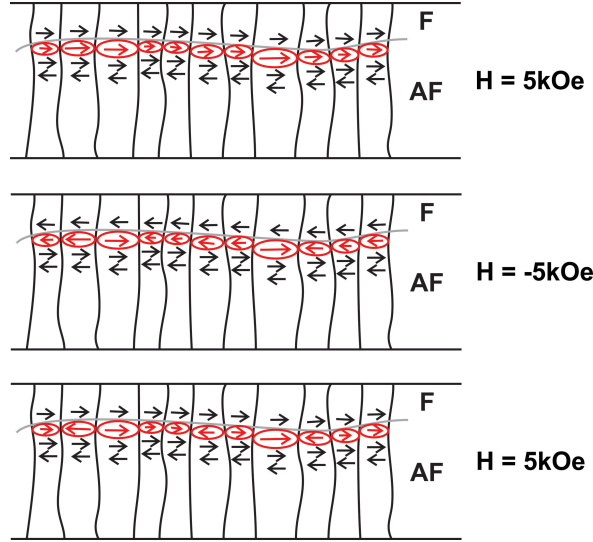


Figure 4.16: A schematic of a F/AF interface showing the spin clusters through one magnetic reversal. The training effect is attributed to the change in magnetic order between the initial and final states [37].

A schematic of the spin clusters at the F/AF interface is shown in fig. 4.16 [37]. The spin clusters are shown through one magnetic reversal. In the initial state they are parallel to the applied field. In negative saturation the majority of spin clusters have reversed. However, the largest spin clusters have not reversed. When the field is returned to the positive direction, some spin clusters remain aligned in the negative sense. Thus the final and initial states are not identical. This difference is proposed as an explanation of the training effect [37]. Spin clusters are also proposed to explain the \vec{H}_{set} dependence of H_{ex} and spin-freezing [11, 67, 91]. Spin clusters have a distribution of sizes which reflects the distribution of temperatures of spin freezing and the \vec{H}_{set} dependence which cannot be explained by single spin effects.

Spin clusters arise from the competing interactions at the interface. In the F layer the exchange integral is positive, while in the AF layer the exchange integral is negative. Thus at the interface there is a competition between the positive, ferromagnetic exchange and the negative, antiferromagnetic exchange. Hence the F

and AF layers are separated by a quasi-independent interfacial layer. This layer is sub-divided into groups of spins with internal F order. These spin clusters interact with each other and with the F and AF layers through direct and indirect exchange. As a consequence, the exchange integral J_{ex} cannot be thought of as a single parameter, but must be considered for each pair of interacting entities [11, 12, 164].

5. Characterisation

This chapter details the methods and equipment required to produce and evaluate thin film samples for reproducible magnetic measurements. Thin films were deposited by a sputtering system. An overview of this apparatus and the deposition procedure will be discussed. The film thickness was measured during deposition using a crystal rate monitor. The characterisation of the samples has two branches: structural and magnetic. The structural characterisation was carried out by XRD and TEM. These techniques are well-suited to determining the texture and grain volume distribution of the film, each of which are essential parameters for this study [11, 37]. The magnetic characterisation was carried out using a temperature-controlled vibrating sample magnetometer (VSM) and superconducting quantum interference device (SQUID) magnetic property measurement System (MPMS). In this section the principles of operation of a VSM and MPMS will be described.

5.1 Sample Preparation

5.1.1 HiTUS System

Multilayer thin film samples were produced using the high target utilisation sputtering (HiTUS) system manufactured by PlasmaQuest Ltd. and which is shown in fig. 5.1. An important difference between HiTUS and conventional sputtering systems is that the plasma is generated in a separate side arm connected to the main sputtering chamber [157, 165, 166]. From where it is generated, the Ar^+ plasma diffuses into the Ar of the main chamber where it is directed onto the

sputtering target by magnetic and electric fields. This isolated plasma generation allows plasma properties and sputtering parameters to be varied independently. A radio frequency (RF) electric field is generated by a three-turn coil coupled to a matching unit which is driven by a 13.56 MHz, 3 kW RF power supply. This RF field generates a plasma in 99.999 % pure Ar via Landau damping.

The plasma diffuses into the sputtering chamber where it is constrained and directed towards the target by two guiding electromagnets operating at 50 and 500 Oe. A negative bias between 0 and 1000 V applied to the target accelerates the Ar^+ ions. At 0 V the sputtering rate is negligible, but increasing the potential difference increases the sputtering rate. This is known to affect film properties such as grain size [157]. However, this voltage is not required to maintain the plasma. Without the steering magnet and applied voltage, the plasma fills the sputtering chamber. This is used to clean the substrate surface, chamber walls and remove gaseous impurities, as will be described in section 5.1.2. In addition to the grounded steel walls acting as a heat sink, the target is also water-cooled.

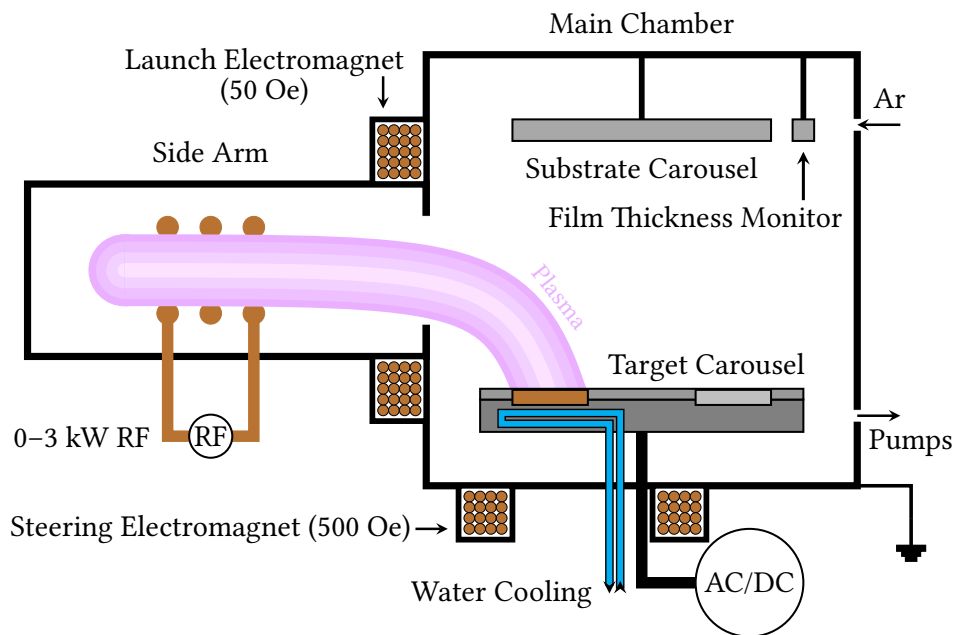


Figure 5.1: Schematic of HiTUS system.

A progressive sequence of rotary pump, turbopump and cryopump is used to reduce the base pressure of the system to 3×10^{-7} mbar. An in-built Programmable Logic Controller (PLC) controls the pumping sequence as well as the RF power, bias voltage and process pressure. Control of process pressure is achieved by a mass flow controller (MFC) which moderates the flow of Ar into the chamber. The process pressure used was 1.86 mTorr and the RF power used was 1.5 kW. These

factors are both known to affect the growth rate. However, they have been tuned to optimal values and the bias voltage used to control the grain size as the bias voltage is the primary influence [165].

The separation of plasma generation and sputtering conditions has several advantages. First, there is the aforementioned independently variable sputtering rate controlled by the bias voltage. Compared to a conventional magnetron sputtering the HiTUS system requires only moderate magnetic fields near the target with a low field gradient. This allows for the use of thick ferromagnetic targets and results in efficient target utilisation compared to magnetron systems. In HiTUS target utilisation can be as high as 95%. Since the erosion of the target is relatively uniform metal pegs can be used to modify the target composition. These pegs are inserted into drilled holes and can either be used to introduce a dopant or to alter an alloy ratio by a few percentage points. Holes drilled into a IrMn target are shown in fig. 5.2(a). In IrMn there is a differential sputtering of Mn and Ir atoms due to iridium's higher binding energy. Ir crystals accumulate on the target surface as the surrounding Mn is sputtered away. This is shown in fig. 5.2(b). The magnetic field near the substrate is low. However, a permanent magnet can be placed on the substrate to deposit a film in field.

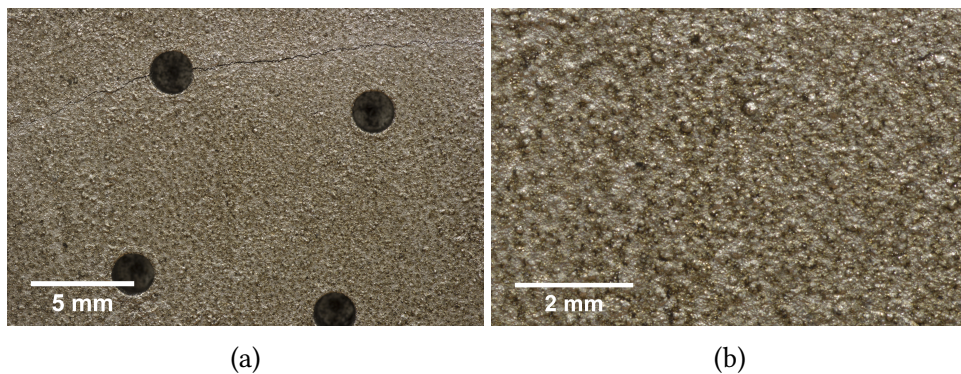


Figure 5.2: The surface of the IrMn target showing (a) the drilled holes which can be filled with material to adjust the effective target composition and (b) Ir crystals on the target surface.

Control of the grain diameter is essential as it, along with layer thickness, gives the grain volume. The grain volume distribution is known to define the characteristics of an exchange-biased material and has been discussed in section 4.2 [11]. In HiTUS the grain size can be modified by variation of target bias voltage, process pressure and ionising RF power [157]. In this study, the bias voltage was used to control grain size as it is the easiest parameter to vary and produces the widest variety of grain sizes.

Another difference between HiTUS and conventional magnetron systems is the relatively large separation of the target and substrate of (20 ± 1) cm. This has two effects. First, the material that deposits on the substrate is not re-sputtered. This is both because there is no bias voltage on the substrate and because the plasma is directed away from the substrate by the guiding electromagnets. Secondly, the deposition across the substrate is uniform as the substrate represents an intersection of a cone of sputtered material.

In HiTUS it is possible to place a carbon-coated TEM grid alongside the substrate. This means that the deposition occurs on both the TEM grid and the substrate simultaneously. A carbon-coated TEM grid is a perforated Cu disc coated in a thin C film. The Cu lattice provides mechanical support to the C film. The combined thickness of the sputtered film and the substrate is too great to allow electron transparency without time-consuming and destructive thinning. Sputtering onto a TEM grid allows electron-transparent, in-plane TEM samples to be deposited due to the much lower combined thickness of the sputtered and C films compared to the sputtered film on the substrate. In-plane TEM samples were used to measure the grain diameter D_g , which is essential for the application of the York Model of Exchange Bias [11]. It has been shown that the grain size on TEM grids is the same as that on the substrate [166].

5.1.2 Sputtering Procedure

The production of reproducible exchange bias samples depends on replicating the sputtering conditions. This includes a procedure to control the condition of the target, substrate and plasma before any material is deposited. This pre-deposition procedure begins with target cleaning. Target cleaning removes contaminants including oxides from the target surface via plasma sputtering. A bias voltage of -900 V is applied to the target and sputtering continues until the sputtering rate reaches a constant value. This indicates that the target is free of surface contaminants. Additionally the sputtered metal will act as a getter, removing free oxygen from the chamber by reacting with it. The target is water-cooled to prevent it from overheating.

During target cleaning, the substrate is concealed by a shutter. Target cleaning is followed by up to five minutes of substrate cleaning, during which the bias volt-

age is removed and lower steering magnet is switched off. This allows the plasma to fill the main chamber where it is grounded by the substrate and chamber walls. This process scours absorbed species such as water and organic contaminants from the substrate and chamber walls. It also removes the oxide layer from the Si substrate [53]. These two cleaning processes prepare the chamber, target and substrate for deposition.

The cleaning processes are followed by two further pre-deposition procedures, plasma conditioning and pre-sputtering. These final procedures directly precede deposition and determine the sputtering parameters. Plasma conditioning is a 30 s period provided for the plasma to reach equilibrium. This allows the system to reach and stabilise at the process pressure. In this time the RF system and matching unit maximise power transfer to the process gas. During pre-sputtering the plasma is again directed onto the target and the bias voltage applied. This ages the target and continues until the deposition rate reaches equilibrium. Once these processes are complete the shutter is opened, exposing the substrate to the sputtered material. The sputtering procedure can be stopped by extinguishing the plasma. Alternatively, the substrate can be concealed by a shutter. This allows the target to be changed without having to extinguish the plasma, which is convenient for depositing multilayer films.

5.1.3 Film Thickness

The deposited film thickness was measured using an INFICON XTM/2 Deposition Monitor. This device operates during deposition to monitor overall film thickness and deposition rate. The sensing apparatus is a piezoelectric quartz crystal which is positioned near the substrate during deposition. An applied voltage causes the piezoelectric crystal to distort, so an alternating voltage causes the crystal to oscillate. The resonant frequency of this oscillation changes when small amounts of material are deposited onto the exposed face. This change is given by

$$\frac{\Delta m_f}{m_q} = \frac{\Delta f_c}{f_q} \quad (5.1)$$

where Δm_f is the change in mass due to accumulating material, m_q is the original mass of the crystal, Δf_c is the change in resonant frequency of the coated system and f_q is the resonant frequency of the uncoated crystal, which has a typical value

of 6 MHz [167]. This high frequency produces resolvable change in a short amount of time which allows for precise measurements.

This equation holds for very thin deposition layers only because it assumes the deposited film is entirely within the antinode region of the resonator. If this is the case, the film experiences no shear deformation and thus the elastic properties of the film can be disregarded. Thicker films can be measured using the Z-Match technique which includes the acoustic impedance ratio of the deposited material to give the film thickness as

$$d_f = \left(\frac{N_q \rho_q}{\pi \rho_f f_c Z_a} \right) \arctan \left(Z_a \tan \left[\frac{\pi(f_q - f_c)}{f_q} \right] \right) \quad (5.2)$$

where N_q is the frequency constant of the quartz which is 1661 Hz m [167], ρ_q and ρ_f are the quartz and film density respectively, f_c is the coated resonant frequency of the system and $Z_a = (\rho_q \mu_q / \rho_f \mu_f)^{1/2}$ is the acoustic impedance ratio and μ_q where μ_f are the quartz and film shear moduli [168].

This technique was calibrated using single-layer films deposited onto substrates of known weight. The deposited films were weighed using a Mettler UMT2 digital microbalance with a sensitivity of 0.1 μg . The thickness of the films were calculated using the bulk densities. However, the film density is unknown and expected to be less than the bulk density. The linear relationship between the thicknesses measured by resonance and by weighing implies the films have a density of $\approx 90\%$ bulk density. This technique is more accurate for films such as IrMn than it is for CoFe due to the tendency for CoFe to oxidise.

In this work the CoFe/IrMn interface of an exchange bias system was modified by the addition of Mn. The addition of Mn at the interface is known to affect the value of exchange bias measured [91, 92]. This is quantified as an ultra-thin layer with thickness d_{Mn} . However, due to diffusion and the small amount of Mn added this is not expected to constitute a distinct layer. Thus adding Mn to the interface is in effect an alteration of the F and AF compositions in that region. In this work d_{Mn} had a value between 0 and 0.6 nm. In order to deposit these ultra-thin layers, exchange bias films were produced by Seagate Technology at their facility in Northern Ireland.

5.2 Structural Characterisation

An understanding of the structure of a system is a requirement for interpreting its magnetic behaviour. This is true in general for magnetic systems and especially for exchange bias systems analysed using the York Model of Exchange Bias. For this reason a series of detailed structural characterisations are carried out on each film. In this study, special interest is paid to the crystallographic ordering and grain size of the film. This section therefore discusses the experimental techniques used to measure these structural properties, namely X-ray crystallography and grain size analysis. In this section, anything not explicitly referenced is sourced from Cullity [13, 169].

5.2.1 X-ray Crystallography

A common technique for analysis of thin films is X-ray crystallography. X-ray crystallographic techniques are used to measure film properties by observing the reflections from a surface irradiated by X-rays. These reflections arise from diffraction from separated atomic planes in accordance with Bragg's Law

$$\lambda = 2d_{hkl} \sin \theta_i \quad (5.3)$$

where λ is the X-ray wavelength, θ_i is the angle of incidence measured from the plane and d_{hkl} is the plane separation which for a cubic crystal is given by

$$d_{hkl} = \frac{a}{\sqrt{h^2 + k^2 + l^2}} \quad (5.4)$$

where a is the lattice constant and h , k and l are the Miller indices of the plane.

Thus a large reflection intensity at a specific angle corresponds to a particular plane separation. This can be used to measure changes in lattice constant of a material and to distinguish between different families of planes. This is possible because the separation of the $\{100\}$ planes of a cubic lattice is greater than that of the $\{110\}$ planes, itself greater than that of the $\{111\}$ planes. Examples of lattice planes and their corresponding Miller indices are shown in fig. 5.3.

The X-ray crystallography in this work was carried out using a Rigaku Smartlab X-ray diffractometer (XRD) system. This system uses a rotating Cu target bombarded by surrounding tungsten-anode filaments. The electron interactions with the target produce both broad-spectrum Bremsstrahlung radiation and so-called characteristic X-rays. These narrow-band characteristic X-rays arise from the electron bombardment ejecting a core electron from a target atom. This core hole is then filled by an outer shell electron, which emits a photon with an energy level equivalent to the energy difference between the two states. Since the Bragg condition for a reflection depends on the wavelength λ , XRD measurements require monochromatic or nearly monochromatic X-rays.

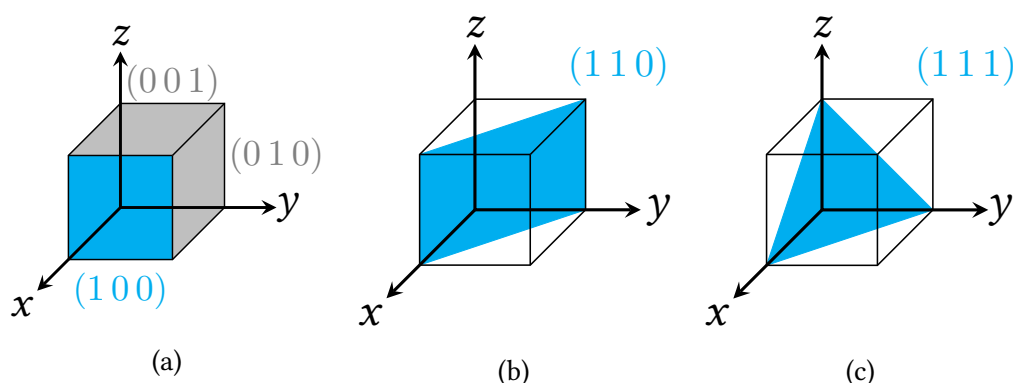


Figure 5.3: Highlighted planes with their corresponding Miller Indices in a unit cube for (a) the family of $\{100\}$ planes, (b) the (110) plane and (c) the (111) plane.

Since the energy of an emitted characteristic X-ray photon is dependent only on the electronic structure of the atom, characteristic X-rays have well-known wavelengths. This makes them ideal for use in XRD. In this study X-rays resulting from the K-L₃ transition in Cu were used. This transition is equivalent to the K α_1 transition in Siegbahn notation which is a transition from the L₃ ($2p_{3/2}$) subshell to the K ($1s$) shell [170]. This transition has an energy difference and thus an emitted X-ray energy of (8047.8 ± 2.3) eV where the error is the FWHM of the spectral line [171]. Thus the corresponding wavelength is (154.059 ± 0.044) pm. This wavelength is ideal for XRD as it is close to the plane spacing of the materials analysed in this study.

In order to use the K-L₃ energy for XRD, the other characteristic X-rays and the Bremsstrahlung radiation must be removed to produce a monochromatic beam. This is achieved with a channel-cut Ge (220) single-crystal, through which the generated X-rays enter and diffract twice. This is shown in fig. 5.4(b) Due to the specificity of the Bragg condition the monochromator effectively filters out all

wavelengths except the $K\text{-}L_3$ wavelength. A two bounce monochromator is capable of eliminating the $K\alpha_2$ energy, which differs from the $K\alpha_1$ energy by only 20 eV or 4 pm.

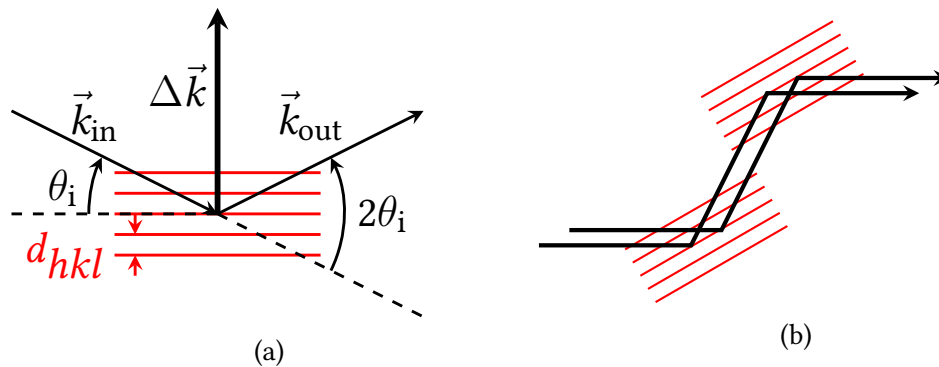


Figure 5.4: (a) X-ray diffraction in θ - 2θ geometry and (b) schematic of a two bounce Ge(220) monochromator which uses the Bragg condition to eliminate all but one wavelength.

X-ray crystallography includes a number of measurement modes, or geometries, in which different properties can be measured. Distinguishing between planes is achieved by use of θ - 2θ geometry, which is shown in fig. 5.4(a). In this geometry the incident wavevector \vec{k}_{in} is reflected by the scattering vector $\Delta\vec{k}$ to become the reflected wavevector \vec{k}_{out} . The X-ray source is moved by θ_i , while the detector is moved by $2\theta_i$. This nomenclature arose with historical XRD systems in which the X-ray source was stationary while the sample rotated. θ - 2θ is limited to measuring planes parallel to the surface.

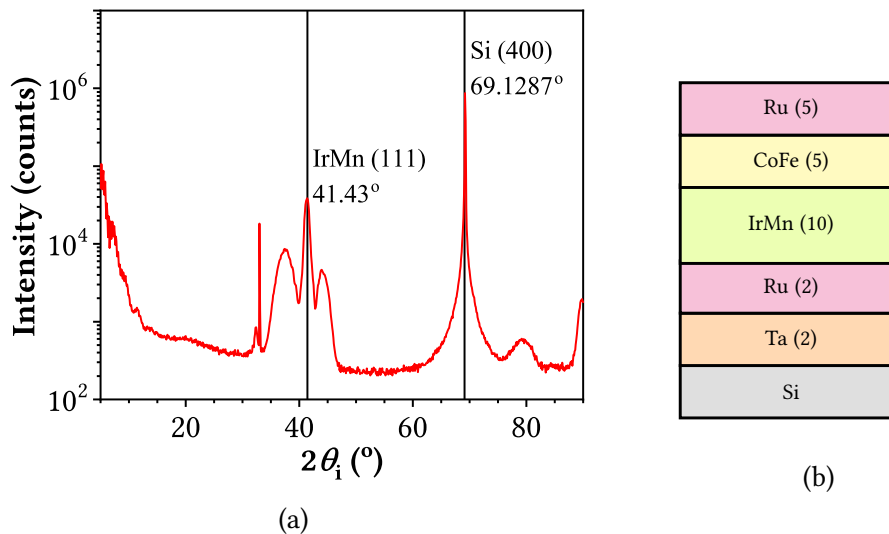


Figure 5.5: (a) Example of typical θ - 2θ XRD data for a sample with a polycrystalline thin film and a single-crystal substrate and (b) structure shown schematically (thicknesses in nm).

A typical example of θ - 2θ XRD data for a polycrystalline thin film is shown in fig. 5.5(a). The sample used for this measurement has composition Si/Ta (2)/Ru (2)/IrMn (10)/CoFe (5)/Ru (5) (thicknesses in nm) and was produced by Seagate Technologies at their facility in Northern Ireland. The film structure is shown schematically in fig. 5.5(b). The area irradiated by the X-ray beam was on the order of 1 mm in width and 5 mm in length. Because of this, it was not possible to measure the reflection from a single grain with size ~ 10 nm. The reflections observed are therefore an average over many grains. In fig. 5.5(a) two peaks are labelled with the corresponding material and the calculated values for the peak positions. These were calculated based on the Bragg angles for plane separations which were themselves calculated from the bulk material lattice parameters. The height and narrowness of the Si substrate peak compared to the IrMn peak is indicative of the greater periodicity in the substrate as compared to the sputtered film and indicates the change in lattice parameter due to residual stress.

If the crystallites of a polycrystalline material are oriented randomly then the material is said to be untextured. A polycrystalline material is described as textured when the crystallites have a preferred orientation [13]. The peak at $(41.4 \pm 0.1)^\circ$ coincides with the calculated reflection of the IrMn $\{1\ 1\ 1\}$ planes which indicates there are $\{1\ 1\ 1\}$ planes parallel to the film surface. Note that none of the peaks correspond to CoFe. Since $\text{Co}_{70}\text{Fe}_{30}$ has fcc structure the $\langle 100 \rangle$ and $\langle 110 \rangle$ reflections are forbidden by the selection rules [13, 169]. Thus a lack of a reflection for CoFe indicates that it has either $\langle 100 \rangle$ or $\langle 110 \rangle$ texture or that it forms an amorphous layer. In any case for the F layer the shape anisotropy is expected to dominate over the magnetocrystalline anisotropy.

The thickness and material of seed layers is known to influence the crystallographic ordering and texture of thin films which has consequences for magnetic properties and exchange bias [33–35, 37, 87, 154, 172, 173]. The films in this work have a dual seed layer of Ta/Ru which has been shown to induce texture in IrMn that is between in-plane easy axis texture and 3-D random texture [32, 67]. The Ta provides a smooth surface and breaks the crystal habit of the substrate. This allows the hexagonal Ru to be deposited with its long axis perpendicular to the surface, seeding the IrMn texture. This will be discussed further in fig. 5.7.

The equivalent to θ - 2θ for measuring planes normal to the surface is termed $2\theta_\chi$ - ϕ geometry. Since it is not possible to illuminate the sample with a truly

in-plane X-ray source, the source is usually offset by a small angle ω . For this Rigaku Smartlab ω is usually offset by less than 0.5° and typically much less. In a $2\theta_\chi$ - ϕ scan the sample is rotated through ϕ and the detector through $2\theta_\chi$, while the source is held still. This is shown on figure fig. 5.6. Using this geometry the same set of planes are observed throughout the measurement. In a polycrystalline sample a combination of θ - 2θ and $2\theta_\chi$ - ϕ scans will indicate the prevalence of crystallographic planes both in and out of plane.

By scanning through the Bragg angles, θ - 2θ and $2\theta_\chi$ - ϕ geometries are able to identify the crystallographic planes present and identify the material they correspond to. However, they are limited to only being able to observe planes aligned either in-plane or out-of-plane. Once θ - 2θ and $2\theta_\chi$ - ϕ have identified the presence of a plane a pole figure scan can be used to find that plane at other orientations.

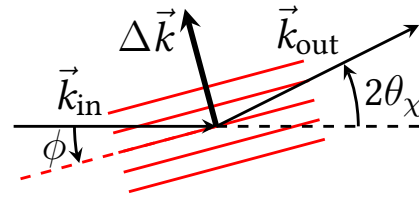


Figure 5.6: Schematic of $2\theta_\chi$ - ϕ geometry where the planes lie perpendicular to the surface.

In a pole figure scan θ_i and $2\theta_i$ are set to a chosen Bragg angle for a specific family of plans in a specific material at the beginning of the measurement and do not change. The sample is rotated in plane through an angle β and the detector moved from in-plane to out-of-plane through an angle α . Since the source and detector are in the Bragg condition, all the reflected intensity comes from the diffraction of the chosen crystal planes. For example, if a θ - 2θ scan identifies the IrMn (1 1 1) plane parallel to the surface, then a pole figure measurement at 41.4278° will find the IrMn {1 1 1} planes oriented in the other directions. For an fcc, single-crystal sample there will be four {1 1 1} reflections visible in the pole figure, one out-of-plane peak and three equidistant peaks arranged on the circumference of a circle 70.53° away from the perpendicular. The peaks at 70.53° arise from the other {1 1 1} planes, which are separated from each other by that amount.

The combination of θ - 2θ , $2\theta_\chi$ - ϕ and pole figure measurements indicate the materials and crystallographic orientations present in a thin film. A fibre texture is a crystallographic texture where the crystallites have a crystal direction parallel to a single direction called the fibre axis. The crystallites in a material with fibre texture are at arbitrary rotations about that axis [13]. Therefore the pole figure

will be spherically symmetric. A thin film with out-of-plane fibrous $\langle 111 \rangle$ texture will have crystallites that tend to have a $\{111\}$ plane parallel to the surface. As well as this the crystallites will be relatively rotated. Due to the rotation a pole figure of a thin film with fibrous, out-of-plane $\langle 111 \rangle$ texture will show a central out-of-plane peak and a ring at 70.53° . The ring arises from the relative rotation of the crystallites around the $\langle 111 \rangle$ direction, which averaged over the whole film appears isotropic in the plane. In IrMn the $\{111\}$ planes are of particular interest as they correspond to the magnetic easy axes [32–36]. For this reason in IrMn systems out-of-plane fibrous $\langle 111 \rangle$ texture is also known as in-plane easy-axis texture with the same meaning [11, 37].

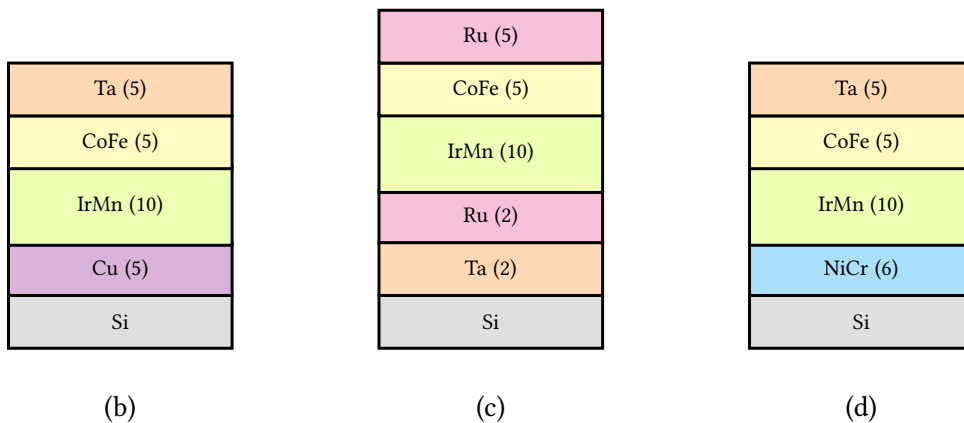
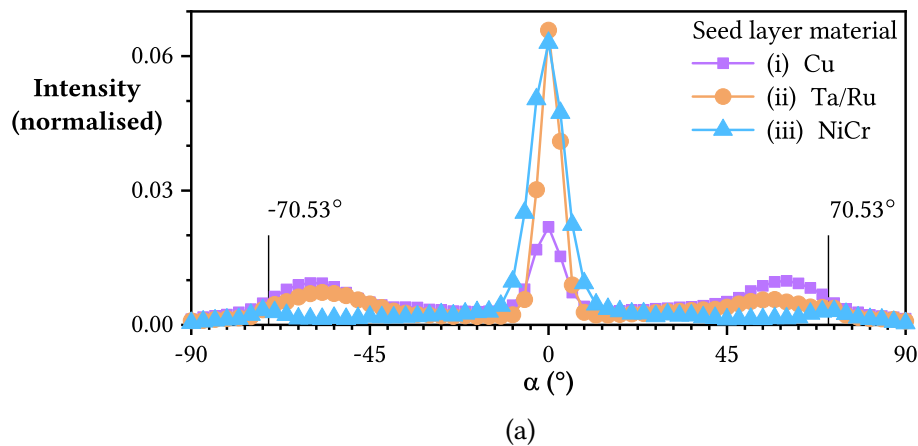


Figure 5.7: (a) Pole figure scans through α with constant value of β . The Measurements were performed at the Bragg angle for IrMn (111) for three samples (i)(ii)(iii) with (b)(c)(d) respective compositions shown schematically (thicknesses in nm). A complete pole figure is made up of one α scan per β angle. For circularly symmetric samples all α scans are identical.

Figure 5.7(a) shows pole figure measurements at the Bragg angle for IrMn (111) for three samples with different seed layers. The pole figure shown in fig. 5.7(a)(i) has composition shown in fig. 5.7(b) (thicknesses in nm). The pole figure shown

in fig. 5.7(a)(ii) has composition shown in fig. 5.7(c). This film was produced by Seagate Technologies at their facility in Northern Ireland. The pole figure shown in fig. 5.7(a)(iii) has composition shown in fig. 5.7(d). The differing appearance of the pole figures is representative of the texture of the IrMn film, which is itself a consequence of the choice of seed layer [32–35, 37, 56, 174].

Pole figures allow the texture of the films to be compared qualitatively. In fig. 5.7(a)(i) the film with a Cu seed layer shows that the IrMn layer is weakly textured, meaning there is no strongly preferred crystallite orientation. This results in a pole figure with relatively uniform intensity. In contrast, in fig. 5.7(a)(iii) the film with a NiCr seed layer has out-of-plane fibrous $\langle 111 \rangle$ texture. This strong texture results in a bright central spot and clear ring at $\alpha = \pm 70.53^\circ$. Thus for this film there will be a large number of crystallites which have easy axes lying in the plane of the film [13]. Intermediately, fig. 5.7(a)(ii) shows the pole figure of a film with Ta/Ru dual seed layer and intermediate texture. This results in a central spot and a faint ring at $\pm 70.53^\circ$.

Texture is important since in IrMn systems the magnetic easy axis is in the $\{111\}$ planes [32–36]. The effect of texture on exchange bias was discussed in section 3.2.2 and section 3.3.1. IrMn $\langle 111 \rangle$ texture has been shown to correlate to large exchange bias and AF anisotropy [32–36, 87, 174]. When using the York Model of Exchange Bias to calculate the anisotropy of a AF material, the value obtained is the effective anisotropy due to the effects of texture [11]. A 3-D random texture will reduce the effective anisotropy of an IrMn film, even if there is no change in the magnetocrystalline anisotropy of the individual AF grains. Texture also has implications for exchange bias phenomena such as training, as discussed in section 3.3.1 [37, 67].

While not strictly a part of XRD or X-ray crystallography, X-ray reflectivity (XRR) is another X-ray technique used to characterise thin films. In XRR the specular reflection of X-rays from a sample are measured at low angles. The reflected intensity deviates from Fresnel reflectivity because the surfaces are not ideal [175]. The surface and interfaces are affected by roughness, porosity, interdiffusion and contamination. In a thin film heterostructure, the reflection forms fringes, the periodicity of which is a function of the materials and layer thickness of the film.

The reflection from the interfaces for the n^{th} layer of a thin film heterostructure is expressed by a recursive formula derived in 1954 by Parratt [175]. It was shown that

$$R_{n-1,n} = \psi_{n-1}^4 \left[\frac{R_{n,n+1} + F_{n-1,n}}{R_{n,n+1}F_{n-1,n} + 1} \right] \quad (5.5)$$

where ψ_{n-1} is a wave-like function of the X-ray wavelength, incident angle, layer thickness and refractive index. $F_{n-1,n}$ is a function of the incident angle and refractive indices of the n^{th} layer and the layer below. $R_{n,n+1}$ and $R_{n-1,n}$ are functions of ψ_{n-1} and the ratio tangential components of the electric vectors of the reflected and incident X-rays. The ratio of the reflected to incident intensity is obtained by multiplying the ratio tangential components of the electric vectors of the reflected and incident X-rays by its complex conjugate.

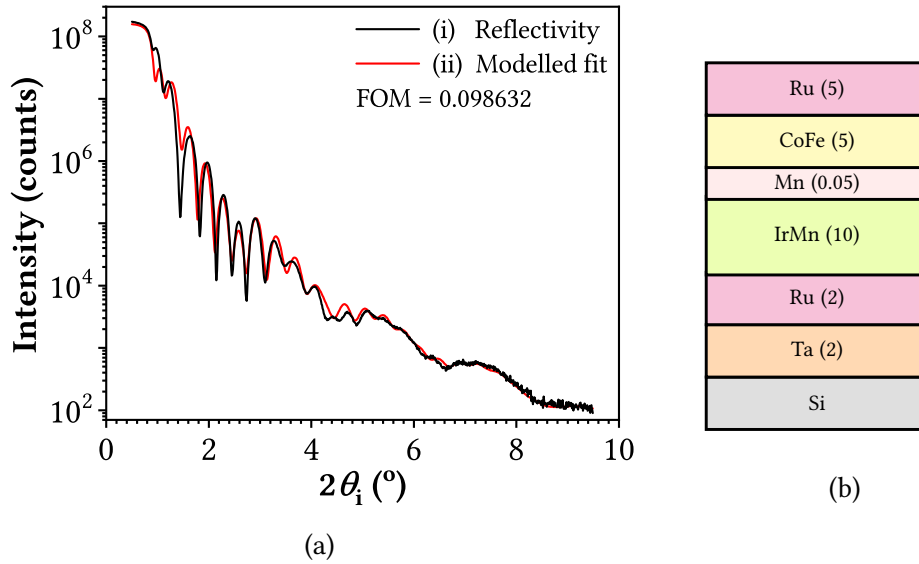


Figure 5.8: Example of typical XRR data showing (a)(i) fringes for film with (b) structure shown schematically (thicknesses in nm) compared to (a)(ii) a modelled film with parameters defined in table 5.1. The figure of merit is 0.098632.

Using modelling software, it is in principle possible to simulate an XRR spectrum [176]. This simulation can then be fitted to the XRR data. It can be used to confirm the nominal film thickness d_f values or to measure the film density ρ_f or interfacial roughness σ_f . However, due to the large number of fitting parameters a fitted solution is unlikely to be unique. In addition, the refractive index is non-trivial to calculate since it is a consequence of the interactions between the oscillating electric and magnetic field components of the wave with the electrons in the material. For this reason fitting software is packaged with experimentally obtained parameters for a library of materials. In this work the parameters were obtained by Henke et al. [177]. That said, this does not always include non-standard alloys such as CoFe or IrMn. Furthermore, the compositions of alloys used in this study

are not known precisely. For this reason XRR fits must be treated with scepticism. The Rigaku Smartlab XRD has in-built XRR fitting software that uses a Fourier transform to produce the initial conditions for the fit.

Figure 5.8(a)(i) shows an example of typical XRR data for a multilayer thin film with composition Si/Ta (2)/Ru (2)/IrMn (10)/Mn (0.05)/CoFe (5)/Ru (5) (thicknesses in nm). The film structure is shown in fig. 5.8(b). This film was produced by Seagate Technologies at their facility in Northern Ireland. Also shown in fig. 5.8(a)(ii) is a fitted simulation made using a specialised modelling software GenX 3 [178]. GenX 3 uses a genetic algorithm to refine multiple parameters simultaneously [179].

It is possible to fine-tune the algorithm by careful selection of the mutation rate. A high mutation rate makes the fit less dependent on the starting conditions. In addition a large population size allows more fits to be analysed per generation. GenX 3 is capable of taking advantage of parallel processing when used with compatible hardware, which greatly decreases the time required to process each generation.

The film roughness was simulated by a Gaussian distribution of correction factors applied to the electric field amplitude at the interface [178]. The fit had a figure of merit (FOM) equal to 0.098632, calculated from comparing the data and the fit on a logarithmic scale [178]. In order to increase consistency between samples the same number of generations were used in all cases, which was equal to 10^5 .

Material	Nominal		Model Parameters		
	d_f (nm)	$\rho_f (\pm 0.01)$ (g/cm ³)	$d_f (\pm 0.1)$ (nm)	$\rho_f (\pm 0.1)$ (g/cm ³)	$\sigma_f (\pm 0.1)$ (nm)
RuO ₂	–	6.97	1.0	6.9	0.7
Ru	5	12.45	3.2	12.1	0.6
Co ₇₀ Fe ₃₀	5	8.59	5.1	9.0	0.6
Mn	0.05	7.21	0.1	8.1	0.2
IrMn ₃	10	11.40	9.0	12.0	0.3
Ru	2	12.45	1.5	12.8	0.5
Ta	2	16.69	2.7	14.0	0.2

Table 5.1: The nominal values and modelling parameters used in the fit of fig. 5.8(a) and film structure shown schematically in fig. 5.8(b) showing film thickness d_f , density ρ_f and interfacial roughness σ_f [26].

For high-quality fits it is necessary to fit the instrument parameters such as intensity, resolution, background and spot size. However, once these values were found they were kept constant to decrease the time required to fit the remaining parameters. A Gaussian beam correction was added to correct for the beam shape, which was important for fitting the critical angle of the film. In addition, an oxide layer was added to the sample surface. The film thickness d_f , density ρ_f and interfacial roughness σ_f found for the film modelling are shown in table 5.1 compared to the nominal values [26].

For all films other than Mn the thicknesses and densities obtained by fitting were close to the nominal values. For the CoFe layer the thickness was 3 % larger than the nominal value and the density was 5 % higher. For the IrMn layer the thickness was 10 % lower than the nominal value and the density was 5 % higher. These increased densities could indicate that the CoFe and IrMn films contain higher proportions of Co and Ir than the sputtering target. This was discussed in section 5.1.1. Table 5.1 shows the film roughness as estimated by the fitting. The film roughness was low and was lowest for the layers closest to the substrate. This is a consequence of the fact that each layer was deposited on top of the layers that came before.

5.2.2 Grain Size Analysis

Measurement of the grain size distribution of a polycrystalline sample is essential for the proper application of the York Model of Exchange Bias which was discussed in more detail in section 4.2. An effective method for measuring this is to analyse TEM images using a particle size analyser. To do this an electron-transparent portion of film is observed in a TEM. This allows the measurement of individual grain diameters. From this, the median grain volume and grain volume distribution can be measured. In this section, anything not explicitly referenced is sourced from Cullity [169] and Williams & Carter [180].

An electron microscope is a type of microscope that uses a beam of electrons to form an image. In a transmission electron microscope (TEM) the electrons interact with the sample as they pass into, through and out of a sample. Since electrons have a smaller wavelength than visible light, an electron microscope is capable of resolving significantly smaller features than a light microscope in accordance with

the Rayleigh criterion

$$\sin\theta_R = 1.22 \frac{\lambda}{D_a} \quad (5.6)$$

where θ_R is the smallest angular separation that can be resolved, λ is the wavelength and D_a is the diameter of a circular aperture. The electrons are produced by an electron gun and focussed by electromagnets to form an image on a charge-coupled device (CCD). A schematic of a TEM optical set up is shown in fig. 5.9.

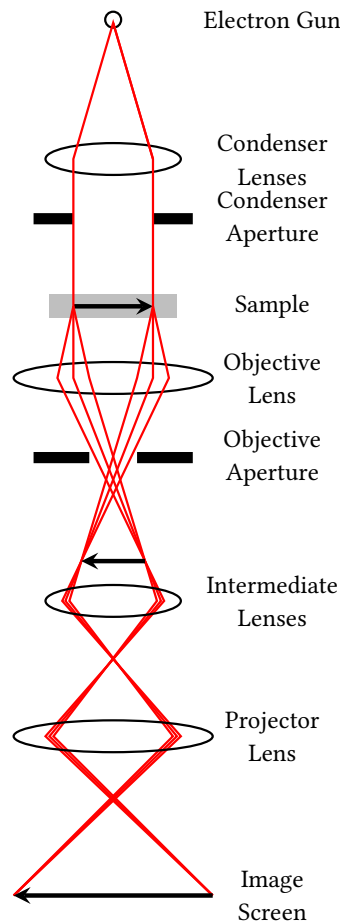


Figure 5.9: Schematic of a TEM.

For TEM it is necessary to prepare electron transparent samples, these being samples through which electrons can pass in sufficient numbers to form a useful image in a reasonable amount of time. This is often achieved by making the sample very thin. The maximum thickness for electron transparency varies by material and electron beam energy. For metals a thickness of hundreds of nm is usually electron transparent. Due to the lower interaction cross-section, this thickness can be up to several μm for organic chemicals. For magnetic measurements, films are deposited on 0.2 mm thick Si wafer substrates. However, these cannot be used in a TEM as the electrons cannot travel through the substrate. For this reason a carbon-coated Cu TEM grid is placed beside the Si substrate in HiTUS during

deposition. This produces a film alongside the main sample with the same grain size distribution [166]. Since the sputtered film is supported only by a thin C film, the ensemble is electron transparent and therefore suitable for TEM imaging.

Since the electrons travel through the sample, contrast in a TEM can be very slight. It is produced by two main mechanisms, mass-thickness contrast and phase contrast. Mass-thickness contrast arises due to the interaction of the electron beam with the sample. For a single atom it is governed by the screened relativistic Rutherford cross section

$$\frac{d\sigma}{d\Omega} = \frac{\lambda_R^4 Z^2}{64\pi r_B^2 \left(\sin^2 \frac{\phi_R}{2} + \left(\frac{\theta_0}{2} \right)^2 \right)^2} \quad (5.7)$$

where $\frac{d\sigma}{d\Omega}$ is the Rutherford differential cross-section, λ_R is the electron relativistic wavelength, Z is the atomic number of the atom, r_B is the Bohr radius of the atom, ϕ_R is the scattering angle and θ_0 is the screening angle. Since mass-thickness contrast is due to the deflection of electrons due to Z , there is sufficient differential interaction to create contrast when using materials of different Z or different thicknesses. An example of mass-thickness contrast is shown in fig. 5.10. This sample is an exchange bias film of CoFe/IrMn on a Si substrate. The film and substrate have been thinned into a wedge shape by focused ion beam (FIB) milling. Since the films used in this study have fairly uniform composition and thickness, mass-thickness contrast does not contribute to the contrast of the TEM images.

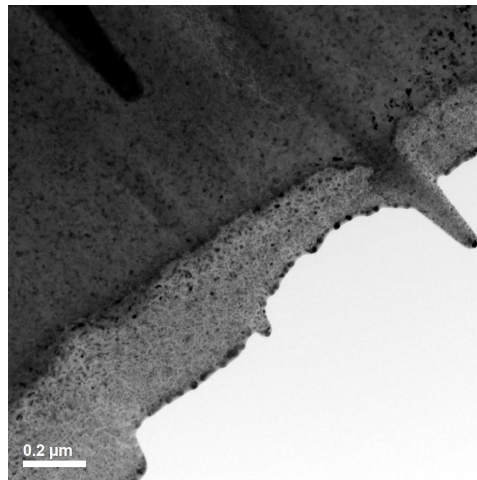


Figure 5.10: Mass-thickness contrast for a wedge-shaped CoFe/IrMn thin film prepared by focused ion beam milling. The white part of the image has no material and so appears bright. The darker parts of the image represent areas where the material is thicker. Sample prepared and imaged by author.

Phase contrast is produced by the wave properties of electrons interacting with a material [180]. For an ordered crystal a Bragg condition will exist for an electron wave. Therefore, the electron wave can be diffracted by a crystal. This can be used to perform electron diffraction measurements on a film in the same way that X-rays can be used. However, for a polycrystalline sample it has an additional use. Since the majority of the crystallites will not be in the Bragg condition the electron beam will interact with them only very little and they will appear transparent. For a crystallite which does match the Bragg condition however, the electron beam will be deflected by $2\theta_i$. Using an aperture, electron beams deflected far from the optical axis can be excluded. This causes the crystallite in question to appear dark in a TEM image. This imaging mode is known as BF imaging because the majority of the image is bright [180].

On the other hand DF imaging selects only crystallites which fulfil the Bragg condition. This is achieved by the use of an aperture to exclude the main through-beam, causing most of the image to appear dark. The aperture selects only the beam which has been diffracted to the same angle. Therefore, in DF imaging the crystallites for which the Bragg condition is met appear bright. The ray diagrams for BF and DF imaging are shown in fig. 5.11.

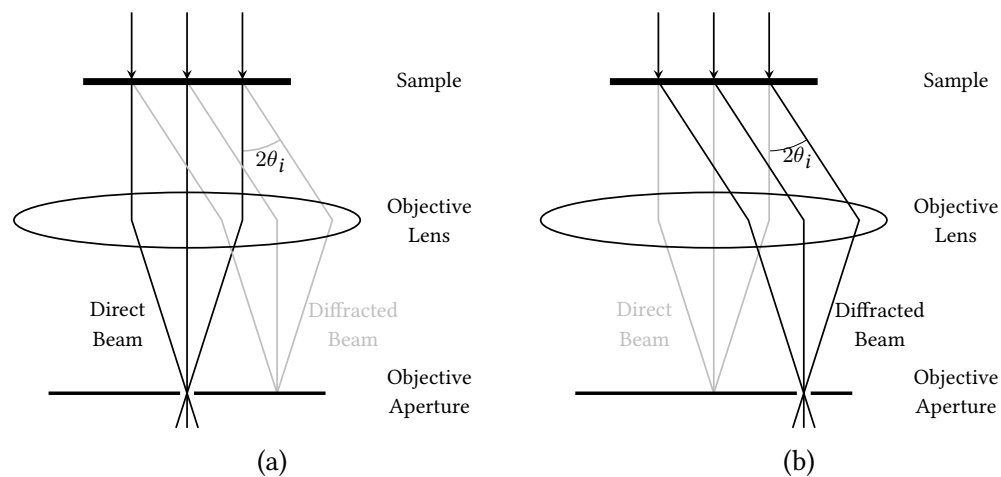


Figure 5.11: Ray diagrams for (a) BF and (b) DF imaging modes [180].

A comparison of BF and DF images is shown in fig. 5.12. As the film is tilted, crystallites enter and leave the Bragg condition. DF imaging demonstrates that the diffracting entities in the film are ordered single crystallites. Since the crystallites that appear in DF images correspond to those seen in BF images, either can be used for determining the grain size distribution. However, there are advantages to using BF images. Crucially, bright grains in DF images oversaturate the detector. This

causes the edges to become unclear, which prevents precise measurement of the grain diameters because it obscures the grain boundaries. In addition, BF images are used as each image contains more visible grains. This is because it is necessary to measure at least 500 crystallites [158].

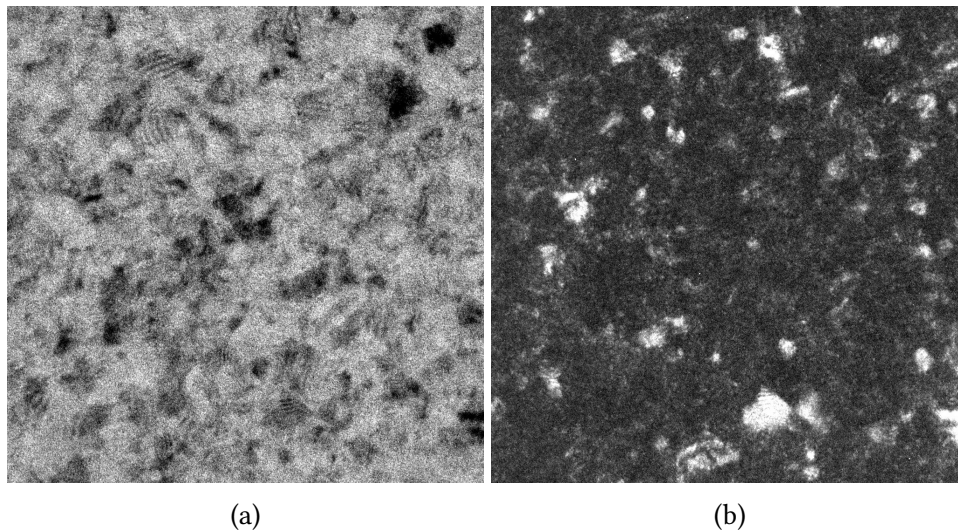


Figure 5.12: A film region imaged in (a) BF and (b) its corresponding DF image showing that the diffracting entities are ordered single crystallites. This CoFe/IrMn was deposited in HiTUS onto a TEM grid.

In both BF and DF imaging it is possible to make out linear patterns within individual grains. These have a superficial resemblance to atomic planes. The origin of these features is stress of the film. The films have been deposited on TEM grids which provide enough mechanical stability to support the film. However, the grid does not prevent the film from bending at the macroscopic level. This results in atomic planes that would be parallel to become misaligned. However, since the sputtered films are polycrystalline they have little long-range order, so this effect does not require consideration. Stress at the crystallite scale is caused by the displacement of atoms from a perfectly symmetric lattice. This is caused by surface effects at the surface of the film and at the crystallite faces. These in turn are caused by the different energy landscape of the surface as compared to the interior of the crystallite. This surface relaxation or contraction will slightly alter the Bragg condition in that region, leading to the appearance of stress fringes.

Grain volumes are analysed using a Zeiss particle size analyser. TEM images are printed and placed on a lightbox and an adjustable iris is matched to the crystallite area via the equivalent circle method. To ensure the quality of the measurement at least 500 grains are measured [158]. As designed the Zeiss particle size analyser is electromechanical in nature. However, it has since been enhanced

with custom Laboratory Virtual Instrument Engineering Workbench (LabVIEW) software, enabling detailed measurements to be made rapidly. Using this method measurements can be made at a rate on the order of 1 s per grain. It is therefore possible for an experienced operator to complete a grain size analysis measurement on up to seven samples in an hour. The Zeiss particle size analyser sorts the measured grain diameters into 48 calibrated bins, from which the grain size distribution can be obtained. A lognormal distribution is fitted to the data in order to find the median grain diameter $\langle D_g \rangle$, and σ_{D_g} the standard deviation of grain diameters. From these, $\langle V_g \rangle$ the median grain volume and σ_{V_g} are calculated by approximating the grains as cylinders with height equal to the film thickness d_f such that

$$V_g = \frac{\pi D_g^2}{4} d_f \quad (5.8)$$

where V_g is the calculated grain volume and D_g is the grain diameter. An example of a typical grain size distribution is shown in fig. 5.13.

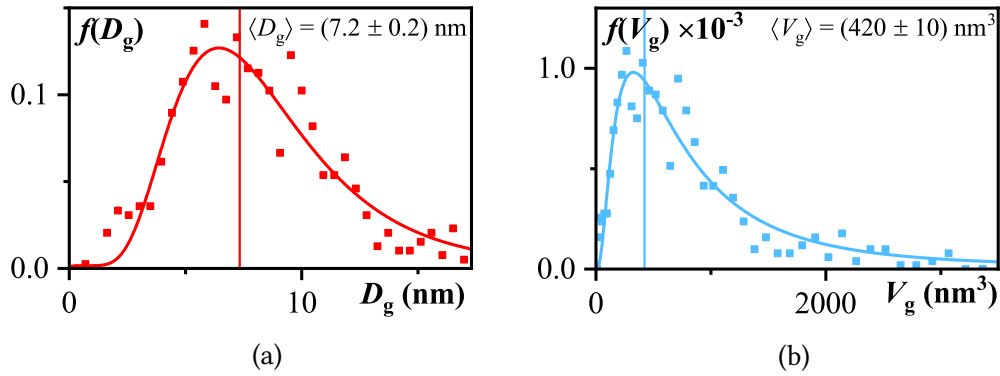


Figure 5.13: Example of a grain size distribution in terms of (a) D_g and (b) V_g for a 10 nm thick IrMn layer. In each case a lognormal fit is shown. However, the median values $\langle D_g \rangle$ and $\langle V_g \rangle$ were calculated from the data rather than the fit.

This method allows the measurement of $\langle V_g \rangle$ to high precision as well as the calculation of σ_{V_g} . These low errors are a result of measuring more than 500 grains [158]. The value of $\langle V_g \rangle$ is used for the calculation of the AF anisotropy in the York Model of Exchange Bias [11].

A notable feature of the lognormal distribution is that if a parameter is lognormally distributed, then the square of that parameter is also lognormally distributed. Thus D_g and V_g are both lognormally distributed. Another feature of a lognormal distribution is that if V_g is lognormal then $\ln V_g$ is Gaussian. In addition, in a Gaussian distribution the mean, median and mode coincide. Because of these two facts the median of a lognormal distribution is $\exp(\text{mean of Gaussian})$ since the mean

and median of a Gaussian distribution are equal. Where the standard deviation of a lognormal distribution of D_g is given, the meaning is the standard deviation of $\ln D_g$.

5.3 Magnetic Characterisation

5.3.1 Vibrating Sample Magnetometer

This study made use of a vibrating sample magnetometer (VSM) [181]. In its most fundamental form, in a VSM a magnetised sample is vibrated near a detection coil. The changing magnetic flux through the coil induces a changing voltage in the coil in accordance with Faraday's Law

$$\mathcal{E} = -N_c \epsilon \frac{d\Phi}{dt} \quad (5.9)$$

where \mathcal{E} is the electromotive force (emf), N_c is the number of turns in the coil, ϵ is the geometric correction factor, Φ is the magnetic flux through the coil and t is time. The sample is magnetised by an external magnetic field \vec{H} . Therefore, the total magnetic flux through the coil is the sum of the external field and the sample magnetisation \vec{M} such that

$$\Phi = (|\vec{H}| + |\vec{M}|) A_c \quad (5.10)$$

where A_c is the area of the detection coil. Thus combining equations eq. (5.9) and eq. (5.10) the voltage induced in the coils is

$$\int \mathcal{E} dt = -N_c \epsilon A_c |\vec{M}| \quad (5.11)$$

where the external field does not contribute to the voltage because it is invariant with time t .

The magnetic samples measured in this study are not point dipoles. The samples measured were up to several mm long and a similar distance from the detection coils. Thus the small dipole approximation cannot be used. This is the origin of ϵ in eq. (5.9). This is accounted for via calibration with a Pauli paramagnetic

(P) sample with the same value of ϵ . For this purpose a 99.99 % pure Pd foil is measured in the VSM. Since Pd has a linear magnetic response with susceptibility $(5.1 \pm 0.1) \times 10^{-6} \text{ cm}^3/\text{g}$ at 288 K the signal from a magnetised Pd foil can be used to calibrate the magnetic moment measured in a VSM [26]. The Pd foil is cut to have the same size and shape as the sputtered films except for its thickness. This additional thickness ensures that the Pd foil has a similar \vec{m} to F sputtered films. While the F thickness of the sputtered film is less than 10 nm, the Pd foil is $(0.250 \pm 0.001) \text{ mm}$ thick. Since the Pd foil is the same size and shape as the sample to be measured, the value of ϵ will be the same for both.

For the majority of measurements in this field, the value of \vec{m} , \vec{M} and M_s are not of significant interest and the AF carries no net moment. For this reason the magnetisation of the sample is often expressed as the ratio \vec{M}/M_s . However, in this study a magnetisation offset is measured and therefore hysteresis loops will not be normalised. When measuring exchange bias samples the crucial parameters are H_{c1} and H_{c2} , which are the two x -intercepts of the hysteresis loop. These values are used to measure the exchange bias H_{ex} , coercivity H_c and training effect ΔH_{c1} of a film. An example of a series F hysteresis loops measured on the Microsense Model 10 VSM is shown in fig. 5.14 where d_{CoFe} is the thickness of a CoFe film. The field is measured using a Hall effect Gauss probe which is calibrated to zero field and to a secondary standard on a monthly schedule. The other important parameter to control is temperature as it is used to control thermal activation processes in the AF layer. This is discussed in section 4.2.

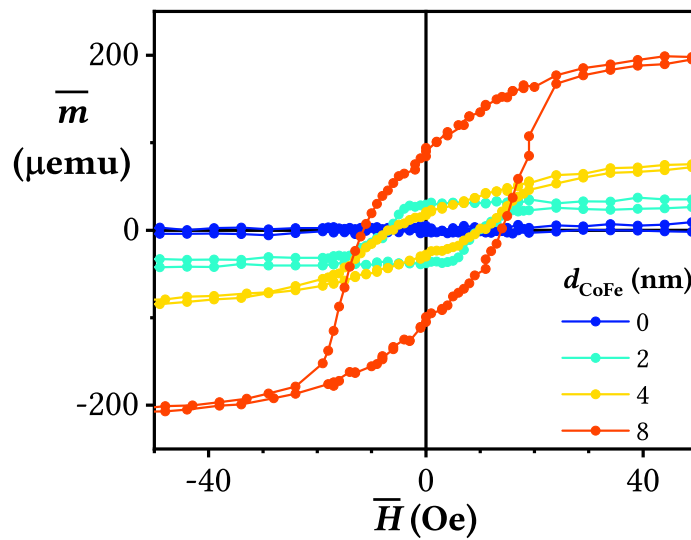


Figure 5.14: Example of data from the Microsense Model 10 VSM for thin layers of CoFe demonstrating the field and moment sensitivities.

The shape of a magnetic sample also has an effect on H_c . This is due to the demagnetising field which is dependent on the sample shape which is in turn dependent on the method used to produce the sample. Films sputtered in HiTUS are sputtered through a mask. This produces shadowing effects at the edge of the film. Sharper corners can be formed by sputtering onto a larger substrate and then cleaving the sample with a diamond scribe. Ultrasonic sample cutting produces a sample with a rough edge. The differing condition of the edge means that the activation energy for domain walls is different. This together with a strong demagnetising field at the edges of the film means that the probability of domain wall nucleation depends strongly on the condition of the film edge [182]. For magnetic transitions dominated by domain wall nucleation, a domain wall will propagate through the film rapidly. Hence if the magnetic transition of a film is dominated by domain wall nucleation then the condition of the film edges will significantly affect H_c . This is indicated by a hysteresis loop with an abrupt and rapid transition. In contrast if the magnetic transition is dominated by domain wall pinning then the transition will not be abrupt, as the domain wall has to propagate through the film as the field overcomes the pinning energies. Therefore the edge conditions of such a film do not have as large an effect on its properties.

The VSMs used in this study were a Microsense Model 10 VSM and a Quantum Design MPMS. These two systems were used because of their complementary temperature capabilities as temperature control is essential for repeatable exchange bias measurements. The Microsense Model 10 VSM has an open-circuit, continuous-flow cryostat that allows measurement from 100 to 700 K using N_2 and Ar. The Microsense Model 10 VSM uses Ar above 575 K due to the tendency for N_2 to form reactive species at high temperatures. The Quantum Design MPMS uses a closed circuit He cryostat with a temperature range from 1.8 to 400 K.

The Microsense Model 10 VSM uses eight detection coils arrayed in two tiers of four. This arrangement is shown in fig. 5.15 with the default applied field direction marked [183]. The signals from the upper and lower coils are subtracted so that the combined signal comes only from the sample region between the coils. This eliminates signals caused by the vibration of the detector coil assembly. The coils are arranged at intervals around the coil assembly in two orthogonal groups, these being called the x-coils and the y-coils. Vector combination of the signals in the x-coils and y-coils allows two-dimensional measurements of \vec{m} . Rotating the electromagnet changes the relative orientation of the sample to the external field.

Since the detector coil assembly does not rotate the sample position relative to the coils is fixed. This means the detector coil sensitivity remains uniform over the full rotation range. In the default position the detector coils are $\pm 45^\circ$ from the external field direction. Aligning the magnetic field with the detection coils at $\pm 45^\circ$ allows the x-coils and y-coils to be calibrated independently, since the coils perpendicular to the field intersect no flux [183].

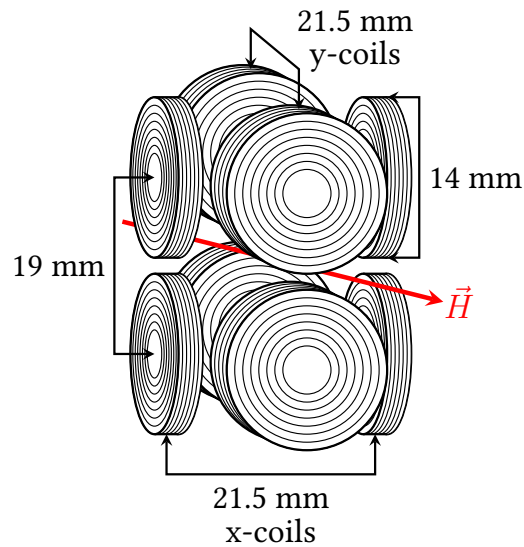


Figure 5.15: Coil arrangement for the Microsense Model 10 VSM [183].

A linear actuator vibrates the sample. A frequency of 75 Hz is used and matched by the reference frequency of a pair of Stamford Research SR830 lock-in amplifiers, one for the x-coils and one for the y-coils. With the cryostat in place the maximum field possible in the Microsense Model 10 VSM is 2.2 T with a 60 mm pole gap.

The use of an open-circuit, continuous-flow cryostat means that the sample vibration is not transmitted to the rest of the measurement system, which is challenging to achieve in a closed-circuit system. The temperature of the sample space is controlled by flowing gaseous N_2/Ar through a dewar of liquid N_2 . The gas/liquid mixture is then directed through a heater element to the sample space. The heater power is adjusted by PID control to heat the mixture to the target temperature. For high temperatures the liquid N_2 dewar can be by-passed to reduce the heater power required. By this method the temperature of the sample space can be specified to ± 0.5 K at 100 K.

The Quantum Design MPMS uses a SQUID to measure \vec{m} . This MPMS VSM is based at Diamond Light Source. The SQUID is the element used to detect flux, which differs from a conventional VSM which uses induction in detection coils.

The Quantum Design MPMS has a temperature range from 1.8 to 400 K and a maximum field of 7 T. The field coil and detection coil are solenoids concentric with the sample position.

A SQUID detects flux using a pair of Josephson Junctions connected in parallel, forming a loop. A Josephson junction is restricted a connection between two superconductors. This restriction can be an insulator, a non-superconducting conductor or a dimensionally narrowed portion of the superconductor. In each case, the restriction acts as a tunnel barrier to Cooper pairs which are the charge-carriers in superconducting circuits. The tunnelling of the supercurrent through the barrier is known as the Josephson Effect.

The tunnelling supercurrent across a Josephson junction is related to the phase difference of the Cooper pair wavefunctions between the superconductors. So by measuring the supercurrent around a loop with two Josephson junctions, the phase difference can be measured. The magnetic flux through the loop can therefore be indirectly measured, since the magnetic flux modifies the phase of this quantum state [184].

The SQUID measures flux by measuring the tunnelling supercurrent around the loop, which alternates at $\Phi = \Phi_0/2$ and reverses again at each increase in integer Φ_0 , where Φ_0 is the Magnetic flux quantum which has a value of 2.07×10^{-15} Wb accurate to 8 significant figures [184]. This requires calibration against a known magnetic field. A LakeShore 8600 Series VSM was used to confirm the trends observed.

6. High-Temperature Behaviour

As discussed in chapter 3, the phenomena associated with exchange bias are highly dependent on temperature. Broadly speaking, they can be divided into two groups, high-temperature and low-temperature behaviour. High-temperature behaviour includes the setting and thermal activation of the bulk of the AF grains, while phenomena such as spin freezing and the training effect, which are interface phenomena, are categorised as low-temperature behaviour. Low-temperature behaviour will be discussed in chapter 7.

In this chapter the high-temperature behaviour of exchange bias systems will be discussed. However, that does not imply that the measurements themselves will be made at high temperatures. The measurements discussed in this chapter take place at the temperature of non-activation T_{NA} . Measurements made at T_{NA} are free of the thermal activation of the spin order in the bulk of the AF grains [11]. Thus there are no changes occurring during the measurement, as discussed in section 4.2. Instead, the AF order changes only during the thermal and magnetic treatment that occurs before the measurement. Measuring at T_{NA} allows a snap-shot of the AF order to be measured. Therefore, despite the measurement occurring at around room temperature, the high-temperature behaviour can be probed. Measurements made at T_{NA} have been shown to be highly reproducible [11].

While the majority of H_{ex} arises from the order of the bulk of the AF grains, the interfacial region will have a significant effect. This was shown when the results of these measurements diverged significantly from the predictions of the York Model of Exchange Bias. In particular, this is highlighted when the interface is doped with an ultra-thin layer of Mn. These films were produced by Seagate Technology at their facility in Northern Ireland.

6.1 Irreversibility of Exchange Bias

6.1.1 Setting and Resetting

Below T_N an antiferromagnetic (AF) grain will be ordered in the sense of having antiparallel sublattices [13]. However, the orientation of the sublattices can change by reversal over an energy barrier. In this sense, it is possible to discuss AF order as the order in the relative orientations of the sublattice directions between grains and thus throughout the film.

In the York Model of Exchange Bias the energy barrier to reverse the magnetic order of an AF grain is given by

$$\Delta E = K_{AF} V_g \quad (6.1)$$

where K_{AF} is the effective AF anisotropy and V_g is the volume of the grain. The reason that K_{AF} is the effective anisotropy is due to the distribution of grain alignments, also known as texture. A polycrystalline film will not have the same magnetocrystalline anisotropy as a single crystal since its constituent grains are not aligned. This is discussed in section 4.2.4.

Since K_{AF} is a function of temperature of the form

$$K_{AF}(T) = K_{AF}(0) \cdot \left(1 - \frac{T}{T_N}\right) \quad (6.2)$$

where T_N is the Néel temperature, the largest grain that can be set at a temperature $T_{set} < T_N$ has a volume of V_{set} . At a lower temperature, V_c is the volume of the smallest grain whose AF orientation is not disordered by thermal energy. Thus the exchange bias H_{ex} is produced by the grains with a volume between V_c and V_{set} [11]. This is shown in fig. 6.1(a) where the grains with volume larger than V_{set} or smaller than V_c do not contribute to exchange bias. At T_{NA} there are no unstable grains because V_c is smaller than any grain in the film. This is shown schematically in fig. 6.1(b). Thus at T_{NA} the order of the AF does not change and there are no changes in H_{ex} .

Since the setting of the AF layer is brought about by thermal activation the degree of order increases as a function of $\ln t$ [11]. As discussed in section 4.2.7, the logarithmic rate of setting is fastest when V_c is closest to the modal grain size since the largest number of grains are being activated. For the samples measured in this study a setting time of 5400 s and a setting temperature of 500 K was sufficient to maximise the exchange bias. Further increases in t_{set} or T_{set} resulted in an increase in H_{ex} smaller than 1 %. Thus setting the film twice in the same direction results in no increase of H_{ex} , in accordance with previous findings [11]. However, setting the film in the opposite direction will reverse the direction of H_{ex} . According to the York Model of Exchange Bias, H_{ex} is determined by the set fraction of the AF film which is in turn determined by the AF grain volume. Thus since the AF grain volume does not change it should be possible in principal to reset the film under the same conditions and achieve the same magnitude of exchange bias in the opposite direction.

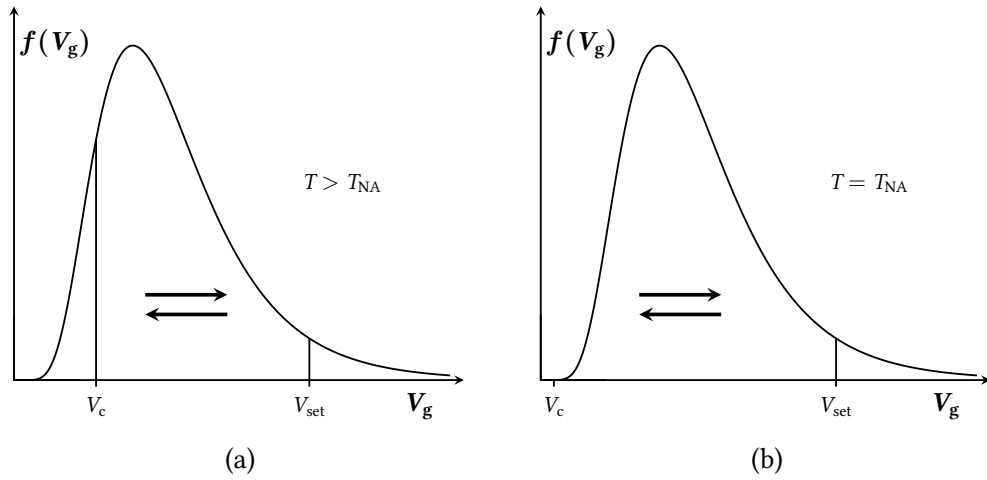


Figure 6.1: The portions of a grain size distribution that contribute to H_{ex} at (a) a temperature greater than T_{NA} and (b) T_{NA} .

A film with composition Si/Ta (2)/Ru (2)/IrMn (10)/Mn (0.05)/CoFe (5)/Ru (5) (thicknesses in nm) was used to investigate the reversibility of the setting procedure. The film structure is shown in fig. 6.2(b). The AF film has a temperature of non-activation T_{NA} of 300 K. The unset film was measured at T_{NA} confirming no initial exchange bias. It was then set in a positive field of $\vec{H}_{\text{set}} = 20\text{kOe}$ at $T_{\text{set}} = 500\text{K}$ for $t_{\text{set}} = 90\text{min}$. The film was cooled to T_{NA} and two loops were measured. These are shown in fig. 6.2(a)(A). The difference between the two loops is the training effect ΔH_{c1} . There were no changes of H_{ex} in subsequent loops, due to the measurements taking place at T_{NA} . The field was applied during both the temperature increase and decrease. The exchange bias value of $(-920 \pm 10)\text{Oe}$ was

measured using the second loop to eliminate the effect of training. The negative sign indicates that the exchange bias has resulted in the loop being shifted to the left. This convention is used for blocking temperature measurements [11].

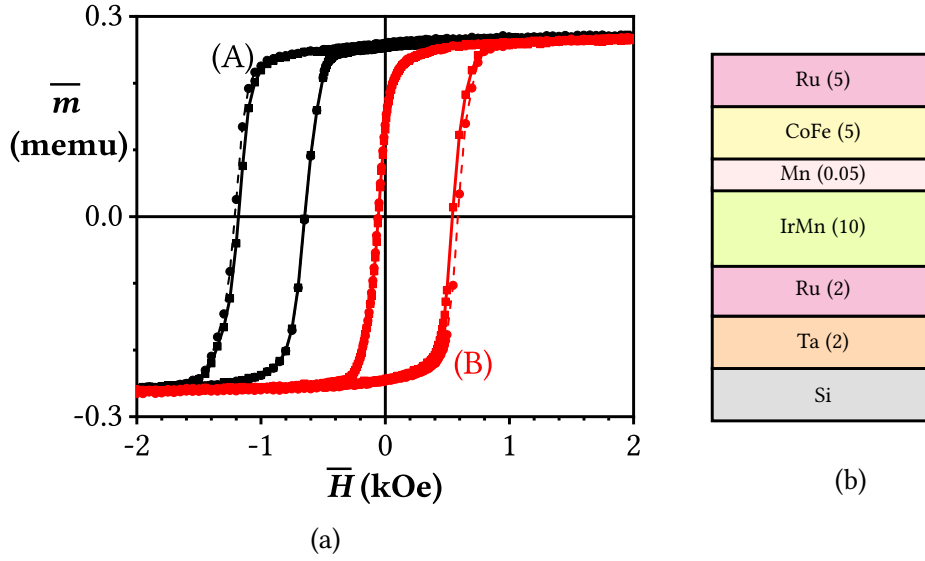


Figure 6.2: (a) An example of irreversible exchange bias for a sample set in (A) 20 kOe and then (B) -20 kOe with (b) structure shown schematically (thicknesses in nm).

The applied field was then changed to $\vec{H}_{\text{act}} = -20$ kOe. This reversed field acts in the opposite direction to the original \vec{H}_{set} . The temperature of the film was increased to $T_{\text{act}} = 500$ K and held there for $t_{\text{act}} = 90$ min, identical to the setting process. The film was then cooled to T_{NA} and two loops were measured starting from negative saturation. These are shown in fig. 6.2(a)(B) showing the training effect.

The resulting exchange bias for the activated loop was (240 ± 10) Oe, where the positive parity indicates the loop is shifted to the right. This exchange bias magnitude is $\approx 25\%$ of the initial value. The initial setting process was not replicated by the second setting process, which implies that some portion of the setting process of the AF layer is irreversible. This correlated with an increase in coercivity. As well as reversing the exchange bias the training effect reappears after the setting process. This training occurs on the first magnetic reversal only. The exchange bias, coercivity and training are shown in table 6.1.

To describe the change in H_{ex} qualitatively, a dimensionless reversibility parameter R_{ex} is defined as

$$R_{\text{ex}} = \frac{H_{\text{ex}}^{\text{A}} - H_{\text{ex}}^{\text{B}}}{2H_{\text{ex}}^{\text{A}}} \quad (6.3)$$

where H_{ex}^{A} is the initial exchange bias and H_{ex}^{B} is the exchange bias after the reversal procedure. Using this definition a film which is fully reversed such that $H_{\text{ex}}^{\text{B}} = -H_{\text{ex}}^{\text{A}}$ has a reversibility of 1, while a film in which the exchange bias does not change during the realignment has a reversibility of 0. This definition excludes grains with size below V_{c} and above V_{set} since they do not contribute to the exchange bias. By definition at $H_{\text{ex}}^{\text{B}} = 0$ the reversibility is 0.5. This reflects that the set grain volume is set in two opposite directions in two equal fractions. Using this definition $R_{\text{ex}} = 0.64$ for the film shown in fig. 6.2 under identical setting conditions.

		fig. 6.2(a)(A)	fig. 6.2(a)(B)	
\vec{H}_{set}	(Oe)	20000	-20000	± 10
H_{ex}	(Oe)	-920	240	± 10
H_{c}	(Oe)	270	300	± 10
ΔH_{c1}	(Oe)	30	40	± 10

Table 6.1: Loop parameters for the loops shown in fig. 6.2 given for (A) a film set in a positive field and (B) the film set in the opposite direction.

A value of R_{ex} lower than 1 indicates that there has been a change between the two setting processes. This change cannot be attributed to the F layer since the setting process is carried out at a field magnitude of 20 kOe. This field is large enough to saturate the F layer in either direction, thus the role of the F layer is the same during both setting processes. During setting the spin order of the AF grains reverses over volume-dependent energy barriers [11]. Thus a reduction in H_{ex} could be explained by an increase in the effective median grain volume, such as by increasing the coupling between AF grains. However, the success of the York Model of Exchange Bias shows that the AF grains do not interact strongly. That said, the possibility exists that they interact through the F layer. In any case, there is no mechanism by which the intergranular coupling could change between the first and second setting process.

The F/AF interface cannot be the source of irreversibility at high temperatures. This is due to the fact that the interface can be reset at temperatures below T_{NA} on a time scale of 1 min. This is shown by the recovery of the training effect which will be discussed in detail in chapter 7.

Since there is no change in the F or AF order the reduction in H_{ex} must be due to an increase in $\langle T_{\text{B}} \rangle$ of the AF grains. Since $\langle V_{\text{g}} \rangle$ does not change, the increase in

$\langle T_B \rangle$ must be due to an increase in K_{AF} . K_{AF} in IrMn can be increased by annealing due to the increasing degree of crystallinity. However, the AF grains are known to be highly crystalline from XRD studies and therefore an increase in crystallinity is unlikely [32, 174].

As shown in fig. 2.11, K_{AF} of IrMn is known to increase as the proportion of Mn increases [53]. The composition and in particular the composition near the interface is known to change during annealing [59]. Thus the increase in K_{AF} could be caused by an enrichment of Mn in the interfacial region due to preferential diffusion of Mn.

At the interface between IrMn and CoFe species can interdiffuse, in particular Co and Mn. This has been shown to have an effect on exchange bias properties [57, 59]. It could also lead to the formation of additional interfacial alloys with distinct magnetic behaviour such as CoMn [63]. This diffusion will be enhanced by heating [59]. Thus the difference between the first and second setting process can be attributed to diffusion that occurs between the two measurements. This hypothesis will be discussed further in section 6.1.4.

6.1.2 Time Dependence of Setting

Magnetic viscosity measurements were carried out to investigate the time dependence of the AF resetting process. The procedure is outlined in section 4.2.7. In a magnetic viscosity measurement the AF film is set in positive field at temperature T_{set} and for time t_{set} . It is then activated in reverse field at an aligning temperature T_{al} for time t_{al} . The sample is periodically cooled to T_{NA} where the exchange bias is measured. Previous work has shown the exchange bias to fully reverse when $T_{al} = T_{set}$ and $t_{al} = t_{set}$ for samples with different structures [11, 38, 91, 152, 185, 186]. However, as discussed in this chapter this is not necessarily the case.

A sample with composition Si/Ta (2)/ Ru (2)/IrMn (10)/CoFe (5)/Ru (5) (thicknesses in nm) was used to investigate the time dependence of the setting procedure. The film structure is shown schematically in fig. 6.3(b). The sample was measured as deposited to confirm no initial exchange bias existed. The sample was then set in a field of $\vec{H}_{set} = 20\text{kOe}$ at a temperature $T_{set} = 500\text{K}$ for $t_{set} = 5400\text{s} = 1.5\text{h}$ and two hysteresis loops were measured. The second measured loop was used to

measure H_{ex} to eliminate the effect of training. This was then followed by alignment in a field of -20 kOe and at $T_{\text{al}} = 500$ K for a period of t_{al} . The cumulative duration of t_{al} was 92×10^3 s. At intervals the film was cooled to T_{NA} and two hysteresis loops were measured. The results show a rapid transition to positive H_{ex} at small values of t_{al} , followed by slower changes at high values of t_{al} . The same measurement is shown on a $\ln t_{\text{al}}$ axis in fig. 6.5(a). The logarithmic form of this behaviour is in accordance with previous measurements as shown by the logarithmic rate of setting in fig. 4.13 [11].

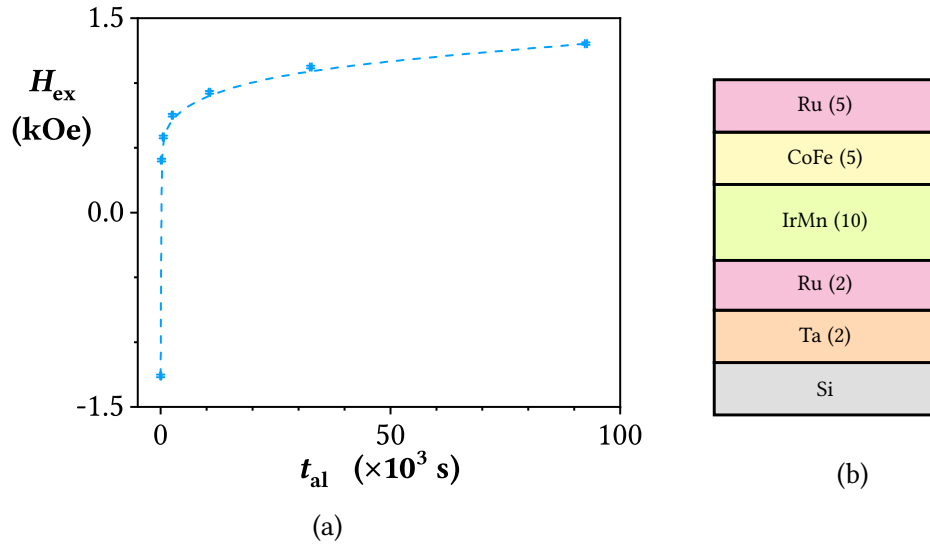


Figure 6.3: (a) The time dependence of H_{ex} for a film with (b) structure shown schematically. The line is a guide to the eye.

A rapid reversal followed by a slow reversal can be understood with reference to the grain volume distribution shown in fig. 6.4. The reversal process is the excitation of the spin order of the AF grains over a volume-dependent energy barrier to reversal [11]. Thus the smallest grain will reverse on the shortest timescales and the largest will reverse on the longest timescales. In fig. 6.4 the integrated area between lines (a) and (b) represent the film volume that is reversed at $t_{\text{al}} \ll t_{\text{set}}$. Since the activation is affecting grains near the median volume, the activation results in a very rapid reversal of H_{ex} . In fig. 6.4 the lines (c) and (d) show the positions on the grain volume distribution that are activated at $t_{\text{al}} \approx t_{\text{set}}$. The separation between lines (c) and (d) is the same as that between (a) and (b). Due to the form of the grain volume distribution between (c) and (d) the integral of the grain volume distribution between (c) and (d) is less than that between (a) and (b). This is the cause of the relatively slow changes in H_{ex} shown in fig. 6.3 as t_{al} approaches t_{set} .

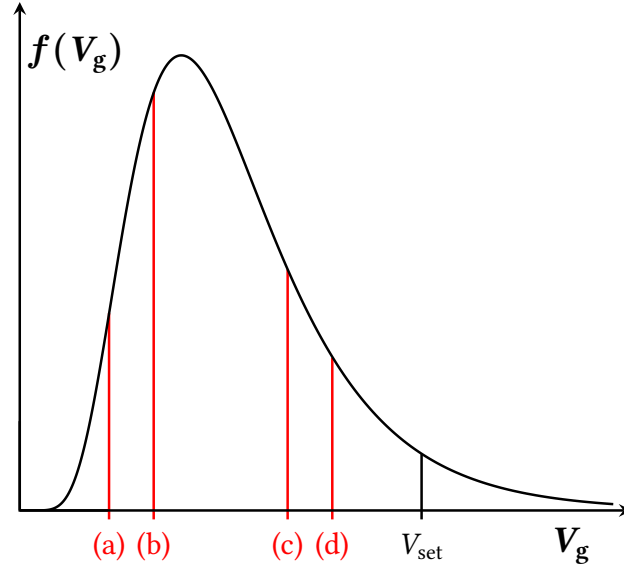


Figure 6.4: In a magnetic viscosity measurement the grains between (a) and (b) activate earlier than the grains between (c) and (d), resulting in a rapid change in H_{ex} followed by a slow change.

After setting, the initial H_{ex} of this film was (-1260 ± 10) Oe where the negative sign indicates a hysteresis loop shift to the negative field. At $t_{\text{al}} = t_{\text{act}}$ the exchange bias had a value of (880 ± 10) Oe, which is approximately two thirds of the magnitude of the initial exchange bias. The measurement was continued until $t_{\text{al}} = 92 \times 10^3$ s, which is equal to 25.5 h and exceeds t_{set} by a factor of ~ 17 . In addition the aligning field and aligning temperature were kept constant and equal to the setting field and setting temperature. Despite this, the maximum positive exchange bias was measured at $t_{\text{al}} = 92 \times 10^3$ s to be (1303 ± 10) Oe. This is larger than the original value of exchange bias by $\approx 3\%$. Thus the positive H_{ex} did not equal the initial, negative exchange bias until $t_{\text{al}} = 17t_{\text{set}}$, at which point the AF layer was fully reversed. The definition of reversibility from eq. (6.3), reproduced here, is

$$R_{\text{ex}} = \frac{H_{\text{ex}}^{\text{A}} - H_{\text{ex}}^{\text{B}}}{2H_{\text{ex}}^{\text{A}}} \quad (6.4)$$

where H_{ex}^{B} is the value of the exchange bias at $t_{\text{al}} = t_{\text{set}}$. Using eq. (6.4) the reversibility of the film shown in fig. 6.3 is 0.85. This is lower than the reversibility approaching 1 that has been previously observed [11, 38, 91, 152, 185, 186].

The magnitude of exchange bias achievable the first time a film is set is greater than that achievable with a subsequent setting in an opposite field. This is clearly demonstrated by experiments where the same field magnitude but opposite field direction is used, in conjunction with the same temperature treatment. By cool-

ing the film to T_{NA} the magnetic order of the AF grains is frozen after the first magnetic reversal. Hysteresis loop measurements at T_{NA} are therefore a snapshot of the spin order of the bulk of the AF grains [11]. In the aligning process the same field magnitude and temperature are used as during the setting process. The measurement demonstrates that the majority of the aligning process is complete at $t_{al} < t_{set}$. Further activation has a much smaller effect on the magnitude of H_{ex} . The different behaviour during and after the initial setting process is evidence of an irreversible process. Subsequent settings are therefore not in the same condition as the initial setting and because of this result in a lower value of H_{ex} . To understand this, the parameter that has changed must be identified.

6.1.3 Origin of Magnetic Irreversibility

According to the York Model of Exchange Bias the exchange bias of a set system is given by

$$H_{ex}(\vec{H}_{set}, T_{set}) = H_{ex}^{INT} C^* (\vec{H}_{set}, T_{set}) \int_{V_c(T_{NA})}^{V_{set}(T_{set})} f(V_g) dV_g \quad (6.5)$$

where H_{ex}^{INT} is the intrinsic exchange bias, C^* is the interfacial coupling parameter, V_c is the volume of the smallest stable grain at T_{NA} , V_{set} is the volume of the largest AF grain the could be set at T_{set} and $f(V_g)$ is the AF grain volume distribution. H_{ex}^{INT} is a constant of proportionality that represents a film set under hypothetical ideal conditions such that the whole grain size distribution contributes to the exchange bias. These conditions would be $T_{set} \geq T_N$ so that the largest grains can be set during the setting process and $T \leq T_{NA}$ so that the smallest grains are stable during the measurement.

The crystallographic order of an IrMn thin film has been observed to increase over time resulting in an increase in exchange bias [173]. However, in that study the development of crystallographic order began immediately and was completed on a timescale of around a month. This occurred in amorphous films in which a crystallographic order was nucleated and propagated. The crystallographic changes were also accompanied by a change in the loop shape and resulted in a single-crystal film. On the other hand, the measurements shown in fig. 6.2 were taken within hours of each other and on the order of years after the films were produced.

There was also no change in the X-ray diffractometer (XRD) spectra which indicates that the film remained polycrystalline. Thus changes in $f(V_g)$ can be ruled out.

As discussed in section 4.2.6, the volume condition for stability at a temperature T is given by

$$V_g(T) = \frac{\ln(t f_0) k_B T}{K_{AF}(T)} \quad (6.6)$$

where t is the measurement time, f_0 is the attempt frequency, k_B is Boltzmann's constant and $K_{AF}(T)$ is the AF anisotropy [11]. When evaluated at T_{set} eq. (6.6) gives the volume of smallest unset grain V_{set} , while when evaluated at T_{NA} it gives the volume of the largest thermally unstable grain V_c . The film in fig. 6.2 was set a T_{set} . Thus every AF grain with a volume less than V_{set} was aligned. During the resetting process the same conditions were used $T_{al} = T_{set}$ and $t_{al} = t_{set}$, and thus the same grains with a volume up to $V_{set} = V_{al}$ was reset. By the same reasoning the measurements were performed at T_{NA} , meaning that every grain with a volume larger than V_c was thermally stable. Since neither T_{NA} or t were different between measurements the same grains were unstable in both measurements. Thus changes in V_{set} and V_c can be ruled out as the causes of the change in H_{ex} .

Interactions between AF grains are negligible due to a number of factors which were outlined in section 2.1.2 and section 4.2.4. On the other hand, the ferromagnetic grains are coupled to each other by the RKKY interaction and by direct exchange. This means that there is a possibility that the AF grains can be indirectly coupled by coupling to the F layer, which is itself coupled to another AF grain. However, the applicability of the York Model of Exchange Bias is itself evidence that coupling between AF grains does not occur to a significant degree, since the York Model of Exchange Bias correlates the value of H_{ex} to the measured grain volumes [11].

The independence of AF grains therefore almost excludes the possibility that the AF grains are acting cooperatively. The small median diameter of the grains $\langle D_g \rangle = (7.3 \pm 0.2)$ nm implies that the AF grains are reversing by domain rotation only, and not by grain nucleation and domain wall motion. Thus V_c , V_{set} and $f(V_g)$ are not the sources of the change in H_{ex} . The value of H_{ex}^{INT} is the theoretical maximum exchange bias for a given grain size distribution. Since the grain size distribution does not change then H_{ex}^{INT} is constant.

In chapter 7 it will be shown that the interface can be reversed at temperatures below $T_{NA} = 300$ K. A setting temperature of 500 K was used for the measurements shown in fig. 6.3. Therefore C^* and the magnetic order of interfacial spin clusters are not the source of irreversibility.

In section 4.3 the role of interfaces in the York Model of Exchange Bias was discussed. Spin clusters are proposed as interfacial spins coupled into clusters with a size similar to the grain diameter distribution [11, 37, 67, 91]. The internal F order of the spin clusters is principally maintained by direct exchange and RKKY exchange cannot be excluded. The spin clusters are coupled to the F and AF regions directly above and below by direct exchange. The spin clusters are coupled to each other by RKKY exchange and indirectly through their coupling to the F layer. In addition there may exist significant dipole-dipole interactions between spin clusters. The F order that exists between the spin clusters is demonstrated by the \vec{H}_{set} dependence of H_{ex} [11, 91].

It is worth highlighting the different forms of magnetic order that occur in F and AF films. Below T_C a F material will have internal order due to the positive exchange integral. However, this order will not extend through the whole F material and it will be subdivided into magnetic domains. By applying a saturating field the F material can be ordered such that there is only one domain, or equivalently that the domains are indistinguishable since they have the same magnetisation direction. When the saturating field is removed the spin order of the material will tend to divide into domains again due to the influence of the demagnetising field. In the ideal case the F material will have no net magnetic order. However, below T_C the internal F order of the domains will be retained.

Likewise for the AF material there are two kinds of magnetic order. The first is the antiparallel alignment of sublattices in the AF which will exist below T_N . In the IrMn thin films used in the work this order will have the same size as the AF grain size [11]. The second is the order that exists between grains which is a result of the thermal activation process described in section 4.2. By the same reasoning there will be two kinds of magnetic order in the spin clusters. Spin clusters will have an internal F order due to direct and indirect exchange. In addition spin clusters will have relative order between adjacent spin clusters which is mediated by RKKY exchange and indirectly through the F layer as well as dipole-dipole interactions.

During deposition, the film is not subject to a saturating magnetic field. Thus the F material is in a multi-domain state and there is no intergranular order in the AF layer. Likewise, the spin clusters are disordered relative to each other. However, there is a possibility that the AF grains can be set if the energy from the sputtering process is sufficient to overcome the energy barriers to reversal. This process would be analogous to print-through, which was a phenomena in magnetic tape recording in which magnetic patterns transfer between portions of tape in contact. However, this phenomena will not be significant after the film is set.

During the setting process the F layer is aligned to the external field and the magnetisation of the AF sublattices align to parallel and antiparallel to the F layer due to direct exchange. Between these layers the spin clusters are also ordered. Once in this ordered state, the cluster-cluster RKKY and dipole-dipole interactions will tend to maintain this alignment. This is because each spin cluster is surrounded by neighbouring spin clusters with the same alignment and coupled to the F layer.

During the realigning process, the F layer will align with the reversed external field. Due to the magnitude of the applied field of 20 kOe it is probable that the spin clusters will be reversed during the aligning process. This tendency to reverse will be enhanced by the reversal of the F layer because of the directed exchange coupling between the F layer and the spin clusters. On the other hand the tendency to reverse will be opposed by the coupling of the spin clusters to the AF layer until the adjacent AF grain reverses. However, the majority of the AF layer is reversed at $t_{al} = t_{act}$ as shown in fig. 6.3(a). Therefore the effect of spin clusters on the aligning process is expected to be low.

6.1.4 Origin of Compositional Irreversibility

As well as discussing the irreversibility of H_{ex} in magnetic terms, the direct effects of heating can also be considered. As discussed in section 2.3.3 and section 3.3.4 there is no clear interface between CoFe and IrMn. This is due to the interdiffusion of the atomic species between the two layers [59]. This results in the interfacial region being composed of a number of phases with varied composition which themselves exist in a number of magnetic phases [63].

During the measurement shown in fig. 6.3, the film was held at 500 K for over 24 h. At higher temperatures the tendency for atomic species near the interface to diffuse will be increased [59, 97, 103–105]. If diffusion is occurring then the composition of the layers will be changing. As shown in fig. 2.11, the anisotropy of IrMn is known to increase as the Mn concentration increases [53]. Thus diffusion can directly influence the energy barrier to reversal of the AF grains. This will also effect $\langle T_B \rangle$ as will be discussed in section 6.2.3.

The time dependence of H_{ex} is shown on a linear axis in fig. 6.3. It is shown in fig. 6.5(a) on a logarithmic axis. The coercivities H_c of the same hysteresis loops are shown in fig. 6.5(b). Note that the errors in t_{al} appear to get smaller as t_{al} increases. This is a consequence of the logarithmic scale. In fact the errors increase in magnitude as t_{al} increases. This is because t_{al} is cumulative and therefore the error in t_{al} is also cumulative. It is known that the time dependence of AF setting is proportional to $\ln t_{\text{al}}$ [11]. This was discussed in section 4.2.7. The effect of the alignment process on the coercivity is shown in fig. 6.5(b).

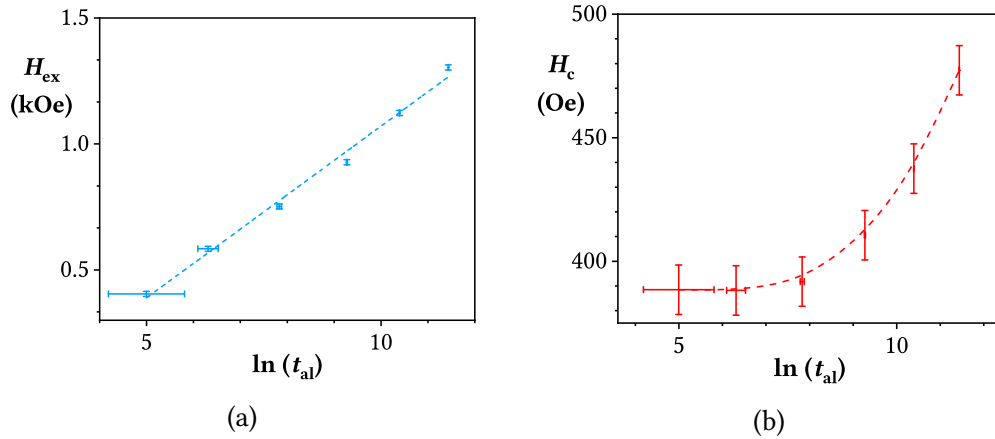


Figure 6.5: The time dependence of (a) H_{ex} and (b) H_c plotted on logarithmic axes. The lines are guides to the eye. Note that the error in t_{al} appears to decrease in size due to the logarithmic scale but in fact is cumulative and therefore increases with t_{al} . The film structure is shown schematically in fig. 6.3(b).

As shown in eq. (3.1) and eq. (3.2), reproduced here

$$H_{\text{ex}} = -\frac{H_{\text{c2}} + H_{\text{c1}}}{2} \quad (6.7)$$

$$H_c = \frac{H_{\text{c2}} - H_{\text{c1}}}{2}$$

exchange bias and coercivity are both calculated from the same points on the hysteresis loop. Diffusion in exchange bias thin films has been shown to correlate

with an increase in H_c [59]. Thus it can be hypothesised that at high temperature diffusion takes place in the film. This results in an intermixing of material at the F/AF interface which results in a phase change. This acts to increase the interfacial stiffness and so causes H_c to increase. This increased interfacial stiffness reduces the interfacial coupling and therefore to get the same value of H_{ex} in the opposite direction requires an aligning time that is longer than the initial setting time.

This diffusion is driven by the heat applied to the film. Thus it is irreversible, which corresponds to the irreversibility of the exchange bias. In fact, applying heat for longer will tend to reduce H_{ex} due to ongoing diffusion [59]. If diffusion is a significant factor in these samples then the final value of H_{ex} can be hypothesised to be the result of two counteracting thermal mechanisms. The first is the increase in exchange bias caused by the setting of the spin order of the bulk of the AF grains by thermal activation over volume-dependent energy barriers through the exchange interaction with a F material, as described in the York Model of Exchange Bias and section 4.2 [11]. The second is the diffusion of atomic species in the interfacial region resulting in an increasing tendency towards AF magnetic phases, resulting in a reduction of H_{ex} [59]. This hypothesis will be discussed further in section 7.2.3.

Both H_{ex} and H_c are shown to increase. However, the magnitude of this increase is not equal. In the range $148\text{ s} < t_{al} < 92 \times 10^3\text{ s}$ shown in fig. 6.5 the exchange bias increases from $(400 \pm 10)\text{ Oe}$ to $(1300 \pm 10)\text{ Oe}$ which is a factor of 3.3. In the same range of t_{al} , the coercivity increases from $(350 \pm 10)\text{ Oe}$ to $(480 \pm 10)\text{ Oe}$ which is a factor of 1.4. In addition the rate of change of H_{ex} in this range is proportional to $\ln t_{al}$ whereas H_c is constant up to $t_{al} = (2500 \pm 200)\text{ s}$ and thereafter deviates from linear. The difference in the rate of change of H_{ex} and H_c suggests that they arise from different sources. It is known that H_{ex} or H_c can be changed without affecting the other, which implies they do not have an identical origin [187]. H_{ex} has been shown to be strongly dependent on the order of the bulk of the AF grains and can be modified by the interfacial order [188]. On the other hand, H_c has been shown to be strongly dependent on the interfacial order and not strongly dependent on the bulk order [73]. Thus the large proportional increase in H_{ex} and smaller change in H_c indicates that the origin of irreversibility is in the AF bulk.

The films were held at $T_{al} = 500\text{ K}$ for a cumulative duration of $t_{al} + t_{set}$ which is equal to $(97.4 \pm 0.3) \times 10^3\text{ s} = 27\text{ h}$. This thermal annealing procedure, while not

carried out at sufficient temperature to increase the grain size distribution, could be high enough to improve the crystallinity of the IrMn grains. This increasing crystallographic order would lead to an increase in the effective anisotropy K_{AF} and thus an increase in the energy barrier to reversal for an AF grain ΔE as a consequence of eq. (6.1), reproduced here

$$\Delta E = K_{AF} V_g \quad (6.8)$$

where V_g is the grain volume [11]. Note that this is not the same as an increase in intergranular order which would be a change in the film texture. However, the origin of anisotropy in IrMn is not yet fully understood. In addition, an increase in crystallographic order is likely to be accompanied by an increase in chemical order, which is known to decrease IrMn anisotropy [42, 52, 53].

It is the case that annealing the film will stimulate diffusion in the film bulk. This is shown in fig. 3.10(b) and fig. 3.12(b) for a Co/IrMn film heated to 673 K [59]. In that film the Mn ions readily diffused out of the IrMn layer and into the Co layer. This preferential diffusion of Mn will decrease the relative proportion of Mn in the AF layer. It is known that the anisotropy of IrMn decreases as the Ir concentration increases. This is shown in fig. 2.11 [53]. For this reason preferential diffusion of Mn out of the AF bulk would result in an increase in K_{AF} for each AF grain and therefore an increase in $f(\Delta E)$. This change in the energy barrier distribution would reduce the reversibility of the film.

The potential origins of H_{ex} irreversibility can therefore be summarised as

1. Increase in the grain volume distribution $f(V_g)$ due to grain growth or indirect coupling through the F layer [11].
2. Decrease in the interfacial coupling parameter C^* due to disordered interfacial spin clusters [67].
3. Decrease in internal order of spin clusters due to diffusion of Mn into the interface resulting from a phase change from F to AF order.
4. Increase in K_{AF} due to annealing which results in an improvement in the crystallinity of the AF grain bulk.
5. Increase in K_{AF} due to a decrease in relative Ir concentration in the AF bulk driven by diffusion [53, 59].

Possibility 1 depends on a change in V_g or a change in the the effective grain volume due to indirect coupling through the F layer. However, the annealing temperature 500 K is too low to result in grain growth and the success of the York Model of Exchange Bias in predicting the logarithmic rate of setting of an exchange bias film which is dependent on $f(V_g)$ almost excludes the possibility of AF grains interacting indirectly through the AF layer [11].

Possibilities 2 and 3 can be excluded because in chapter 7 the training effect and therefore the interfacial spin order is shown to be recovered at temperatures below T_{NA} and on a time scale of 1 min. This demonstrates that interfacial spin clusters cannot be blocked at 500 K. In addition, these possibilities affect the F/AF interface more than the bulk. This contradicts the measurements shown in fig. 6.5 because it is known that H_c is more sensitive to changes in the interface than H_{ex} [73, 188].

The effect of crystallinity described in possibility 4 is likely to be small due a corresponding increase in chemical order in IrMn which is known to decrease K_{AF} [42, 52, 53]. In addition the crystallinity of IrMn grains is known to be high and therefore increases in crystallinity are unlikely [32, 174].

Therefore the most likely possibility is 5. The effects of diffusion will be discussed further in section 6.2. Interfacial stiffness and spin clusters will be discussed in chapter 7.

6.2 Thermal Activation

6.2.1 Blocking Temperature for Films with Manganese-Doped Interfaces

A York Protocol blocking curve measures the progressive thermal activation of the grains of an AF film as it is heated to a series of activation temperatures T_{act} . The procedure is outlined in section 4.2.3 and in fig. 4.7. In a blocking curve a film is set in a positive field at temperature T_{set} and for time t_{set} . The exchange bias of the film is measured by taking two hysteresis loops at T_{NA} . Due to the training effect discussed in section 3.2.2, the exchange bias changes between the first and second

magnetisation reversal. For this reason H_{ex} is measured from the second hysteresis loop. The AF grains are then progressively thermally activated by heating them to a temperature T_{act} in a reverse field. The film is held at T_{act} in reverse field for an activation time t_{act} . It is then cooled to T_{NA} and the exchange bias H_{ex} is measured. Two hysteresis loops are measured to account for the training effect.

The blocking curve was performed for films with composition Si/Ta (2)/Ru (2)/IrMn (10)/Mn (d_{Mn})/CoFe (5)/Ru (5) (thicknesses in nm) where d_{Mn} is the thickness of a Mn layer at the F/AF interface. The film structure is shown schematically in fig. 6.6(b). For this blocking curve T_{NA} was taken to be 300 K.

When d_{Mn} is smaller than $\approx (0.140 \pm 0.005)$ nm, the atomic radius of Mn, the ultra-thin layer is in effect an alteration of the composition near the interface [189]. This additional Mn will act to replace Mn lost by diffusion. The median grain size of the films was $\langle V_{\text{g}} \rangle = (420 \pm 10) \text{ nm}^3$ measured using TEM images as was discussed in section 5.2.2. The film was set in $\vec{H}_{\text{set}} = 20 \text{ kOe}$ at $T_{\text{set}} = 560 \text{ K}$ for $t_{\text{set}} = 5400 \text{ s}$. Temperatures every 20 K between 300 and 560 K were used for T_{act} . The activation field was -20 kOe and the activation time was kept constant at $t_{\text{act}} = 1800 \text{ s}$. This activation time was chosen because of the $\ln t$ dependence of the AF order. The blocking curves for these films is shown in fig. 6.6(a).

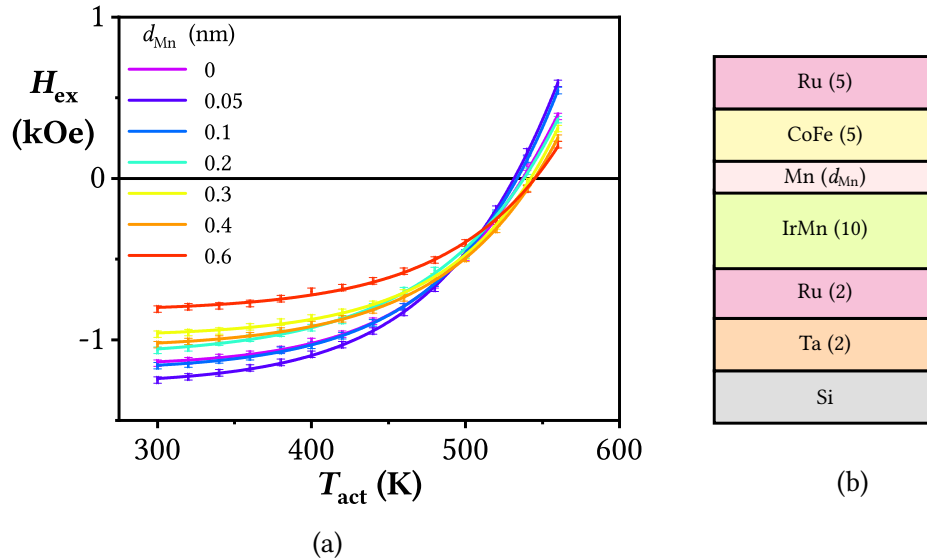


Figure 6.6: (a) York Protocol blocking curves for films with (b) structure shown schematically (thicknesses in nm).

The blocking curves show the films with negative exchange bias after setting, which here indicates that the hysteresis loops were shifted to the left. The change in H_{ex} is small for $T_{\text{act}} \leq 320 \text{ K}$. This confirms that a T_{NA} of 300 K was appropriate.

H_{ex} changes rapidly at higher temperatures indicating the thermal activation of the AF layer. The change is rapid since the portion of the grain size distribution being activated is close to the median grain volume. The final H_{ex} is positive meaning that the loops are shifted to the right.

The final value of H_{ex} is in the positive direction and its magnitude is significantly smaller than the initial value. Therefore the exchange bias is not fully reversed. For $d_{\text{Mn}} = 0 \text{ nm}$ the initial exchange bias was $(-1160 \pm 10) \text{ Oe}$ while the final exchange bias was $(390 \pm 10) \text{ Oe}$. The initial exchange bias of the films varies with d_{Mn} . This will be discussed in section 6.2.2. d_{Mn} also had an effect on $\langle T_{\text{B}} \rangle$, which will be discussed in section 6.2.3.

6.2.2 Effect of Interfacial Mn on Maximum Exchange Bias

The effect of d_{Mn} on H_{ex} is shown in fig. 6.7. Here the y-axis is $-H_{\text{ex}}$ for clarity. The initial exchange bias peaked at $d_{\text{Mn}} = 0.05 \text{ nm}$, reaching $(-1260 \pm 10) \text{ Oe}$ which is $(100 \pm 10) \text{ Oe}$ greater in magnitude than the exchange bias of the un-doped interface. When $d_{\text{Mn}} \geq 0.2 \text{ nm}$ the exchange bias is reduced compared to the un-doped case. A layer of Mn at the F/AF interface is correlated with a peak in the exchange bias and exchange anisotropy followed by an overall reduction above a critical d_{Mn} [91, 92]. However, previously published results show the peak occurring at $d_{\text{Mn}} = 0.3$ or 0.5 nm respectively. This implies more than one atomic layer of Mn, unlike the measurements shown in fig. 6.7 which show the peak occurring at values of d_{Mn} less than the atomic radius of Mn [189].

In fig. 6.7 a curve to guide the eye is shown that excludes the H_{ex} measured for the $d_{\text{Mn}} = 0.4 \text{ nm}$ sample. This does not change the broad observation that H_{ex} is higher for $d_{\text{Mn}} = 0 \text{ nm}$ than $d_{\text{Mn}} \geq 0.2 \text{ nm}$, or that there is a peak in H_{ex} at $d_{\text{Mn}} = 0.05 \text{ nm}$. However, it does reveal a smooth decline in H_{ex} for $0.05 \text{ nm} \leq d_{\text{Mn}} \leq 0.6 \text{ nm}$. There are two reasons to doubt the validity of the measurement of d_{Mn} at 0.4 nm . The first is that the measurement of d_{Mn} is based on the measurement of the mass accumulated during deposition. However, the distribution of that mass is not measured, so there is a possibility that the Mn layer can be either continuous or distributed in discontinuous regions. Secondly, the sample measured was cleaved from a larger wafer. This means the result could be due to a macroscopic variation in the composition of the film in the region that was measured.

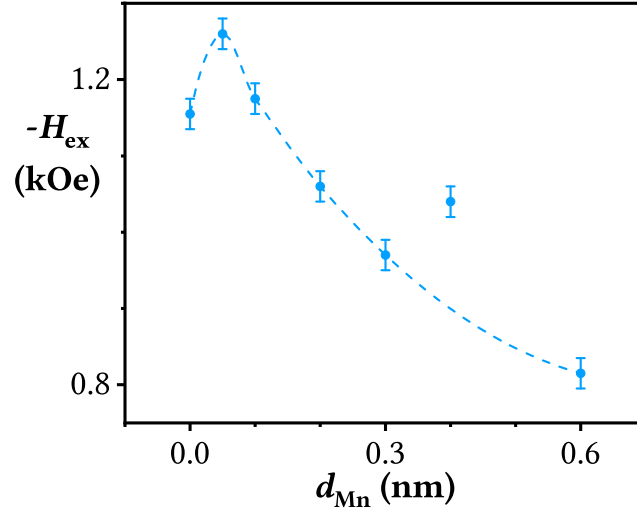


Figure 6.7: The exchange bias of films with interfacial Mn layers. The curve is a guide to the eye. The film structure is shown schematically in fig. 6.6(b).

There are a number of possible explanations for the dependence of H_{ex} on d_{Mn} . The first is the hypothesis postulated by Tsunoda in which the Mn layer changes the magnetic structure of the interface [92]. Structural change in the F layer or bulk of the AF grains was discounted since the XRD spectra did not change as interfacial Mn layers are inserted. The study proposed that the Mn formed a two-monolayer epitaxial layer above the IrMn_3 bulk AF. However, this structure would be susceptible to diffusion since Mn is soluble in IrMn and CoFe [57, 59]. This was investigated in a study by Carpenter [91]. In this study the films were thermally annealed, but this did not eliminate the enhancement of H_{ex} . This implies that the Mn does not form a distinct interfacial layer which can be subsequently destroyed by interdiffusion. The study proposed that the enhancement in H_{ex} was due to changes in the spin clusters. In particular, ΔH_{c1} increased with d_{Mn} . This was attributed to the clusters increasing in size with the addition of interfacial Mn.

Alternatively, the Mn could be diffusing into the IrMn layer. An increase in Mn concentration is correlated with an increase in K_{AF} as shown in fig. 2.11 [53]. This was discussed in detail in section 3.3.4 and 6.1.4. This increase in the AF anisotropy would result in a smaller value of V_{c} and V_{set} . Above T_{NA} this will result in an overall increase in the set volume of the film as a consequence of the lognormal grain size distribution because $f(V_{\text{g}})$ changes more rapidly in the region of V_{c} than V_{set} . However, the measurements all occur below T_{NA} and therefore V_{c} is smaller than any grain [11]. Therefore the effect of increasing K_{AF} will decrease the set fraction of the film by decreasing V_{set} while the change in V_{c} will not have a significant effect. This decrease in the set fraction of the film will therefore decrease H_{ex} .

However, this monotonic decrease cannot account for the peak in H_{ex} shown in fig. 6.7 unless combined with other effects.

A further hypothesis can be suggested based on the inter-diffusivity of the materials in a IrMn/Mn/CoFe interface [57, 59]. The magnetic behaviour of CoMn was investigated between 0 and 50 at.% Mn by Men'shikov [63]. In their pure form, Co is a F material while Mn is an AF material. When alloyed, the materials display a range of magnetic behaviour dependent on the ratio of the components and the temperature. The magnetic phase diagram is shown in fig. 6.8 [63]. This is relevant due to the diverse alloys that exist at the IrMn/Mn/CoFe interface, which will each exist in a range of compositions. The composition of CoMn will vary from near the CoFe layer where Co will dominate to near the IrMn layer where Mn will dominate [59]. The transition of CoMn from F to AF occurs as the concentration of Mn increases from 0 to 50 at.%. This will develop as a function of depth through the film layers.

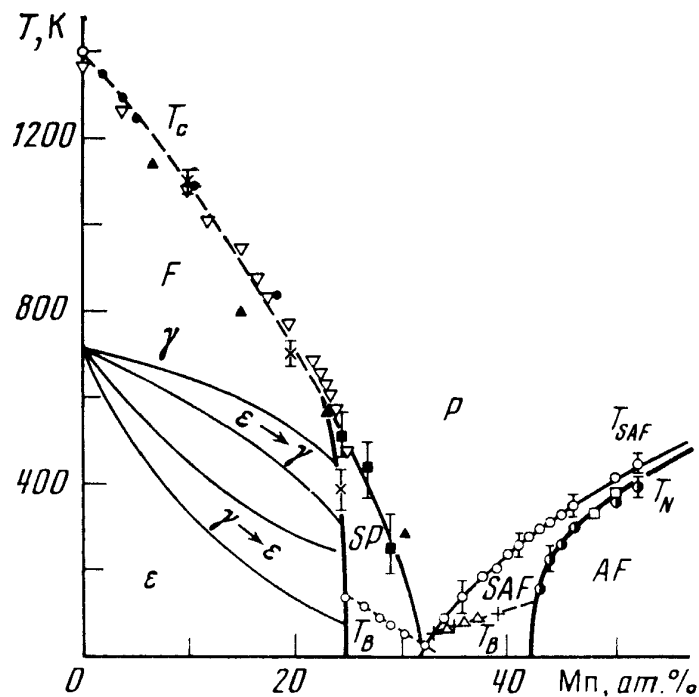


Figure 6.8: The magnetic phase diagram of CoMn alloys. CoMn exhibits diverse magnetic behaviour dependent on T and the Mn concentration [63].

In general, this will be representative of a trend from the F region where F alloys will be dominant to the AF region where AF materials will be dominant. Between these two regions there will be a mixture of paramagnetic particles as well as clusters that have internal F or AF order. In this hypothesis both F and

AF spin clusters are proposed, distributed in a matrix of weakly-coupled particles with spin-glass-like properties. The addition of d_{Mn} changes the amount and distribution of these components, which alters the exchange bias properties of the film. The peak in H_{ex} when d_{Mn} is less than the atomic diameter of Mn suggests that the interfacial composition is a significant factor in exchange bias. This will be discussed further in section 7.2.3.

Since the Mn does not form a distinct layer, it can instead be modelled as an addition to the IrMn layer. The Mn layers measured had a maximum nominal thickness of $d_{\text{Mn}} = 0.6$ nm. Added to the 10 nm IrMn layer this represents an increase in the AF layer thickness of 6%. Since the AF grains are modelled as cylinders it follows that there is a grain volume increase of 6%. This would correspond to an increase in the median blocking temperature [11].

6.2.3 Effect of Interfacial Mn on the Median Blocking Temperature and Anisotropy

The blocking curves shown in fig. 6.6 show that d_{Mn} has an effect on $\langle T_{\text{B}} \rangle$. This trend is the opposite of the trend for H_{ex} , such that the films with the largest H_{ex} at 300 K have the lowest value of $\langle T_{\text{B}} \rangle$. This is shown in fig. 6.9. The correspondence of this result to fig. 6.7 justifies the exclusion of the measurement of H_{ex} at $d_{\text{Mn}} = 0.4$ nm. In accordance with the York Model of Exchange Bias the origin of $\langle T_{\text{B}} \rangle$ is in the grain volume distribution and the AF anisotropy. $\langle T_{\text{B}} \rangle$ is given by eq. (4.26), reproduced here

$$\langle T_{\text{B}} \rangle = \frac{K_{\text{AF}}(\langle T_{\text{B}} \rangle) \langle V_{\text{g}} \rangle}{k_{\text{B}} \ln(t_{\text{act}} f_0)} \quad (6.9)$$

where $K_{\text{AF}}(\langle T_{\text{B}} \rangle)$ is the AF anisotropy at $\langle T_{\text{B}} \rangle$, $\langle V_{\text{g}} \rangle$ is the median grain size, k_{B} is the Boltzmann constant, t_{act} is the time the film was activated at $\langle T_{\text{B}} \rangle$ and f_0 is the attempt frequency. Since the films have the same median grain volume and received the same magnetic and thermal treatment, the changes seen in fig. 6.9 are due to changes in K_{AF} . The effective anisotropy of the AF layer can be evaluated at $\langle T_{\text{B}} \rangle$ when $\langle V_{\text{g}} \rangle$ is known, hence

$$K_{\text{AF}}(\langle T_{\text{B}} \rangle) = \frac{\ln(t_{\text{act}} f_0)}{\langle V_{\text{g}} \rangle} k_{\text{B}} \langle T_{\text{B}} \rangle \quad (6.10)$$

where t_{act} is 1800 s, f_0 has a value of $(2.1 \pm 0.4) \times 10^{12}/\text{s}$, $\langle V_g \rangle$ is $(420 \pm 10) \text{ nm}^3$ for all films and k_B has a value of $1.381 \times 10^{-16} \text{ erg/K}$ in cgs units [11, 146]. This anisotropy calculation gives the effective anisotropy, which is modified by the texture of the sample.

To compare the films to each other the anisotropy at room temperature must be calculated. The temperature dependence of the anisotropy is given by eq. (6.2), reproduced here

$$K_{\text{AF}}(T) = K_{\text{AF}}(0) \cdot \left(1 - \frac{T}{T_{\text{N}}}\right) \quad (6.11)$$

where T_{N} is the Néel temperature. If room temperature is $T_{295} = 295 \text{ K}$ then it can be shown that eq. (6.11) can be expressed as

$$K_{\text{AF}}(T_{295}) = K_{\text{AF}}(\langle T_{\text{B}} \rangle) \cdot \frac{T_{\text{N}} - T_{295}}{T_{\text{N}} - \langle T_{\text{B}} \rangle} \quad (6.12)$$

by dividing the expression for $K_{\text{AF}}(T_{295})$ by the expression for $K_{\text{AF}}(\langle T_{\text{B}} \rangle)$. The IrMn bulk value of $T_{\text{N}} = 690 \text{ K}$ was used to calculate the anisotropy [4, 13]. The anisotropy and other measured parameters are shown in table 6.2. The error in K_{AF} is dominated by the error in the attempt frequency of the AF grains which is $f_0 = (2.1 \pm 0.4) \times 10^{12}/\text{s}$ [146]. Since f_0 is the same for all the films the error in K_{AF} is systematic. Therefore the error represents a numerical inaccuracy. However, comparatively the value of K_{AF} changes and that trend is not affected by the systematic error.

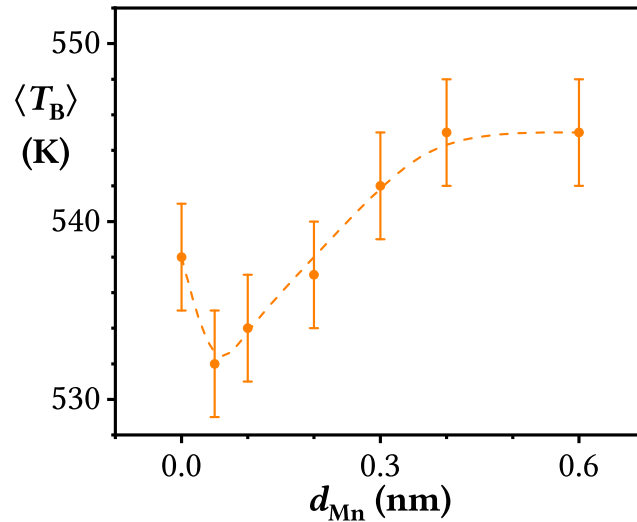


Figure 6.9: The median blocking temperature of films with interfacial Mn layers. The line is a guide to the eye. The film structure is shown schematically in fig. 6.6(b).

The calculated values of K_{AF} are comparable to other fully set IrMn/CoFe systems with in-plane easy axis texture [11, 32, 91]. K_{AF} is the same within error for all the measured films. However, some general trends can be identified. The highest value of H_{ex} was observed for the film with an interfacial layer of Mn of thickness $d_{Mn} = 0.05$ nm. This coincided with the lowest $\langle T_B \rangle$ and K_{AF} . The reversibility R_{ex} of the exchange bias was also calculated and is shown in table 6.2. R_{ex} is defined in eq. (6.3) and was calculated using the value of the exchange bias at setting H_{ex}^A and after activation at $T_{act} = T_{set}$ which is H_{ex}^B . The training effect was removed by measuring the second magnetisation loop. R_{ex} was highest for $d_{Mn} = 0.05$ nm, meaning the fraction of the set portion of the film that was reversed was larger than for any other film. The film that exhibited the highest anisotropy and blocking temperature and the lowest exchange bias and reversibility was the film with an interfacial Mn layer $d_{Mn} = 0.6$ nm, the thickest measured. In all cases, the reversibility was lower than the reversibility approaching 1 that is seen in published blocking curves [11, 38, 91, 152, 185, 186].

d_{Mn} (nm)	H_{ex}^A (± 0.01) (kOe)	H_{ex}^B (± 0.01) (kOe)	R_{ex} at $T_{act} = T_{set}$ (± 0.01)	$\langle T_B \rangle$ (± 3) (K)	$K_{AF}(295 \text{ K}) \times 10^6$ ($\pm 3 \times 10^6$) (erg/cm ³)
0	-1.16	0.39	0.67	538	16
0.05	-1.26	0.59	0.73	532	15
0.1	-1.18	0.55	0.73	534	15
0.2	-1.06	0.37	0.67	537	16
0.3	-0.97	0.31	0.66	542	17
0.4	-1.04	0.25	0.62	545	17
0.6	-0.82	0.21	0.63	545	17

Table 6.2: Summary of the initial and final exchange bias H_{ex}^A and H_{ex}^B , reversibility R_{ex} , median blocking temperature $\langle T_B \rangle$ and effective anisotropy K_{AF} for the blocking curves in fig. 6.6(a). The film structure is shown schematically in fig. 6.6(b).

The reverse correlation between H_{ex} and K_{AF} can at first glance appear paradoxical. The effect of IrMn composition on H_{ex} and K_{AF} was discussed in section 2.3.2 where they were shown not to be directly connected. In section 4.2 it was shown that H_{ex} is proportional to the set fraction of the AF film. However, if the AF film can only be partially set, then a higher anisotropy will act to reduce the overall H_{ex} [53, 174]. An example of this is shown in fig. 6.10.

Figure 6.10 shows energy barrier distributions $\Delta E = K_{AF} V_g$ for two example films A and B. The films have the same grain size distribution but film B has a higher anisotropy constant. The energy barrier distribution for film B therefore

appears to the right of the distribution for film A. At T_{set} the largest grain that can be set has an energy barrier equal to $K_{\text{AF}} V_{\text{set}}$. In fig. 6.10 the portion of the film that can be set is labelled (a), while (b) is the portion of the film which cannot be set according to the setting process described in section 4.2.5. When subsequently cooled to T_{NA} the exchange bias of a film is given by the set portion of the film. The area under the curve below $K_{\text{AF}} V_{\text{set}}$ is larger for film A than for film B. Therefore the total exchange bias will be larger because film A has a lower AF anisotropy constant.

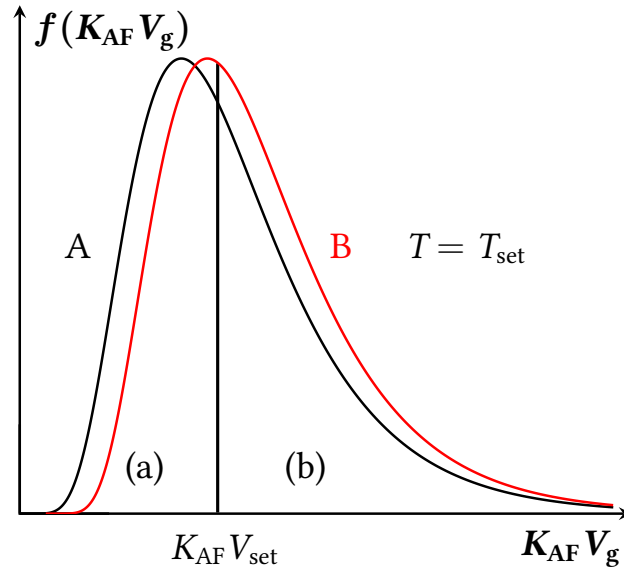


Figure 6.10: Schematic of the energy barrier distribution of two films with the same grain size distribution and different K_{AF} showing (a) the fraction of the film that can be set and (b) the unset fraction. In each case the B film is a film with a higher value of K_{AF} than the A film.

A summary of the potential origins of the effect of d_{Mn} on H_{ex} , K_{AF} , $\langle T_{\text{B}} \rangle$ and R_{ex} can be given as

1. Increase in the thickness and therefore volume of the AF grains resulting in an increase in ΔE [11].
2. Increase in J_K by the modification of an AF Mn spin structure at the interface [92].
3. Increase in K_{AF} due to a diffusion of Mn into the IrMn layer [53].
4. Interdiffusion of CoFe, Mn and IrMn layers resulting in the formation of diverse magnetic phases at the interface [57, 59].

5. Increase in spin cluster volume resulting in increased interfacial coupling [37, 91].
6. Increase in spin cluster moment and therefore an increase in the importance of spin cluster interactions [190].

The unmodified York Model of Exchange Bias can be applied to possibility 1 on the assumption that the additional Mn is fully incorporated into the AF layer. This would increase the layer thickness and therefore the volume of the AF grains. As discussed in section 4.2, the energy barrier to reversal for an AF grain is given by eq. (4.17), reproduced here

$$\Delta E = K_{AF} V_g \quad (6.13)$$

where ΔE is the energy barrier to thermal activation, K_{AF} is the AF anisotropy constant and V_g is the volume of the AF grain [11, 129, 142, 144]. Thus an increase in $\langle V_g \rangle$ will increase $\langle T_B \rangle$. It follows that an increase in AF grain volume will reduce H_{ex} . This is because a smaller fraction of the grain size distribution will be below V_{set} . The reduction of V_c has no effect since at T_{NA} there are no grains smaller than V_c . The apparent increase in K_{AF} shown in table 6.2 and calculated from $\langle T_B \rangle$ could then be interpreted as an increase in V_g . However, the grain volume increase between $d_{Mn} = 0$ and 0.6 nm is 6 % while the increase in $\langle T_B \rangle$ is 1 %. In contrast the initial exchange bias is reduced by 40 %. Therefore the effect of the grain volume increase is too large to account for the changes in $\langle T_B \rangle$ and too small to account for the changes in H_{ex} . In addition, the changes in R_{ex} are not explained.

Possibility 2 is suggested by measurements which show that J_K goes through a peak with the addition of Mn to the interface [92]. This was proposed to be due to a change in the magnetic structure of the interface influenced by the formation of an epitaxial Mn layer. However, this peak occurred at 0.5 nm whereas the peak found in this work was found at 0.05 nm. Furthermore, it is known that Mn is subject to diffusion in both CoFe and IrMn [59]. Hence a distinct Mn layer would be destroyed by annealing. However, annealing studies have not shown this result and therefore the existence of an epitaxial Mn layer can be discounted [37, 91].

Possibility 3 arises because it is known that the K_{AF} of IrMn increases as the proportion of Mn increases [53]. During heating, Mn will tend to diffuse out of the IrMn bulk. This will reduce the Mn concentration and decrease K_{AF} . This tendency

to diffuse is counteracted by the addition of interfacial Mn which replenishes the Mn concentration in the IrMn bulk. However, possibility 3 cannot account for the measurements which show that K_{AF} , $\langle T_B \rangle$, H_{ex} and R_{ex} do not vary monotonically. That said, when $d_{Mn} \geq 0.05$ nm there is a consistent trend of increasing $\langle T_B \rangle$ as d_{Mn} increases. The value of $\langle T_B \rangle$ when $d_{Mn} = 0$ nm is (538 ± 3) K which is almost within error of the value at $d_{Mn} = 0.05$ nm. Since these samples were cleaved from a larger wafer it is possible that there are macroscopic variations in the film thickness or composition which could cause an error of this scale.

Possibility 4 considers the interdiffusion of CoFe, Mn and IrMn layers. This results in the formation of diverse magnetic phases at the interface [57, 59]. The addition of Mn would act to replenish the interfacial Mn which otherwise diffuses into the CoFe and IrMn. The magnetic phase diagram of CoMn alloys is shown in fig. 6.8 [63]. It shows that CoMn can exist in F, AF or P phases dependent on the composition. In addition, there are two mixed phases superparamagnetic (SP) and superantiferromagnetic (SAF). In a SP material there are local regions of F order in a matrix that does not have magnetic order. The same is the case for a SAF material except that the regions have internal AF order. The SP phases have similar behaviour to the proposed interfacial spin clusters discussed in section 4.3 [37]. The SAF phases will be discussed in chapter 7.

Possibility 5 assumes that the Mn behaves magnetically as an addition to the disordered spins at the interface. If the interfacial spins are organised in clusters then the addition of Mn is effectively an increase in the volume distribution of the clusters [91]. As the volume of the spin clusters increases they become more thermally stable and hence more ordered. Therefore the coupling across the F/AF interface is increased. However, this would result in trends opposite to those observed. For this reason possibility 5 cannot alone explain the trends shown in table 6.2 but in combination with other explanations it could be used to explain the peaks in H_{ex} and $\langle T_B \rangle$.

Finally, possibility 6 considers changes to the spin clusters other than volume [190]. Mn carries a significant atomic moment and therefore the addition of Mn could increase the magnetisation of the interface. In particular, this would effect the strength of cluster-cluster interactions and therefore the order between clusters. This would have the effect of stiffening the interface and increasing C^* . On the other hand, the addition of Mn could increase the formation of AF IrMn or

CoMn phases at the interface [53, 63]. This would have the effect of decreasing the interfacial magnetisation. For this reason an increase in interfacial magnetisation is unlikely.

There is therefore no complete explanation of fig. 6.9. The fact that V_g does not change indicates that the explanation must be a change in K_{AF} , of which the most probable cause is a change in the composition of the IrMn. However, of these possibilities the most likely explanation is a combination of effects. In particular, a combination of possibilities 3, 4 and 5 will be considered. Possibilities 3 and 4 are based on diffusion, which is known to have a significant effect on CoFe/IrMn films both with and without annealing [59]. The F and AF layers interdiffuse forming diverse magnetic phases which vary across an interfacial region. As Mn is added, the proportion of phases that are AF increases [63]. In addition, the K_{AF} of the IrMn layer increases [53]. This is consistent with the decrease in H_{ex} shown in fig. 6.7. For $d_{Mn} \leq 0.05$ nm the Mn increases the spin cluster size distribution, leading to an increase in H_{ex} and a decrease in $\langle T_B \rangle$ due to an increase in thermal stability. However, for $d_{Mn} > 0.05$ nm the increasing K_{AF} of IrMn reduces H_{ex} and increases $\langle T_B \rangle$. The only way to resolve the effects of diffusion would be to apply an atomistic computer model which is beyond the scope of this work.

The condition of the interface is crucial for the determination of the exchange bias properties of the system. In order to investigate the interface, changes in the AF bulk must be eliminated. This is achieved by measuring below T_{NA} . However, due to the temperature dependence of K_{AF} measurements at lower temperatures will also affect the interface. For this reason the low-temperature behaviour at $T < 100$ K was investigated.

7. Low-Temperature Behaviour

In the context of exchange bias, low temperature behaviour describes phenomena that occur below the temperature of non-activation T_{NA} . T_{NA} was discussed in section 4.2. In the previous chapter measurements were carried out at $T_{\text{NA}} = 300\text{ K}$ in order to observe phenomena occurring during the preceding heat treatment. Here, phenomena that occur below the boiling temperature of liquid nitrogen will be discussed.

It is not necessarily the case that the spins at the F/AF interface are also thermally stable below the T_{NA} of the AF grains. At the interface, spins are subject to competing interactions between the positive exchange of the F layer and the negative exchange of the AF layer. In addition, the interfacial composition and therefore magnetic behaviour differs from the bulk of the AF grains due to interface roughness and atomic interdiffusion [57, 59, 63]. By excluding changes in the bulk of the AF grains, measuring at low temperature allows the behaviour of the interface to be investigated. The interfacial conditions were modified by the addition of ultra-thin layers of Mn at the F/AF interface. These films were produced by Seagate Technology at their facility in Northern Ireland.

An initial study was carried out using a Quantum Design MPMS 3 VSM at Diamond Light Source. It is capable of producing fields up to 70 kOe in a solenoidal superconducting electromagnet. However, the effects studied occurred at $\leq 2\text{ kOe}$. These low field measurements are necessary for the measurement of exchange bias H_{ex} , coercivity H_{c} and training ΔH_{c1} . However, a superconducting magnet is not suitable for low-field measurements due to the flux pinning in the magnet. This produces a systematic error in the measurement of \vec{H} . For this reason, the measurements were repeated in a resistive-magnet LakeShore 8600 Series VSM with a nominal field resolution of $< 1\text{ Oe}$.

7.1 Spin Freezing

The low-temperature behaviour of films is of interest due to a number of phenomena including the increase in exchange bias H_{ex} that occurs at $T < 50\text{K}$ [106, 107]. This phenomenon was discussed in section 3.4.3. In the York Model of Exchange Bias the exchange bias of a film is given by

$$H_{\text{ex}}(\vec{H}_{\text{set}}, T) = H_{\text{ex}}^{\text{INT}} C^* (\vec{H}_{\text{set}}, T) \int_{V_{\text{c}}}^{V_{\text{set}}} f(V_{\text{g}}) dV_{\text{g}} \quad (7.1)$$

where $H_{\text{ex}}^{\text{INT}}$ is the intrinsic exchange bias, C^* is the interfacial coupling parameter, V_{c} is the volume of the smallest stable grain at T_{NA} , V_{set} is the volume of the largest grain the could be set at T_{set} and $f(V_{\text{g}})$ is the AF grain volume distribution. $H_{\text{ex}}^{\text{INT}}$ is a constant of proportionality that represents a film set under hypothetical ideal conditions such that the whole grain size distribution contributes to the exchange bias [11]. Equation (7.1) can be used to identify the origin of the temperature dependence of H_{ex} .

The films discussed in this chapter are metallic, polycrystalline thin films of CoFe/IrMn with thickness and grain diameter $\sim 10\text{ nm}$. The samples were prepared with an ultra-thin Mn layer at the F/AF interface with thickness d_{Mn} .

T_{C} for $\text{Co}_{70}\text{Fe}_{30}$ is $(1040 \pm 10)\text{ K}$ [13, 25, 26]. Therefore there will be no significant changes in the magnetisation of the F layer between 0 and 300 K. In addition, the order of the F layer is dominated by the applied field \vec{H} . The presence of a AF layer has been shown to increase the domain wall pinning field in a coupled F film [191]. However, this increase is $\sim 100\text{ Oe}$ for a set AF film and $\sim 5\text{ Oe}$ for an unset film and is therefore small compared to the applied field applied in this study $\sim 1\text{ kOe}$. The effect of texture is more significant $\sim 200\text{ Oe}$ as discussed in section 3.3.1, but this is due to variations in sample structure and not a temperature effect [37]. Low-temperature exchange bias phenomena are observed in fields above the saturating field of CoFe. Thus changes in the F layer cannot be the origin of low-temperature exchange bias phenomena [11].

By the process of elimination, the origin of low-temperature exchange bias phenomena must be the F/AF interfacial region. Thus the parameter of interest

in eq. (7.1) is $C^*(\vec{H}_{\text{set}}, T)$. C^* is known to be a function of \vec{H}_{set} due to the \vec{H}_{set} dependency discussed in section 3.4.1. Likewise, it is known to be a function of T due to the spin freezing effect discussed in section 3.4.3.

7.1.1 Spin Freezing of Exchange Bias

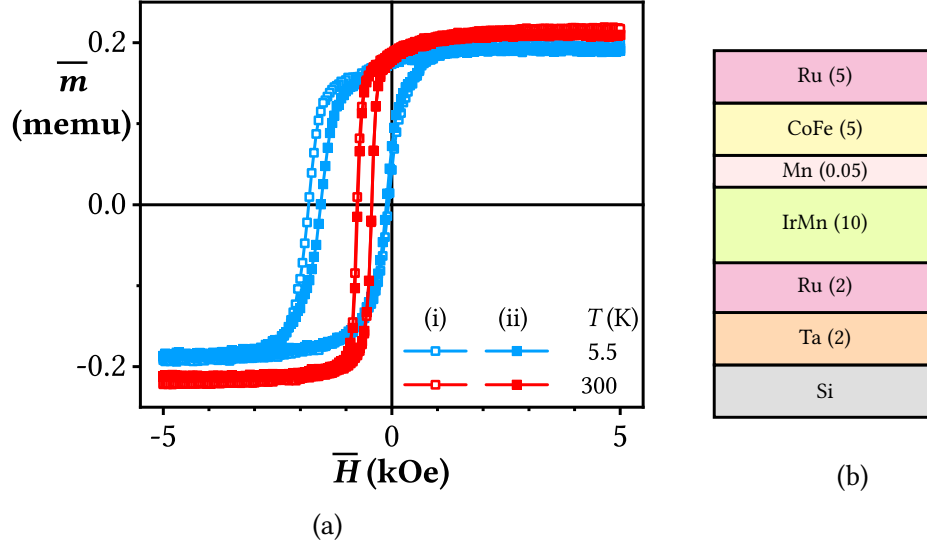


Figure 7.1: (a)(i) The first hysteresis loop and (ii) the second hysteresis loop at 5.5 and 300 K for film with (b) structure shown schematically (thicknesses in nm).

To investigate the spin freezing effect a F/AF film was set by thermal activation at a temperature T_{set} in a positive field \vec{H}_{set} . This setting process was necessary to induce exchange bias [11]. It was then cooled to the measurement temperature T and two loops were measured. The exchange bias and coercivity were measured from the second loop. This eliminated the training effect which was discussed in section 3.2.2. By measuring two loops, the training effect was calculated from the change that occurred between the two measurements. The film was then reheated to 400 K in a positive field for less than 1 min before being cooled again. This reheating process recovered the training effect, since if the film were not reheated then the training effect could be measured only once. However, the short duration of the heating and to a temperature much lower than the setting temperature prevented thermal activation of the AF film.

A film with composition Si/Ta (2)/Ru (2)/IrMn (10)/Mn (0.05)/CoFe (5)/Ru (5) (thicknesses in nm) was set in a field of $\vec{H}_{\text{set}} = 20\text{kOe}$ at $T_{\text{set}} = 500\text{K}$ for $t_{\text{set}} = 90\text{min}$. The film composition is shown schematically in fig. 7.1(b). After setting

the film was cooled in field to a temperature T and two hysteresis loops were measured. Figure 7.1(a) shows an example of the hysteresis loops obtained measured at 5.5 and 300 K. The loop parameters are summarised in table 7.1.

T	5.5	300	± 0.5	(K)
H_{ex}	840	590	± 10	(Oe)
H_c	720	150	± 10	(Oe)
ΔH_{c1}	260	10	± 10	(Oe)

Table 7.1: Summary of the exchange bias H_{ex} , coercivity H_c and training ΔH_{c1} of the hysteresis loops shown in fig. 7.1(a) at 5.5 and 300 K showing the effect of spin freezing. The film structure is shown schematically in fig. 7.1(b).

The training effect ΔH_{c1} is shown at 5.5 K in fig. 7.1(a) as the change in H_{c1} between the first loop (i) and the second loop (ii). However, at 300 K ΔH_{c1} is almost equal to 0 within error and therefore demonstrates that the blocking of the interface occurs below T_{NA} . There is a significant loop asymmetry in the loop measured at 5.5 K. In addition, the loop asymmetry changed as the temperature was increased. At 300 K the reversal progressed by rapid domain wall motion resulting in a loop with vertical sides. On the other hand, the 5.5 K loops show a more gradual magnetic transition, which is the result of domain wall pinning which at higher temperatures were overcome by thermal energy. This is consistent with the work of Carpenter et al. [37]. Note that H_{ex} is low compared to ~ 1 kOe at 300 K shown in fig. 6.7. This is because the sample was cleaved from a wafer and therefore there may be macroscopic variations in composition or layer thickness across the wafer which result in a reduction in H_{ex} .

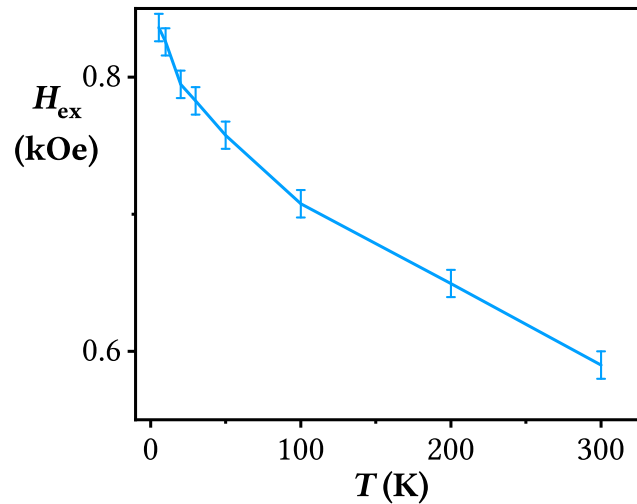


Figure 7.2: H_{ex} for low-temperature measurements. The film structure is shown schematically in fig. 7.1(b).

A summary of the effects of temperature on exchange bias is shown in fig. 7.2 for a film with structure shown schematically in fig. 7.1(b). H_{ex} increased as the measurement temperature was reduced. The exchange bias measured at 300 K was (590 ± 10) Oe. This increased to (840 ± 10) Oe at $T = 5.5$ K. This represents a factor of ~ 1.5 increase over the exchange bias at room temperature. The changes in H_{ex} were monotonic with no indication of saturation. In fact H_{ex} changes most rapidly below 20 K. The error bars shown in fig. 7.2 represent an inaccuracy due to the resolution of the magnetic measurements and not a random Gaussian error.

Spin clusters are proposed to have a blocking temperature distribution in the range 0 to 100 K which is independent of the blocking temperature distribution of the AF grains [11, 12, 37, 67, 91, 107, 164]. The initial H_{ex} is caused by the setting of the bulk of the AF grains. As the film is cooled the spin clusters become blocked. Since the cooling occurs with an applied field the blocked spin clusters have F order. This increases the interfacial order which correlates to the increase in H_{ex} . However, at 200 K H_{ex} is enhanced compared to H_{ex} at 300 K. This implies that the highest spin cluster blocking temperatures are much larger than 100 K. In addition, the enhancement of H_{ex} has not been shown to saturate at low temperatures. This implies that the modal spin cluster blocking temperature is below 5.5 K. Therefore the spin cluster blocking temperatures are broadly distributed.

7.1.2 Spin Freezing of Coercivity and Training

During this measurement the temperature dependencies of H_c and ΔH_{c1} were measured. For ΔH_{c1} this required heating the film in field to 400 K and then field-cooling back to T . This is because the training effect only occurs between the first and second magnetisation reversals after heating. If the film were not heated between each measurement temperature then H_{ex} and H_c could be measured but ΔH_{c1} could not. The temperature dependencies of H_c and ΔH_{c1} are shown in fig. 7.3 for a film with structure shown schematically in fig. 7.1(b).

As is shown in fig. 7.1(a) and fig. 7.3(a) the coercivity of an exchange bias film increases at low temperature for a film with structure shown schematically in fig. 7.1(b). The similarity of the temperature dependence of H_c and ΔH_{c1} below 300 K shows that they have a common interfacial origin. The greatest value of coercivity was measured at the minimum measurement temperature of 5.5 K and had

a value of (720 ± 10) Oe. This represents an increase in H_c by a factor larger than 4 over H_c at 300 K. The training effect continued to increase down to 5.5 K. This is shown in fig. 7.3(b) for a film with structure shown schematically in fig. 7.1(b). ΔH_{c1} reached a maximum value of 260 Oe in the range available for measurement which is 20 times the value of ΔH_{c1} at 300 K. For H_c and ΔH_{c1} there is no indication that the values will saturate. If there is a peak in these quantities then it lies below 5.5 K.

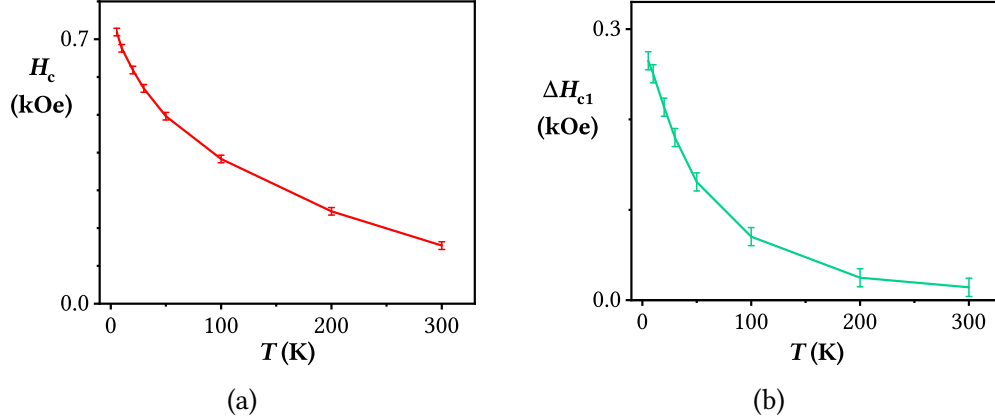


Figure 7.3: The temperature dependence of (a) H_c and (b) ΔH_{c1} . The film structure is shown schematically in fig. 7.1(b).

The increase in H_c and ΔH_{c1} as the temperature is reduced can be discussed in the context of spin clusters. As the film is cooled in an applied field the spin clusters become blocked. This increases the number of domain wall pins and their strength. This increases the field required to reverse the F film, which is an increase in H_c . As the F layer reverses some portion of the spin clusters will reverse under the influence of the applied field and the exchange field from the F layer. However, as \vec{H} returns to the positive direction not all of the reversed spin clusters will align parallel to it. This is due to the lack of sufficient thermal energy and time to change the alignment of the spin clusters for the second time. Thus when the second hysteresis loop is measured the overall order of the interface is reduced, which reduces H_{c1} compared to the value measured in the first hysteresis loop.

There is a notable similarity to the forms of the temperature dependence of H_{ex} , H_c and ΔH_{c1} shown in fig. 7.2 and fig. 7.3. Using normalised values, the congruence of the temperature dependence of H_{ex} , H_c and ΔH_{c1} is shown in fig. 7.4 for a film with structure shown schematically in fig. 7.1(b). For all three parameters, the highest value is recorded at the lowest temperature. Cooling to 5.5 K increased H_{ex} by a factor of ~ 1.5 , H_c by a factor of ~ 4 and ΔH_{c1} by a factor of ~ 20 compared to their values at 300 K. Below $T_{NA} = 300$ K there are no temperature-dependent

changes in the spin order of the F layer or the bulk of the AF grains [11]. Therefore the temperature dependence below T_{NA} must have a common interfacial origin.

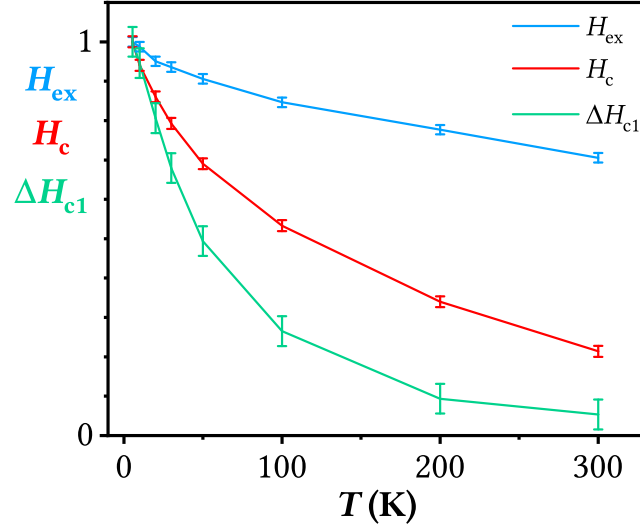


Figure 7.4: The normalised H_{ex} , H_c and ΔH_{c1} show a similar dependence on T . The film structure is shown schematically in fig. 7.1(b).

The increase in H_{ex} is correlated with an increase in the F order of the interfacial spins [11, 91]. H_{ex} has been shown to be strongly dependent on the order of the bulk of the AF grains and can be modified by the interfacial order [188]. On the other hand, H_c has been shown to be very strongly dependent on the interfacial order and less strongly dependent on the bulk order [73]. This is reflected in fig. 7.4 where the increase in interfacial order as T is reduced results in a larger proportional increase in H_c than H_{ex} . Since ΔH_{c1} increases by the largest factor, it must be almost entirely dependent on the interfacial order.

Taken together, the measurements summarised in fig. 7.4 can be interpreted as a stiffening of the interface as T is reduced. At low temperature, the tendency of the spin clusters to reverse is reduced. This results in increased H_{ex} because of increases the interfacial order. H_c increases at low temperature because a larger field is required to overcome the increased number of domain wall pins that arises from the blocked spin clusters. For ΔH_{c1} the increase seen at low temperature is due to the reduced tendency of the spin clusters to reverse. To return to the initial position the spin clusters must reverse twice. Thus the lower the temperature the lower the chances that a reversed spin cluster will return to its initial position. This increase in interfacial stiffness is similar to the result shown in section 6.2.3, although induced by T rather than d_{Mn} .

7.2 Magnetisation Offset

7.2.1 Temperature Dependence of m_s Offset

Exchange bias measures the field shift in the hysteresis loop of a coupled F/AF film. However, a magnetisation offset of an exchange biased hysteresis loop has also been observed, although not in an IrMn system [108–112, 114–117]. This was discussed in section 3.4.4. As in equation eq. (3.10), reproduced here, the magnetisation offset Δm_s is defined as

$$\Delta m_s = |m_s^+| - |m_s^-| \quad (7.2)$$

where m_s^+ is the magnetic moment at positive saturation and m_s^- is the moment at negative saturation. For a loop shifted upwards $|m_s^+| > |m_s^-|$ and Δm_s is positive.

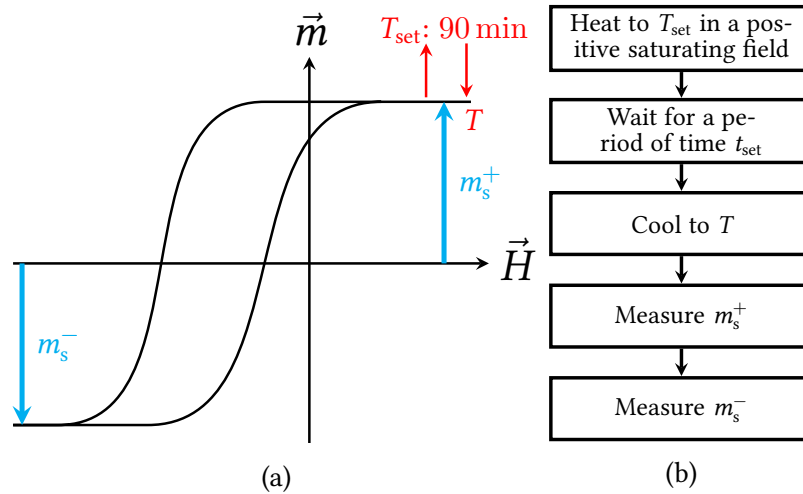


Figure 7.5: The measurement protocol to measure m_s^+ and m_s^- shown (a) schematically and (b) as a series of steps.

To investigate the \vec{m} offset a F/AF film was heated to T_{set} in a positive saturating field \vec{H}_{set} . This setting process was discussed in section 4.2. The film was then cooled to the measurement temperature T and two loops were measured. In these measurements, T was lower than the temperature of non-activation for the bulk of the AF grains $T_{\text{NA}} = 300 \text{ K}$. Measuring two loops allowed Δm_s to be measured before and after training. The measurement protocol is shown schematically in fig. 7.5.

The film was then heated to 300 K in a positive field for less than 1 min before being cooled to a new measurement temperature. This process of reheating recovered the training effect allowing multiple measurements. The short duration of the heating and to a temperature lower than T_{NA} prevented further thermal activation of the bulk of the AF grains. The recovery of the training effect at a temperature below T_{NA} shows that the training effect is an interfacial effect. In addition, it shows that the thermal stability of the interface is lower than the thermal stability of the AF bulk.

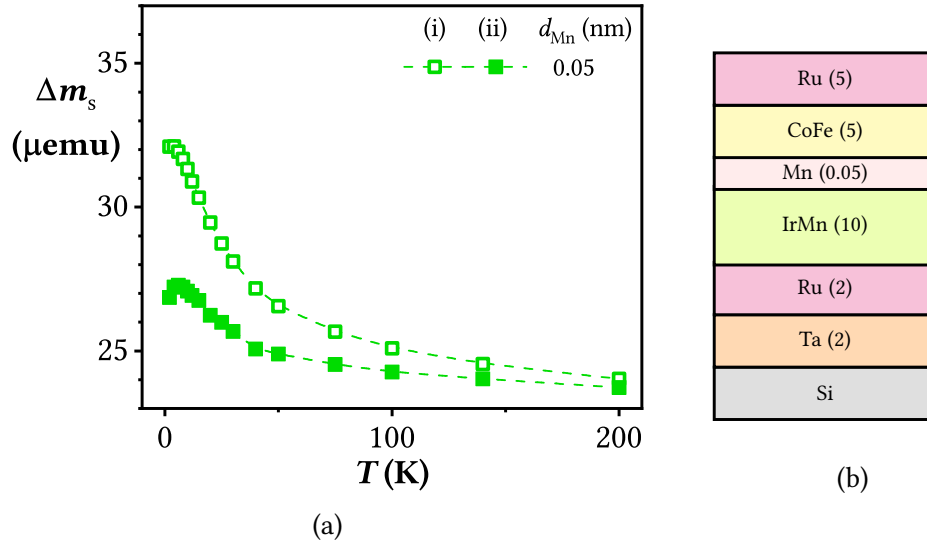


Figure 7.6: (a) The temperature dependence of Δm_s for the (i) first and (ii) second hysteresis loop for film with (b) structure shown schematically (thicknesses in nm). The line is a guide to the eye [192].

A film with composition Si/Ta (2)/Ru (2)/IrMn (10)/Mn (0.05)/CoFe (5)/Ru (5) (thicknesses in nm) was set in a field of $\vec{H}_{\text{set}} = 20\text{kOe}$ at $T_{\text{set}} = 500\text{K}$ for $t_{\text{set}} = 90\text{min}$. The film composition is shown schematically in fig. 7.6(b). As discussed in section 2.2.5, $a_{\text{CoFe}} = 0.286\text{nm}$ and $a_{\text{IrMn}} = 0.378\text{nm}$ [41, 42]. The IrMn layer has fcc structure measured by XRD as shown in fig. 5.5. The AF film has a texture intermediate between 3-D random texture and in-plane easy axis texture as was measured by the pole figure shown in fig. 5.7. Note that since the atomic radius of Mn is $\approx (0.140 \pm 0.005)\text{nm}$ the interfacial Mn layer has a thickness equivalent to approximately one sixth of an atom [189]. Thus this ultra-thin layer is in effect a compositional alteration to the F/AF interface. The film was cooled to the measurement temperature and two hysteresis loops were measured. The positive and negative moments m_s^+ and m_s^- were measured at $\pm 5\text{kOe}$. Δm_s was calculated using eq. (7.2) and the results for both the first and second loops these being before and after training are shown in fig. 7.6(a) [192]. Δm_s measurements were taken

from hysteresis loops taken in both an increasing and decreasing temperature sequence.

These measurements were made with a Quantum Design MPMS 3 VSM based at Diamond Light Source. The temperature dependence of Δm_s was reproduced by confirmatory measurements with a larger temperature step using a LakeShore 8600 Series VSM. Discussion of the changes in Δm_s before the first measured hysteresis loop will be discussed in section 7.2.2. It should be noted that the origin of this change is changes in m_s^+ while m_s^- remains constant.

There is a general trend for Δm_s of the second hysteresis loop measured to increase as the temperature is reduced. This continues to an apparent peak at 6 K where the trend saturates. There is an indication that this is then followed by a reduction in Δm_s down to the minimum measured temperature 2 K. It should be noted that $|m_s^+|$ and $|m_s^-|$ were $\sim 200 \mu\text{emu}$. In principle the measurement of \vec{m} has an error related to the resolution of the magnetometer which is itself a consequence of the linear amplifier system. A conservative estimate of the resolution of the Quantum Design MPMS 3 VSM is $\pm 0.5 \mu\text{emu}$. However, this error is systematic rather than a random error and therefore cannot be propagated to Δm_s . Therefore the errors in fig. 7.6 have been removed for clarity. This removal is validated by the low random error of the measurements. The errors in T are $\sim 0.1 \text{ K}$. Δm_s at $T = 2 \text{ K}$ is $27 \mu\text{emu}$. This represents an increase of $\approx 10\%$ over Δm_s at $T = 200 \text{ K}$, which was $24 \mu\text{emu}$ for the second measurement which is after training.. The value of Δm_s before training will be discussed in section 7.2.2.

If the film was not saturated then the measured moment will not be the saturation moment. In a typical F material this is not an issue because the hysteresis loop is symmetric. For an exchange biased film the loop shift means that measuring the saturation moment is non-trivial. In addition, H_{ex} and H_c are temperature dependent which further complicates the measurement. That said, the trend shown in fig. 7.6 was not strongly dependent on the chosen measurement fields. The absolute values of Δm_s changed by $< 10\%$ while the temperature dependence was not affected. For consistency \vec{m} was measured at the maximum measurement field which was $\pm 5 \text{ kOe}$. It was not necessary to correct for the diamagnetic contribution of the substrate due to the low diamagnetic susceptibility and low field used.

An offset in \vec{m} indicates that the film has a greater moment and magnetisation in one direction than the other. Since the hysteresis loop is shifted upwards, the direction of increased magnetisation is the same as the setting field direction. Thus an explanation for Δm_s must account for a greater magnetisation in the setting field direction than in the reverse field direction. Firstly, changes in the F layer can be discounted because m_s^+ and m_s^- were measured at saturation. Secondly, changes in the AF layer do not occur after the setting procedure since the film is thereafter not heated to above T_{NA} . If the bulk of the F and AF layers can be excluded, then Δm_s must originate in the F/AF interfacial region.

Since a material with ideal AF order has no net \vec{m} , the interfacial contribution to Δm_s must arise from an increase in F order. However, this contribution cannot be reversed which distinguishes it from other instances of F order. This could be due to the interfacial spins behaving in a manner analogous to a magnetic spin glass with a thermoremanent magnetisation [193, 194].

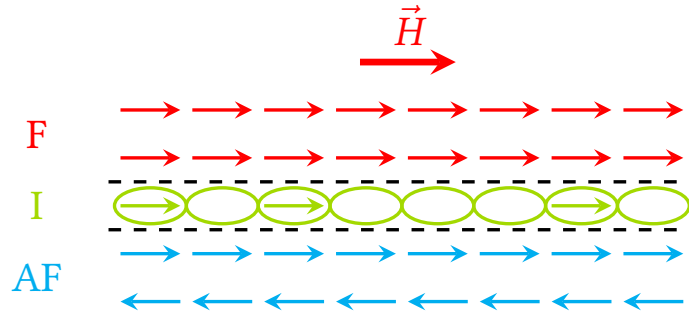


Figure 7.7: Schematic of the F/AF interface of a set exchange bias film showing three regions. Spin clusters are shown both with and without moments to represent partial saturation which is indicated by the setting field dependence of H_{ex} [67].

Figure 7.7 shows a schematic of the F/AF interface of an exchange bias film after the field setting process in a positive saturating field \vec{H} . The schematic shows a pair of flat interfaces dividing F, AF and interfacial regions. This is used to represent the interfacial region created by the diffuse F/AF interface for an AF grain [11, 59]. This is not equivalent to the atomically flat interface used by Meiklejohn and Bean to calculate H_{ex} [1, 2]. The interface is further sub-divided into locally-ordered spin clusters [11, 37, 67].

The IrMn film has a $\{111\}$ plane parallel to the interface, thus the plane separation perpendicular to the interface is given by eq. (5.4), reproduced here,

$$d_{hkl} = \frac{a_{\text{IrMn}}}{\sqrt{h^2 + k^2 + l^2}} \quad (7.3)$$

where the lattice parameter of IrMn is $a_{\text{IrMn}} = 0.378 \text{ nm}$ and h , l and k are all equal to 1 [42, 169]. In the measured sample the AF layer is 10 nm thick. This corresponds to ≈ 45 atomic layers. For clarity the schematic shows two layers. As discussed in section 5.2.1, the texture of the CoFe layer is not known or amorphous [13, 169]. However, the 5 nm CoFe layer contains ≈ 17 atomic layers given that $a_{\text{CoFe}} = 0.286 \text{ nm}$ [41]. Two are shown in fig. 7.7.

The interfacial region is shown between the F and AF layers in fig. 7.7. The interfacial region is shown to be one layer thick and to have flat interfaces with the F and AF layers. However, this is not the case in the film due to the diffusion of Fe, Co and particularly Mn [59]. This was discussed in section 3.3.4. The interdiffusion of these species leads to the formation of diverse magnetic alloys such as CoMn which have both F and AF phases dependent on composition and temperature [63]. There is a possibility these phases will be coupled to the F layer by direct exchange. In addition F spin clusters could be coupled to each other by RKKY exchange. Thus the interface will exhibit complex magnetic behaviour.

In fig. 7.7 the film is shown with the F layer magnetised by an external field parallel to the setting direction. While the F layer is fully saturated, the interfacial layer is partially saturated. This is represented by a mixture of interfacial clusters both with and without moments. The set fraction of the interface is not known. The moment of the interfacial clusters can be reduced or eliminated due to the formation of AF phases by compositional variation of Co, Fe and Mn [63]. The partial setting of the interfacial layer is evidenced by the setting field dependence discussed in section 3.4.1 and the increase in H_{ex} that occurs at low temperatures discussed in section 7.1 [11, 91]. The AF layer adjacent to the interface is aligned parallel to the F layer which is a result of the setting process. This is known to be the case as H_{ex} is induced by the exchange field from the AF layer [1, 2, 125]. The atomic moments in the positive field direction will contribute to m_s^+ while the atomic moments aligned in the opposite direction will reduce m_s^+ .

The F layer will be reversed by the application of a sufficient negative field. In addition some portion of the interfacial spins will reverse. However, the spins of the bulk of the AF grains will not reverse as there is not sufficient thermal energy below T_{NA} [11]. In this case the spins aligned in the negative field direction will increase the magnitude of m_s^- . Thus m_s^- will be made up of the moment of the F layer, the reversed fraction of the interface and the net moment of the AF layer, if any.

Conventionally an AF bulk material has no net magnetic moment due to the antiparallel alignment of adjacent sublattice magnetisations [13]. However, in an exchange bias thin film the surface magnetisation of the AF layer is responsible for interfacial exchange anisotropy and hence exchange bias [1, 2, 11, 47, 121, 125, 129, 131, 144]. This was discussed in section 2.2.6 and chapter 4. Thus the AF layer closest to the interface will be aligned parallel to it and contribute to the moment in the setting field direction m_s^+ . With an even number of sublattices the AF layer will have no net moment. On the other hand if there is an odd number of sublattices and therefore a net magnetic moment, that moment will be in the setting field direction due to the tendency for the layer closest to the interface to be aligned in that direction.

The contribution to the moment by a unit area of film can be expressed as

$$\begin{aligned} m_s^+ &= \mu_B (N_F + 1 + R_1') \\ m_s^- &= -\mu_B (N_F - 1 + R_1'') \end{aligned} \quad (7.4)$$

where m_s^+ is the saturation moment in the positive field direction and m_s^- is the saturation moment in the opposite direction. The conversion factor between the number of spins and the moment is μ_B . This is negative in the case of m_s^- because $m_s^- < 0$.

The number of F layers is given by N_F . The contribution of the AF layer is given by ± 1 . This represents the AF layer closest to the interface which is additive in the m_s^+ case and subtractive in the m_s^- case.

There are two reversibility factors which represent the aligned portion of the interface. R_1' is the fraction of the interface that is initially aligned in the m_s^+ state and R_1'' is the fraction of the interface that is aligned in the negative field direction in the m_s^- state.

This treatment assumes that the F layer is saturated in positive field and reverses completely in a saturating negative field. The AF layer is treated as contributing one atomic layer of moment in the positive field direction. It also assumes that the spin order of the AF layer does not change between the measurements of m_s^+ and m_s^- . This is a reasonable assumption if the measurements occur below T_{NA} [11]. Thus the AF layer moment will increase m_s^+ and reduce the magnitude of m_s^- . Equation (7.4) also treats the interfacial spins as equivalent to single spins in one layer. The model further assumes that the atomic moment of all species in the F/AF material does not vary as a function of depth through the sample. However this is a significant approximation due to diffusional effects discussed in section 3.3.4 [59].

The reversible fraction of the interface has not been measured. However, by definition R'_I has a value between 0 and 1. In fig. 7.7 the interface is shown to be one layer thick while the F layer has a calculated thickness of ≈ 17 atomic layers. Thus the minimum contribution of the interface to m_s^+ is 0 for $R'_I = 0$. On the other hand, the maximum contribution occurs if $R'_I = 1$, in which case the interfacial contribution is 6 % of the F layer contribution since the F layer contains 17 times as many atoms. In addition, the contribution of the AF film will be equivalent to an additional 6 % atomic layer due to the positively aligned atomic layer closest to the interface.

Thus the overall contribution of the interface and AF layer will be between 6 and 12 % of the total moment, dependent on the value of R'_I . Since the F layer reverses in negative field it does not contribute to Δm_s .

At $T = 2\text{ K}$, m_s^+ is $(207 \pm 1)\ \mu\text{emu}$ and m_s^- is $(-181 \pm 1)\ \mu\text{emu}$. This gives a magnetisation offset of $(27 \pm 1)\ \mu\text{emu}$ which is shown in fig. 7.6 and gives a total change from m_s^- to m_s^+ of $(388 \pm 1)\ \mu\text{emu}$. Thus Δm_s accounts for 7 % of the total moment reversal. This is within the range of 6 and 12 % found in the calculation based on the proportion of the spins in each layer.

The match between the experimental results and the calculation based on atomic layer moments in a unit area suggests that the model has merit. However, further measurements would be required to establish if this explanation is representative. In fact, there are several limitations to the model in addition to the assumptions already described. Significantly, in the model the number of F and AF atomic lay-

ers is calculated based on the nominal thicknesses of the layers. Therefore the interface is implicitly taken to have zero thickness.

Furthermore, this calculation does not account for strain which could displace atoms from their expected positions or induce an interfacial stress anisotropy [13, 39, 40]. This is a weakness in the calculation as the lattice mismatch between CoFe and IrMn is 32 %. As discussed in section 2.2.5, $a_{\text{CoFe}} = 0.286 \text{ nm}$ and $a_{\text{IrMn}} = 0.378 \text{ nm}$ [41, 42]. However, stress anisotropy is typically on the order of 10^4 to 10^5 erg/cm^3 and therefore is smaller than the AF anisotropy for IrMn measured in section 6.2.3 and shown in table 6.2 by a factor of 10^2 or 10^3 [11, 13, 43]. Thus the anisotropy of the AF layer will dominate.

The calculation was made based on the measurement at 2 K. However, fig. 7.6 shows a dependence of Δm_s on T . $\Delta m_s = (24 \pm 1) \mu\text{emu}$ at 200 K which increases by $\approx 10\%$ to $(27 \pm 1) \mu\text{emu}$ at 2 K. This can be understood if reducing the temperature reduces the reversible fraction of the interfacial spins. As the temperature is reduced R'_1 decreases due to the reduction in reversibility of the interfacial spins. When the field and F layer are reversed, these spins remain magnetised in the positive field direction. Thus they contribute to an increase m_s^+ and a decrease in m_s^- . At higher temperatures the difference between the m_s^+ and m_s^- states is smaller than at lower temperatures. This increases Δm_s at low temperatures.

Interestingly, changes in the reversibility of the interfacial layer are ongoing at least between 10 and 100 K and possibly across a temperature range of 2 to 200 K. There are two potential explanations for the wide temperature range of these changes. The first is that the interfacial spins are arranged in clusters and reverse over energy barriers which are proportional to the number of spins in a cluster. This process is analogous to the reversal of the spin order of the AF grains that gives rise to changes in H_{ex} in the York Model of Exchange Bias [11, 91]. However, if the temperature dependence is indicative of a volume distribution then the wide range of temperatures involved implies a wide distribution of spin cluster sizes. The spin clusters that freeze at 200 K would have a volume similar to the volume of the AF grains. On the other hand, if spin freezing is dependent on cluster size only then those that freeze at 2 K would be on the order of single spins. There is no mechanism by which the interfacial layer could be sub-divided into clusters with a size distribution of this width.

The second possible explanation is a magnetic phase change in the interfacial layers. Due to diffusion the F/AF interface will be composed of a number of phases including CoMn [59]. As was shown in fig. 6.8, CoMn has both F, AF and P phases dependent on composition and temperature [63]. In CoMn at 4.2 K there is a transition from F to AF ordering which begins as the Mn content is increased above 30 at.% and is not complete until the Mn content reaches 45 at.%. Between these concentrations CoMn is paramagnetic on large scales with local regions of F and AF order. This transition takes place across a wider range of compositions at higher temperatures. Therefore cooling a P alloy of CoMn to 5.5 K will induce a magnetic phase change to either F or AF order unless the composition is between 30 and 45 at.% Mn. In a thin film is made more likely by the influence of the F and AF layers adjacent to the interface. Due to these layers the interface is influenced by competing F and AF interactions in a way that is not possible or observable in a bulk material. However, fig. 7.6 shows a temperature range between 5.5 and 200 K. In that range the phase change between P and F order is almost independent of temperature. For this reason a temperature-dependent magnetic phase changes can be discounted.

7.2.2 Effect of Training on m_s Offset

As shown in fig. 7.6 there is a decrease in Δm_s after the first magnetisation reversal. This is an indication of the effect of training on Δm_s . The difference is largest at low temperatures. At $T = 2\text{ K}$, m_s^+ is $(213 \pm 1)\ \mu\text{emu}$ before training and m_s^- is $(-181 \pm 1)\ \mu\text{emu}$. This results in a magnetisation offset of $(32 \pm 1)\ \mu\text{emu}$ which is 20% larger than the value Δm_s measured in subsequent loops. There are three important observations that can be taken from fig. 7.6. The first is that $T < T_{\text{NA}}$. The second is that $|m_s^+| \neq |m_s^-|$. The third is the form of $\Delta m_s(T)$.

Since the measurement temperature is below the temperature of non-activation of the AF grain bulk, the interface must be behaving independently of the AF layer. Thus Δm_s and the changes in Δm_s between the first and second measurement have their origins in the interface. The interface spins are aligned parallel to the F layer due to the exchange field from the F layer as shown by the setting field dependency discussed in section 3.4.1 [11, 67, 91]. In addition, heating to 300 K was required to recover the original order of the spin clusters, leading to a training effect in both \vec{H} and \vec{m} . Therefore thermal energy is required to induce order in the interface in a manner analogous to a thermoremanent state in a spin glass [193, 194].

The inequality of m_s^+ and m_s^- shows that the magnetisation of the interface is composed of both reversible and irreversible parts. The reversible contribution is aligned at a measurement temperature T by an external field and the exchange field from the F layer. The irreversible contribution can only be aligned at an elevated temperature.

The form of $\Delta m_s(T)$ is wide and has a peak at low temperatures. If interpreted according to a modified Stoner-Wohlfarth model, this implies that the energy barriers to reversal and therefore the spin cluster volumes are widely distributed and lower than the corresponding energy barrier distribution of the AF grains. If the spin cluster diameter distribution matches the grain diameter distribution, then the spin clusters must have either a low anisotropy or a low thickness since the energy barrier is the product of the anisotropy and the volume. This can be expressed by a restatement of eq. (4.14) and eq. (4.17) for the interfacial spin clusters, such that

$$\Delta E_{SC} = K_{SC} V_{SC} \quad (7.5)$$

where ΔE_{SC} is the energy barrier to reversal, K_{SC} is the anisotropy of the spin cluster and V_{SC} is the volume of the spin cluster [129, 142, 144, 148, 149]. A low spin cluster anisotropy could be a consequence of a low M_s since $H_K \propto \frac{\vec{M}}{M_s}$.

It should be noted that the change in Δm_s is dominated by a change in m_s^+ , rather than in m_s^- . Between the first and second loop m_s^+ decreases from (213 ± 1) to $(207 \pm 1) \mu\text{emu}$. At the same time, the changes to m_s^- are within error as it changes from (-181 ± 1) to $(-180 \pm 1) \mu\text{emu}$. Therefore there is not only a training effect on the switching field of first reversal but also on M_s before the first and second reversal.

For this reason m_s^+ can be separated into two parts where $m_{s,i}^+$ is the moment in the positive direction in a saturating field before the first magnetic reversal and $m_{s,ii}^+$ is the positive moment in a saturating field after one magnetic reversal. The equivalent to these in terms of magnetisation are $M_{s,i}^+$ and $M_{s,ii}^+$, respectively. Since m_s^- does not change significantly, an explanation for the changes in Δm_s must focus on changes that occur between measurements of $m_{s,i}^+$ and $m_{s,ii}^+$.

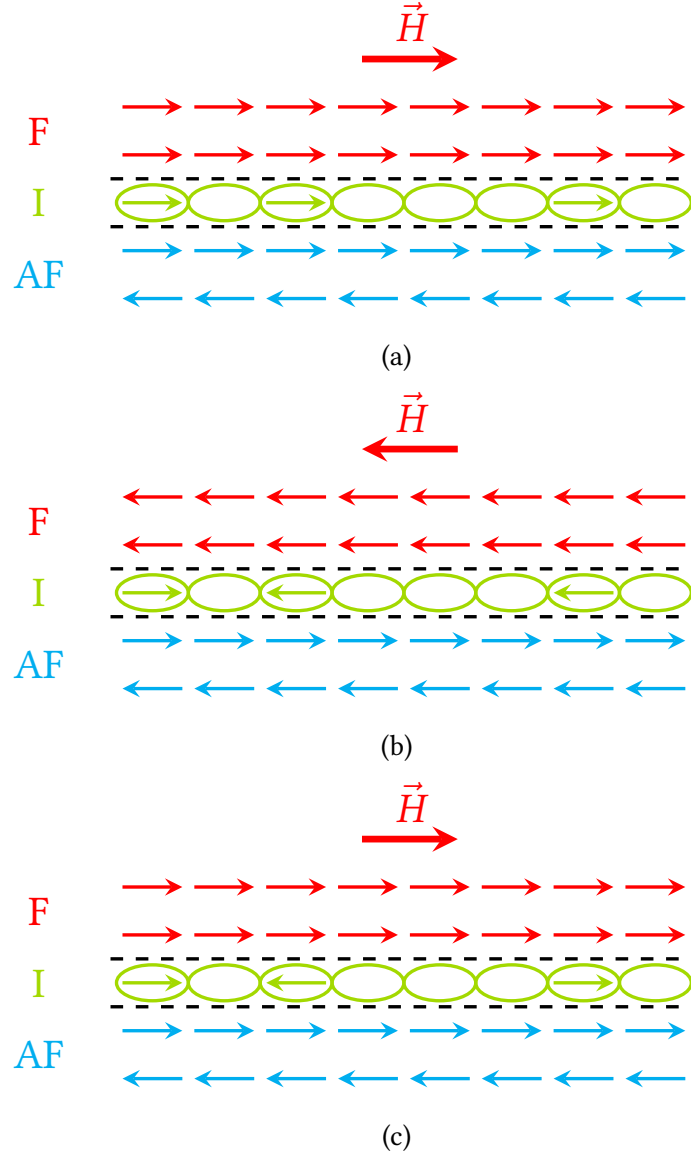


Figure 7.8: Schematic of the F/AF interface showing regions of F and AF order separated by the interface I during measurement of (a) $m_{s,i}^+$, (b) m_s^- and (c) $m_{s,ii}^+$.

To reflect this the expressions discussed in section 7.2.1 and shown in eq. (7.4) can be modified to include the change in state due to the training effect, giving

$$\begin{aligned}
 m_{s,i}^+ &= \mu_B (N_F + 1 + R_I^I) \\
 m_s^- &= -\mu_B (N_F - 1 + R_I^{II}) \\
 m_{s,ii}^+ &= \mu_B (N_F + 1 + R_I^{III})
 \end{aligned} \tag{7.6}$$

where $m_{s,i}^+$ is the saturation moment in the positive field direction before the first reversal and m_s^- is the saturation moment in the opposite direction which is independent of the number of magnetisation cycles. $m_{s,ii}^+$ is the saturation moment in the positive field direction after the first reversal which is different from $m_{s,i}^+$ due

to the effects of training. The conversion factor between the number of spins and the magnetisation is μ_B . This is negative in the case of m_s^- because $m_s^- < 0$.

The number of F layers is given by N_F . The contribution of the AF layer is given by ± 1 . This represents the AF layer closest to the interface which is additive in the $m_{s,i}^+$ and $m_{s,ii}^+$ cases and subtractive in the m_s^- case.

There are three reversibility factors which represent the aligned portion of the interface. R_1' is the fraction of the interface that is initially aligned in the $m_{s,i}^+$ state, R_1'' is the fraction of the interface that is aligned in the negative field direction in the m_s^- state and R_1''' is the fraction of the interface that is aligned in the $m_{s,ii}^+$ state.

Thus Δm_s after training is given by the difference between $m_{s,ii}^+$ and m_s^- while the effect of training results in a difference between $m_{s,i}^+$ and $m_{s,ii}^+$. At 200 K the effect of training is small because $m_{s,i}^+$ and $m_{s,ii}^+$ have similar values. Thus R_1' and R_1''' must be similar. That is to say that the reversible fraction of the interface does not change as the field is cycled. On the other hand at 2 K the effect of training causes $m_{s,i}^+$ to be 20 % larger than $m_{s,ii}^+$. This indicates a significant difference in the reversible fraction of the interface. The interfacial order is largest before the first reversal, resulting in the largest moment occurring in the $m_{s,i}^+$ state. During subsequent hysteresis loops the interfacial order is reduced to the $m_{s,ii}^+$ state.

Figure 7.8 shows the effect of training on the F/AF interface. In fig. 7.8(a) the F/AF interface is shown after the setting process and field cooling. \vec{H} is applied in the setting direction and the F layer is saturated in the same direction. The spin order of the AF layer has been set by the exchange interaction from the F layer, which has ordered the AF grain by reversal of the spin order over a volume-dependent energy barrier [11]. A portion of the interface R_1' is magnetised parallel to the setting field direction and contributes to m_s^+ . In fig. 7.8(b) the applied field has been reversed for the measurement of m_s^- . The F layer has reversed with the field and is saturated. Since the film is below T_{NA} there is no change in the AF layer. The reversal of the F layer has caused a fraction of the interfacial spins R_1'' to reverse.

Figure 7.8(c) shows the interface after a hysteresis loop has been measured. For this film the field has been reversed and then returned to the setting direction. A part of the interfacial layer has not changed since the setting procedure. This part

has therefore remained unchanged which is similar to the bulk of the AF layer. Of the fraction of the interface that reversed a portion has reversed again. This portion of the film has therefore followed the F layer during the magnetic treatment. This portion plus the portion that never reversed is the origin of R_1''' . However, there is a portion of the interface that reversed during the initial reversal from positive to negative field but then did not reverse back to the positive direction when the F layer did. For further magnetic cycles the film alternates between the states shown in fig. 7.8(b) and fig. 7.8(c).

This interpretation qualitatively describes Δm_s being larger before the first reversal than after. As well as that, it is also consistent with both $m_{s,i}^+$ and $m_{s,ii}^+$ being larger than m_s^- . However, it does not account for the effect of crystallographic texture. Texture is a preference in the preferred orientation of crystallites in a polycrystalline material. As discussed in section 3.3.1, the texture of the AF layer can alter and even eliminate ΔH_{c1} [37]. A film with out-of-plane fibrous $\langle 111 \rangle$ texture showed no training while a film with 3-D random texture did. The effect of texture can be included as a modification to the reversibility hypothesis.

In fig. 7.9 two interfacial spin arrangements are shown schematically [11, 37, 67]. In fig. 7.9(i) the spins are both aligned and parallel while in fig. 7.9(ii) the spins are aligned but not parallel. The overall moment of the parallel case is larger than the non-parallel case since the moment is measured parallel to the interface. Thus a difference between R_1' and R_1''' could be explained by a transition from a parallel to non-parallel alignment of interfacial spins as well as, or instead of, a difference in reversibility.

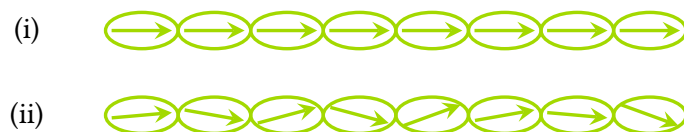


Figure 7.9: Schematic of the F/AF interface showing spins that are (i) parallel and (ii) aligned but not parallel [190].

The magnetic easy axis in IrMn is the $\{111\}$ planes [32]. This is shown by the increase in effective anisotropy when an IrMn polycrystalline thin film is grown with out-of-plane fibrous $\langle 111 \rangle$ texture [11, 32–36]. Thus the magnetisation of the AF sublattices will lie in the easy direction which will be parallel to the interface for a film with out-of-plane fibrous $\langle 111 \rangle$ texture. For this reason in CoFe/IrMn systems out-of-plane fibrous $\langle 111 \rangle$ texture is equivalently known as in-plane easy-

axis texture. Thus a film with in-plane easy-axis texture did not display training while a film with 3-D random texture did [37].

In an IrMn film with 3-D random texture the AF easy axes will be randomly distributed since each crystallite has its own easy axis direction. The magnetisation direction of an interfacial spin will be dependent on and parallel to the easy axis direction of the adjacent AF crystallite. This is a consequence of coupling to the AF layer by the exchange interaction.

During the setting process the F layer is saturated. Together with the setting temperature this orders the spins of the AF layer due to the exchange interaction and thermal activation over volume-dependent energy barriers [11]. After field cooling the interfacial spins are largely aligned and parallel [67, 91]. This parallel alignment is shown in fig. 7.9(i) and is maintained by the exchange interaction from the F layer and the dipole-dipole and RKKY exchange interactions of neighbouring spin clusters in a manner analogous to a thermoremanent state in a spin glass [193].

When the applied field is reversed the F layer reverses with it. The interfacial spins are then exposed to both a negative exchange field and a negative Zeeman energy. This results in some of the interfacial spins reversing.

When the field is again applied in the setting direction there is no further heating. This asymmetric process is the origin of the difference between the first and second measured loops. While the F layer will be saturated, the interfacial spins will not align parallel. They will revert to their local easy axes since there is insufficient thermal energy to align them parallel. This aligned but non-parallel state is shown in fig. 7.9(ii) where the spins are held along the crystalline easy axes by magnetocrystalline anisotropy. However, if the film has in-plane easy-axis texture then the magnetocrystalline anisotropy will act to align the spins in the plane of the film [13, 32–36]. Thus the interfacial spins will return to a state that is both aligned and parallel, as is shown in fig. 7.9(i). This hypothesis would result in no change between the $m_{s,i}^+$ and $m_{s,ii}^+$ states and means $\Delta H_{c1} = 0$. Thus fig. 7.9 can be considered to show the interface (i) in a film with in-plane easy-axis texture and (ii) with 3-D random texture after the first magnetic reversal [190].

As well as increasing Δm_s , a reduction in T increases the effect of training. The temperature dependence of the effect of training on Δm_s can be discussed in

terms of the temperature dependence of anisotropy given eq. (2.16) and eq. (2.20) in section 2.2.7, reproduced here,

$$\begin{aligned} K_F(T) &= K_F(0) \cdot \left(1 - \frac{T}{T_C}\right)^{\frac{1}{3}} \\ K_{AF}(T) &= K_{AF}(0) \cdot \left(1 - \frac{T}{T_N}\right) \end{aligned} \quad (7.7)$$

where K_F is the F anisotropy constant, K_{AF} is the AF anisotropy constant, T is the temperature, T_C is the Curie temperature and T_N is the Néel temperature [11, 13, 32, 38, 43, 47, 48]. It can be proposed that in the interfacial region a similar temperature dependence of anisotropy exists.

As the temperature is reduced the interfacial anisotropy increases. This results in an increase in the aligned fraction of the interface R'_I after setting as compared to at higher temperatures. In turn this increases $m_{s,i}^+$. After one magnetic cycle the interfacial spins are aligned in the positive field direction. As before, the increase in anisotropy at low temperatures increases the interfacial alignment. This is the cause of the temperature dependence of Δm_s discussed in section 7.2.1. However, the degree of alignment after a magnetic cycle is not the same as before due to the tendency for spins to reverse to the negative field direction and then remain there due to coupling to the AF layer. This tendency to reverse only once will be increased at low temperatures due to the increase in anisotropy. Also, the degree of alignment will be reduced due to the increased tendency for the interfacial spins to align with the anisotropy of the adjacent AF grain, which may not be parallel to the interface. Because of these two effects the condition of the interface between measurements of $m_{s,i}^+$ and $m_{s,ii}^+$ will become increasingly divergent as the temperature is decreased.

7.2.3 Effect of Interfacial Mn on m_s Offset

In section 7.2.1 and section 7.2.2 the film being discussed had an ultra-thin Mn dusting layer at the F/AF interface with $d_{Mn} = 0.05$ nm. This is equivalent to approximately one sixth of an atomic layer and therefore has the effect of a compositional variation at the F/AF interface. This film was discussed as it had the largest values of Δm_s and H_{ex} . The temperature dependence of Δm_s with and without training is shown in fig. 7.6. However, by varying d_{Mn} the interfacial

properties of the film can be adjusted. In this section, the effect of d_{Mn} on Δm_s will be discussed.

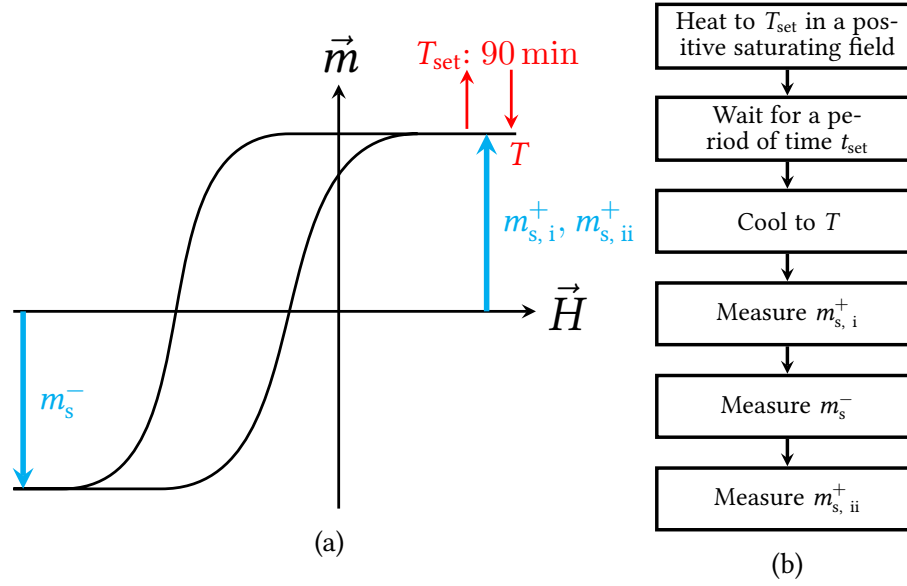


Figure 7.10: The measurement protocol to measure $m_{s,i}^+$, m_s^- and $m_{s,ii}^+$ shown (a) schematically and (b) as a series of steps.

As discussed previously, the procedure to measure Δm_s is shown schematically in fig. 7.5. This has been reproduced in fig. 7.10 with the addition of steps to measure both $m_{s,i}^+$ and $m_{s,ii}^+$. It is necessary to distinguish between $m_{s,i}^+$ and $m_{s,ii}^+$ due to the changes that occur due to training, which were discussed in section 7.2.2. The magnetisation offset before and after training is calculated using

$$\begin{aligned}\Delta m_{s,i} &= m_{s,i}^+ + m_s^- \\ \Delta m_{s,ii} &= m_{s,ii}^+ + m_s^-\end{aligned}\tag{7.8}$$

where $\Delta m_{s,i}$ is the magnetisation offset before training, $\Delta m_{s,ii}$ is the magnetisation after training $m_{s,i}^+$ and $m_{s,ii}^+$ are the saturation moments in the positive field direction before and after training and m_s^- is the saturation moment in the negative field direction which is not affected by training. Where Δm_s is to be measured without reference to training then $\Delta m_{s,ii}$ should be used to remove the effect of training. This is equivalent to the established use of the second hysteresis loop when measuring H_{ex} and H_c to remove the effect of training [11]. The measurement procedure is identical to the procedure described in section 7.2.1. This measurement was performed for films with composition Si/Ta (2)/Ru (2)/IrMn (10)/Mn (d_{Mn})/CoFe (5)/Ru (5) (thicknesses in nm) where d_{Mn} is the thickness of a Mn layer at the F/AF interface. The film structure is shown schematically in fig. 7.11(b). The resulting values of Δm_s are shown in fig. 7.11(a) [192]. These measurements

were made with a Quantum Design MPMS 3 VSM based at Diamond Light Source. The thickness dependence of Δm_s was reproduced by confirmatory measurements using a LakeShore 8600 Series VSM. As discussed in section 7.2.1 error bars are not shown due to the systematic nature of the errors.

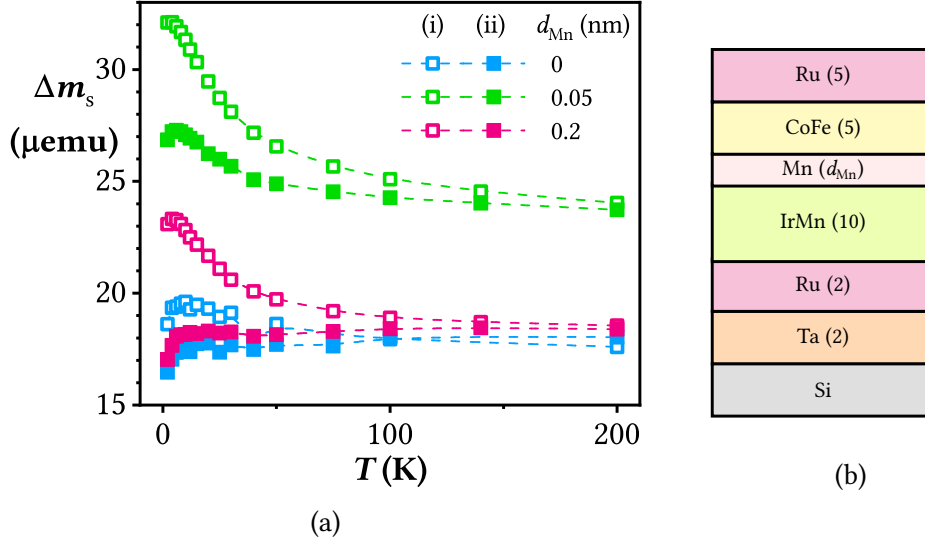


Figure 7.11: (a) The temperature dependence of Δm_s for the (i) first and (ii) second hysteresis loop for three films with (b) structure shown schematically (thicknesses in nm). The line is a guide to the eye [192].

There is a magnetisation offset for all three of the samples. The magnetisation offset after training, $\Delta m_{s, \text{ii}}$, is lower for $d_{\text{Mn}} = 0 \text{ nm}$ and 0.2 nm compared to that for $d_{\text{Mn}} = 0.05 \text{ nm}$. In addition, the temperature dependence is significantly different. For $d_{\text{Mn}} = 0 \text{ nm}$ and 0.2 nm there is no significant variation in $\Delta m_{s, \text{ii}}$ with temperature above $(50 \pm 2) \text{ K}$. This is in contrast to the temperature dependence of $\Delta m_{s, \text{ii}}$ for the sample with $d_{\text{Mn}} = 0.05 \text{ nm}$ which varies over the range from 2 to $\approx 100 \text{ K}$. Furthermore, the temperature dependence of $\Delta m_{s, \text{ii}}$ for $d_{\text{Mn}} = 0 \text{ nm}$ and 0.2 nm below $(10 \pm 2) \text{ K}$ is characterised by a reduction in $\Delta m_{s, \text{ii}}$ as the temperature is reduced. This does not show signs of saturating and reduces $\Delta m_{s, \text{ii}}$ at 2 K to 90 % of its value at 10 K. This is the opposite of the effect observed for the AF film where $d_{\text{Mn}} = 0.05 \text{ nm}$, for which $\Delta m_{s, \text{ii}}$ increased by 10 % when cooled from 200 to 2 K.

The proportional error in Δm_s is larger than that of either m_s^+ or m_s^- because Δm_s is the difference of these values. Thus although the absolute error is of the same order, the proportional error of Δm_s is larger due to the lower absolute value of Δm_s . A conservative estimate of the resolution of the Quantum Design MPMS 3 VSM is $\pm 0.5 \mu\text{emu}$. This corresponds to an error in Δm_s of $\pm 0.7 \mu\text{emu}$.

The difference between the magnetisation offset before and after training, $\Delta m_{s, i}$ and $\Delta m_{s, ii}$, for $d_{\text{Mn}} = 0.05$ nm was discussed in section 7.2.2. There the effect of training was to reduce the magnetisation offset after the first magnetisation reversal. This occurred below 100 K and was larger at lower temperatures. For the films where $d_{\text{Mn}} = 0.05$ nm and 0.2 nm, $\Delta m_{s, i}$ is higher than $\Delta m_{s, ii}$ after the first reversal up to ≈ 100 K. On the other hand when $d_{\text{Mn}} = 0$ nm the effect of training is not significant above ≈ 50 K. At low temperatures training reduces Δm_s between the first and second magnetisation loops for all three films and the largest changes occur at the lowest temperatures.

d_{Mn} (nm)	$\Delta m_s(2)$ (± 1) (μemu)		$\Delta m_s(200)$ (± 1) (μemu)		$\frac{\Delta m_{s, i}(2)}{\Delta m_{s, ii}(2)}$	$\frac{\Delta m_{s, ii}(2)}{\Delta m_{s, ii}(200)}$
	i	ii	i	ii		
	0	19	16	19	18	1.20
0.05	32	27	23	23	1.20	1.20
0.2	23	17	18	18	1.35	0.95

Table 7.2: Summary of $\Delta m_s(T)$ for films with different values of d_{Mn} (i) before and (ii) after training [192]. The film structure is shown schematically in fig. 7.11(b).

Table 7.2 shows $\Delta m_s(T)$ at 200 and 2 K before and after training [192]. The error in Δm_s is rounded up to $\pm 1 \mu\text{emu}$. Note that this error is systematic rather than random and arises from the resolution of the magnetisation measurement of the VSM. The ratio $\Delta m_{s, i}(2)/\Delta m_{s, ii}(2)$ is the proportional change in the value of Δm_s which is a result of the training effect when measured at 2 K. For all the films $\Delta m_{s, i}(2)/\Delta m_{s, ii}(2) > 1$ since the magnetisation offset is largest before the first magnetic reversal. The temperature dependence of $\Delta m_{s, ii}$ is given by the ratio $\Delta m_{s, ii}(2)/\Delta m_{s, ii}(200)$. This shows the value of $\Delta m_{s, ii}$ at 2 K compared to a the normalised value at 200 K. Since the error in Δm_s is systematic, the error in the ratio of Δm_s measurements cannot be calculated. The largest proportional reduction in Δm_s at 2 K due to training occurs for the F/AF film for which $d_{\text{Mn}} = 0.2$ nm. However, the magnitude of this reduction is the same as for $d_{\text{Mn}} = 0.05$ nm.

The peak in Δm_s implies that Δm_s is affected by two parameters with different temperature dependencies. The F material used in this study was $\text{Co}_{70}\text{Fe}_{30}$ which has a Curie temperature of (1040 ± 10) K [13, 25, 26]. The anisotropy constant of $\text{Co}_{70}\text{Fe}_{30}$ at room temperature is

$$K_{\text{CoFe}}(T_{295}) = (450 \pm 20) \times 10^3 \text{ erg/cm}^3 \quad (7.9)$$

for a single-crystal sample [25, 27]. The effective anisotropy will be lower for polycrystalline samples unless the film is strongly textured. The anisotropy constant of the IrMn films used in this study was calculated at room temperature in section 6.2.3 based on a measurement of $\langle T_B \rangle$ using the York Protocols. The AF easy axis is in the $\{111\}$ planes. The lowest value of $K_{AF}(T_{295})$ calculated was $(15 \pm 3) \times 10^6 \text{ erg/cm}^3$ which corresponded to the film for which $d_{Mn} = 0.05 \text{ nm}$. This exceeds the value of K_{CoFe} by a factor of ≈ 30 [11, 27].

As discussed in section 6.2.3 K_{AF} can be calculated for an arbitrary temperature T using

$$K_{AF}(T) = K_{AF}(T_{295}) \cdot \left(\frac{T_N - T}{T_N - T_{295}} \right) \quad (7.10)$$

where T_N is the Néel temperature which for IrMn is 690 K [4, 38]. Thus at 2 K the anisotropy of IrMn increased to $(26 \pm 5) \times 10^6 \text{ erg/cm}^3$. For an F material the same equation has the form

$$K_F(T) = K_F(T_{295}) \cdot \left(\frac{T_C - T}{T_C - T_{295}} \right)^{\frac{1}{3}} \quad (7.11)$$

where T_C is the Curie temperature [11, 13, 32, 38, 43, 47, 48]. The difference between T_N of IrMn and T_C of CoFe as well as the additional power of $1/3$ result in different rates of the temperature dependence of K_F and K_{AF} . At 2 K the anisotropy of CoFe increased to $(500 \pm 20) \times 10^3 \text{ erg/cm}^3$. Therefore at 2 K K_{AF} exceeds K_F by a factor of ≈ 50 . Interfacial spins are subject to competing F and AF interactions. As the temperature is reduced the AF anisotropy increases relative to the F anisotropy.

It has been hypothesised that the relationship between training and texture is a result of interfacial spins which are aligned during the setting procedure becoming unaligned during a magnetic reversal [11, 37, 190]. This was discussed in section 7.2.2 in the context of the change in Δm_s that occurs after the first magnetic reversal. However, the hypothesis is untested and unproven. In this model, the interfacial spins have internal F order. This was proposed to account for the \vec{H}_{set} dependence of H_{ex} which was discussed in section 3.4.1. This phenomenon occurs for fields much larger than the saturating field of the F layer. It is proposed that the increasing field increases the proportion of aligned spin clusters which increases the coupling between the F and AF layers [11, 91].

In this study an ultra-thin layer of Mn was added to the F/AF interface. This has the effect of altering the film composition near the interface because there is

insufficient additional Mn for it to form a distinct monolayer and because Mn will readily diffuse into the IrMn and CoFe layers. This diffusion will also occur for the Mn and Co in the adjacent layers forming a continuum of solid solutions [59]. At one end of this continuum there will be Mn-doped F phases while at the other there will be Co-doped AF phases.

The rate of diffusion is a function of temperature and results in a composition that evolves with time. This was discussed in section section 3.3.4. The temperature dependence of the diffusion coefficient was given in eq. (3.7), reproduced here

$$\mathcal{D}_d = \xi a^2 \omega_D \exp\left(-\frac{\Delta E_{\text{diff}}}{k_B T}\right) \quad (7.12)$$

where \mathcal{D}_d is the diffusion coefficient in the dislocation network, ξ is a dimensionless factor dependent on the lattice and of order unity, a is the lattice spacing, ω_D is the Debye frequency ΔE_{diff} is the energy barrier to moving an atom between sites, k_B is the Boltzmann constant and T is the temperature [105]. This contributes to a concentration gradient that evolves as given by eq. (3.8), reproduced here

$$C \propto \frac{1}{\sqrt{\mathcal{D}_d t}} \exp\left(-\frac{\delta^2}{4\mathcal{D}_d t}\right) \quad (7.13)$$

where t is time and δ is the diffusion depth of the tracer [97].

Likewise, in the York Model of Exchange Bias the setting of the AF layer is a function of both temperature and time as expressed by the Néel-Arrhenius law

$$\tau^{-1} = f_0 \exp\left[-\frac{\Delta E}{k_B T}\right] \quad (7.14)$$

where τ^{-1} is the relaxation time, f_0 is the attempt frequency ΔE is the energy barrier to reverse the magnetic order of an AF grain which is equal to $K_{\text{AF}} V_g$ where K_{AF} is the AF anisotropy, V_g is the AF grain volume. k_B is the Boltzmann constant and T is the temperature [11, 38, 146, 152]. This was discussed in section 4.2.4.

This results in a value of H_{ex} given by eq. (4.23), reproduced here

$$H_{\text{ex}}(\vec{H}_{\text{set}}, T_{\text{set}}) = H_{\text{ex}}^{\text{INT}} C^*(\vec{H}_{\text{set}}, T_{\text{set}}) \int_{V_c(T_{\text{NA}})}^{V_{\text{set}}(T_{\text{set}})} f(V_g) dV_g \quad (7.15)$$

where \vec{H}_{set} is the setting field, T_{set} is the setting temperature, $H_{\text{ex}}^{\text{INT}}$ is the intrinsic

exchange bias, C^* is the interfacial coupling parameter V_c is the volume of the smallest ordered grain at T_{NA} , T_{NA} is the temperature of non-activation, V_{set} is the volume of the largest grain that could be set during the setting process and $f(V_g)$ is the grain volume distribution. This is shown in fig. 4.11 where the grains in region (a) have volume lower than V_c and are disordered by thermal energy at T_{NA} , the grains in region (c) have volume larger than V_{set} and were not set during the setting process and the grains in region (b) contribute to exchange bias [11].

Thus in principle during the setting process there will be a competition between diffusive and magnetic ordering effects. A competition between two effects could explain the peaks shown in fig. 7.11. On one hand a high T_{set} and a long t_{set} will increase the number of set grains by increasing V_{set} and therefore H_{ex} [11]. On the other hand a larger T_{set} and longer t_{set} will allow more diffusion to occur which reduces H_{ex} [59]. In addition, longer annealing times are also correlated with a reduction in M_s [59]. In CoFe/IrMn diffusion results in the formation of a number of phases at the interface with complex magnetic behaviour due to the interdiffusion of Co and Mn. This results in the formation of CoMn which has both F and AF phases.

In CoMn at 4.2 K there is a transition from F to AF ordering which begins as the Mn content is increased above 30 at.% and is not complete until the Mn content reaches 45 at.% [63]. This transition takes place across a wider range of compositions at higher temperatures. This is shown in fig. 6.8 [63]. Between these concentrations CoMn is paramagnetic on large scales with local regions of F and AF order. The collective magnetic behaviours of the F regions is equivalent to superparamagnetism SP, meaning that single-domain F elements have an overall P behaviour [13]. Similarly, there are single-domain AF regions which are described as being superantiferromagnetic SAF [63]. Thus as the composition varies through the sample then overall the material will be mictomagnetic [65]. Furthermore, low temperature measurements made at 4.2 K show F and AF phases coexisting at 35 at.% Mn [195]. At 35 at.% Mn the CoMn alloy exhibited both a Néel and a Curie temperature where $T_N = (10 \pm 5) K$ and $T_C = (140 \pm 5) K$ [195]. These coexisting phases are significant enough to induce self-exchange bias at 4.2 K in cylindrical ingots 12.7 mm in length and 6.4 mm in diameter [64].

The phase diagram shown in fig. 6.8 is for CoMn alloys and will not be identical to the situation in CoFe/IrMn thin films [63]. However, it is indicative of

the interfacial region of CoFe/IrMn thin films due to the interdiffusion of Co and Mn [59]. For an un-annealed IrMn/Co system the Mn varies as a function of depth through the sample due to diffusion. The transition from 30 to 45 at.% Mn occurs on a length scale of ~ 1 nm [59, 63]. While it is not definitive, fig. 6.8 suggests that the addition of Mn will lead to an increase in AF order at the IrMn/CoFe interface. This will manifest both as bulk-like AF order and clusters of SAF order.

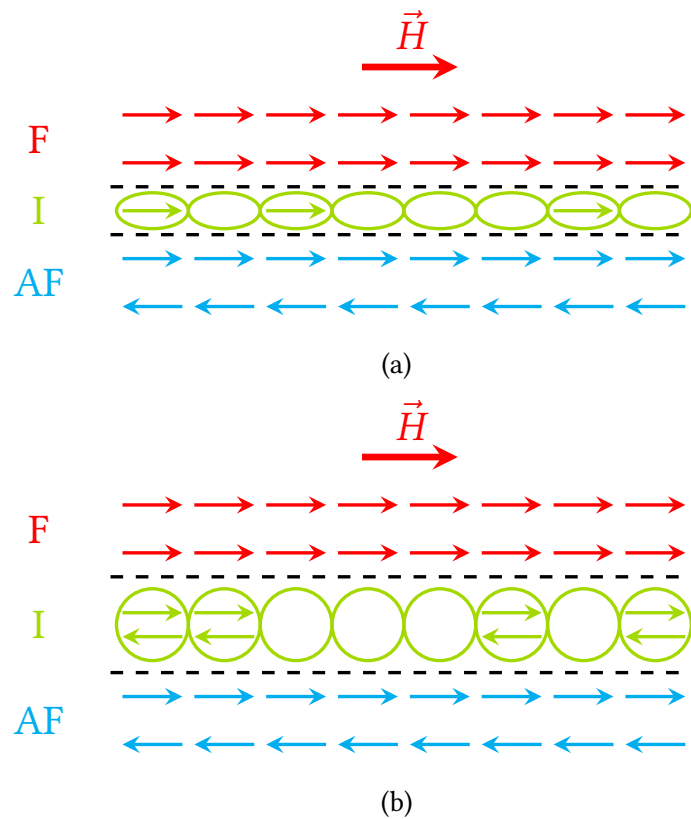


Figure 7.12: Schematic of the F/AF interface with (a) F and (b) AF spin clusters. The F spin clusters are shown as one atom thick while the AF spin clusters are shown as two atoms thick [190]. Spin clusters are shown both with and without moments to represent partial saturation which is indicated by the setting field dependence of H_{ex} [67].

Figure 7.12(a) is a schematic of the F/AF interface including an interfacial region with F clusters. The \vec{H}_{set} dependence of H_{ex} is a result of the order of the F spin clusters [11, 67, 91]. This was discussed in section 3.4.1. In contrast fig. 7.12(b) is a schematic of a F/AF interface with AF spin clusters [190]. These hypothetical structures could in principal mediate the coupling between the F and AF layers through their internal and external coupling. The coupling between the AF region and the interfacial spins would be negative direct exchange. The interfacial spins are internally ordered by negative direct exchange. The interfacial spins are coupled to the F region by positive direct exchange. The effective coupling across the

F/AF interface would therefore be by means of a proposed combination of F and AF coupling.

A requirement for ferromagnetic-antiferromagnetic (F-AF) coupling would be positive exchange coupling between the F layer and the interface, negative exchange coupling between the AF layer and the interface and for the interfacial region to be an even number of atomic layers thick, which is to say that opposite sublattices would be present at the F and AF interfaces. Therefore, if F-AF coupling is a significant factor in how the interface mediates the coupling between the F and AF layers then the coupling strength would be expected to oscillate as the thickness of the region alternates between even and odd parity [190]. Testing this hypothesis would require a large scale atomistic model with interfacial diffusion.

The low-temperature exchange bias behaviour of a CoFe/IrMn discussed in this chapter can be summarised as the increase in H_{ex} , H_{c} , ΔH_{c1} and Δm_{s} that occurs when the film is cooled below T_{NA} to $\approx 10\text{K}$. The increase in H_{ex} is the spin freezing effect discussed in section 3.4.3. This work shows that H_{c} , ΔH_{c1} and Δm_{s} have a similar temperature dependence. In addition, Δm_{s} was measured and shown to change between the first and second magnetisation reversal. The origin of this change was shown to be due to changes in m_{s}^+ while m_{s}^- remains constant. There is therefore a training effect in \vec{m} similar to the well-known training effect in \vec{H} discussed in section 3.2.2. Δm_{s} was shown to be most significant when $d_{\text{Mn}} = 0.05\text{ nm}$. The effect of training on Δm_{s} was largest at low temperatures $\approx 2\text{K}$ and when $d_{\text{Mn}} < 0\text{ nm}$.

It is known that there is significant interdiffusion between the F and AF layers [59]. This is a result of the sputtering process and room-temperature diffusion and further develops during annealing and setting as part of a York protocol measurement.

This results in the formation of an interfacial region with mixed phases. Studies in CoMn suggest the possibility of F, AF and P phases and clusters of local F and AF order in a P matrix [63]. Changes in H_{ex} , H_{c} , ΔH_{c1} and Δm_{s} are ongoing over a wide distribution of temperatures $5.5\text{K} < T < 100\text{K}$. This implies a wide distribution in cluster parameters such as volume or anisotropy.

Cooling the film in a field sufficient to saturate the F layer could have an ordering effect on the interface in a manner analogous to a thermoremanent state in a spin glass. This is shown by the fact that ΔH_{c1} and the training effect in Δm_s could be observed only after cooling in field and not by field or temperature alone. The spin alignment of this state is not known. Two hypotheses have been suggested. The first was shown in fig. 7.8 where the interface is aligned after cooling in field. During the magnetic reversal there are clusters which reverse once, twice or never which result in differing values for $m_{s,i}^+$, m_s^- and $m_{s,ii}^+$. The second was shown in fig. 7.9 where the interfacial moment changes from an aligned and parallel state to an aligned but non-parallel state [190]. These hypotheses do not contradict each other and neither has been ruled out. That said, the dependence of the training effect on texture discussed in section 3.3.1 supports the second hypothesis [37].

In order to produce a peak in a temperature dependence of Δm_s such as is shown in fig. 7.11 it is necessary that there be two competing effects with a different temperature dependence [192]. By proposing that the interfacial region is micro-magnetic and therefore contains both F and AF spin clusters, it can be hypothesised that these two effects are the temperature dependence of F and AF anisotropy.

It can also be hypothesised that the dependence of Δm_s on d_{Mn} is a result of F-AF coupling. Δm_s first increases and then decreases as d_{Mn} increases. This could speculatively be a period of an oscillation that would continue at larger values of d_{Mn} . This could be confirmed by further low temperature measurements of Δm_s for films with modified interfacial compositions.

In addition, Δm_s has been shown to be dependent on T . Only a small portion of fig. 6.8 shows the expected magnetic behaviour of CoMn below 300 K. However, it shows that as T is reduced P phases will tend to give way to SP and superantiferromagnetic (SAF) phases. Structurally these resemble F and AF spin clusters. Thus as T decreases the number and size of spin clusters will increase. This will increase the importance of spin clusters in mediating the exchange across the F/AF interface.

That said, the origin of the peaks in fig. 7.11 cannot be conclusively explained without knowledge of the phases of the interface. This explanation would be related to the diffusion of Mn from the IrMn layer and the replenishment of Mn as d_{Mn} increases. To resolve this a large-scale diffusive atomistic model would be

required to establish the role of interfacial spin clusters. Such a model would be beyond the scope of this work.

7.2.4 Ferromagnetic-Antiferromagnetic Coupling

The hypothesised mechanism of ferromagnetic-antiferromagnetic (F-AF) coupling via AF spin clusters is worth discussing in the context of the measurements made in this study. In section 6.1 the irreversibility of exchange bias was discussed. There it was observed that the value of H_{ex} achieved during the setting process was reduced after the first setting process. In order to reproduce the initial H_{ex} in the opposite direction, it was necessary to set in a reverse field for ~ 17 times as long. It is known that at thermal annealing increases the diffusion of Mn and Co across the interface of a CoFe/IrMn system [59]. Thus diffusion occurring during the setting and aligning processes cannot be ruled out. If diffusion is occurring then the interfacial composition will be varying throughout the measurement. Thus the ratio of F and AF spin clusters will be altered which will affect the interfacial coupling and thus the value of H_{ex} .

In section 6.2 measurements were made that showed the dependence of H_{ex} on d_{Mn} . This could be the result of the proportions of F and AF spin clusters changing as d_{Mn} is increased. As more Mn is added the interface will tend towards more AF behaviour. This would change the interfacial coupling and hence H_{ex} .

Diffusion and d_{Mn} are not the only factors that could change the proportions of F and AF spin clusters. The temperature dependence of F and AF anisotropy is given by eq. (7.10) eq. (7.11), reproduced here

$$K_{\text{F}}(T) = K_{\text{F}}(T_{295}) \cdot \left(\frac{T_{\text{C}} - T}{T_{\text{C}} - T_{295}} \right)^{\frac{1}{3}} \quad (7.16)$$

$$K_{\text{AF}}(T) = K_{\text{AF}}(T_{295}) \cdot \left(\frac{T_{\text{N}} - T}{T_{\text{N}} - T_{295}} \right)$$

where K_{F} and K_{AF} are the F and AF anisotropies, T is the measurement temperature, T_{295} is room temperature, T_{C} is the Curie temperature of the F material and T_{N} is the Néel temperature of the AF phase [11, 13, 32, 38, 43, 47, 48]. These show that K_{F} and K_{AF} do not change at the same rate and therefore the proportions of F and AF spin clusters will vary with temperature. This has implications for the spin

freezing effect which is the increase in H_{ex} as T is reduced. This is correlated with an increase in H_c and ΔH_{c1} and was discussed in section 3.4.3 and section 7.1.

As discussed in section 7.2.3, Δm_s could be a result of a mixture of F and AF spin clusters. The temperature dependence of Δm_s can be hypothesised to originate in a transition from AF to F clusters as the temperature is reduced. This results in a decrease in the interfacial moment and thus a decrease in Δm_s . Furthermore the dependence of Δm_s on d_{Min} could be a result of a thickness dependence of internal F and AF spin cluster order which is a result of the even or odd layer thickness of the spin clusters.

The coercivity of a F film is increased when it is coupled to an AF layer [69, 73]. This was discussed in section 3.1.3. This could be the effect of non-reversible AF spin clusters acting as pinning sites for domain walls in the F layer. However, further measurements would be required to establish if this is the case.

The training effect is the change in H_{c1} between the first and second hysteresis loops [80]. This was discussed in section 3.2.2, section 7.1 and section 7.2.2. In negative saturation the moment of the F layer is reversed. However, below T_{NA} there is no change in the alignment of the spin order of the bulk of the AF grains [11]. Thus the spins at the F/AF interface will be subject to opposite influences from the adjacent layers. This could result in a transition from F to AF spin cluster order. This reduction in F order at the interface could reduce the interfacial coupling and therefore H_{ex} .

8. Conclusions and Further Work

A number of phenomena which have not been previously measured systematically or explained have been described in the course of this work for the first time. These can be summarised as

1. H_{ex} has been shown to be irreversible under thermal activation as discussed in section 6.1.
2. The well-known spin freezing of H_{ex} is accompanied by a similar spin freezing effect of H_c and ΔH_{c1} over the same temperature range, as discussed in section 7.1.
3. A magnetisation offset Δm_s has been measured in an exchange bias multilayer film containing IrMn. Furthermore, the temperature dependence of Δm_s was measured, as discussed in section 7.2.1.
4. A training effect in Δm_s has been shown to exist as discussed in section 7.2.2 which is analogous to the training effect in the field offset ΔH_{c1} .
5. The training effect in ΔH_{c1} and Δm_s can be recovered by field-cooling the film from a temperature below the activation temperature of the bulk of the AF grains as discussed in sections 7.1 and 7.2.
6. The training effect in Δm_s has been shown to be asymmetric, originating from changes in m_s^+ before and after magnetic reversal while m_s^- remains constant, as discussed in section 7.2.2.
7. The effect of interfacial Mn doping was measured as the magnitude and temperature dependence of Δm_s and the training in Δm_s for films of varied interfacial composition, as discussed in section 7.2.3.

This builds on previous work on exchange bias in polycrystalline CoFe/IrMn thin films summarised in chapter 3 which shows that exchange bias is a multifaceted effect much broader than the exchange field itself. The York Model of Exchange Bias has been successful in describing the behaviour of the bulk of the AF grains as discussed in chapter 4 [11]. The phenomena discussed in this work can be explained by Mn diffusion at the F/AF interface. The preferential diffusion of Mn increases the interfacial stiffness and changes the composition of the AF layer in the region of the interface [59]. Mn enrichment of the IrMn can increase or decrease H_{ex} and K_{AF} [53]. In addition, diffusion results in the formation of mixed magnetic phases of CoMn at the F/AF interface [63]. This results in a wide distribution of spin cluster freezing temperatures [11].

It was shown in section 6.1.1 that the setting process is not reversible, meaning that H_{ex} in the reverse setting direction was lower than in the first setting direction when set for the same time. The setting was shown to be logarithmic in section 6.1.4. The reversibility of the film was maximised when 0.05 nm of Mn was added to the F/AF interface but decreased at greater thicknesses, as shown in section 6.2.1. This is probably a consequence of diffusion during the setting process which increases K_{AF} and therefore $\langle T_{\text{B}} \rangle$ [11, 59]. This interpretation is supported by the study of Aley et al. [53].

The median AF grain blocking temperature was measured for films with varied thickness of interfacial Mn using the York Model of Exchange Bias and were discussed in section 6.2. In this measurement the spin order of the AF film is progressively reversed. These showed a dependence of H_{ex} , $\langle T_{\text{B}} \rangle$ and K_{AF} on the amount of interfacial Mn. The maximum H_{ex} measured was (1260 ± 10) Oe for a film with 0.05 nm of Mn added to the F/AF interface. This film had median blocking temperature (532 ± 3) K, the lowest of the measured films. This is probably due to a combination of diffusion resulting in an increase in AF anisotropy and changes to the F/AF interface [53]. This is consistent with the work of Letellier et al. [59].

The spin freezing effect was demonstrated at low temperatures in section 7.1. The large number of measurements at low temperatures confirms that H_{ex} does not saturate. In fact H_{ex} continues to increase each time the temperature is reduced. The effect of spin freezing on H_{c} and ΔH_{c1} was also measured. They showed a similar increase as T was reduced. The increase in ΔH_{c1} as temperature is reduced confirms that it is not a result of thermal activation of the AF bulk.

The extent to which these properties are affected by temperatures below T_{NA} is indicative of their dependence on interfacial effects. H_{ex} is strongly dependent on interfacial contributions since at 5.5 K it has been increased by $\approx 50\%$ over its value at room temperature. ΔH_{c1} is almost entirely dependent on interfacial effects since the effect is ≈ 20 times larger at 5.5 K compared to at 300 K. H_{c} has an intermediate dependence of the interface, increasing by a factor of ≈ 4 when cooled from 300 to 5.5 K.

The existence of a magnetisation offset in CoFe/IrMn exchange bias thin films has been demonstrated and measured in section 7.2. This confirms the existence of irreversible spins in exchange bias systems. The irreversibility of these spins means they cannot be part of the F bulk. On the other hand their net moment means they cannot be part of a conventional AF bulk. Thus the spins must exist at the F/AF interface as an effective surface moment of the AF layer.

The magnetisation offset has been shown to be sensitive to the composition of the F/AF interface in section 7.2.3. This indicates that the effect originates in this region. The temperature dependence of the magnetisation offset was also observed. Changes in Δm_{s} were ongoing in the range 2 to 50 K. This showed that the temperature dependence is widely distributed.

The athermal training effect has been understood as a reduction in ΔH_{c1} between the first and second magnetic reversals. It must now also be understood as a reduction in the magnetisation offset of the hysteresis loop. This was discussed in section 7.2.2.

The effects described in this work imply the existence of AF spin clusters or superantiferromagnetic phases at the interface between the F and AF layers in thin films of CoFe/IrMn. These AF spin clusters coexist with F spin clusters and both mediate the coupling between the F and AF layers. In the case of F spin clusters this is through direct exchange and the RKKY interaction while AF spin clusters could hypothetically couple the layers through a combination of F and AF coupling as described in section 7.2.4. This is consistent with the work of Men'shikov et al. [63]. However, direct evidence of AF spin clusters does not yet exist and will be the subject of further research.

8.1 Further Work

Given the complex nature of exchange bias and the large number of new phenomena described in this work there is significant research still to do. The main obstacle to analysis in the CoFe/IrMn system is in the chemical analysis of the materials. This is due to the fact that Ir does not dissolve in any acid which makes conventional chemical analysis impossible [51]. In addition, the diffusion of chemical species into adjacent layers underlines the importance of measuring the composition of the film as a function of depth [59]. At this time the most effective tool for such a measurement is atom probe tomography. At the time of writing a research grant application is in preparation for a study of this kind. However, atom probe tomography has a number of drawbacks including its high cost and the fact it requires the destruction of the sample. Cross-sectional TEM is a cheaper alternative to atom probe tomography although similarly destructive.

Atom probe tomography can be used to measure the concentration profile of each atomic species as a function of depth [59]. Use of this technique could show the temperature and grain size dependence of diffusion in CoFe/IrMn thin films. In addition, this would measure the stoichiometry of CoFe and IrMn after sputtering, which in the case of IrMn is non-trivial. In addition, atom probe tomography can be performed on prepared samples with cross-sectional area of $5 \times 5 \text{ nm}^2$ which in principle allows composition to be measured on a grain-by-grain scale [59].

In this work the magnetic phase diagram of CoMn was used as indicative of the phases that exist at the CoFe/IrMn interface [63, 195]. However, these phase diagrams have a small number of measurements at $< 300 \text{ K}$. Because of this there is a limit to how useful these phase diagrams can be. A full study of the magnetic phase diagram of CoMn below 300 K and between 30 and 40 at.% Mn would improve the reliability of the conclusions of this work. Of course a phase diagram for CoMn does not include Fe, which will play a significant role in diffusion CoFe/IrMn films. This is both because of the diffusion of Fe and because of its effect on the overall crystallographic order. Thus a low temperature phase diagram for CoFeMn or CoFeMnIr films would improve the reliability of the conclusions of this work.

It may be possible to limit diffusion across the F/AF interface using a diffusion barrier. It is known that Cu does not diffuse into CoFe [59]. By placing a layer of

Cu or another metal at the CoFe/IrMn interface the diffusion between layers may be inhibited. However, Cu is unsuitable in this system since it has been shown that Cu at the F/AF interface reduces H_{ex} [94]. Thus a diffusion barrier material has to meet three criteria, these being not diffusing into the F or AF layer, preventing the diffusion of the F and AF material and not reducing the exchange coupling across the F/AF interface. Identifying this material would require a combination of York Protocol techniques to measure the exchange bias of the films and cross-sectional TEM or atom-probe tomography to investigate diffusive behaviour. Potential materials that may be suitable are known to increase or at least not reduce H_{ex} are Fe, Ni and Ni₈₀Fe₂₀ also known as permalloy [93].

The low temperature measurements described in this work could be both repeated and extended. This work has discussed the importance of phenomena that occur below the temperature of liquid nitrogen and demonstrated changes that are ongoing <10 K. A LakeShore 8600 Series VSM with a measurement temperature range between 5.5 and 400 K has been purchased for this reason. However, due to social distancing guidelines and workplace shutdowns caused by the 2019-2020 pandemic it has not been possible to undertake these measurements in the timescale of the project.

Because the majority of the effects observed in this work and their interpretation is based on diffusion of Mn at the interface, firm conclusions can only be drawn once the extent of the diffusion is known. This will require the use of 3-D atom probe tomography or cross-sectional TEM studies to determine the precise degree of diffusion under different conditions such as annealing and the use of diffusion barriers. In addition, once the degree of diffusion can be established for different samples, it will be necessary to use atomic scale computer modelling to determine the atomic state of the resulting CoMn alloys that form [58]. This would allow a significant extension to the work of Men'shikov et al., particularly at low temperatures [63].

A research plan has been drawn up to undertake such studies in the interface.

List of Acronyms and Abbreviations

Notation	Description
AF	antiferromagnetic. 2, 3, 6, 9, 10, 16, 18–27, 30–33, 38, 40, 41, 43–47, 50, 53–56, 58–74, 76–95, 101, 108, 116, 118, 122–151, 153, 155–157, 159–186
bcc	body-centred cubic. 11
BF	bright-field. 79, 80, 114, 115
CCD	charge-coupled device. 112
cgs	gram-centimetre-second unit system. 5, 6, 143
DF	dark-field. 79, 114, 115
DMI	Dzyaloshinskii-Moriya interaction. 9, 10
DRAM	dynamic random-access memory. 2
emf	electromotive force. 117
F	ferromagnetic. 2, 3, 6, 7, 9, 11, 13, 14, 16, 18–27, 30, 31, 33, 36–38, 41, 44, 46, 47, 50, 53–56, 58–72, 74, 76–79, 82, 86, 91–95, 101, 105, 118, 126, 131–133, 135–141, 147–151, 153–171, 173–181, 183–186
fcc	face-centred cubic. 12, 13, 29, 36, 37, 45, 89, 105, 106, 157
FIB	focused ion beam. 113
FOM	figure of merit. 109, 110
FWHM	full-width of half-maximum. 43, 44, 103
GMR	giant magnetoresistance. 1–3, 23, 27, 42
HAMR	heat-assisted magnetic recording. 2
hcp	hexagonal close-packed. 13, 18
HDD	hard disk drive. 1–3, 23, 58, 73

Notation	Description
HiTUS	high target utilisation sputtering. 28, 44, 53, 80, 84, 96, 98, 99, 112, 115, 119
LabVIEW	Laboratory Virtual Instrument Engineering Workbench. 116
MFC	mass flow controller. 97
MPMS	magnetic property measurement System. 96, 119–121, 149, 158, 172
MRAM	magnetoresistive random-access memory. 2
P	paramagnetic. 31, 66, 118, 141, 147, 164, 176, 178, 179
RF	radio frequency. 97, 98, 100
RKKY	Ruderman-Kittel-Kasuya-Yosida. 9, 79, 131–133, 160, 169, 184
rms	root mean square. 48
SAF	superantiferromagnetic. 147, 176, 177, 179, 184
SI	international system of units. 5, 6
SP	superparamagnetic. 147, 179
SQUID	superconducting quantum interference device. 96, 120, 121
TEM	transmission electron microscope. 4, 79, 80, 84, 96, 99, 111–115, 138, 185, 186
TMR	tunneling magnetoresistance. 1, 2, 23, 27
VSM	vibrating sample magnetometer. 96, 117–121, 149, 158, 172, 173, 186
XRD	X-ray diffractometer. 4, 29, 96, 103–105, 108, 110, 127, 131, 140, 157
XRR	X-ray reflectivity. 108–110

List of Symbols and Units

Notation	Description
A_{AF}	area of an AF grain. 63, 64
A_c	area of coil. 117
A_{rms}	area of the surface of spherical, rms displacement of a diffusing material. 48
C^*	interfacial coupling parameter in the York Model of Exchange Bias. 3, 80, 83, 85, 86, 88, 90–92, 130, 132, 136, 147, 150, 151, 175, 176
C	concentration gradient. 50, 51, 175
D_a	diameter of aperture. 112
D_g	diameter of grain. 49, 78, 79, 86, 99, 116, 117, 131
E_J	coupling energy. 64
E_K	anisotropy energy density. 64
E_{AF}	energy of an AF grain. 63
E_I	interfacial energy. 61, 62, 66
E_{ex}	exchange energy. 7
E_{ms}	magnetostatic energy. 21
E_u	energy of a uniaxial single domain particle in the Stoner-Wohlfarth model. 17
$F_{n-1,n}$	function of the incident angle and refractive indices of adjacent layers in the Parratt recursive formula. 109
G	distribution function for E_K and E_J in the Fulcomer and Charap model of exchange bias. 64
H_K^*	pseudo-anisotropy field. 78, 80
H^*	exchange field from the F layer. 76, 78, 80

Notation	Description
H_K	anisotropy field. 12, 16–18, 165
H_{c1}	first point of reversal to negative saturation. 33, 35–37, 39–42, 61, 62, 91, 118, 134, 152, 154, 181
H_{c2}	second point of reversal to positive saturation. 33, 35–37, 39, 41, 42, 61, 62, 91, 118, 134
H_c	coercivity. 13, 33, 37–39, 42, 51, 54, 55, 59, 61, 62, 64, 65, 68, 74, 91, 118, 119, 126, 134, 135, 137, 149, 152–155, 158, 171, 178, 181–184
H_{ex}^A	initial exchange bias. 125, 126, 129, 144
H_{ex}^B	final exchange bias. 125, 126, 129, 144
H_{ex}^{INT}	intrinsic exchange field. 83, 92, 93, 130, 131, 150, 175
H_{ex}	exchange field. 23, 27, 28, 30–33, 35, 36, 38–40, 42–47, 51, 53–56, 58, 59, 61–64, 66–69, 73–77, 79, 80, 82–94, 118, 122–126, 128–142, 144–150, 152–155, 158–160, 163, 170, 171, 174–178, 180–184, 186
H_i	exchange field at the interface. 91–94
J_K	exchange anisotropy. 23, 47, 61–63, 145, 146
J_{ex}	exchange integral. 7, 8, 26, 27, 29, 95
J_{net}	effective interfacial coupling per spin in the Stiles and McMichael model of exchange bias. 66
K_{CoFe}	ferromagnetic anisotropy constant of CoFe. 173, 174
K_{AF}	effective antiferromagnetic anisotropy. 20, 23–25, 28, 32, 40, 45, 61–63, 68, 73, 78–82, 84, 88–90, 123, 127, 131, 136, 137, 140, 142–148, 170, 174, 175, 180, 183
K_F	effective ferromagnetic anisotropy. 24, 62, 72, 73, 170, 174, 180
K_{SC}	anisotropy of interfacial spin clusters. 165
K_u	uniaxial anisotropy of a single domain particle in the Stoner-Wohlfarth model. 12, 17, 18
K	anisotropy energy density. 12

Notation	Description
L	Langevin function. 93
N_d	demagnetising factor. 21
N_{AF}	number of AF grains. 64
N_F	number of F layers. 161, 166, 167
N_S	number of spins. 66, 93, 94
N_c	number of turns of coil. 117
N_q	frequency constant of the quartz piezoelectric crystal. 101
$N_{\bar{H}}$	number of magnetisation cycles. 38
R_I	reversibility of the F/AF interface. 161–163, 166–168, 170
R_{ex}	reversibility of exchange bias. 125, 126, 129, 144–147
$R_{n,n+1}$	function of ψ_{n-1} and reflected intensity for a layer and the layer above in the Parratt recursive formula. 109
$R_{n-1,n}$	function of ψ_{n-1} and reflected intensity for a layer and the layer below in the Parratt recursive formula. 109
S_{AF}	antiferromagnetic time dependence coefficient. 71, 72
S_F	ferromagnetic time dependence coefficient. 69, 70
T_{295}	room temperature. 143, 173, 174, 180
T_B^{MAX}	maximum blocking temperature. 40, 43, 44, 55, 56, 76, 77, 83
T_B	blocking temperature. 40, 43, 55, 59, 64, 67, 70, 71, 76–78, 80, 81, 84, 88, 90, 93, 126, 127, 134, 139, 142–148, 174, 183
T_C	Curie temperature. 8, 11, 13, 24, 26, 31, 39, 132, 150, 170, 174, 176, 180
T_{NA}	temperature of non-activation. 4, 5, 40–42, 56, 73–77, 82–84, 87, 91, 122–128, 130–132, 137, 138, 140, 145, 146, 148–150, 152, 154–157, 159, 161, 162, 164, 167, 175, 176, 178, 181, 184

Notation	Description
T_N	Néel temperature. 8, 20, 25–27, 31, 45, 46, 60–63, 66, 67, 71, 73, 78, 81, 82, 123, 130, 132, 143, 170, 174, 176, 180
T_{act}	activation temperature. 75–77, 91–93, 125, 137, 138, 144
T_{al}	aligning temperature. 87, 88, 127, 128, 131, 135
T_{set}	setting temperature. 74, 82–84, 86, 87, 93, 123, 124, 127, 130, 131, 137, 138, 144, 145, 150, 151, 156, 157, 175, 176
T	temperature. 15, 24, 25, 50, 51, 56, 57, 59, 69, 70, 72, 78, 82, 83, 92, 123, 130, 131, 143, 148, 150–153, 155, 156, 158, 162–165, 169, 170, 173–175, 178–181, 183
V_{SC}	volume of a spin cluster. 165
V_{al}	the largest grain volume that is set after a given time t_{al} . 131
V_{c}	the critical volume below which a grain is thermally active in the York Model of Exchange Bias. 82–85, 123, 124, 126, 130, 131, 140, 146, 150, 175, 176
V_{f}	volume of film. 64
V_{g}	volume of grain. 17, 72, 76–78, 80, 82–84, 88–90, 92, 116, 123, 126, 130, 131, 136–138, 140, 142–144, 146, 148, 150, 175, 176
V_{set}	the smallest grain volume that is too large to set at a given T_{set} in the York Model of Exchange Bias. 82–85, 123, 126, 130, 131, 140, 145, 146, 150, 175, 176
Z_{a}	acoustic impedance ratio. 101
Z	atomic number. 113
ΔE_{SC}	activation energy for an interfacial spin cluster. 165
ΔE_{diff}	bulk diffusion coefficient. 50, 175
ΔE	activation energy. 17, 70–72, 78, 82, 89, 123, 136, 144–146, 175

Notation	Description
ΔH_{c1}	athermal training effect. 33, 39–41, 91, 118, 124, 126, 140, 149, 152–155, 168, 169, 178, 179, 181–184
$\Delta \vec{k}$	scattering vector $\vec{k}_{\text{out}} - \vec{k}_{\text{in}}$. 104
ΔM_s	magnetisation offset $ M_s^+ - M_s^- $ of a hysteresis loop. 57
Δm_s	magnetisation offset $ m_s^+ - m_s^- $ of a hysteresis loop. 57, 156–159, 162–165, 167–174, 178, 179, 181, 182, 184
$\Delta m_{s, \text{ii}}$	magnetisation offset of a hysteresis loop after training. 171–173
$\Delta m_{s, \text{i}}$	magnetisation offset of a hysteresis loop before training. 171, 173
α_{AF}	angle of the AF magnetisations in the Meiklejohn and Bean model of exchange bias. 61
α	direction cosine. 12
$\beta_{\vec{M}}$	angle of the F magnetisation in the Meiklejohn and Bean model of exchange bias. 22, 61, 62
δ	depth of diffusion. 51, 175
ϵ	geometric correction factor. 117, 118
$\frac{d\sigma}{d\Omega}$	differential cross-section. 113
\hat{u}	unit vector of the AF easy axis direction. 65, 66
\hbar	reduced Planck constant. 7
λ_{R}	relativistically corrected wavelength. 113
λ	wavelength. 102, 103, 112
K_{α_1}	Siegbahn notation for the K-L ₃ transition. 103, 104
\mathcal{D}_{b}	bulk diffusion coefficient. 48, 49
\mathcal{D}_{d}	diffusion coefficient in the dislocation network. 48–51, 175
\mathcal{D}	diffusion coefficient. 48
μ_{f}	shear modulus of film. 101
μ_{q}	shear modulus of quartz. 101
μ_{B}	Bohr magneton. 93, 161, 166, 167
ω_{D}	Debye frequency. 50, 175

Notation	Description
ω	XRD axis expressing the out-of-plane sample rotation in $2\theta_\chi$ - ϕ geometry. 106
ϕ_F	angle of the F magnetisation to the F easy axis. 22, 63
ϕ_R	Rutherford scattering angle. 113
$\phi_{\vec{M}}$	angle between the applied field and particle magnetisation in the Stoner-Wohlfarth model. 15–18
ϕ	XRD axis expressing the in-plane sample rotation in $2\theta_\chi$ - ϕ geometry. 106
π	circle constant. 62, 78, 101, 113, 116
ψ_{AF}	angle of the AF easy axis in the Fulcomer and Charap model of exchnage bias. 63
ψ_F	angle between the magnetisation and the major axis of a particle in the Stoner-Wohlfarth model. 15
ψ_{n-1}	function of wavelength, incident angle, layer thickness and index of refraction for a layer in the Parratt recursive formula. 109
ρ_f	density of film. 101, 109–111
ρ_q	density of quartz. 101
σ_{DW}	domain wall energy per unit area in the Stiles and McMichael model of exchange bias. 66
σ_f	film roughness. 109–111
σ	standard deviation. 116
τ^{-1}	relaxation time. 70, 78, 175
θ_0	screening parameter. 113
θ_χ	XRD axis expressing the in-plane angle of the reflected X-ray in $2\theta_\chi$ - ϕ geometry. 106
θ_{AF}	angle of the AF sublattice magnetisation in the Fulcomer and Charap model of exchnage bias. 63
θ_P	angle between the major axis of a particle and the applied field in the Stoner-Wohlfarth model. 15

Notation	Description
θ_R	angular resolution. 112
θ_i	angle of incidence. 102, 104, 106, 114
$\theta_{\vec{H}}$	angle of the applied field \vec{H} in the Meiklejohn and Bean model of exchange bias. 36, 37, 61
$\theta_{\vec{M}}$	angle of the saturation magnetisation to the applied field. 14
α	XRD axis expressing out-of-plane rotation in pole figure geometry. 106, 107
β	XRD axis expressing in-plane rotation in pole figure geometry. 106, 107
Φ_0	magnetic flux quantum. 121
Φ	magnetic flux. 117, 121
\vec{B}	magnetic flux density. 67
\vec{H}_{act}	activation field. 125
\vec{H}_{set}	setting field. 53, 54, 83, 86, 93, 94, 124–127, 130, 132, 138, 150, 151, 156, 157, 174, 175, 177
\vec{H}_d	demagnetising field. 21
\vec{H}	magnetic field. 13–17, 19, 22, 33, 37, 40, 55, 61, 62, 69, 70, 117, 149, 150, 154, 159, 164, 167, 178
\vec{M}_0	initial magnetisation. 69
\vec{M}_F	F magnetisation. 15, 65, 66
\vec{M}	magnetisation. 12–14, 16, 17, 21–23, 33, 37, 40, 61, 62, 69, 71, 86, 117, 118, 165
\vec{P}_0	initial AF order parameter. 71
\vec{P}_1	interfacial order parameter. 93
\vec{P}	AF order parameter. 71
\vec{S}	total spin angular momentum. 7
\vec{k}_{in}	incident wavevector. 104
\vec{k}_{out}	reflected wavevector. 104
\vec{m}_{AF}	magnetic moment. 25
\vec{m}_I	magnetic moment at the interface. 66
\vec{m}	magnetic moment. 24, 36, 37, 53, 64, 78, 91, 118–120, 156, 158, 159, 164, 178
ξ	dimensionless factor of order unity. 50, 175
a_{CoFe}	lattice parameter of CoFe. 22, 157, 160, 163

Notation	Description
a_{IrMn}	lattice parameter of IrMn. 22, 157, 160, 163
a_{\circ}	major semi-axis of an ellipse. 15
a	lattice parameter. 50, 66, 102, 175
b_{\circ}	minor semi-axis of an ellipse. 15
c_{I}	contact fraction in the Fulcomer and Charap model of exchange bias. 63, 64
d_{CoFe}	thickness of CoFe film. 118
d_{Mn}	thickness of Mn ultra-thin interfacial layer. 46, 53, 101, 138–140, 142, 144–148, 150, 155, 170–174, 178–181
d_{AF}	thickness of AF film. 59, 62–64, 67–69, 78, 79, 81, 84, 86
d_{F}	thickness of F film. 23, 62
d_{f}	thickness of film. 101, 109–111, 116
d_{gb}	thickness of the grain boundary. 48
d_{hkl}	separation of crystal planes. 102, 160
d_{seed}	thickness of seed layer. 44
f_0	attempt frequency. 70–72, 78, 80, 81, 84, 90, 131, 142, 143, 175
f_c	resonant frequency of the film-coated system. 100, 101
f_q	resonant frequency of quartz piezoelectric crystal. 100, 101
h	Miller index. 102, 160
k_{B}	Boltzmann constant. 50, 70–72, 78, 80, 84, 90, 93, 131, 142, 143, 175
k	Miller index. 102, 160
l	Miller index. 102, 160
m_{f}	mass of film. 100
m_{q}	mass of quartz piezoelectric crystal. 100
r_{3d}	radius of the 3d shell. 7
r_{a}	atomic radius. 7
r_{B}	Bohr radius. 113
t_{act}	activation time. 75, 76, 90, 93, 125, 129, 133, 138, 142, 143

Notation	Description
t_{al}	aligning time. 87, 88, 127–131, 133–135
t_{m}	measurement time. 71, 72, 84
t_{set}	setting time. 84, 86, 87, 93, 124, 127–131, 135, 137, 138, 151, 157, 176
t	time. 38, 48–51, 64, 69, 71, 74, 75, 80, 88, 117, 124, 131, 138, 175
M_{s}	saturation magnetisation. 12–14, 16–18, 51, 52, 56, 57, 64, 68, 70, 118, 165, 176
M_{s}^{+}	saturation magnetisation in the + direction. 56, 57
M_{s}^{-}	saturation magnetisation in the – direction. 57
$M_{\text{s,ii}}^{+}$	saturation magnetisation in the + direction after one magnetic reversal. 165
$M_{\text{s,i}}^{+}$	saturation magnetisation in the + direction before the first magnetic reversal. 165
\mathcal{E}	induced electromotive force (emf). 117
m_{s}	saturation magnetic moment. 56
m_{s}^{+}	saturation magnetic moment in the + direction. 56, 57, 156–165, 167, 172, 178, 182
m_{s}^{-}	saturation magnetic moment in the – direction. 57, 156–159, 161–168, 171, 172, 178, 179, 182
$m_{\text{s,ii}}^{+}$	saturation magnetic moment in the + direction after one magnetic reversal. 165–171, 179
$m_{\text{s,i}}^{+}$	saturation magnetic moment in the + direction before the first magnetic reversal. 165–171, 179
K-L ₃	Electron transition denoting the filling of a 1s hole by a $2p_{3/2}$ electron. 103, 104

References

- [1] W. H. Meiklejohn, C. P. Bean, *Phys. Rev.* **102**, 1413 (1956).
- [2] W. H. Meiklejohn, C. P. Bean, *Phys. Rev.* **105**, 904 (1957).
- [3] L. Neel, *Science (80-.)*. **174**, 985 (1971).
- [4] J. Nogués, I. K. Schuller, *J. Magn. Magn. Mater.* **192**, 203 (1999).
- [5] W. Zhang, K. M. Krishnan, *Mater. Sci. Eng. R Reports* **105**, 1 (2016).
- [6] M. Mallary, A. Torabi, M. Benakli, *IEEE Trans. Magn.* **38**, 1719 (2002).
- [7] S. A. Wolf, A. Y. Chtchelkanova, D. M. Treger, *IBM J. Res. Dev.* **50**, 101 (2006).
- [8] R. Fujiwara, T. Shinshi, E. Kazawa, *Sensors Actuators A Phys.* **220**, 298 (2014).
- [9] K. Elphick, G. Vallejo-Fernandez, T. J. Klemmer, J.-U. Thiele, K. O'Grady, *Appl. Phys. Lett.* **109**, 052402 (2016).
- [10] S. Bhatti, *et al.*, *Mater. Today* **20**, 530 (2017).
- [11] K. O'Grady, L. Fernandez-Outon, G. Vallejo-Fernandez, *J. Magn. Magn. Mater.* **322**, 883 (2010).
- [12] G. Lhoutellier, *et al.*, *J. Phys. D. Appl. Phys.* **48**, 115001 (2015).
- [13] B. Cullity, C. D. Graham, *Introduction to Magnetic Materials* (John Wiley & Sons, Inc., Hoboken, NJ, USA, 2009), second edn.
- [14] P. I. Good, J. Hardin, *Sources of Error* (John Wiley & Sons, Inc., Hoboken, NJ, USA, 2012).
- [15] S. S. P. Parkin, N. More, K. P. Roche, *Phys. Rev. Lett.* **64**, 2304 (1990).
- [16] J. Mathon, *Contemp. Phys.* **32**, 143 (1991).

- [17] J. Mathon, *J. Magn. Magn. Mater.* **100**, 527 (1991).
- [18] M. Ruderman, C. Kittel, *Phys. Rev.* **96**, 99 (1954).
- [19] T. Kasuya, *Prog. Theor. Phys.* **16**, 45 (1956).
- [20] K. Yosida, *Phys. Rev.* **106**, 893 (1957).
- [21] M. Futamoto, N. Inaba, Y. Hirayama, K. Ito, Y. Honda, *MRS Proc.* **517**, 243 (1998).
- [22] I. Dzyaloshinsky, *J. Phys. Chem. Solids* **4**, 241 (1958).
- [23] T. Moriya, *Phys. Rev.* **120**, 91 (1960).
- [24] M. L. Néel, *Ann. Phys. (Paris)*. **3**, 137 (1948).
- [25] R. C. O’Handley, *Modern Magnetic Materials - Principles and Applications* (John Wiley & Sons, Inc., Hoboken, NJ, USA, 2000).
- [26] D. R. Lide, *CRC Handbook of Chemistry and Physics, Internet Version 2005* (CRC Press, Boca Raton, FL, USA, 2005), 2085th edn.
- [27] R. C. Hall, *J. Appl. Phys.* **30**, 816 (1959).
- [28] F. Sánchez-De Jesús, A. M. Bolarín-Miró, C. A. Cortés Escobedo, G. Torres-Villaseñor, P. Vera-Serna, *J. Metall.* **2016**, 1 (2016).
- [29] H. S. Jung, W. D. Doyle, S. Matsunuma, *J. Appl. Phys.* **93**, 6462 (2003).
- [30] E. C. Stoner, E. P. Wohlfarth, *Philos. Trans. R. Soc. A Math. Phys. Eng. Sci.* **240**, 599 (1948).
- [31] L. Fernandez-Outon, K. O’Grady, S. Oh, M. Zhou, M. Pakala, *IEEE Trans. Magn.* **44**, 2824 (2008).
- [32] N. Aley, *et al.*, *IEEE Trans. Magn.* **44**, 2820 (2008).
- [33] J. van Driel, F. R. de Boer, K.-M. H. Lenssen, R. Coehoorn, *J. Appl. Phys.* **88**, 975 (2000).
- [34] I. L. Castro, *et al.*, *J. Appl. Phys.* **113**, 203903 (2013).
- [35] G. Anderson, Y. Huai, L. Miloslawsky, *J. Appl. Phys.* **87**, 6989 (2000).
- [36] M. Fecioru-Morariu, G. Güntherodt, M. Rührig, A. Lamperti, B. Tanner, *J. Appl. Phys.* **102**, 053911 (2007).

- [37] R. Carpenter, G. Vallejo-Fernandez, K. O'Grady, *J. Appl. Phys.* **115**, 17D715 (2014).
- [38] G. Vallejo-Fernandez, L. E. Fernandez-Outon, K. O'Grady, *Appl. Phys. Lett.* **91**, 212503 (2007).
- [39] M. Sonehara, T. Shinohara, T. Sato, K. Yamasawa, Y. Miura, *J. Appl. Phys.* **107**, 09E718 (2010).
- [40] X. Zhang, *et al.*, *Appl. Phys. Lett.* **102**, 022412 (2013).
- [41] W. B. Pearson, *A Handbook of Lattice Spacings and Structures of Metals and Alloys* (Pergamon Press, Oxford, England, GB, 1957), first edn.
- [42] A. Kohn, *et al.*, *Sci. Rep.* **3**, 2412 (2013).
- [43] S. Chikazumi, *Physics of Magnetism* (John Wiley & Sons, Inc., 1964), first edn.
- [44] M. N. Baibich, *et al.*, *Phys. Rev. Lett.* **61**, 2472 (1988).
- [45] G. Binasch, P. Grünberg, F. Saurenbach, W. Zinn, *Phys. Rev. B* **39**, 4828 (1989).
- [46] R. Jungblut, R. Coehoorn, M. T. Johnson, J. aan de Stegge, A. Reinders, *J. Appl. Phys.* **75**, 6659 (1994).
- [47] M. D. Stiles, R. D. McMichael, *Phys. Rev. B* **60**, 12950 (1999).
- [48] G. Vallejo-Fernandez, N. P. Aley, L. E. Fernandez-Outon, K. O'Grady, *J. Appl. Phys.* **104**, 033906 (2008).
- [49] A. Hirohata, *et al.*, *IEEE Trans. Magn.* **51**, 0800511 (2015).
- [50] M. Dunz, B. Büker, M. Meinert, *J. Appl. Phys.* **124**, 203902 (2018).
- [51] J. Emsley, *Nature's Building Blocks : An A-Z Guide to the Elements* (Oxford University Press, Oxford, England, GB, 2003).
- [52] M. Tsunoda, K.-I. Imakita, M. Naka, M. Takahashi, *J. Magn. Magn. Mater.* **304**, 55 (2006).
- [53] N. P. Aley, K. O'Grady, *J. Appl. Phys.* **109**, 07D719 (2011).
- [54] K. O'Grady, *et al.*, *J. Appl. Phys.* **128**, 040901 (2020).
- [55] I. Tomeno, H. N. Fuke, H. Iwasaki, M. Sahashi, Y. Tsunoda, *J. Appl. Phys.* **86**, 3853 (1999).

- [56] N. Aley, *et al.*, *IEEE Trans. Magn.* **45**, 3869 (2009).
- [57] G. Vinai, *et al.*, *J. Phys. Conf. Ser.* **903**, 012061 (2017).
- [58] S. Jenkins, R. F. L. Evans, *J. Appl. Phys.* **124**, 152105 (2018).
- [59] F. Letellier, *et al.*, *J. Appl. Phys.* **116**, 203906 (2014).
- [60] J. D. Dutson, *et al.*, *J. Phys. D. Appl. Phys.* **40**, 1293 (2007).
- [61] K. A. Seu, *et al.*, *J. Appl. Phys.* **93**, 6611 (2003).
- [62] V. L. Sedov, *J. Exptl. Theor. Phys.* **15**, 124 (1962).
- [63] A. Z. Men'shikov, *et al.*, *Sov. Phys. JETP* **62**, 734 (1985).
- [64] J. Kouvel, *J. Phys. Chem. Solids* **16**, 107 (1960).
- [65] P. A. Beck, *J. Less Common Met.* **28**, 193 (1972).
- [66] V. P. Antropov, Y. A. Dorofeev, V. A. Kazantsev, A. Z. Men'shikov, A. E. Teplykh, *Sov. Phys. JETP* **67**, 336 (1988).
- [67] N. C. Cramp, R. Carpenter, K. O'Grady, *IEEE Trans. Magn.* **48**, 2881 (2012).
- [68] A. Hoffmann, *Phys. Rev. Lett.* **93**, 097203 (2004).
- [69] L. Fernandez-Outon, G. Vallejo-Fernandez, S. Manzoor, K. O'Grady, *J. Magn. Mater.* **303**, 296 (2006).
- [70] K. O'Grady, R. W. Chantrell, J. Popplewell, S. W. Charles, *IEEE Trans. Magn.* **16**, 1077 (1980).
- [71] K. Zhang, *et al.*, *J. Appl. Phys.* **89**, 7546 (2001).
- [72] L. Fernandez-Outon, K. O'Grady, *J. Magn. Mater.* **290**, 536 (2005).
- [73] G. Vallejo-Fernandez, M. Vopsaroiu, L. Fernandez-Outon, K. O'Grady, *IEEE Trans. Magn.* **42**, 3008 (2006).
- [74] K. O'Grady, L. Holloway, W. Antel, *IEEE Trans. Magn.* **38**, 2741 (2002).
- [75] S. G. E. te Velthuis, A. Berger, G. P. Felcher, B. K. Hill, E. D. Dahlberg, *J. Appl. Phys.* **87**, 5046 (2000).
- [76] K. Zhang, T. Zhao, H. Fujiwara, *J. Appl. Phys.* **89**, 6910 (2001).
- [77] C. Binek, *Phys. Rev. B* **70**, 014421 (2004).

- [78] S. Polisetty, S. Sahoo, C. Binek, *Phys. Rev. B* **76**, 184423 (2007).
- [79] S. Polisetty, S. Sahoo, A. Berger, C. Binek, *Phys. Rev. B* **78**, 184426 (2008).
- [80] D. Paccard, C. Schlenker, O. Massenet, R. Montmory, A. Yelon, *Phys. status solidi* **16**, 301 (1966).
- [81] E. Pina, C. Prados, A. Hernando, *Phys. Rev. B* **69**, 052402 (2004).
- [82] K. Zhang, T. Zhao, H. Fujiwara, *J. Appl. Phys.* **91**, 6902 (2002).
- [83] M. K. Chan, J. S. Parker, P. A. Crowell, C. Leighton, *Phys. Rev. B* **77**, 014420 (2008).
- [84] P. A. A. van der Heijden, *et al.*, *Appl. Phys. Lett.* **72**, 492 (1998).
- [85] H. Xi, *et al.*, *Phys. Rev. B* **64**, 184416 (2001).
- [86] A. Goodman, K. O'Grady, M. Parker, S. Burkett, *J. Magn. Magn. Mater.* **198-199**, 12 (1999).
- [87] M. Pakala, Y. Huai, G. Anderson, L. Miloslavsky, *J. Appl. Phys.* **87**, 6653 (2000).
- [88] M. Fecioru-Morariu, S. R. Ali, C. Papusoi, M. Sperlich, G. Güntherodt, *Phys. Rev. Lett.* **99**, 097206 (2007).
- [89] N. Aley, C. Bonet, B. Lafferty, K. O'Grady, *IEEE Trans. Magn.* **45**, 3858 (2009).
- [90] T. Yamaoka, M. Mekata, H. Takaki, *J. Phys. Soc. Japan* **36**, 438 (1974).
- [91] R. Carpenter, N. C. Cramp, K. O'Grady, *IEEE Trans. Magn.* **48**, 4351 (2012).
- [92] M. Tsunoda, *et al.*, *Phys. Status Solidi B* **244**, 4470 (2007).
- [93] M. Ali, C. H. Marrows, B. J. Hickey, *Phys. Rev. B* **77**, 134401 (2008).
- [94] L. Thomas, A. J. Kellock, S. S. P. Parkin, *J. Appl. Phys.* **87**, 5061 (2000).
- [95] A. Fick, *J. Memb. Sci.* **100**, 33 (1995).
- [96] I. Langmuir, *J. Franklin Inst.* **217**, 543 (1934).
- [97] C. C. Koch, *Nanostructured Materials: Processing, Properties and Applications* (William Andrew Publishing, Norwich, NY, United States, 2006), second edn.
- [98] R. S. Barnes, *Nature* **166**, 1032 (1950).

- [99] R. E. Hoffman, D. Turnbull, *J. Appl. Phys.* **22**, 634 (1951).
- [100] D. Turnbull, R. Hoffman, *Acta Metall.* **2**, 419 (1954).
- [101] L. G. Harrison, *Trans. Faraday Soc.* **57**, 1191 (1961).
- [102] T. Surholt, C. Herzig, *Acta Mater.* **45**, 3817 (1997).
- [103] R. Balluffi, J. Blakely, *Thin Solid Films* **25**, 363 (1975).
- [104] D. Gupta, *Mater. Sci. Forum* **1**, 257 (1984).
- [105] A. S. Edelstein, R. C. Cammarata, *Nanomaterials : synthesis, properties, and applications* (Institute of Physics Publishing, Bristol, England, GB, 1996).
- [106] L. E. Fernandez-Outon, G. Vallejo-Fernandez, S. Manzoor, B. Hillebrands, K. O'Grady, *J. Appl. Phys.* **104**, 093907 (2008).
- [107] V. Baltz, B. Rodmacq, A. Zarefy, L. Lechevallier, B. Dieny, *Phys. Rev. B* **81**, 052404 (2010).
- [108] J. Keller, *et al.*, *Phys. Rev. B* **66**, 014431 (2002).
- [109] R. K. Zheng, G. H. Wen, K. K. Fung, X. X. Zhang, *J. Appl. Phys.* **95**, 5244 (2004).
- [110] A. Mumtaz, K. Maaz, B. Janjua, S. Hasanain, M. Bertino, *J. Magn. Magn. Mater.* **313**, 266 (2007).
- [111] E. Passamani, *et al.*, *J. Magn. Magn. Mater.* **299**, 11 (2006).
- [112] E. Passamani, *et al.*, *J. Magn. Magn. Mater.* **314**, 21 (2007).
- [113] B. Henne, V. Ney, M. de Souza, A. Ney, *Phys. Rev. B* **93**, 144406 (2016).
- [114] R. Rana, P. Pandey, R. P. Singh, D. S. Rana, *Sci. Rep.* **4**, 4138 (2014).
- [115] P. Tho, D. Kim, T. Phan, N. Dang, B. Lee, *J. Magn. Magn. Mater.* **462**, 172 (2018).
- [116] J. Nogués, C. Leighton, I. K. Schuller, *Phys. Rev. B* **61**, 1315 (2000).
- [117] U. Nowak, *et al.*, *Phys. Rev. B* **66**, 014430 (2002).
- [118] N. Kurti, ed., *Selected Works of Louis Néel* (Gordon and Breach Science Publishers, London, England, GB, 1988).

- [119] H. Xi, *J. Magn. Magn. Mater.* **288**, 66 (2005).
- [120] D. Mauri, H. C. Siegmann, P. S. Bagus, E. Kay, *J. Appl. Phys.* **62**, 3047 (1987).
- [121] A. P. Malozemoff, *Phys. Rev. B* **35**, 3679 (1987).
- [122] A. P. Malozemoff, *J. Appl. Phys.* **63**, 3874 (1988).
- [123] N. C. Koon, *Phys. Rev. Lett.* **78**, 4865 (1997).
- [124] T. C. Schulthess, W. H. Butler, *Phys. Rev. Lett.* **81**, 4516 (1998).
- [125] Stamps R L, *J. Phys. D. Appl. Phys.* **33**, R247 (2000).
- [126] R. E. Camley, *et al.*, *J. Vac. Sci. Technol. A* **17**, 1335 (1999).
- [127] J. Saha, R. H. Victora, *INTERMAG 2006 - IEEE Int. Magn. Conf.* (IEEE, 2006), pp. 411–411.
- [128] W. H. Meiklejohn, *J. Appl. Phys.* **33**, 1328 (1962).
- [129] E. Fulcomer, S. H. Charap, *J. Appl. Phys.* **43**, 4190 (1972).
- [130] M. Grimsditch, A. Hoffmann, P. Vavassori, H. Shi, D. Lederman, *Phys. Rev. Lett.* **90**, 257201 (2003).
- [131] M. D. Stiles, R. D. McMichael, *Phys. Rev. B* **59**, 3722 (1999).
- [132] P. A. A. van der Heijden, *et al.*, *J. Appl. Phys.* **83**, 7207 (1998).
- [133] M. D. Stiles, R. D. McMichael, *Phys. Rev. B* **63**, 064405 (2001).
- [134] M. Ali, C. H. Marrows, B. J. Hickey, *Phys. Rev. B* **67**, 172405 (2003).
- [135] U. Nowak, A. Misra, K. Usadel, *J. Magn. Magn. Mater.* **240**, 243 (2002).
- [136] H. Sang, Y. W. Du, C. L. Chien, *J. Appl. Phys.* **85**, 4931 (1999).
- [137] T. Ambrose, C. L. Chien, *J. Appl. Phys.* **83**, 6822 (1998).
- [138] K.-i. K. Imakita, M. Tsunoda, M. Takahashi, *J. Magn. Magn. Mater.* **286**, 248 (2005).
- [139] H. Uyama, *et al.*, *Appl. Phys. Lett.* **71**, 1258 (1997).
- [140] R. Street, J. C. Woolley, P. B. Smith, *Proc. Phys. Soc. B* **65**, 679 (1952).
- [141] P. Gaunt, *Philos. Mag.* **34**, 775 (1976).

- [142] R. Street, J. C. Woolley, *Proc. Phys. Soc. Sect. A* **62**, 562 (1949).
- [143] M. El-Hilo, K. O'Grady, J. Popplewell, R. W. Chantrell, N. Ayoub, *Le J. Phys.* **49**, 1835 (1988).
- [144] E. Fulcomer, S. H. Charap, *J. Appl. Phys.* **43**, 4184 (1972).
- [145] E. F. Kneller, F. E. Luborsky, *J. Appl. Phys.* **34**, 656 (1963).
- [146] G. Vallejo-Fernandez, N. P. Aley, J. N. Chapman, K. O'Grady, *Appl. Phys. Lett.* **97**, 222505 (2010).
- [147] J. Moritz, *et al.*, *Appl. Phys. Lett.* **86**, 063512 (2005).
- [148] D. Weller, A. Moser, *IEEE Trans. Magn.* **35**, 4423 (1999).
- [149] A. Moser, D. Weller, *IEEE Trans. Magn.* **35**, 2808 (1999).
- [150] D. Choo, R. W. Chantrell, R. Lamberton, A. Johnston, K. O'Grady, *J. Appl. Phys.* **101**, 09E521 (2007).
- [151] S. Soeya, T. Imagawa, K. Mitsuoka, S. Narishige, *J. Appl. Phys.* **76**, 5356 (1994).
- [152] G. Vallejo-Fernandez, B. Kaeswurm, L. Fernandez-Outon, K. O'Grady, *IEEE Trans. Magn.* **44**, 2835 (2008).
- [153] C. G. Granqvist, P. A. Burhman, *J. Catal.* **46**, 238 (1977).
- [154] C. Thompson, R. Carel, *Mater. Sci. Eng. B* **32**, 211 (1995).
- [155] G. Vallejo-Fernandez, L. E. Fernandez-Outon, K. O'Grady, *J. Phys. D. Appl. Phys.* **41**, 112001 (2008).
- [156] M. J. Carey, N. Smith, B. A. Gurney, J. R. Childress, T. Lin, *J. Appl. Phys.* **89**, 6579 (2001).
- [157] M. Vopsaroiu, M. Thwaites, S. Rand, P. Grundy, K. O'Grady, *IEEE Trans. Magn.* **40**, 2443 (2004).
- [158] G. R. Jones, M. Jackson, K. O'Grady, *J. Magn. Magn. Mater.* **193**, 75 (1999).
- [159] M. El-Hilo, K. O'Grady, R. Chantrell, *J. Magn. Magn. Mater.* **109**, L164 (1992).
- [160] A. Ehresmann, D. Junk, D. Engel, A. Paetzold, K. Röhl, *J. Phys. D. Appl. Phys.* **38**, 801 (2005).

- [161] J. Fassbender, *et al.*, *Appl. Phys. A Mater. Sci. Process.* **77**, 51 (2003).
- [162] G. Vallejo-Fernandez, K. O'Grady, *IEEE Trans. Magn.* **47**, 3304 (2011).
- [163] A. Berkowitz, K. Takano, *J. Magn. Magn. Mater.* **200**, 552 (1999).
- [164] G. Lhoutellier, D. Ledue, R. Patte, V. Baltz, *J. Appl. Phys.* **120**, 193902 (2016).
- [165] M. Vopsaroiu, M. J. Thwaites, G. Vallejo-Fernandez, S. Lepadatu, K. O'Grady, *J. Optoelectron. Adv. Mater.* **7**, 2713 (2005).
- [166] M. Vopsaroiu, *et al.*, *J. Phys. D. Appl. Phys.* **38**, 490 (2005).
- [167] E. Benes, *J. Appl. Phys.* **56**, 608 (1984).
- [168] C. S. Lu, O. Lewis, *J. Appl. Phys.* **43**, 4385 (1972).
- [169] B. D. Cullity, *Elements of X-ray Diffraction* (Addison-Wesley Publishing Company Inc., Boston, MA, USA, 1956).
- [170] R. Jenkins, R. Manne, R. Robin, C. Senemaud, *X-Ray Spectrom.* **20**, 149 (1991).
- [171] M. H. Mendenhall, *et al.*, *J. Phys. B At. Mol. Opt. Phys.* **50**, 115004 (2017).
- [172] Y.-T. Chen, *Nanoscale Res. Lett.* **4**, 90 (2009).
- [173] A. Migliorini, *et al.*, *Nat. Mater.* **17**, 28 (2018).
- [174] N. P. Aley, M. Bowes, R. Kröger, K. O'Grady, *J. Appl. Phys.* **107**, 09D722 (2010).
- [175] L. G. Parratt, *Phys. Rev.* **95**, 359 (1954).
- [176] M. Tolan, *X-Ray Scattering from Soft-Matter Thin Films*, vol. 148 of *Springer Tracts in Modern Physics* (Springer Berlin Heidelberg, Berlin, Heidelberg, 1999).
- [177] B. Henke, E. Gullikson, J. Davis, *At. Data Nucl. Data Tables* **54**, 181 (1993).
- [178] M. Björck, G. Andersson, *J. Appl. Crystallogr.* **40**, 1174 (2007).
- [179] M. Wormington, C. Panaccione, K. M. Matney, D. K. Bowen, *Philos. Trans. R. Soc. London. Ser. A Math. Phys. Eng. Sci.* **357**, 2827 (1999).
- [180] D. B. Willaims, C. B. Carter, *Transmission Electron Microscopy* (Plenum Press, New York, NY, USA, 1996).

- [181] S. Foner, *Rev. Sci. Instrum.* **27**, 548 (1956).
- [182] R. Hussain, B. Kaeswurm, K. O'Grady, *J. Appl. Phys.* **109**, 07E533 (2011).
- [183] E. O. Samwel, T. Bolhuis, J. C. Lodder, *Rev. Sci. Instrum.* **69**, 3204 (1998).
- [184] J. Clarke, A. I. Braginski, *The SQUID Handbook: Applications of SQUIDs and SQUID Systems, Volume II* (Wiley-VCH, Weinheim, Baden-Württemberg, DE, 2006).
- [185] G. Vallejo-Fernandez, L. E. Fernandez-Outon, K. O'Grady, *J. Appl. Phys.* **103**, 07C101 (2008).
- [186] G. Vallejo-Fernandez, *et al.*, *J. Appl. Phys.* **107**, 09D709 (2010).
- [187] G. Scholten, K. D. Usadel, U. Nowak, *Phys. Rev. B* **71**, 064413 (2005).
- [188] L. E. Fernandez-Outon, G. Vallejo-Fernandez, K. O'Grady, *J. Appl. Phys.* **103**, 07C106 (2008).
- [189] J. C. Slater, *J. Chem. Phys.* **41**, 3199 (1964).
- [190] K. O'Grady, private communication (to be published) (2019).
- [191] I. Polenciuc, *et al.*, *Appl. Phys. Lett.* **105**, 162406 (2014).
- [192] Measured using a MPMS VSM based at Diamond Light Source.
- [193] J. Tholence, R. Tournier, *Phys. B+C* **86-88**, 873 (1977).
- [194] L. Néel, *Adv. Phys.* **4**, 191 (1955).
- [195] M. Matsui, T. Ido, K. Sato, K. Adachi, *J. Phys. Soc. Japan* **28**, 791 (1970).

List of Publications

- *Coercivity and Training in Exchange Bias Systems*,
J. Gompertz, R. Carpenter, S. Hussain, G. Vallejo-Fernandez, K. O'Grady
Presented at York-Tohoku-Kaiserslautern Research Symposium on New Concept Spintronics Devices (2019)
- *Interface Doping Effects in IrMn/CoFe Exchange Bias Systems*
J. Gompertz, S. A. Cavill, R. Carpenter, G. Vallejo-Fernandez, K. O'Grady.
Presented by co-author at International Conference on Magnetism (2018)
- *Interface Effects in Coercivity and Training in Exchange Bias Systems*
J. Gompertz, R. Carpenter, G. Vallejo-Fernandez, S. A. Cavill, K. O'Grady.
Presented at IOP Magnetism (2018)
- *Interface Effects on Coercivity and Training in Exchange Bias Systems*
K. O'Grady, S. A. Cavill, J. Gompertz, G. Vallejo-Fernandez, R. Carpenter.
Presented by co-author at Intermag (2018)
- *Interface Effects on Coercivity and Training in Exchange Bias Systems*
K. O'Grady, J. Gompertz, G. Vallejo-Fernandez, S. A. Cavill, R. Carpenter.
Presented at RIEC International Workshop on Spintronics (2017)